HARVARD UNIVERSITY
Graduate School of Arts and Sciences



DISSERTATION ACCEPTANCE CERTIFICATE

The undersigned, appointed by the

Department of Physics

have examined a dissertation entitled

Probing Natural Supersymmetry With Initial State Radiation:
The Search For Stops And Higgsinos At ATLAS

presented by Julia Lynne Gonski

candidate for the degree of Doctor of Philosophy and hereby certify that it is worthy of acceptance.

Signature _____

Typed name: Professor Masahiro Morii, Chair

Signature _____

Typed name: Professor Melissa Franklin

Signature _____

Typed name: Professor Matthew Reece

Date: May 3, 2019

Probing Natural Supersymmetry With Initial State Radiation: The Search For Stops And Higgsinos At ATLAS

A DISSERTATION PRESENTED
BY
JULIA LYNNE GONSKI
TO
THE DEPARTMENT OF PHYSICS

IN PARTIAL FULFILLMENT OF THE REQUIREMENTS
FOR THE DEGREE OF
DOCTOR OF PHILOSOPHY
IN THE SUBJECT OF
PHYSICS

HARVARD UNIVERSITY
CAMBRIDGE, MASSACHUSETTS

MAY 2019

©2019 – Julia Lynne Gonski
all rights reserved.

Thesis advisor: Professor Masahiro Morii Julia Lynne Gonski

Probing Natural Supersymmetry With Initial State Radiation: The Search For Stops And Higgsinos At ATLAS

Abstract

Natural supersymmetry has earned a unique focus in the search for new physics, in part because of its solution to the hierarchy problem. Minimizing fine tuning in this solution often puts the superpartners of the Higgs boson (higgsino) and top quark (stop) well within LHC reach. In the most natural scenario, the higgsino and stop masses are expected to be close to the masses of their Standard Model partners. Additionally, in the case of higgsinos with multiple mass eigenstates, these masses should be close to each other. Such small mass splittings are known as a compressed spectrum. In a decay chain this presents several experimental challenges, since the final state objects are very soft and there is little missing energy. In order to build a sensitive analysis around these difficulties, a variety of new techniques are utilized, including improvements with ISR-assisted topologies using the Recursive Jigsaw Reconstruction (RJR) method. In this thesis, these novel strategies and the idea of naturalness are used as a lens to interpret the status of stop and higgsino searches with ATLAS at the conclusion of the Large Hadron Collider Run II.

Contents

0 Introduction 1

I Theory 6

1 The Standard Model 7
1.1 Particles, Forces, & Symmetries . . . 8
1.2 Experimental Verification . . . 12

2 Supersymmetry 18

3 Natural Phenomenology & Compressed Spectra 34
3.1 Compressed Stops . . . 36
3.2 Compressed Higgsinos . . . 40
3.3 Making E_T^{miss} with Initial State Radiation . . . 45

II Experiment 48

4 The Large Hadron Collider 50

5 The ATLAS Detector 56
5.1 Inner Detector . . . 62
5.2 Calorimeters . . . 64
5.3 Muon Spectrometer . . . 71
5.4 Magnet System . . . 75
5.5 Trigger System . . . 76
5.6 Event Reconstruction . . . 78

III Strategies 89

6 Recursive Jigsaw Reconstruction 91
6.1 Methodology . . . 92
6.2 Application . . . 96

7 Event Cleaning 104
7.1 Jet Cleaning Variables . . . 106
7.2 Run II Procedure & Performance . . . 110

8 Statistical Methods 116
8.1 Hypothesis Testing . . . 117
8.2 Likelihood Fitting . . . 119
8.3 Analysis Strategy & `HistFitter` . . . 121

IV Searches 125

9 For Third Generation SUSY 127
9.1 Data/MC Samples . . . 129
9.2 Object Requirements . . . 131
9.3 Signal Regions . . . 133
9.4 Background Estimation . . . 152
9.5 Systematic Uncertainties . . . 173
9.6 Results . . . 180

10 For Electroweak SUSY 188
10.1 Data/MC Samples . . . 191
10.2 Object Requirements . . . 193
10.3 Signal Regions . . . 197
10.4 Background Estimation . . . 208
10.5 Systematic Uncertainties . . . 231
10.6 Results . . . 239

V Outlook 248

11 Future Efforts 249

12 Conclusion 253

Appendix A Jet Quality Variables 256
A.1 Good and Fake Jet Regions . . . 256
A.2 EM Jet Kinematic Variables . . . 259
A.3 LCW Jet Quality Variables . . . 259

Appendix B For Electroweak SUSY: Additional Material 264
B.1 Low-E_T^{miss} Higgsino Regions 264
B.2 1L+Track Higgsino Regions 268

References 283

Acknowledgments

In a high energy physics dissertation, there are always a lot of people to thank. I have had the true privilege of working with many talented physicists throughout my time in LHC experimental research thus far, for whom I have immense respect, affection, and gratitude.

I first began doing research in collider physics as an undergraduate at Rutgers University, and owe this opportunity to my mentor Mohan Kalelkar, as well as my adviser Eva Halkiadakis, whose continuing support has been essential to my development as a scientist.

My first years in graduate school were spent working on the micromegas cosmic ray test stand at Harvard, and I thank Paolo Giromini, Hugh Skottowe, and Nathan Felt, who provided me with hardware education and training for this project.

A huge thanks to Chris Rogan, Paul Jackson, and Siyuan Sun for generative conversations about the Recursive Jigsaw Reconstruction method, providing the foundation for this dissertation work.

My authorship qualification task at ATLAS was completed in the jet/E_T^{miss} working group, where I had several fantastic colleagues and mentors who deserve mention, including Max Swiatlowski, Kate Pachal, Teng Jian Khoo, Chris Young, Jeff Dandoy, and many others. I particularly thank David Miller, for managing my qualification and my various other performance projects in the group, along with Emma Tolley and Valerio Ippolito, who gave me a thorough knowledge base.

I had the pleasure of interacting with lots of wonderful physicists in the SUSY group throughout my degree. Thanks to Javier Montejo Berlingen, Keisuke Yoshihara, and Sophio Pataraia, for coordinating the stop 1L search; Joana Machado Miguens and Mike Hance, who have done excellent work with electroweak SUSY; and my teammates on the compressed electroweak analysis, including Jesse Liu, Jeff Shahinian, Joey Reichert, Michael Holzbock, Elodie Resseguie, Lorenzo Rossini, Shunichi Akatsuka, and Andy Aukerman; as well as Till Eifert and Federico Meloni, for their efforts as convenor. Special mention goes to Zach Marshall, whose knowledge, help, and advice on so many aspects of LHC physics was irreplacable.

My professional development would not have been complete without a network of other colleagues, both in and outside the field, that gave me a community beyond research and supported me in various side projects. I thank my outreach collaborators, especially Steve Goldfarb and Sarah Charley, who enabled me and gave me inspiration in such an influential aspect of my time as a graduate student. My colleagues at the US LHC User's Association, notably Harvey Newman and Corrinne Mills, gave me innumerable opportunities and connections in the physics community for which I am very grateful. I also owe recognition to the American Physical Society, in particular to Tim Gay, John Rumble, Roger Falcone, David Gross, and Kate Kirby, for steadfastly backing me and giving me invaluable experience on navigation of the American physics enterprise.

I am grateful for everyone in the Harvard ATLAS group that I have had the pleasure of working alongside through these five years, in particular John Huth and Roxanne Guenette. Special thanks go to my committee members Matthew Reece and particularly Melissa Franklin, for thought-provoking conversations throughout my time as a graduate student.

I owe everything I know to my adviser Masahiro Morii, who I can truly never thank enough for the years of wisdom, support, and encouragement; and to Stefano Zambito, whose physics acumen and extensive experience kept my enthusiasm high through both successes and inevitable challenges.

Finally, thanks to my family, without whom none of this would have been possible; my genuinely awe-inspiring crew of friends, who always have my back; and of course Sam, for just everything.

It's tough to get through a Ph.D. without a good amount of luck. To have known all of these people, I really am fortunate beyond words. Thank you.

Sometimes you have to play a long time to be able to play like yourself.

Miles Davis

0

Introduction

The goal of modern particle physics is to understand the fundamental laws of nature. Such a simple statement of the task belies its size and complexity. Achievement requires knowledge of the elementary constituents of the universe, their interactions with one another, and how those interactions manifest at all possible energy levels. This does not come without difficulties. Since

the birth of the universe 13.8 billion years ago, these fundamental laws of nature have taken varying forms, requiring increasingly innovative forensics efforts to trace them back to their origins. Another key obstruction is the unavoidable consequence of quantum mechanics, which dictates a base level of uncertainty that shrouds any statement in probabilistic terms.

Trapped within such confines, the journey towards this complete knowledge of nature is marked by the building and testing of models, working ever closer to a complete picture. Throughout this pattern of question and answer, numerous campaigns have been made against these limiting factors, to great success on the part of physics research. The probabilistic quality of physics led to a reinterpretation of the elementary degrees of freedom as fields rather than particles, translating the classical lexicon of elements, atoms, and protons into a new language, that of quantum field theory. Furthermore, technical advances in particle acceleration & detection have allowed research to take place at energies rivaling the environment of the Big Bang, bringing the frontiers of knowledge tantalizingly close to the absolute beginning.

Centuries of this steady and persistent progress have brought the field to an appealing, yet palpably imperfect, resting point: the Standard Model. This model contains a set of particles known at present to be fundamental, provides a framework through which they all communicate, and most importantly, it does all this in a way that is predictive of reality and verifiable by experiment. The Standard Model is a remarkable achievement; however, some questions and flaws persist. It is clear that the Standard Model is incomplete, and that some beyond the Standard Model physics must exist to fill in the gaps and make sense of the remaining mysteries.

Supersymmetry is a novel and refined option for this task. Its genesis can be traced back several

decades, although the discovery of a 125 GeV Higgs-like boson in 2012 positioned it under a unique spotlight. Supersymmetry extends the Standard Model to a vast number of new fundamental particles, along the way providing a viable dark matter candidate, a sensible motivation for the value of the physical Higgs mass, and a unification of fundamental forces, among other things. Perhaps as importantly for physicists, it can take a huge variety of forms, leading to a proliferation of ideas for experimental investigation. In the context of solving problems in the Standard Model, some of these forms are more compelling than others. Given that a search has to start somewhere, the most well-motivated models are often used as the compass for experimental forays. A particular category of supersymmetry models known as natural has assumed this role for many physicists, encircling a set of theories that are both theoretically well-motivated and testable at accessible energy levels.

Two of the new particles proposed in supersymmetry, called the stop and higgsino, have a particularly notable role in these natural models. As a result, searches for stops and higgsinos have been an integral part of the supersymmetry program, with the theory providing a clear and encouraging notion of how such particles appear in modern detectors, and where they are likely to exist in the vast phase space of supersymmetry. A first pass through these clear and encouraging options, performed with past experiments like the Tevatron at Fermilab and the first run of the Large Hadron Collider at the European Organization for Nuclear Research (CERN), was not successful. No evidence for the existence of stops or higgsinos appeared in collider datasets. This is not to say that they do not exist, but rather, that the task of finding them is more complicated than was initially assumed. This thesis is about some of the hard searches, the ones that must be done when the first ideas don't work out, and the ways in which physicists get creative to make the impossible possible.

The telling of this story necessarily begins with an overview of the theoretical landscape, both known and unknown, which is provided in Part I. Chapter 1 introduces the Standard Model of particle physics, followed by a synopsis of the theory of supersymmetry in Chapter 2. Chapter 3 provides a phenomenological perspective on the detector signatures of natural supersymmetry models, connecting the theoretical idea to the observation possibilities.

Part II details the experimental means to test the theory. Chapters 4 describes the Large Hadron Collider, the largest experiment in the world, colliding protons at nearly the speed of light outside the city of Geneva in Switzerland. Chapter 5 introduces a detector of these collisions, ATLAS, and explains the subsystems and data-taking capacity that enable the modern high energy physics analyses detailed here.

In doing such analyses, various techniques are applied to the process of sifting through data and quantifying its characteristics. Part III details a subset of this methodology, discussing three techniques that are especially relevant to the work discussed in this treatment. Chapters 6 introduces the Recursive Jigsaw Reconstruction method used to provide additional sensitivity to certain natural supersymmetry searches. Chapter 7 gives the motivation and mechanism of the event cleaning procedure, which eliminates particular sources of non-collision and noise-related backgrounds from sensitive analysis regions. The last strategy is the use of common particle physics statistical methods to quantify and characterize the results of searches, as discussed in Chapter 8.

Part IV then dives into the searches themselves, discussing two in detail; one for the stop in Chapter 9, and one for the higgsino in Chapter 10. These two chapters describe the motivation, construction, and results of each analysis, highlighting where the strategies of Part III are utilized. This thesis

concludes with an outlook in Part V, including a discussion of future search prospects in Chapter 11, and conclusions in Chapter 12.

Part I

Theory

1

The Standard Model

To discuss what particle physics is working towards, it is necessary to describe where it stands at present. The Standard Model is the current best theory for describing the fundamental interactions of all known elementary particles. It is a composite theory patched together from decades of speculation and subsequent discovery, culminating in a model that has been strikingly

predictive throughout decades of experiments. In this chapter, the Standard Model is discussed; Section 1.1 describes its contents, and Section 1.2 gives a history of its experimental victories as well as its imperfections.

1.1 Particles, Forces, & Symmetries

The Standard Model (SM) of particle physics is a renormalizable quantum field theory that is invariant under transformations of the local symmetry G_{SM} given in Equation 1.1. It is spontaneously broken as follows:

$$G_{SM} = SU(3)_C \otimes SU(2)_L \otimes U(1)_Y \;\Rightarrow\; SU(3)_C \otimes U(1)_{EM} \tag{1.1}$$

Each symmetry is, by definition, a group of field transformations that leave the Lagrangian invariant. The representations of this group constitute the spin-1/2 fermions, organized into three mass generations, which make up all known matter in the universe. There are three generators of the group, corresponding to three gauge boson degrees of freedom that represent fundamental forces, along with a single scalar field. To determine how the interplay between these constituents forms a viable description of nature, it is assistive to examine the most generic renormalizable Lagrangian that contains the fermionic and bosonic fields that emerge from this symmetry (Equation 1.2).

$$\mathcal{L} = \mathcal{L}_{kin} + \mathcal{L}_{\psi} + \mathcal{L}_{Yuk} + \mathcal{L}_{\phi} \tag{1.2}$$

Each of these allowable groups of terms can be traced to physical realities in particle physics.

- $\mathcal{L}_{kin}$ describes the propagation of the fields in spacetime and the gauge interactions:

$$\mathcal{L}_{kin} = -\frac{1}{4}(F^a_{\mu\nu})^2 + \bar{\psi}(i\not{D})\psi - |D_\mu\phi|^2 \tag{1.3}$$

  Here, $F^a_{\mu\nu} = \partial_\mu A^a_\nu - \partial_\nu A^a_\mu + g f^{abc} A^b_\mu A^c_\nu$, $D_\mu = \partial_\mu - igA^a_\mu t^a_r$, and $\not{D} = \gamma^\mu D_\mu$ for fermion fields ψ, scalar field ϕ, gauge fields A, representation matrices t^a_r, structure constants f^{abc} ($= 0$ for the electroweak force), and matrices γ^μ that are representations of the Clifford algebra. This part of the Lagrangian determines the fundamental forces (electromagnetism, the strong force, and the weak force), with one such term for each of the gauge boson degrees of freedom. Each force corresponds to a group in Equation 1.1: $SU(3)_C$ is the symmetry group of the strong interaction, and $SU(2)_L \times U(1)_Y$ corresponds to the electroweak interaction, which is spontaneously broken in electromagnetic and weak force components. Forces are mediated by a designated spin-1 gauge boson, specifically the gluon and photon/$W^\pm$/Z^0 bosons for the strong and electroweak interactions respectively. Gravity is not included in the theory.

- $\mathcal{L}_\psi$ gives the Dirac or Majorana fermion mass terms. This part is equal to 0 in the SM.

$$\mathcal{L}_\psi = 0 \tag{1.4}$$

- $\mathcal{L}_{Yuk}$ describes the Yukawa interactions:

$$\mathcal{L}_{Yuk} = y_{ij}\bar{\psi}_i\psi_j\phi \tag{1.5}$$

  These terms connect all fermions to one another via the scalar field and the Yukawa coupling y_{ij}, where i and j represent different fermion representations.

- $\mathcal{L}_\phi$ gives the scalar potential:

$$\mathcal{L}_\phi = -\mu^2\phi^\dagger\phi - \lambda(\phi^\dagger\phi)^2 \tag{1.6}$$

  which leads to spontaneous electroweak symmetry breaking via the Higgs mechanism. Here, μ and λ are parameters that determine the shape of the Higgs potential.

This Lagrangian provides a complete description of nature at its fundamental level, consisting of three forces, five bosons (gluon g, photon γ, $W^{\pm}$, Z^0, and Higgs), and twelve fermions (six quarks and six leptons). Since all of the forces emerge from symmetries in the SM, Noether's theorem dictates that they each introduce a conservation law and thus a charge. Particles that interact via the electromagnetic force carry electrical charge; the same relationship exists for the strong force and color, and the weak force and weak charge.

The strong force is unique in that is a non-Abelian group as described by quantum chromodynamics (QCD); that is, the structure constant $f^{abc} \neq 0$ and the gluon carries color charge. This leads to a gluon self-interaction and a strong coupling constant α_s that "runs" as a function of interaction scale, generating several interesting properties. One of these is *asymptotic freedom*, meaning that as the interaction energy goes to ∞, the coupling constant approaches zero, the interaction is diminishingly weak, and quarks can propagate as free particles. The other side of this effect is *confinement*: at very low energies, α_s goes to ∞, and the strong force diverges. As a result, quarks and gluons can never be observed as free particles. Instead, strong force bound states called hadrons form out of two or three quarks, creating particles known as mesons and baryons, respectively.

The complete Standard Model can be seen diagrammatically in Figure 1.1, where its constituents are organized by type and mass generation. Each particle represents an entity that has no further internal structure and can be uniquely characterized by a set of quantum numbers. Three of these numbers are listed along with each entry: mass, electrical charge, and spin. A particle's mass and spin are derived from their representation of the Poincaré group, which is an external symmetry group in that it describes actions taken in spacetime such as rotations, translations, and boosts. In contrast,

other quantum numbers describing a particle's ability to participate in the various fundamental interactions are derived from internal symmetries of the Lagrangian. All known stable matter can be found in the first mass generation, while the heavier generations decay into lighter particles according to their allowed interactions.

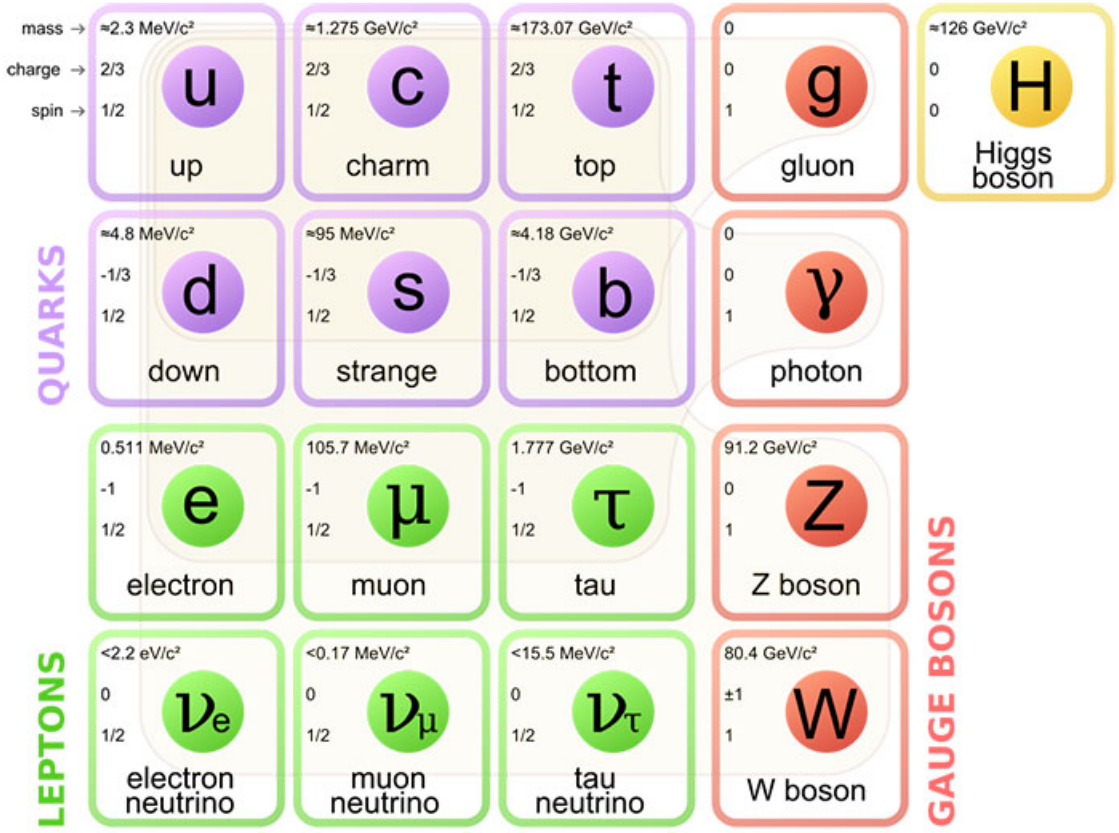


Figure 1.1: The Standard Model of particle physics.

As a relativistic quantum field theory, the Standard Model is invariant under the combined reversal of three fundamental symmetries (CPT):

1. Charge conjugation (C), which transforms particles into their *anti-particles* by reversing their charge and all internal quantum numbers. Neutral bosons (photon, Z^0, Higgs) are their own

antiparticles.

2. Parity conjugation (P), which transforms a left-handed particle into a right-handed particle by the reversal of spatial coordinates. The weak interaction violates parity maximally; no right-handed particles feel the weak force.
3. Time reversal (T).

The combined operation CP transforms matter into anti-matter. There is a small amount of CP violation in the Standard Model, discovered via the decay of strange-flavored mesons [1]. This is attributable to the presence of a phase in the Cabibbo-Kobayashi-Maskawa (CKM) matrix, which describes mixing between quark flavors in weak interactions. Since the universe appears to be dominated by matter, the amount of CP violation in the SM is especially relevant to the evolution of the universe and the reason behind this asymmetry.

1.2 Experimental Verification

The parameters of the Standard Model are experimentally determined, demonstrating an extensive landscape of accelerator and detector technology elapsing over decades. Yet just as there is ample evidence that bolsters the theory, there are results that reveal its deficiencies. Reviewing both successes and failures is necessary to understand the current state of the field.The following is a brief historical overview of these influential experimental results, covered in much greater detail in other works [2].

1.2.1 Historical Timeline

The Standard Model coalesced into a unified theoretical framework in the 1960s through the work of Glashow, Weinberg, Salam, and others on the unification of electromagnetism and the weak in-

teraction [3, 4, 5]. At the time, this early version of the SM had recently expanded from a simple relation of leptons and forces to include a quark model and the foundations of QCD, a spontaneous symmetry breaking mechanism by which all particles acquired mass, and renormalizability [6]. The following decades gave way to a cascade of new particles, each solving a different problem in the existing model.

The charm quark, discovered in 1974 by way of the J/ψ particle [7, 8], explained the absence of flavor-changing neutral currents. The τ lepton [9] (1975) and bottom quark [10] (1977) gave rise to a third matter generation, giving a mechanism for the observed CP violation through the complex phase of the CKM matrix [11]. The $W^{\pm}$ and Z^0 bosons, long predicted to have masses on the weak scale, were discovered at the CERN Super Proton Synchrotron in 1983 [12]. The top quark discovery at the Fermilab Tevatron in 1995 [13, 14] and the Higgs boson observation at the Large Hadron Collider in 2012 [15, 16] were the final pieces missing from the puzzle. As of 2012, all particles concretely predicted to be in the Standard Model had been found.

This current version of the Standard Model has remarkable capabilities for describing the natural world. An an example, the running of the strong coupling constant α_s predicted by QCD has been corroborated in a variety of different particle interactions, as shown in Figure 1.2. Furthermore, the compatibility of theoretically computed and experimentally determined cross sections for processes of interest is strong (see Figure 1.3).

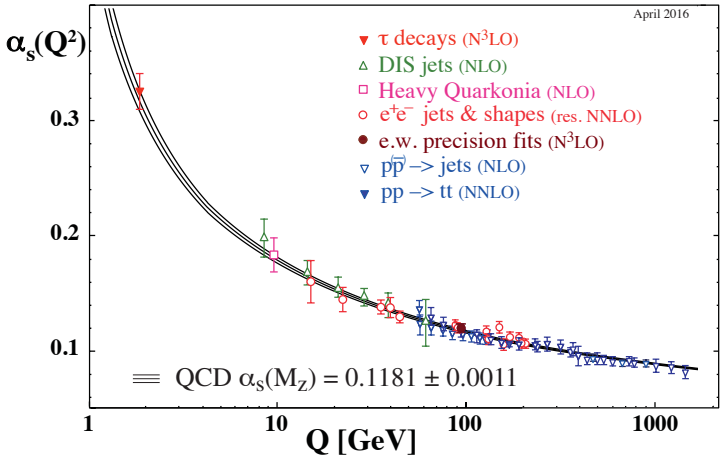


Figure 1.2: Summary of measurements of α_s as a function of the energy scale Q [17].

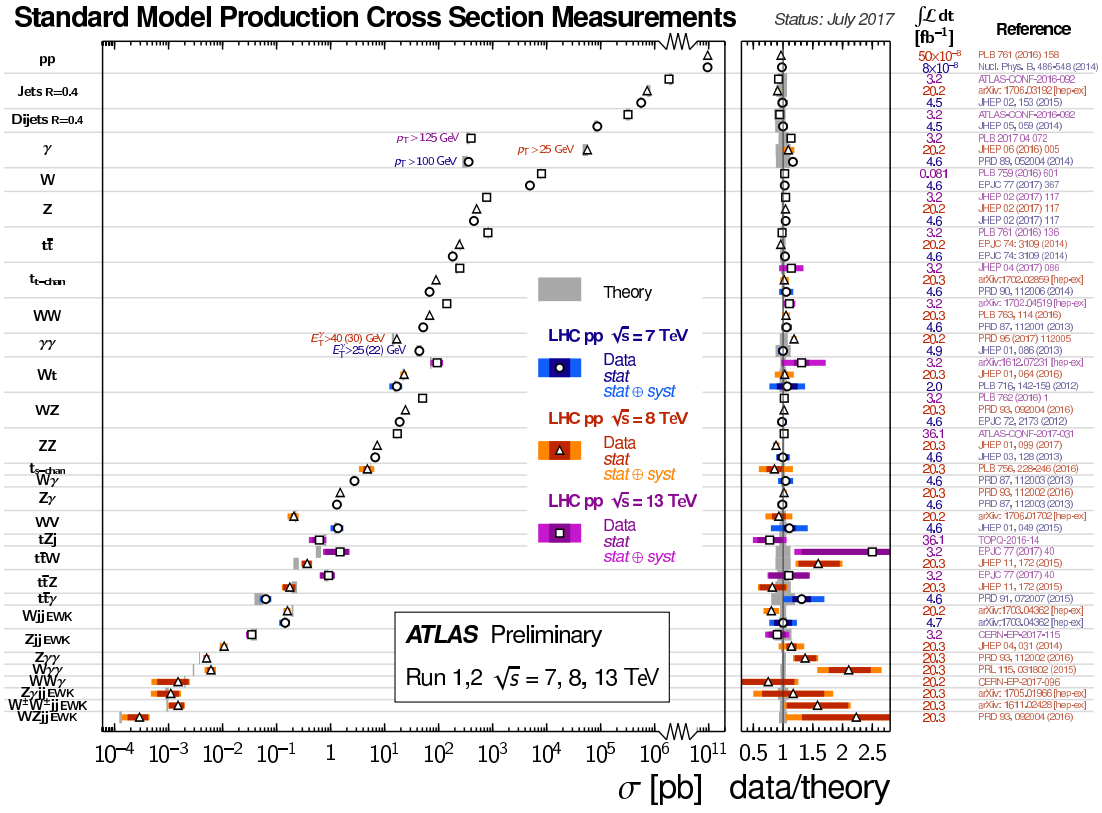


Figure 1.3: Overview of cross section measurements for several processes of interest, as obtained by the ATLAS Experiment [17].

1.2.2 Shortcomings

Armed with a strong theoretical foundation and extensive experimental confirmation, the Standard Model is a solid theory. However, there are some problems that remain unsolved.

- Despite having a clear explanation for the strong, weak, and electromagnetic forces, the Standard Model does not describe gravity.
- It also does not have a viable candidate for dark matter (DM), a nonluminous, noninteracting, and long-lived form of matter that must exist to account for the total gravitational strength in rotating galaxies [18].
- Though spontaneous electroweak symmetry breaking is required to explain the observed particle spectrum, it is not clear through what mechanism this process occurs.
- The SM has 19 free parameters, which span several orders of magnitude. This large difference across parameter values, and characteristic interaction energy/length scales as a corollary, is known as the *hierarchy problem*.
- It is not understood why the Higgs couplings to fermions and thus their masses are so unequal, known as the *flavor puzzle*.
- Recent experimental evidence via neutrino oscillations points to small but non-negligible masses for these particles [19], though the mechanism that gives this mass is still unclear.
- The large discrepancy between matter and anti-matter density in the universe today is not sufficiently explained by the known amount of CP violation in the SM, prompting questions about the origin of this asymmetry.

These issues are all key components of the global high energy physics research program, because they indisputably point to the necessity of new beyond the Standard Model (BSM) physics. Furthermore, the lack of evidence for new physics thus far indicates that this hypothetical but necessary new physics must exist at energies larger than the current experimental reach.

This relationship between physics realization and energy emerges from the notion that each interaction has its own characteristic energy scale, which in turn determines the masses of participating particles. The running of the strong coupling determines its characteristic scale at 200 MeV, which is also the mass of hadrons made of light quarks. The electroweak scale is an order of magnitude higher, at the Higgs vacuum expectation value (vev) of 246 GeV, again similar to the masses of the Higgs, W, and Z bosons. It is clear that probing BSM physics will reveal new interactions, and thus introduce higher mass scales where new particles can exist.

Discussing this hierarchy of different gauge strengths, further confusions with the Standard Model are uncovered. As determined from Newton constants of classical gravitational interactions, the characteristic scale of gravity is the Planck scale, $M_{Pl} \sim 10^{19}$ GeV. Is it possible that nature has a "gauge desert" (see Figure 1.4), in that are no emergent scales between the electroweak and gravitational forces? If so, why are the magnitudes of the fundamental forces so different? Even if this inequality was accepted as truth, the stability of the existing hierarchy is under question in the context of quadratically divergent corrections to the Higgs mass, discussed more in the next chapter.

All of these questions unequivocally point to the necessity of beyond the Standard Model physics. There is no end to the prospective theories that attempt to solve these problems. However, one of them in particular deserves mention due to its mathematical elegance and expansive manifestations: *supersymmetry*.

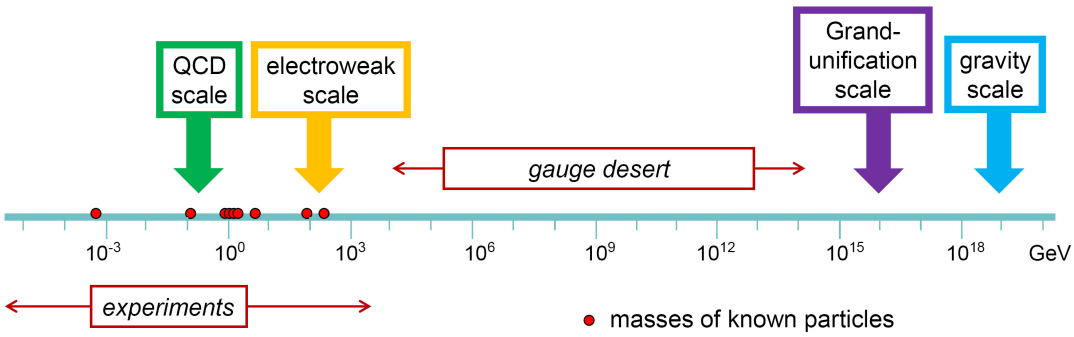


Figure 1.4: Scan of energy ranges in particle physics, annotated by relevance of fundamental forces, known particle masses, and experimental reach.

2

Supersymmetry

One of the primary motivations for the theory of supersymmetry is solving the *hierarchy problem*. This unanswered question in the Standard Model pertains to the visible mass of the Higgs boson. In the SM, the physical mass of the Higgs is given as the sum of two terms, shown in Equation 2.1.

$$m_H^2 = m_{H,tree}^2 + \Delta m^2 \tag{2.1}$$

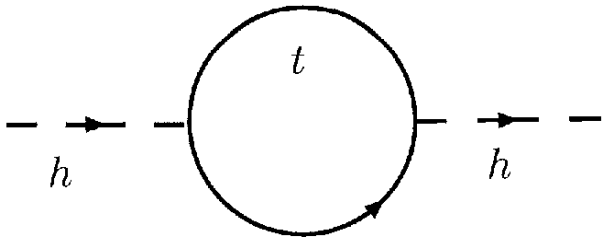


Figure 2.1: Feynman diagram showing top quark loop in the Higgs boson propagator.

Here, $m_{H,tree}$ is the tree mass of the Higgs, which is a free parameter, and Δm is a radiative corrections term. These corrections stem from loop Feynman diagrams in the Higgs propagator, an example of which can be found with a top loop as shown in Figure 2.1. This diagram contributes especially strongly because the top is the most massive quark, and therefore has the largest coupling to the Higgs. Taking the top loop as an example, this corrections term Δm takes the form shown in Equation 2.2.

$$\Delta m^2 = -\frac{|y_t|^2}{16\pi^2}\left[2\Lambda^2 + \mathcal{O}\left(m_t^2 \ln\left(\frac{\Lambda}{m_t}\right)\right)\right] \tag{2.2}$$

Here, y_t is the Yukawa coupling of the top quark t and Λ is the cutoff energy of the theory, above which the SM ceases to be valid and new physics must enter. It is evident that Δm goes as the cutoff scale Λ. If there is no new physics outside of the Standard Model, these corrections will be on the order of the Planck scale, as shown in Figure 1.4.

The 2012 discovery of a Higgs-like particle at 125 GeV put this relationship into the spotlight [15, 16]. With a physical mass on the order of the weak scale (10^4 GeV^2), and a quadratic corrections term of order 10^{38} GeV^2, only a dramatic coincidence of 1 in 10^{34} could put the value of the tree

mass parameter $m_{H,tree}$ at precisely the right place to maintain Equation 2.1. Such a coincidence represents a very large amount of *fine tuning*, meaning that free parameters are constrained and required to cancel to an extremely high precision. A general quantifiable measure of fine tuning Δ is given in Equation 2.3 [20]. Qualitatively, avoiding fine tuning means that Δ is kept small, indicating that the size of the corrections term is smaller than $m_{H,tree}$.

$$\Delta \equiv \frac{2\Delta m_H^2}{m_{H,tree}^2} \tag{2.3}$$

The solution offered by supersymmetry is the existence of a second corrections term $\Delta\tilde{m}$, arising from a new particle being introduced with spin differing by 1/2 with respect to the original SM partner. In the previously used example of a SM top quark t, this means an SM boson S is introduced, with the following analogous coupling as given in Equation 2.4. Note that the sign of the corrections term is opposite to that in Equation 2.2.

$$\Delta\tilde{m}^2 = +\frac{|y_S|^2}{16\pi^2}\left[2\Lambda^2 + \mathcal{O}\left(m_S^2 \ln\left(\frac{\Lambda}{m_S}\right)\right)\right] \tag{2.4}$$

Since this new particle only differs from its SM partner by a spin of 1/2, it can reasonably be expected to have a similar coupling to the Higgs, and the magnitudes of y_t and y_S can be approximately equal. Therefore, since both radiative corrections terms are equal and opposite, they can essentially cancel out. The residual correction term in the case of the top can then be written as shown

Equation 2.5.

$$\Delta m_H^2 = \Delta m^2 + \Delta \tilde{m}^2 = \frac{y_t^2}{16\pi^2}|m_S^2 - m_t^2| \tag{2.5}$$

Equation 2.3 can now be used to imagine the upper limit on the amount of fine tuning in the theory. To relieve the pressure of fine tuning constraints in this expression and ensure that the corrections term is reasonably on the scale of the tree mass parameter, the masses of the partner particles are further constricted:

$$|m_S^2 - m_f^2| \lessapprox 1\, TeV^2 \tag{2.6}$$

This relationship indicates that in such a desirable manifestation of supersymmetry, with cancellation of Higgs mass radiative corrections to first order and little fine tuning, new particles could emerge at the TeV scale.

With the inclusion of this new boson S and $\Delta\tilde{m}$ necessarily comes partner loop diagrams in the Higgs propagator, as reflected in Figure 2.2, and in turn these new loops represent new particles. However, this example so far has only utilized the top loop contribution. In reality, all particles that couples to the Higgs participate in similar loop diagrams, and thus new partner particles will be generated to provide a cancellation of corrections terms. In this way, the resolution of the hierarchy problem via the addition of a second Higgs mass corrections term creates not just one but many new particles, each of which is a partner to a Standard Model particle, and a new symmetry that relates them, supersymmetry (SUSY) [21]. The prediction of superpartners for each SM particle generates a

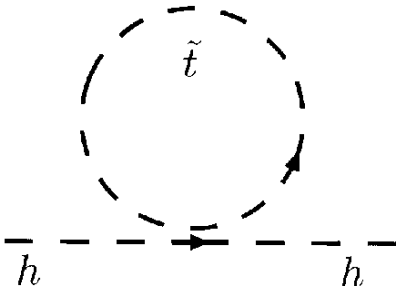


Figure 2.2: Feynman diagram showing the supersymmetric top partner loop in the Higgs boson propagator.

vast new phase space in which to search for yet-to-be-discovered particles (see Figure 2.3).

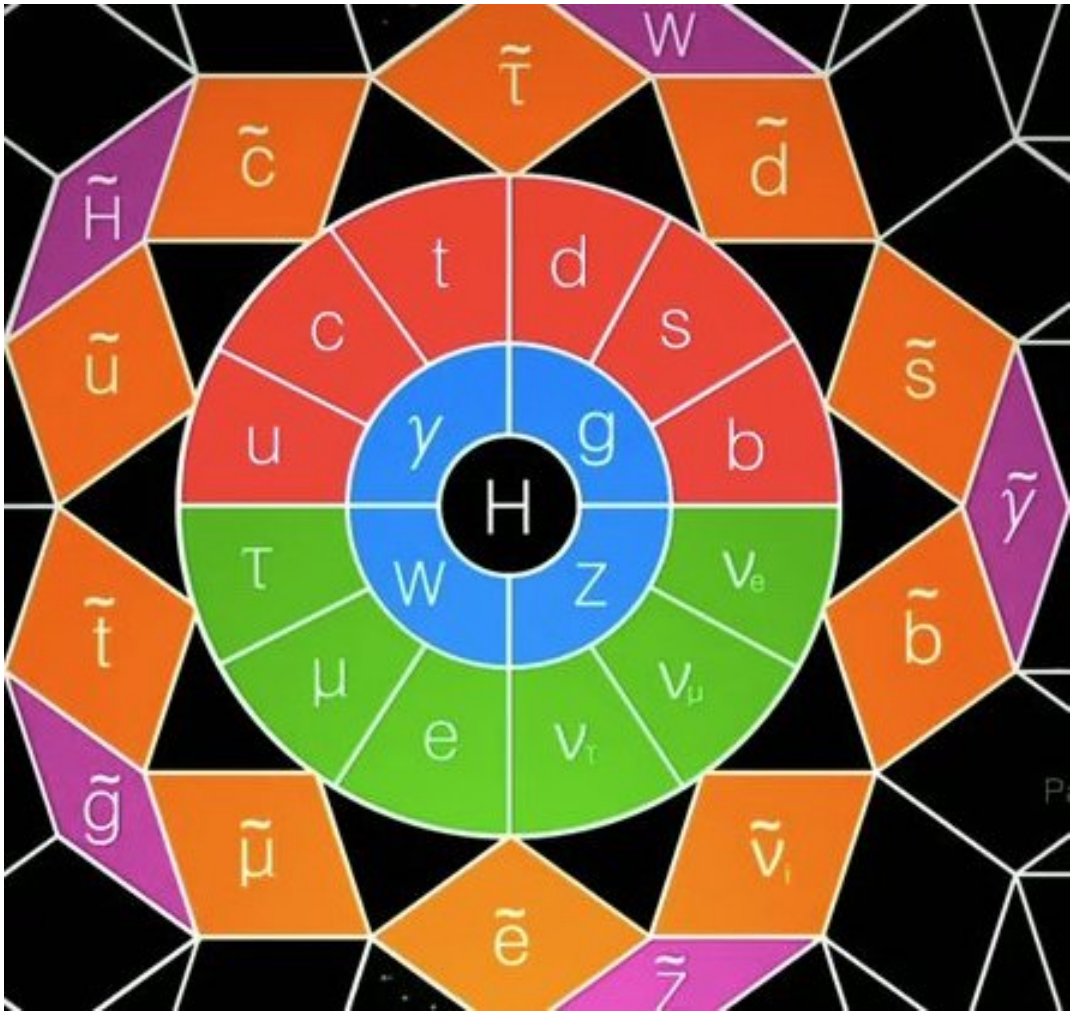


Figure 2.3: Illustration of new sparticles predicted in supersymmetry [22].

The new states predicted by SUSY all differ from their SM partners by half a unit of spin. All fermions in the Standard Model have bosonic superpartners and vice versa. Of these new particles, all partners of SM bosons are named with the suffix "-ino", and all partners of fermions are named with the prefix "s-". For example, the SUSY partner of the gluon is called a *gluino*, and the partner of a Standard Model quark is called a *squark*. Supersymmetric partners are indicated by the addition of a $\tilde{}$ to the SM particle symbol. The masses of these superpartners (or *sparticles*) can in principle be the same as their SM counterparts, but the lack of observation of supersymmetric particles at common collider energy scales rules this mass relationship out. SUSY must therefore be a broken symmetry, with superpartner masses heavier than current SM particles and above the current experimental reach.

The extension of the SM Lorentz group through an additional supersymmetry has many possible manifestations, given the number of generators in the symmetry group and the arrangement of particles into supermultiplets. As a result, a huge variety of SUSY models and frameworks exist that extend the SM in this way. The one that introduces the smallest number of new particles is the minimal supersymmetric extension to the Standard Model (MSSM) [23, 24, 25, 26]. Because of its relative simplicity in a vast field of potential SUSY workings, the MSSM can be used as a useful benchmark for further discussions.

A new quantum number, R, is defined to have values that distinguish between standard and supersymmetric particles. It is a function of baryon number B, lepton number L, and particle spin

as seen in Equation 2.7.

$$P_R = (-1)^{3B+L+2s} \tag{2.7}$$

With this definition, all SM particles have P_R = +1, and all SUSY particles have P_R = -1. In the MSSM, the discrete symmetry of R-parity is conserved in all interactions. This has several effects. First, it ensures that the MSSM accurately reflects the observed universe, specifically that baryon or lepton number violating operators do not exist. Additionally, it means that SUSY particles can only be produced in pairs in collisions of SM particles, and that the lightest supersymmetry particle (LSP) cannot decay and thus must be stable.

In the MSSM, the Higgs sector is extended to include two Higgs doublets. After electroweak symmetry breaking, they mix with the other supersymmetric electroweak boson partners to form six fermionic mass eigenstates, two of which are charged ($\widetilde{\chi}^{\pm}_{1,2}$) and four of which are neutral ($\widetilde{\chi}^{0}_{1,2,3,4}$). These mass eigenstates are referred to as charginos and neutralinos, respectively. In this scenario, the lightest neutralino $\widetilde{\chi}^{0}_{1}$ can be assumed to be the LSP. Since it is naturally massive, neutral, stable (due to R-parity conservation), and weakly interacting, the LSP can be taken as a viable dark matter candidate. In this way, though SUSY was motivated in this treatment by the hierarchy problem, it has the potential to solve the dark matter mystery as well [27, 28].

In the sfermionic sector, a similar mixing occurs between left- and right-handed squarks. The difference between mass eigenstates is only non-negligible for the third generation squarks, since the mixing depends on the mass of the SM fermion. Therefore, mixing between left- and right-handed

top squarks yields two distinct mass eigenstates denoted $\widetilde{t_1}$ and $\widetilde{t_2}$ where $\widetilde{t_1}$ is the lighter of the two (hereafter referred to as the *stop*). The stop is again a particularly important discussion point because it is a dominant contributor to the stabilization of the Higgs mass, as described earlier in this section (see Figure 2.2).

This role of the stop quark in solving the hierarchy problem gives rise to an additional set of requirements on its mass, which are crucial in determining the feasibility of a SUSY discovery in the current collider search program. However, to observe a particle, it must be possible to produce it. Unfortunately the production cross sections for supersymmetric particles are strikingly low at the LHC, in many cases several orders of magnitude below typical SM processes (Figure 2.4). This adversity in the course of producing such particles in an experimental environment motivates creative and effective novel analysis strategies, to ensure that in the rare collision where such a particle might have been made, it is likely to be detected. These aspects of SUSY production and hunting will be discussed in later chapters of this thesis.

Naturalness

The notion that certain mass choices for sparticles can minimize the amount of fine tuning in the theory is known as *naturalness*. Specifically, a fully natural manifestation of supersymmetry would allow the quadratic corrections terms in Equations 2.2 and 2.4 to cancel each other out to high precision. A corollary of this cancellation is that the stop mass is equal to that of the top mass, so that the loop diagrams of Figures 2.1 and 2.2 cancel evenly as well. However, as discussed, the current state of particle physics prohibits this, and SUSY particles must be heavier than their SM partners.

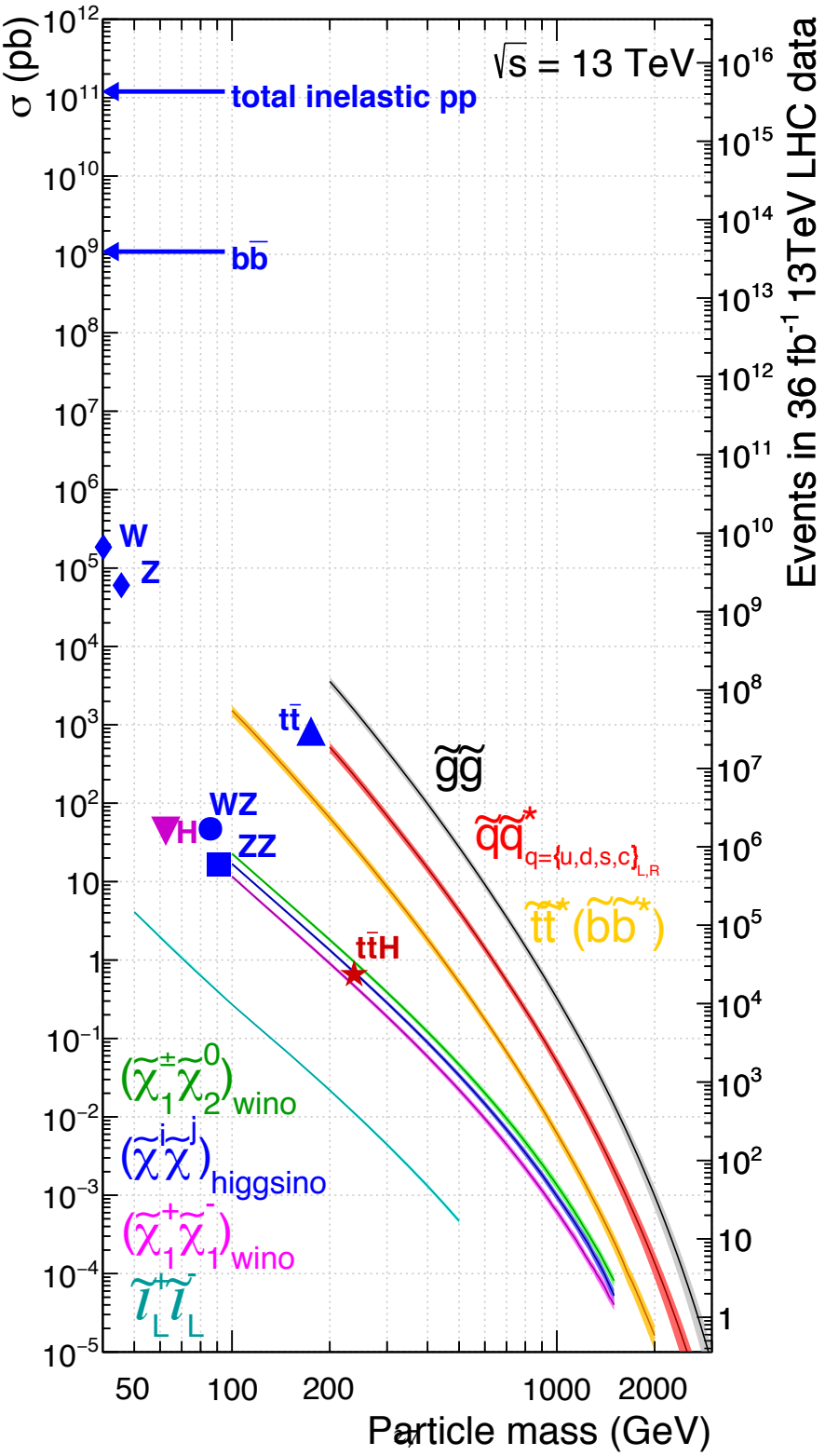


Figure 2.4: Theory cross sections for selected SM and SUSY processes [29].

Though an exact replication of SM masses to their superpartners is ruled out, the idea of minimizing fine tuning in the Higgs mass is still a driving feature of SUSY model building. At tree level, the value of the physical Higgs mass is driven by the mass parameter μ, with other contributions at loop level, specifically the top quark diagram at one-loop and the gluon at two-loop. It is therefore especially crucial from a fine tuning perspective that the partners of the Higgs, top, and gluon have small masses, so as to maintain a natural cancellation of SM and SUSY contributions to the Higgs mass. Additional mass parameters, such as those associated to the other electroweakino components (M1 and M2), are not as influential in placing the Higgs at the observed mass of 125 GeV, and therefore can exist at an arbitrarily high scale. This decoupling of mass scales also provides a valuable simplification, reducing the number of new parameters to be considered in a search.

The mass spectrum of a natural SUSY theory will therefore relegate certain particles to lower masses, on the order of the weak scale, based on their importance in determining the physical Higgs mass [30, 20]. Figure 2.5 gives an example mass spectrum driven by the aforementioned naturalness arguments. More specifically, natural SUSY theories with a chosen upper bound of 10% fine tuning as defined in Equation 2.3 predict a stop with a mass below 1.5 TeV and a higgsino with a mass of a few hundreds of GeV [31]. Moreover, this mass spectrum demonstrates that sparticles like the first generation squarks and sleptons are decoupled from naturalness pursuits. In this line of the reasoning, the stop and higgsino are the first frontier for natural SUSY.

The implications of naturalness do not only affect the scales of supersymmetric particle masses. They additionally influence the mass splitting between these particles of interest. Before the process of electroweak symmetry breaking, the superpartners of the electroweak bosons exist in fermionic

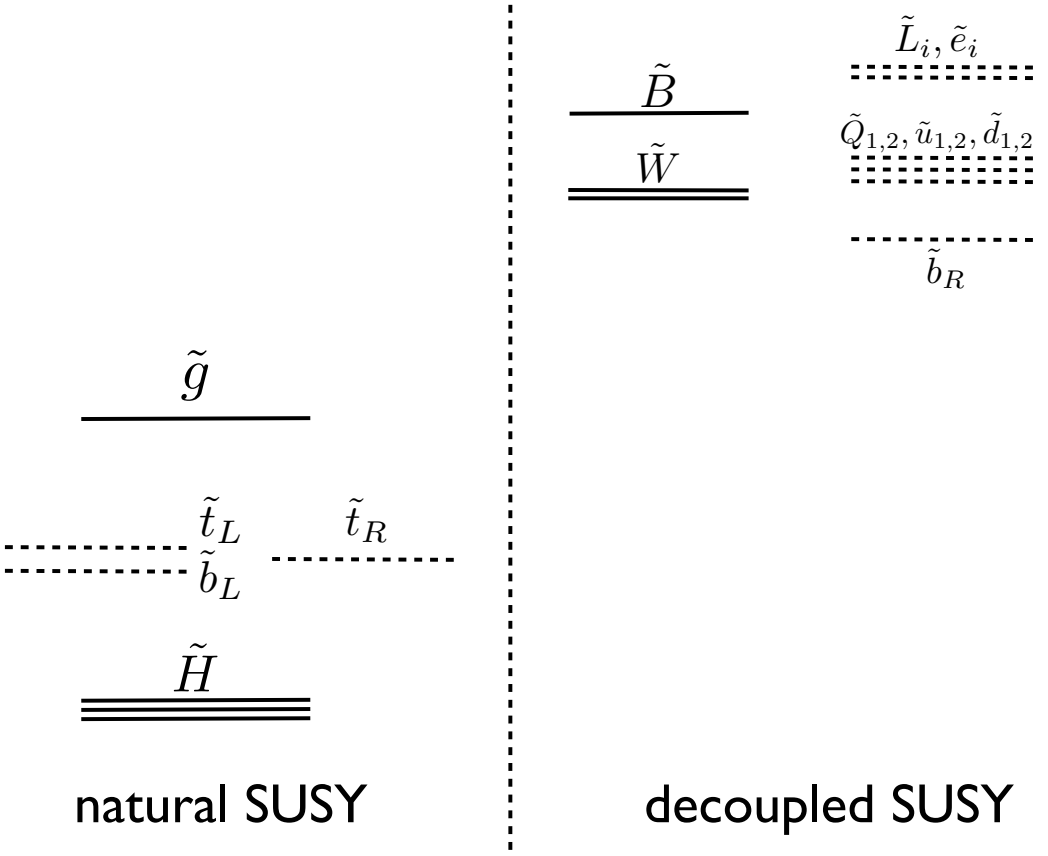


Figure 2.5: Natural electroweak symmetry breaking constrains the superpartners on the left to be light. Meanwhile, the superpartners on the right can be heavy ($\gg$ 1 TeV), without spoiling naturalness [20] .

electroweak eigenstates, called the wino, bino, and higgsino. The higgsino multiplet is composed of two neutral fermions and one electrically charged fermion, the wino multiplet has one charged and one neutral component, and the bino has one neutral component. Only the higgsino component, driven by μ, is required to be light, and the M1 and M2 parameters that govern the bino and wino mass respectively can be arbitrarily larger, generating the relationship seen in Equation 2.8.

$$\mu \ll M1, M2 \tag{2.8}$$

After electroweak symmetry breaking and the creation of the mass eigenstates as seen in Equation 2.9, each of the resulting six charged/neutral mass eigenstates denoted by χs are a mix of wino, bino, and higgsino components.

$$\tilde{B}, \tilde{W}, \tilde{H} \rightarrow \widetilde{\chi}^0_{1,2,3,4}, \widetilde{\chi}^{\pm}_{1,2} \tag{2.9}$$

The extent of this mixing is a key factor in determining the mass structure of the electroweakinos. With no mixing of electroweak states, all of the mass eigenstates would be degenerate; more mixing drives the mass eigenstates further apart.* In the parameter scenario of interest given by Equation 2.8, a small amount of wino and bino components are given to the Higgsino multiplet states. This is just enough mixing to break the degeneracy of the lightest two neutral states, $\widetilde{\chi}^0_1$ and $\widetilde{\chi}^0_2$, and the lightest charged state, $\widetilde{\chi}^{\pm}_1$, generating a mass splitting of a few GeV between these sparti-

*Pure higgsinos have a very small mass splitting on the order of hundreds of MeV due to radiative corrections [32].

cles. Therefore, in this particular natural SUSY scenario, there are three light electroweakinos with the mass hierarchy $m_{\widetilde{\chi}_2^0} > m_{\widetilde{\chi}_1^\pm} > m_{\widetilde{\chi}_1^0}$ [33], and and three electroweakinos that can be heavier.[†] This is reflected in Figure 2.5 by the three Higgsinos $\tilde{H}$ at the bottom of the mass spectrum, which have a notably small space between them. Knowing that these sparticles are expected to be light, and incorporating information about their mass splittings, provides a road map for the experimental study of natural SUSY. It reduces the unwieldy task of searching for a whole second Standard Model worth of particles, to a few precision strike points.

Dark Matter

The aforementioned sparticle mass hypothesis was initially motivated by naturalness arguments. However, the mass of the $\widetilde{\chi}_1^0$ or LSP is of particular interest to other aspects of the theory. As discussed in Section 1.2.2, the lack of an explanation for dark matter (DM) in the Standard Model is a fundamental shortcoming. As a result, many theories of beyond the Standard Model physics propose solutions to this problem, and SUSY is no exception. Earlier in this chapter the viability of the $\widetilde{\chi}_1^0$ as a DM candidate was introduced, specifically that it is inherently massive, neutral, stable, and weakly interacting. This description is consistent with the identifying criteria associated to a particular type of dark matter candidate called a Weakly Interacting Massive Particle, or WIMP.

Introducing cosmological evidence can further constrain this set of characteristics, specifically on the mass of the proposed dark matter particle. The cosmological abundance of dark matter is

[†]The value and hierarchy of mass parameters, as well as the value of μ, affects both the amount of wino/bino/higgsino mixing and the number of mass eigenstates that must be light.

hypothesized to stem from WIMPs pair-interacting at thermal equilibrium with SM particles pairs in the early universe. At some point in time as the universe expanded and cooled, this DM-SM interaction ceased to occur, and pair production of DM particles reached a point of"freeze-out". The annihilation cross section of WIMPs into SM matter sets this freeze-out point, which in turn sets the relic density of WIMPs left after this point. The observed density of dark matter in the universe is consistent with an annihilation cross section that corresponds to a DM particle with weak scale interactions and a mass on the weak scale, of order 100 GeV [34, 35]. This fits remarkably well with the picture of electroweakinos with a mass driven by μ and thus on the weak scale as well, adding another component of excitement to an already well-motivated picture.

The constraints from cosmological DM searches have been an important ingredient of modern supersymmetry theories. Given that the amount of wino-bino-higgsino mixing, the mass of the electroweakinos, and the WIMP annihilation cross section are all separate but interrelated features of the model, the issue of fine tuning is prone to resurfacing. The Well-Tempered Neutralino [36] and Not-So-Well-Tempered Neutralino [37] evolved to address some of these fine tuning concerns, by motivating a mixed-state LSP with a mass on the order of 100 GeV, with small mass splittings between the neighboring $\widetilde{\chi}_1^{\pm}$ and $\widetilde{\chi}_2^0$ on the order of 10 GeV. Figure 2.6 gives hypothetical masses for the lightest four electroweakinos as a function of μ in the Not-So-Well-Tempered Neutralino model.

All of these constraints lead to a picture of supersymmetry that encouragingly predicts new sparticles on the weak scale, nicely within the energy range that is currently accessible by experiment. These new particles are at the forefront of importance in exploring beyond the Standard Model physics, as a result of the many current issues in physics that are solved by SUSY. With this idea in

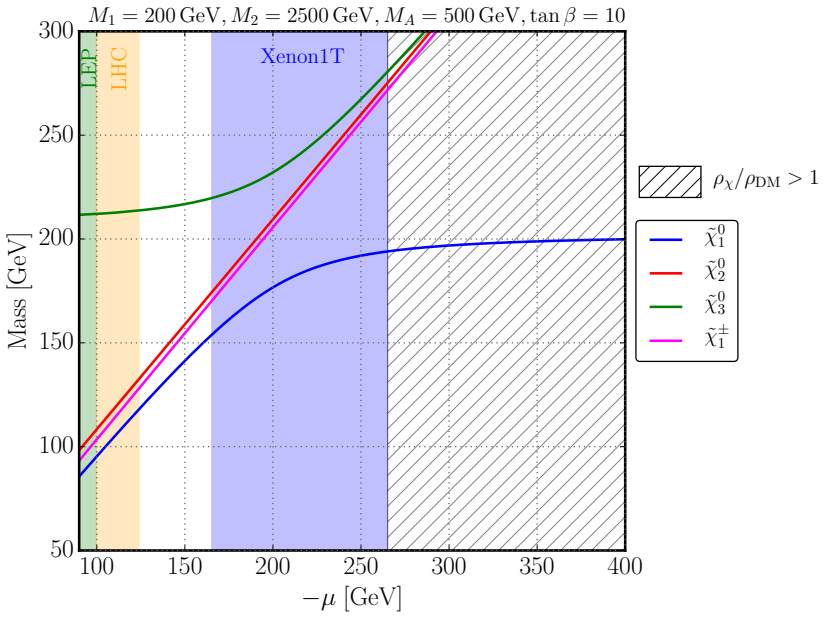


Figure 2.6: Electroweakino mass spectrum as function of the Higgsino mass parameter μ in the Not-So-Well Tempered Neutralino DM scenario [37].

hand, a phenomenological discussion is required to determine the physical signatures of this well-motivated scenario.

3

Natural Phenomenology & Compressed Spectra

The concept of naturalness provides a beautiful manifestation of supersymmetry, but more importantly, it is a relevant consideration when designing a search. With no additional information about the parameters introduced in SUSY, the phase space available for new particles is discouragingly vast.

However, by using theory to determine the particles most likely to be light, and incorporating the existence of a TeV-scale proton collider, naturalness provides a map which can be used to determine the fastest route to experimental sensitivity. This map connects the mathematics of SUSY to its collider phenomenology, giving focus to the most well-motivated search scenarios: those that have minimal fine tuning and are accessible with the LHC.

As discussed in Chapter 2, SUSY is a broken symmetry, and the masses of the supersymmetric particles must be heavier than those of Standard Model particles. Given the relationship between SM and SUSY partners in the Higgs mass, the most natural possible scenario is to have stop and higgsino masses that are close to the masses of their SM partners. In fact, from a standpoint of solving the hierarchy problem, the smaller the mass difference between sparticle and Standard Model counterpart, the less fine tuning in the Higgs mass radiative correction terms. Furthermore, because of the discussed mass parameter hierarchy where $\mu \ll M_1, M_2$, the expectation of mass splitting between the lightest three electroweakinos is expected to be small, on the order of a few GeV.

This revelation has a common effect: the most interesting mass hierarchies from a naturalness standpoint will somewhere have small splittings between particles in a decay chain. This is known as a *compressed mass spectrum*: the mass of the parent particle is almost equal to the sum of the masses of the daughter particles. The kinematic potential for such a decay to occur is narrow. Almost of the mass energy of the parent particle must go into the masses of the daughter particles, leaving little additional energy that can be imparted to the daughters as momentum. Such a decay occurs on the edge of phase space; small changes in the mass hierarchy would render the decay kinematically impossible.

The result of such a compressed decay is that the daughters, and their final state decay products, are very soft. This is problematic for detection because of the nature of collider experiments, in which rare signals of interest must be distinguished from the myriad events containing only known SM processes. Since SUSY particles are often predicted to decay to some SM daughter particles, the unique characteristics of those decay byproducts can be used to trigger on potential SUSY events. If all final state products are soft, no features of the event can be observed that could potentially denote the presence of a sparticle production upstream, making signal acceptance a significant challenge.

This interesting scenario can appear in a variety of hypothetical sparticle decays. Since naturalness dictates that higgsinos and stops are likely the lightest SUSY particles, the consequences of compressed mass spectra on these two searches are especially relevant to the LHC research program. In this chapter, the nature of compression in each decay* and the ramifications on Run I searches are discussed.

3.1 Compressed Stops

To assess where compressed mass spectra could affect stop phenomenology, it is necessary to first determine how the stop can decay. These decay prospects are shaped by the masses of the particles involved. The simplest scenario is a $\tilde{t}$ decaying to a t quark and a $\widetilde{\chi}_1^0$ (or a b quark and a $\widetilde{\chi}_1^\pm$), known as a two-body decay. However, if $\Delta m(\tilde{t}, \widetilde{\chi}_1^0) < m_t$, the stop can instead decay to a $\mathrm{W}^\pm$, a b, and a $\widetilde{\chi}_1^0$. This is referred to as a three-body decay. Pushing the mass splitting even lower, there exists

*The following discussion employs a simplified model treatment consistent with natural SUSY tenants, assuming the masses of other sparticles are arbitrarily high.

a further kinematic limitation, where the stop mass is less than the sum of the b, W boson, and $\widetilde{\chi}_1^0$ masses. This can result in a four-body decay: a b quark, two fermions, and a $\widetilde{\chi}_1^0$.[†] Given that the initial state is pair-produced stops, the final state is the same for these three decays: top-antitop ($t\bar{t}$), which decays to a pair of b quarks and two pairs of fermions (either qq or $\ell\nu$), and the $\widetilde{\chi}_1^0$. Since the $\widetilde{\chi}_1^0$ does not interact with the detector, it can only be noticed through the imbalance in total transverse event momentum that it generates, referred to as *missing transverse energy*.

Scanning over the masses of the sparticles involved in this process, there are several places where a compressed mass spectrum inevitably occurs. Each kinematic breaking point corresponds to a diagonal line in $(m_{\tilde{t}}, m_{\widetilde{\chi}_1^0})$ phase space: $m_{\tilde{t}} > m_t + m_{\widetilde{\chi}_1^0}$ (two body), $m_{\tilde{t}} > m_W + m_b + m_{\widetilde{\chi}_1^0}$ (three body), and $m_{\tilde{t}} > m_b + m_f + m_{f'} + m_{\widetilde{\chi}_1^0}$. As the masses of the stop and LSP are scanned, the points in this 2D plane close to these diagonal lines correspond to compressed spectra where there is almost insufficient mass to produce the daughter particles.

Figure 3.1 illustrates these kinematic regimes of these three dominant decay modes across the stop-LSP mass plane, along with the diagonal line that represents each kinematic edge. Note that the leftmost diagonal, where $m_{\tilde{t}} < m_{\widetilde{\chi}_1^0}$, represents the boundary of the kinematically forbidden region, in which the decay cannot proceed by any means. An additional decay possibility is also shown for the four body scenario, where the stop has insufficient mass to produce a top or W boson. This four-body region can also proceed via a flavor-changing neutral current (FCNC), where the stop decays via a loop-suppressed diagram to a c quark and a $\widetilde{\chi}_1^0$.

[†]Stop decays into supersymmetric particles other than the LSP, such as the $\widetilde{\chi}_2^0$, are possible, but not discussed here.

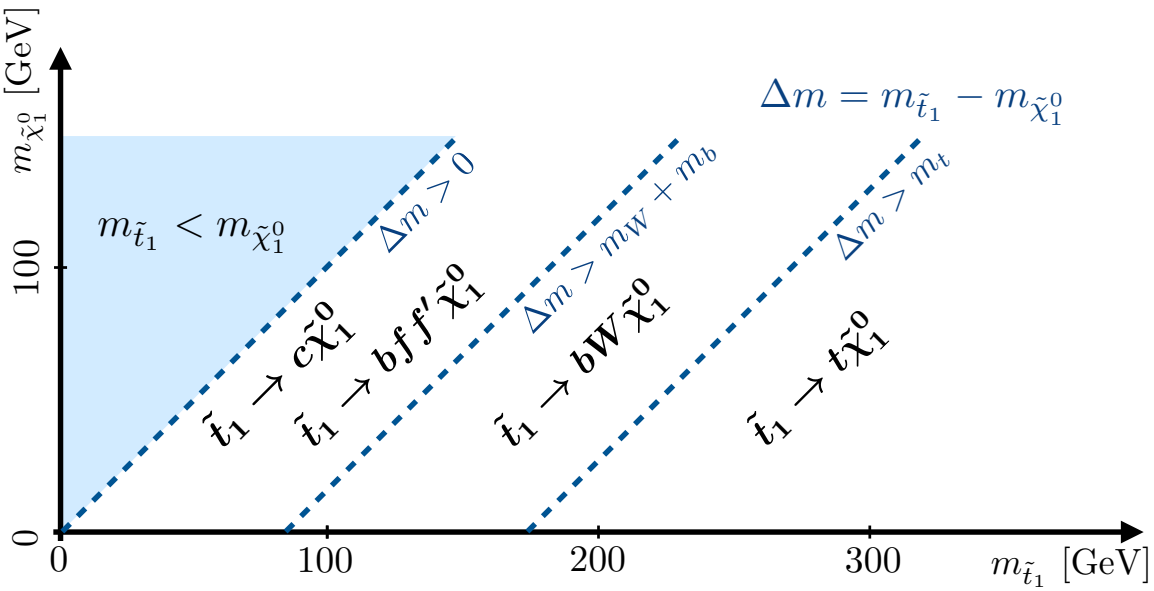


Figure 3.1: Illustration of preferred stop decay modes for several $\tilde{t}/\tilde{\chi}_1^0$ mass scenarios, assuming the $\tilde{\chi}_1^0$ is the lightest supersymmetric particle [38].

The most challenging of these four diagonals from a search perspective is the two-body diagonal, where the lack of missing energy from the $\tilde{\chi}_1^0$ means that the signal looks very much like Standard Model $t\bar{t}$. Therefore, on this diagonal, there is no obvious handle in the event that can distinguish the signal and thus provide sensitivity. The effect of compression on the analysis potential for this diagonal is immediately evident. Figure 3.2 shows the summary exclusions from Run 1 of the ATLAS experiment, incorporating all of the decay possibilities discussed above. Each of the three kinematic boundary diagonals are overlaid on the plot, with a noticeable lack of coverage near the two-body diagonal across the full range of values for $m_{\tilde{t}}$. These specific region of phase space is hereafter referred to as the *"diagonal"* region. With a lack of evidence for the stop across all Run I searches, such uncovered areas are especially crucial for future examination.

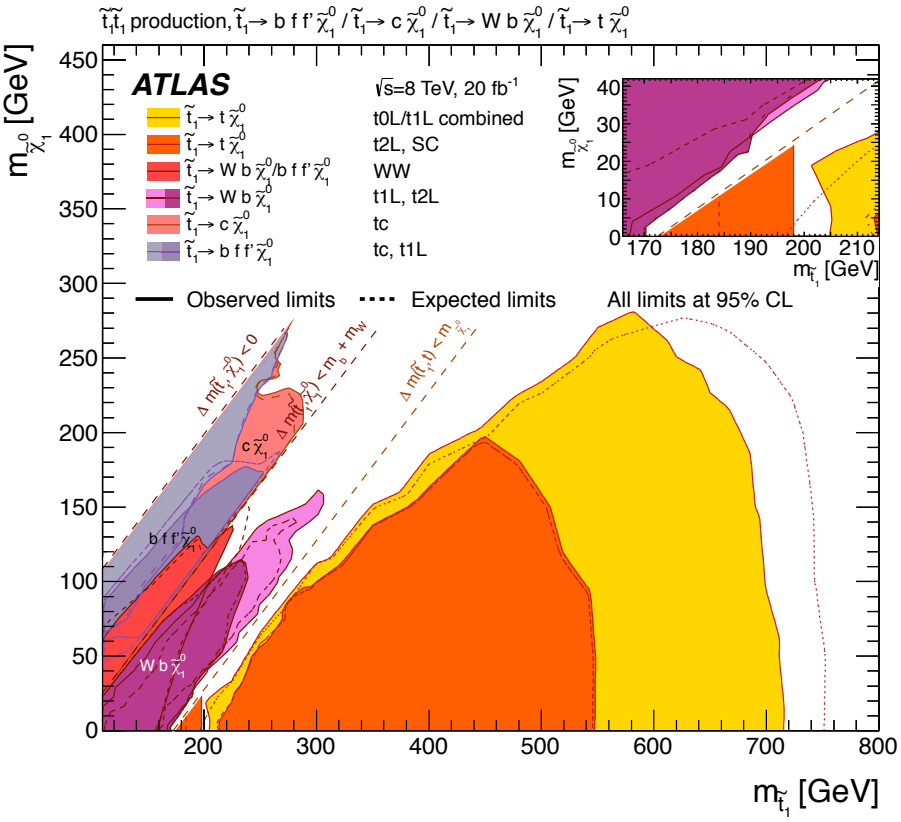


Figure 3.2: Summary of the 95% CL exclusion limits in the stop-neutralino mass plane based on 20 fb^{-1} of $\sqrt{s}$ = 8 TeV data from Run I of the ATLAS Experiment [39].

3.2 Compressed Higgsinos

The discussion of compression in the higgsino mass spectrum similarly begins with their decays. The heavier of the three lightest electroweakinos, one neutralino $\widetilde{\chi}_2^0$ and one chargino $\widetilde{\chi}_1^\pm$, can each decay to the lightest neutralino $\widetilde{\chi}_1^0$ which is assumed to be the LSP. The byproduct of both decays is a Standard Model electroweak boson; the $W^\pm$ in the case of $\widetilde{\chi}_1^\pm$ decay, and the Z^0 or Higgs for the $\widetilde{\chi}_2^0$ decay depending on the composition of the LSP.

There is a key difference in this compressed decay as compared to the stop scenario, which is that the SM electroweak boson in the decay can go off its mass shell. This allows these three electroweakinos to be almost degenerate. The kinematic challenge in such a decay is then for the parent particle to produce a daughter particle that is almost of the same mass. The resulting event has the trademark of the compressed mass spectrum: all of the parent mass energy goes into mass of daughters, which means it is produced almost at rest.

While compressed spectra in the stop search present some persistent challenges, the difficulties are in many ways even more significant with a higgsino search. As higgsino production takes place via a weak interaction, the cross section for these processes is orders of magnitude lower than that of stop pair production, making the soft final state objects and resulting loss of signal acceptance even more problematic. Furthermore, the virtual $W^{\pm *}$ or Z^{0*} in the decay each have a mass corresponding to the small electroweakino splitting, resulting in a final state of leptons or quarks that have a few GeV of momentum and thus are all but indetectable.

Because of these difficulties, the most stringent constraint on natural electroweakinos at the be-

ginning of Run II came from the LEP experiments, as shown in Figure 3.3. The lower bounds on chargino production from this result corresponds to $m(\widetilde{\chi}_1^{\pm}) > 103.5$ GeV for $\Delta m(\widetilde{\chi}_1^{\pm},\widetilde{\chi}_1^0) > 3$ GeV. This constraint weakens to $m(\widetilde{\chi}_1^{\pm}) > 92.4$ GeV for even smaller mass splittings.

In Run I, both ATLAS [40] and CMS [41] performed searches for excesses in events with on-shell W and Z bosons decaying to a three lepton final state. Such a signal could be interpreted as higgsino production; however, mass splittings larger than $m_{W^{\pm}}$ do not correspond to the natural scenario described here. Since both of these analyses use lepton triggers, the sensitivity to higgsinos drops off rapidly for mass splittings below $m_{W^{\pm}}$, due to the softer expected leptons and inherent difficulties in detecting leptons below lepton trigger thresholds. These searched were repeated in Run II, and have furthered sensitivity to such higher mass splitting scenarios, consistent with dominantly wino $\widetilde{\chi}_1^{\pm}/\widetilde{\chi}_2^0$ and referred to as "on-shell" searches, at both ATLAS [42, 43, 44, 45] and CMS [46].

Only a few years into Run II was the integrated luminosity sufficiently high to gain sensitivity to electroweakino production in compressed scenarios, leading to the first hadron collider sensitivity to higgsinos from both ATLAS [48] and CMS [49, 50]. Figure 3.4 gives the resulting phase space exclusion from ATLAS, as a function of the mass of the $\widetilde{\chi}_1^{\pm}$ and the mass splitting between the $\widetilde{\chi}_1^{\pm}$ and the $\widetilde{\chi}_1^0$. This result extends the LEP limits out to mass splittings between 2 and 35 GeV.

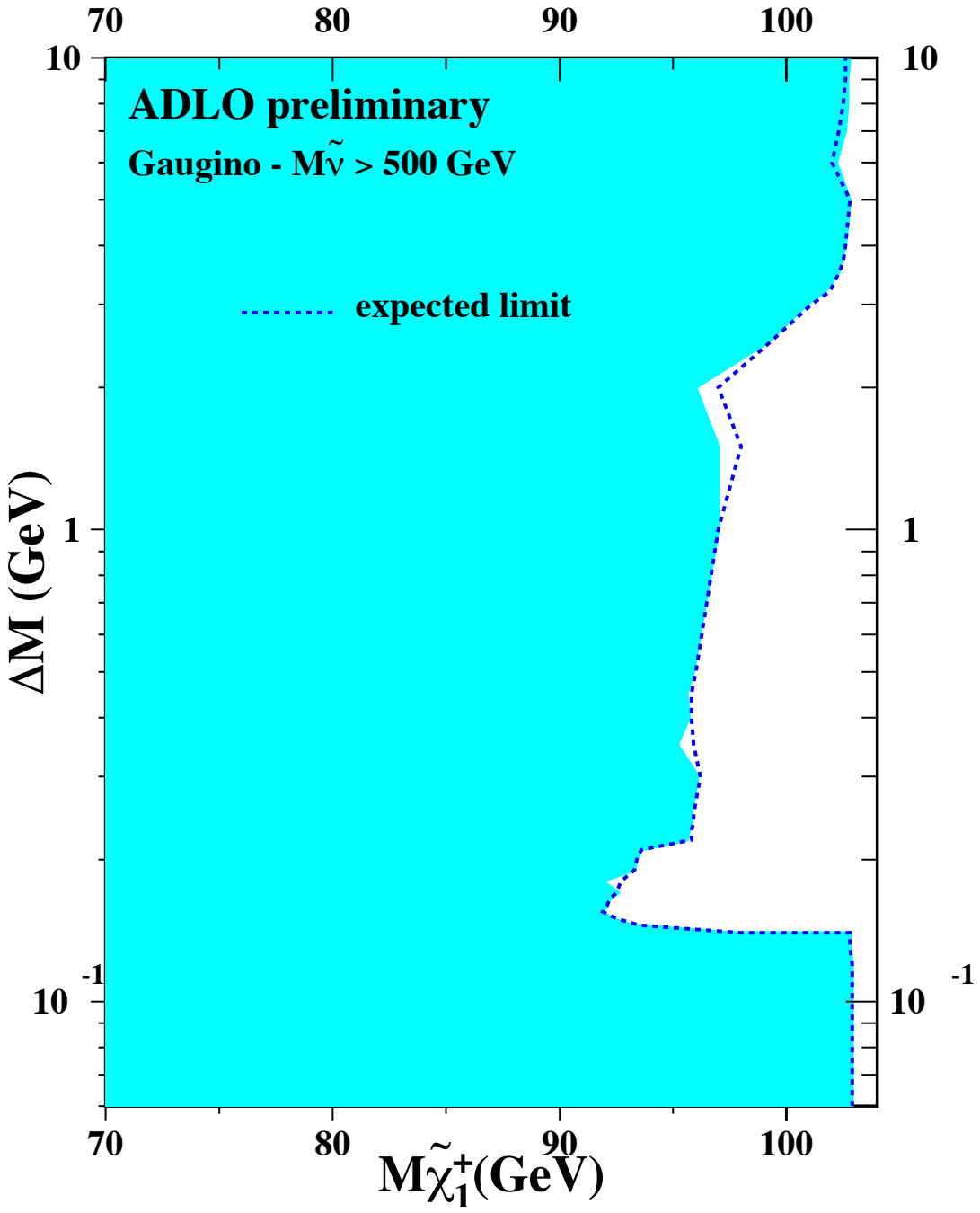


Figure 3.3: Summary of the 95% CL exclusion limits [47].

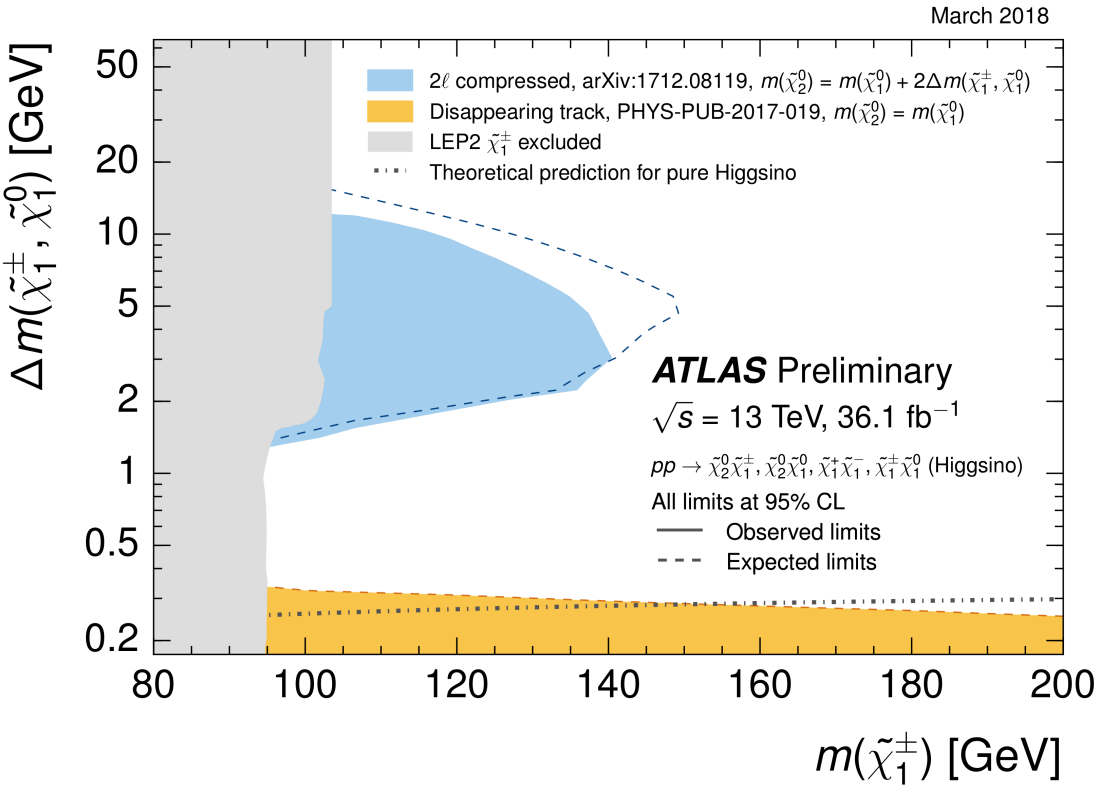


Figure 3.4: First limits for the compressed higgsino LSP scenario from ATLAS in Run II [51], using 36.1 fb^{-1} of ATLAS data [48] (light blue). Also shown are the higgsino limits from the reinterpretation of the disappearing track analysis (yellow), focusing on the nearly degenerate electroweakino mass scenario corresponding to order MeV mass splittings [52].

This discussion reveals some key oversights in the natural SUSY search program thus far, in the form of well-motivated but uncovered areas of phase space. Given the experimentally troublesome nature of such regions, what techniques can be used to acquire sensitivity and determine if these areas are hiding new physics? The answer to this question involves the soft LSP, and thus the negligible missing energy (E_T^{miss}) in the event. A larger amount of E_T^{miss} would allow signal discrimination in the stop case, and would eliminate reliance on lepton triggers in the higgsino case.

Events with small mass splittings do not inherently contain a large amount of missing energy. However, taking compressed decay kinematics and experimental environment into account, it is possible to generate more. The method offered here for generating additional E_T^{miss} in an event can be performed with negligible impact on the other event features, while providing a crucial handle for sensitivity to compressed signals.

3.3 Making E_T^{miss} with Initial State Radiation

Searching for evidence of a $\widetilde{\chi}_1^0$ in an event amounts to the search for E_T^{miss}, since it is very weakly interacting and not likely to directly interact with the detector. The methodology for measuring missing energy is well-established, given the need to measure neutrinos that are similarly non-interacting and often produced in proton-proton collisions. This is done using the knowledge that the initial state of a collision has no momentum in the plane perpendicular to the beamline, called the transverse plane. A neutrino or $\widetilde{\chi}_1^0$ produced in this collision carries momentum into the transverse plane, but from conservation laws, the total momentum in this plane after the collision must still be zero. Thus the momentum of the invisible particle is generally defined as that which is necessary to balance the momentum in the transverse plane.

Identifying a $\widetilde{\chi}_1^0$ is different from searching for another non-interacting particle like a neutrino for one fundamental reason: the $\widetilde{\chi}_1^0$ is expected to be massive, on the order of the weak scale. This provides a valuable means by which the $\widetilde{\chi}_1^0$ can receive momenta from a source other than its parent particle. One such source is initial state radiation (ISR), which is a strong emission coming from the interacting partons before the primary collision. Such an emission will alter the initial state momentum in the transverse plane of the event, thereby providing a "kick" to whatever particles are produced in the primary interaction.

In the cases discussed here, those particles are stops or higgsinos which then decay to some visible and some invisible particles. If the invisible particles produced have significant mass relative to the visible particles, they will absorb a larger fraction of the momentum imparted by the ISR.

Figure 3.5 shows diagrammatically how this effect works in the transverse plane of an event. Boosting the $\widetilde{\chi}_1^0$ has another valuable consequence, generating enough missing energy in the event to get above E_T^{miss} trigger thresholds and alleviating reliance on lepton or jet triggers in an event with soft final state objects.

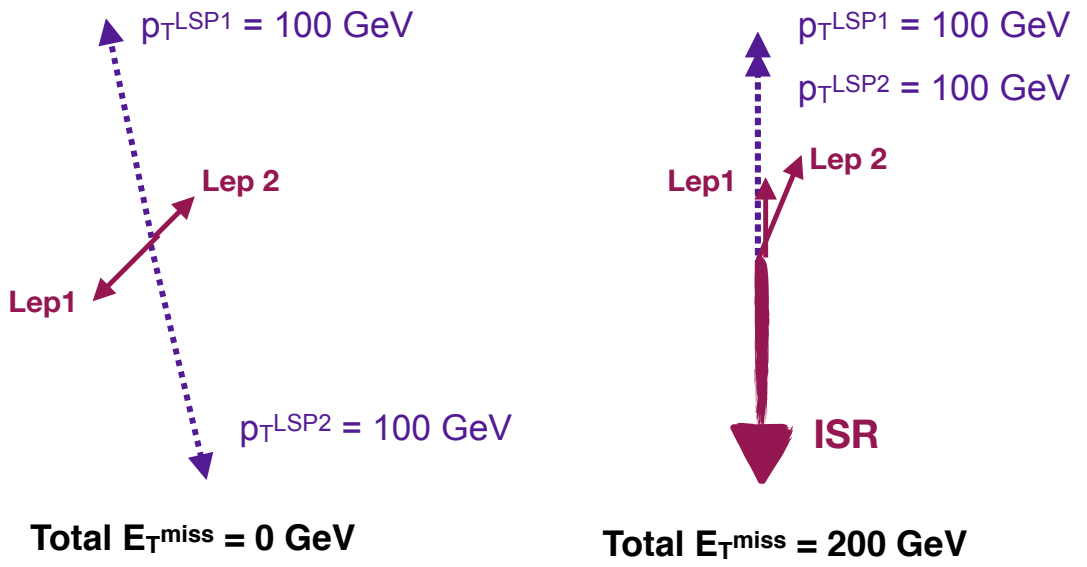


Figure 3.5: Transverse view of an event containing two LSPs and two leptons, with (right) and without (left) an ISR jet, to demonstrate how ISR can be used to boost invisible particles and generate E_T^{miss}.

This strategy has been commonly used in the past for collider searches for massive invisible particles, such as the monojet search for dark matter [53]. It has been predicted to be adaptable in principle for SUSY searches, where the system that is "kicked" contains more particles than just the DM candidate or LSP [33, 54]. The idea of adding an ISR jet to generate missing energy is the basis of the dedicated reconstruction method described in Chapter 6.

The two analyses presented in this thesis represent adaptations of ISR boosting for sensitivity to

compressed stop and higgsino searches. These scenarios are not only theoretically well-motivated by naturalness, but they posit SUSY particles to exist in areas of phase space not excluded by current collider constraints, making them exceptionally appealing from a scientific standpoint. With a signature in mind and idea of how to observe it, the onus is shifted onto the experiment, where a discussion of detector capabilities proves necessary to determine the feasibility and application of this technique in data.

Part II

Experiment

The experimental prowess necessary to study nature at such a fundamental level is significant, and the machines that have been built in this effort represent the vanguard of technology. Particle accelerators and detectors developed in the service of high energy physics research have spawned advancements in numerous other fields, from computing to medicine. This development has been driven by the ambition of examining and probing the unsolved issues within the Standard Model, including the search for supersymmetry. For this, it is necessary to manipulate matter at increasingly smaller scales, via the most energetic particle accelerator ever built. Part II discusses this accelerator, the Large Hadron Collider (Chapter 4), and the ATLAS Experiment that detects, reconstructs, and analyzes the collisions (Chapter 5).

4

The Large Hadron Collider

The Large Hadron Collider (LHC) is a circular proton accelerator and collider located at CERN (European Organization for Nuclear Research) in Geneva, Switzerland [55]. The LHC is the newest and largest installment at a laboratory with decades of history in the field of particle physics, a fact which is integral to its successful operation. From its location to its components, the LHC is built upon the foundation of its experimental predecessors. The 27 km synchrotron is housed in an un-

derground tunnel straddling the French-Swiss border that was originally dug in 1985 for the Large Electron-Positron (LEP) collider. Protons entering the LHC first travel through a series of accelerator rings, many of which have previously been experiments in their own right.

The process of accelerating protons at the LHC complex starts from stripping hydrogen of its electrons. Resulting protons travel through a series of accelerators; a linear accelerator (LINAC) raises their energy to 50 MeV; a booster to 1.4 GeV; the Proton Synchrotron (PS) to 25 GeV; and the Super Proton Synchrotron (SPS) to 450 GeV. Finally, from SPS, the protons are injected directly into the LHC, where they reach their final collision energy. In Run II, this is a center-of-mass energy of $\sqrt{s}$ = 13 TeV; the LHC design energy is $\sqrt{s}$ = 14 TeV. Figure 4.1 shows the CERN accelerator complex, including all of the aforementioned injector rings and the LHC.

Once in the LHC, the protons reach their final energy via eight radio-frequency (RF) cavities positioned around the ring, each of which deliver 2 MV with a 40 MHz radiofrequency. Maintenance of the beam is provided by 9593 superconducting electromagnets which surround the ring. The magnets are kept at their operational temperature of 1.9 K with a superfluid helium cooling system. There are two categories of these magnets, each with their own specific function in the accelerator. Lattice magnets (both dipole and quadrupole) ensure stability, steering, and compression of the transverse beam size as it travels around the ring. When the beam approaches a collision point, specialized insertion magnets provide the additional squeezing necessary to ensure a high quality collision. This takes the form of eight triplets of quadrupole magnets, two at each of the four primary detectors. Dipole magnets also spread the beam out after a collision, and deflect the beam from the accelerator in order to dump it.

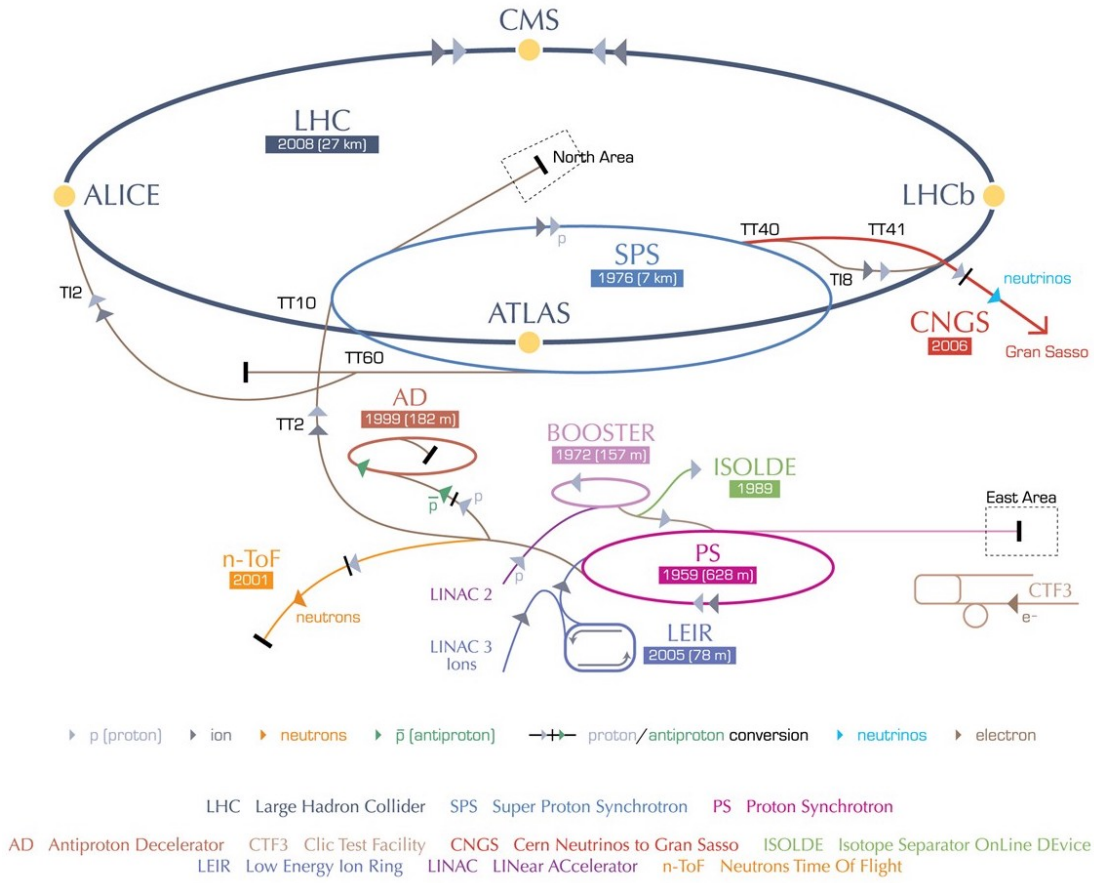


Figure 4.1: An overview of the CERN accelerator complex [56].

During a typical run, the LHC is filled with thousands of bunches, each containing about 10^{11} protons. They travel in opposite directions through two separate beam pipes under a vacuum of 10^{-13} atm. These beam pipes intersect at four points around the LHC, where detectors are positioned to record their collision. The ATLAS [57] and CMS [58] experiments are both multi-purpose detectors with a variety of physics programs, including Standard Model measurements and searches for new physics. LHCb [59] is a forward detector specifically designed to detect b-hadrons, and ALICE [60] focuses on heavy ions (which replace protons in the LHC for a few weeks at the end of every year.)

At these interaction points, the intensity of bunch collisions is described by the instantaneous luminosity, given in Equation 4.1. Here, f_{rev} is the revolution frequency, N_1 and N_2 are the number of protons per bunch crossing in beams 1 and 2 respectively, and σ_x and σ_y characterize the horizontal and vertical convolved beam widths.

$$L = \frac{f_{rev} \cdot N_1 N_2}{2\pi\sigma_x\sigma_y} \tag{4.1}$$

The peak instantaneous luminosity measured in the LHC during Run II is 2.05×10^{34} cm^{-2} s^{-1}, more than double the original design luminosity. Integrating the instantaneous luminosity over time gives a way of quantifying the amount of recorded data. This integrated luminosity $\mathcal{L}$ is commonly used to describe the size of a dataset (see Chapter 5 for a description of data collected by ATLAS in Run II.)

The goal of physics analyses at the LHC experiments is to find and study processes of interest

within a recorded dataset. The number of events for any given process can be found by multiplying the integrated luminosity by the cross section of the process (σ), as seen in Equation 4.2. Cross sections give an estimation of the probability of a process, and at the LHC they are measured in barns (b), a unit equal to 10^{-28} m^2. Since the number of events is a unitless value, this means that integrated luminosity is commonly measured in inverse barns (b^{-1}). The cross sections for most processes of interest are several orders of magnitude below the total cross section of the LHC (see Figure 2.4). It is therefore crucial to collect a large amount of data, thereby enhancing the probability of observing a rare process. To this end, maximizing the instantaneous luminosity is a driving factor in future collider design.

$$N = \int L\,dt \times \sigma = \mathcal{L} \times \sigma \tag{4.2}$$

Since collisions occur with a frequency of 40 MHz and each collision contains billions of protons, there is a high probability that multiple collisions will occur simultaneously. In this case, the highest energy collision is called the primary interaction, while the other interactions are known as *pile-up* vertices. These vertices are classified as in time or out of time, depending on whether the spurious collisions occurred in the same or adjacent bunch crossing as the primary collision in question. In Run II, the mean number of interactions per bunch crossing $\langle\mu\rangle$ reached a maximum of 64, and this value will increase with luminosity.

The first proton beams circulated in the LHC in 2008, and in the decade following, the LHC underwent two multi-year Runs and two Long Shutdown (LS) periods, as reflected in the timeline

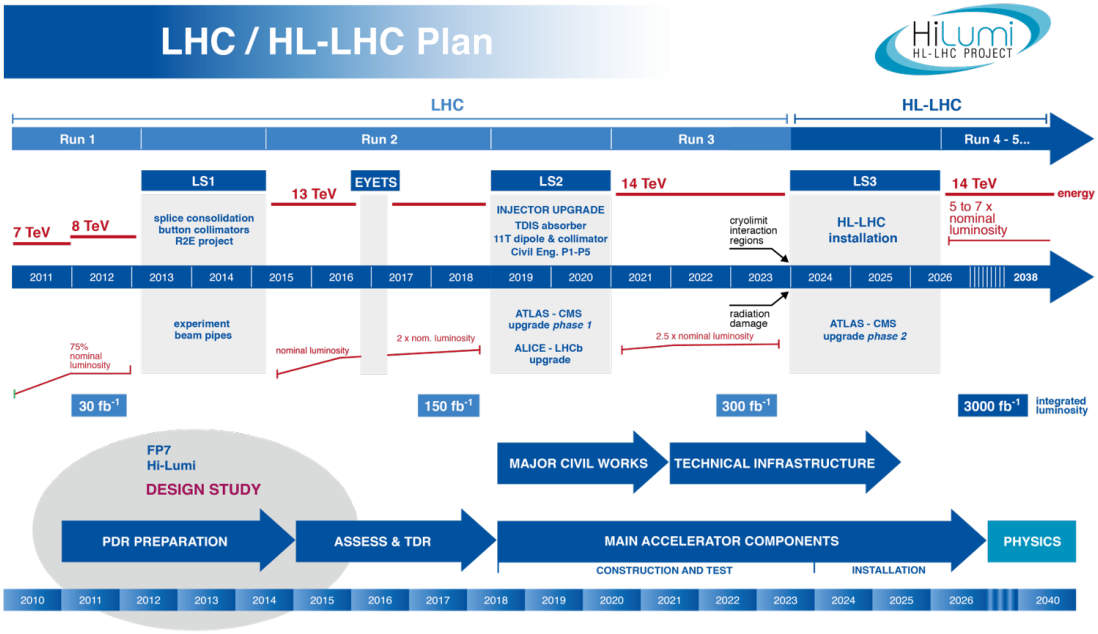


Figure 4.2: Project schedule of the LHC over several decades, including notable runs and shutdown periods [61].

shown in Figure 4.2. From 2019 to 2021, the LHC is in its second Long Shutdown (LS2) phase, to upgrade and repair the experiments in preparation for Run III, the final run of the LHC as it is known today. Run III is expected to last from 2021 to 2023; during this time the LHC will provide collisions at the design energy of 14 TeV and nearly double the existing dataset. In 2024 the LHC will enter another shutdown, LS3, during which the accelerator and detector upgrades for the HL-LHC will take place. The HL-LHC is expected to deliver around 3000 fb^{-1} of proton collision data at $\sqrt{s} = 14$ TeV over several years, renewing its global leadership in particle physics and further advancing the boundaries of human knowledge.

5

The ATLAS Detector

Once the collisions of interest have been provided by the LHC, the role of the detector emerges. It is at the detector level that the proton collisions are reconstructed, providing a window into the edges of the Standard Model and the prospects for new physics. The detection principles used in the LHC experiments rely on knowledge not only of what the fundamental particles are, but how they interact with one another and with the macroscopic world around them.

A Toroidal LHC ApparatuS, otherwise known as the ATLAS detector (Figure 5.1), is a multipurpose experiment at the LHC, standing 25m high and weighing over 7000 tons. It consists of several cylindrical layers of subsystems, each with a designated purpose for particle identification. Starting at the beamline and moving radially outward, those subsystems are the inner detector, calorimeters, and muon spectrometer; each of these is described in detail in Sections 5.1 to 5.3. Working in conjunction with these detectors are solenoidal and toroidal magnet systems, described in Section 5.4. All of these subdetectors work together to provide unique particle identification, along with energy and momenta measurements, that allow for a comprehensive picture of a proton-proton collision event. A trigger system determines which events are recorded for later analysis (Section 5.5), and these events are subsequently reconstructed using the procedure described in Section 5.6.

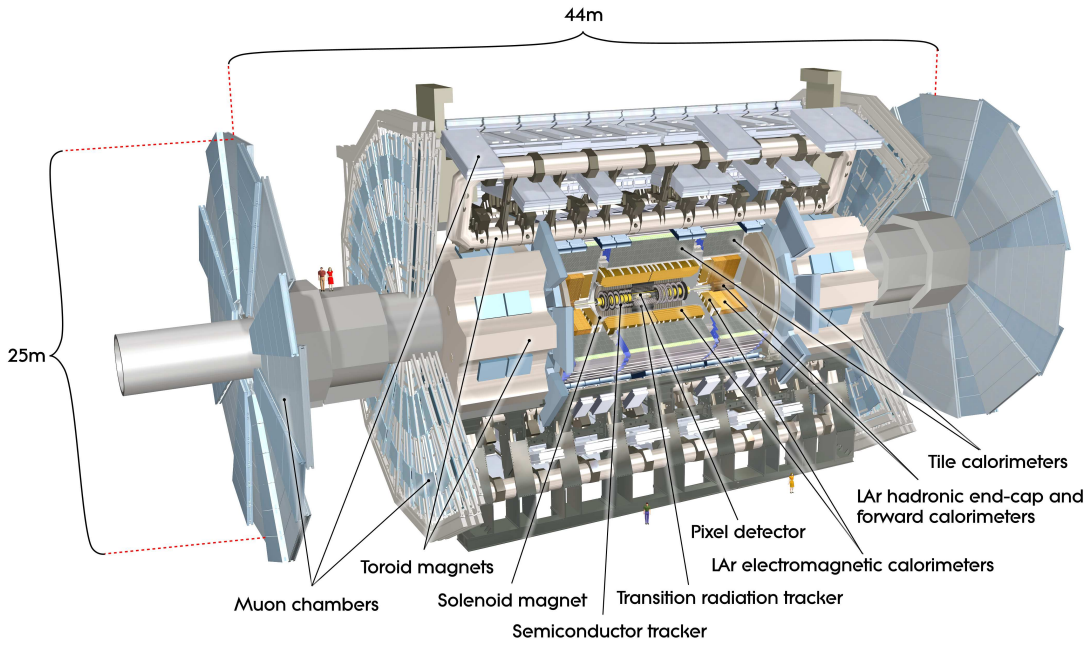


Figure 5.1: The ATLAS detector and its subsystems, drawn to scale [57].

The ATLAS coordinate system is right-handed, with the positive z-axis lying along the beam axis and pointing counterclockwise to the beam direction, the positive y-axis pointing vertically upwards, the positive x-axis pointing towards the center of the accelerator ring, and the origin at the interaction point (IP). The x-y plane is referred to as the transverse plane. In polar coordinates, the azimuthal angle ϕ is measured around the beam axis, with the polar angle θ measured as a rotation from the beam axis. Since the momentum of the colliding partons along the z-axis is unknown, polar coordinates in the transverse plane are used in the computation of many important quantities such as transverse momentum ($p_T = p \sin\theta$) or missing transverse energy ($E_T^{miss} = E \sin\theta$). Because many of the particles that pass through ATLAS are relativistic, it is helpful to also define the rapidity y, which is a boost invariant representation of the polar angle, and the pseudorapidity η, which is equal to the rapidity in the limit of zero particle mass.

$$y = \frac{1}{2} \ln\left(\frac{E + p_z}{E - p_z}\right); \quad \eta = -\ln\tan\left(\frac{\theta}{2}\right) \tag{5.1}$$

η is especially commonly used in ATLAS analyses because differences in η are invariant under boosts along the z-axis, and most particles produced at the LHC can be assumed to be massless compared to their energies. Thus, the η-ϕ coordinate space is thus the most common one used to describe position and direction in the detector. Particles emerging perpendicular to the beam axis have $\eta = 0$, and particles emerging parallel to the beam have $\eta = \pm\infty$. In this coordinate space, the

distance between particles is often defined using ΔR:

$$\Delta R = \sqrt{\Delta\eta^2 + \Delta\phi^2} \tag{5.2}$$

ATLAS is divided into "barrel" elements, which cover the low-η region, and "endcap" elements for the high-η region. Combined, these elements provide nearly full coverage up to $|\eta| < 4.9$, with most performance recommendations and analyses focusing on objects with $|\eta| < 2.5$. All of the coordinates described above and the space they map out on the ATLAS detector can be seen in Figure 5.2.

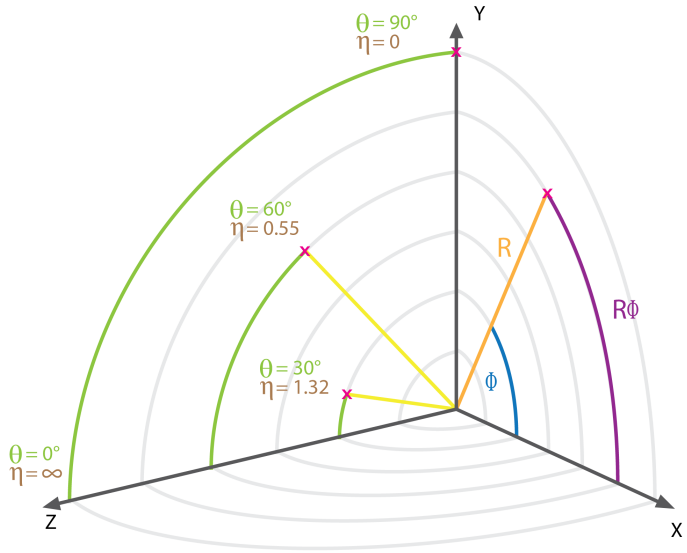


Figure 5.2: The ATLAS coordinate system, demonstrating relative spans of the Cartesian and polar coordinate systems, along with the pseudorapidity η [62].

The technical requirements for any detector on the LHC are stringent, given the high interaction rate. Table 5.1 lists the performance of each subdetector in terms of energy and momentum resolu-

Detector System	Resolution
Tracking	$\sigma_{pT} / p_T = 0.05\% \, p_T \bigoplus 1\%$
EM Calorimeter	$\sigma_E / E = 10\% / \sqrt{E} \bigoplus 0.7\%$
Hadronic Calorimeter	$\sigma_E / E = 50\% / \sqrt{E} \bigoplus 3\%$
Forward Calorimeter	$\sigma_E / E = 100\% / \sqrt{E} \bigoplus 10\%$
Muon Spectrometer	$\sigma_{pT} / p_T = 10\% \, p_T$ at $p_T = 1$ TeV

Table 5.1: Performance requirements for the ATLAS detector [57]. Units of energy and momentum are GeV.

tion required. Each resolution has a term that is a function of momentum or energy, summed in quadrature with a constant term.

The data-taking capabilities of ATLAS throughout Run II are impressive in light of these expectations. The total integrated luminosity of the ATLAS Experiment collected throughout Run II from 2015 to 2018 is approximately 140 fb^{-1}. Figure 5.3 shows the amount of data collected by ATLAS as a function of time, along with the total data delivered by the LHC. This comparison gives a sense of the data-taking efficiency; almost 90% of collisions delivered to ATLAS were deemed good for physics analysis [63]. The number of interactions per bunch crossing μ provided by the LHC is a crucial feature of data-taking, as it dictates the amount of pile-up, or overlapping simultaneous proton-proton collisions, in the detector. Figure 5.4 shows the average value of μ for each year of collisions, as well as for the entire Run II period.

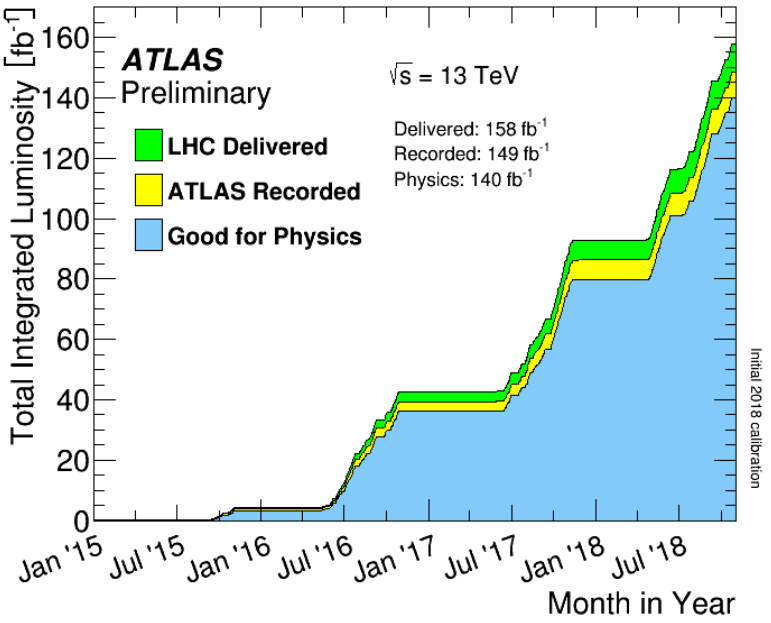


Figure 5.3: Cumulative luminosity versus time delivered to ATLAS (green), recorded by ATLAS (yellow), and certified to be good quality data (blue) during stable beams for pp collisions at $\sqrt{s}$ = 13 TeV in 2015-2018[64].

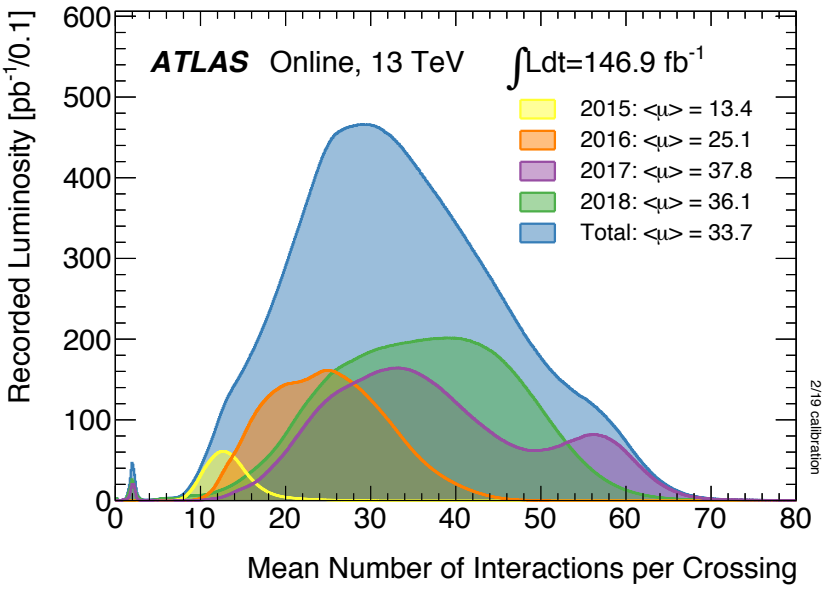


Figure 5.4: Luminosity-weighted distribution of the mean number of interactions per crossing μ for each year of data-taking, and for the full Run II[64]. All data recorded by ATLAS during stable beams is shown.

5.1 Inner Detector

The inner detector (ID) is the layer of the ATLAS detector that is closest to the beam pipe, and thus to the interaction point. There are three primary components of this subsystem, which work in conjunction to provide precise tracking for charged particles. The innermost sublayer is the pixel detector, followed by the silicon microstrip trackers (SCT) and the Transition Radiation Tracker (TRT). Together, these detectors provide primary vertex information for sufficiently high-p_T tracks and secondary vertex information for long-lived particle taggers. The entire ID is enclosed in a solenoidal magnetic field, bending charged particles and allowing for momentum measurement of reconstructed objects. A cutaway diagram of the ID layout can be found in Figure 5.5.

5.1.1 Silicon Detectors

Both the Pixel Detectors and SCT are silicon detectors, which use n-type Si semiconductors to record the passage of charged particles via electron-hole pairs. This detector technology provides high granularity and resolution on the order of microns, and readout times less than the 25 ns LHC bunch crossing interval, providing key information that can associate hits to a particular primary interaction.

The Pixel Detector has over 80 million readout channels which provide precision tracking for the innermost, and thus most populated, layer of the ATLAS detector. It has four concentric cylindrical layers in the barrel, and three disks in each of the two endcaps, giving a coverage of $|\eta| < 2.5$. The layer closest to the beamline is called the Insertable B-Layer (IBL), due to its importance in identi-

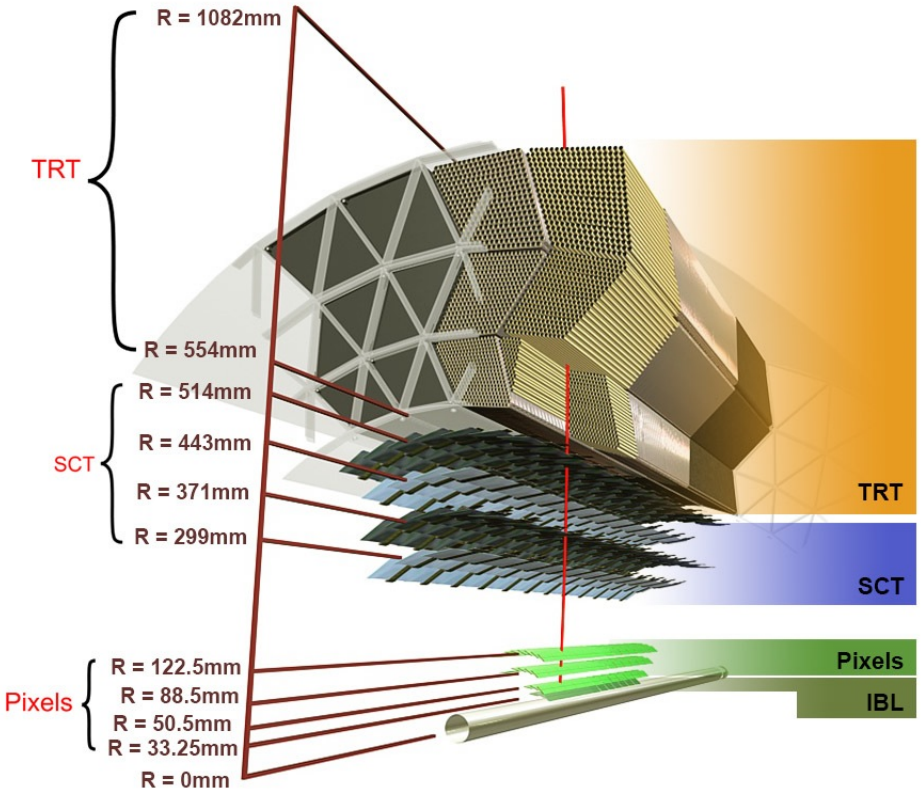


Figure 5.5: Cutaway view of the ATLAS inner detector system (top) and illustration of a charged particle traversing the detectors (bottom) [57].

fying secondary vertices associated to B-hadrons. The Pixel measurements are accurate to 10 μm in R-ϕ and 115 μm in z (for the barrel) or R (for the endcap).

The SCT consists of four concentric barrel layers and nine disks at each endcap. Each of these layers is composed of double-sided modules of silicon microstrip sensors. The SCT measurements are accurate to 17 μm in R-ϕ and 580 μm in z (for the barrel) or R (for the endcap). On average, a charged particle gets at least three measurement points from the Pixel detector and eight strip measurements from the SCT.

5.1.2 Transition Radiation Tracker (TRT)

The TRT is the outermost layer of the ID, and is composed of polyimide straw tubes 4 mm in diameter that are filled with a gas mixture of70% Xe, 27% CO_2, and 3% O_2. When a charged particle passes through a tube, it emits transition radiation in the form of photons, which can be used to distinguish electrons from photons and aid in electron identification. The barrel of the TRT consists of straws that are 144 cm long and arranged radially, while the endcap straws are 37 cm in length and arranged parallel to the beam axis, with a coverage of $|\eta| < 2.0$. The TRT is not needed to provide precision hit measurements, which is performed by the silicon detectors, but its larger radial size is assistive in determining track momenta.

5.2 Calorimeters

The ATLAS calorimeter is composed of two primary subsystems, the electromagnetic (EM) and hadronic calorimeters (HCal). Both are sampling detectors, meaning that they utilize alternating

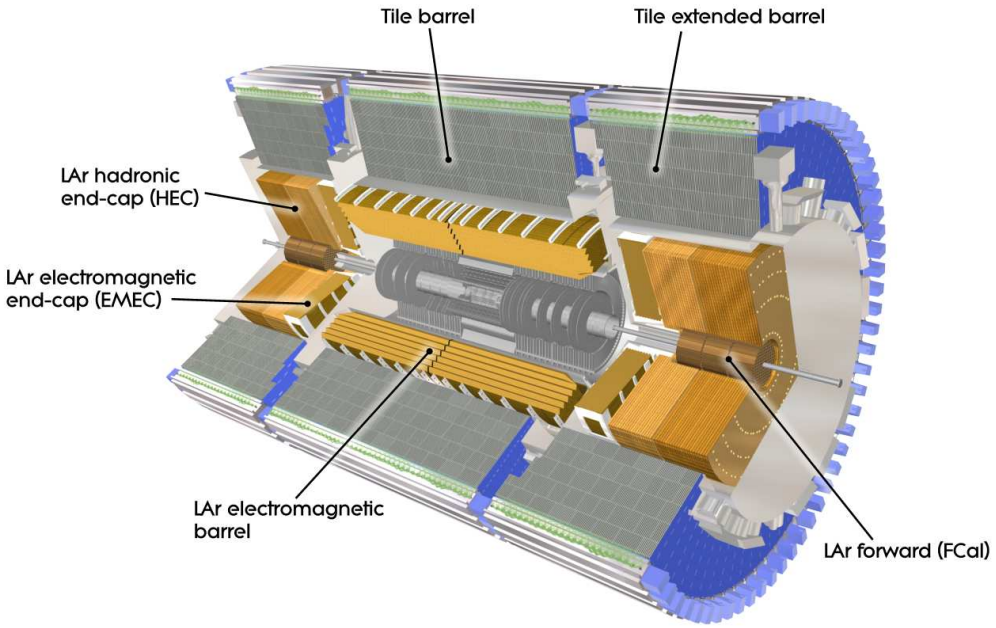


Figure 5.6: Layout of the ATLAS calorimeter system [57].

layers of an active detecting medium with a dense absorbing material. Such a structure allows the calorimeter system to fully absorb all jets, electrons, and photons, while recording valuable position and momentum information. The calorimeters are also integral in determining missing transverse energy to sufficient accuracy. As shown in Figure 5.6, the EM calorimeter is the first layer, located closer to the beam pipe, followed concentrically outward by the hadronic calorimeter. The endcaps of these two calorimeters provide coverage of $|\eta| < 4.9$.

5.2.1 Liquid Argon Detection

LAr is used as an active medium in both EM and hadronic calorimeter systems. It was chosen for this purpose because of its linear response and radiation hardness. The detection principle is the

collection of electrons that are released when a charged particle traverses the material, which are accelerated by an electric field towards electrodes, inducing a current proportional to the energy deposited by the particle.

An example of the induced signal and its drop-off as a function of time can be seen in Figure 5.7. The amplitude of the signal A (in ADC counts) is found using Equation 5.3, where s_j are the signal samples, p is the ADC pedestal, and a_j are the Optimal Filtering Coefficients (OFC) computed per cell[65]. The amplitude is proportional to the cell energy, and is also used to compute the signal peak time t_{cell} (Equation 5.3), where b_j are time-OFCs. The signal time is measured as the difference between the digitization time and the chosen phase, and thus is expected to be close to zero. This signal is then shaped using the front end boards (FEBs), which also compute the energy deposited and pass the result to the data acquisition system (DAQ). The default number of samples j used for each signal in the calculation of A and t_{cell} is five, although many more can be used depending on reconstruction needs.

$$A = \sum_{j=1}^{N_{samples}} a_j(s_j - p); \quad t_{cell} = \frac{1}{A} \sum_{j=1}^{N_{samples}} b_j(s_j - p) \tag{5.3}$$

Figure 5.7 also reveals that a signal pulse is much longer than the 25 ns nominal bunch spacing at the LHC. This aspect of the calorimetry has the potential to cause out-of-time energy to occur in a given event. This effect is mitigated by the bipolar shaping of the pulse, which has a positive peak and a negative tail, allowing most energy from previous bunch crossings to be cancelled out over time.

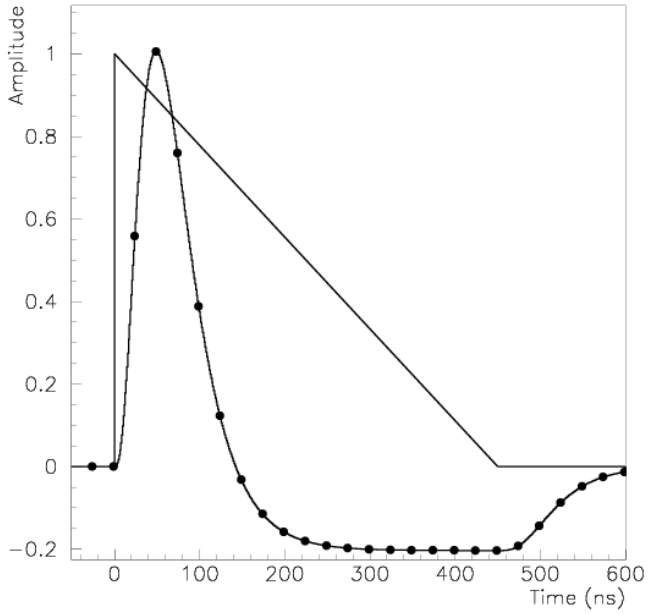


Figure 5.7: LAr detector raw signal shape (triangle) and after shaping (dotted line) [66].

To distinguish between real energy deposits and cell noise, the shape of the pulse output by the FEBs is compared to the expected pulse shape as derived from simulation. The cell quality Q_{cell}^{LAr} is thus defined in Equation 5.4 as the quadratic difference between the measured and expected pulse shapes, where A is the measured signal amplitude, T is the measured signal time, s_j is the amplitude of each sample in ADC counts, g_j is the normalized predicted ionization shape, and g'_j is its derivative [65]. The number of samples used for each signal in the calculation of Q_{cell}^{LAr} is four. Lower values of Q_{cell}^{LAr} are more likely to be real energy deposits, while higher values are often associated to noise. This criteria can thus be used to distinguish real physics object energy from spurious sources,

as in the *event cleaning* procedure discussed in Chapter 7.

$$Q_{cell}^{LAr} = \sum_{j=1}^{N_{samples}} (s_j A \times (g_j - \mathrm{T} g'_j))^2 \tag{5.4}$$

5.2.2 Electromagnetic Calorimeter

The electromagnetic calorimeter in ATLAS is primarily used to measure the energy of electrons and photons. These particles will lose energy via *bremsstrahlung* and pair production when incident on a thick absorber material, generating an electromagnetic shower that can be used to give an initial energy measurement of the particle. The number of particles in the shower is proportional to the incident energy of the particle, and its intensity attenuates exponentially as a function of distance as described by Equation 5.5:

$$I(x) = I_0 e^{-x/X_0} \tag{5.5}$$

where I is the intensity, x is the distance travelled, and X_0 is the radiation length.

The EM calorimeter uses lead as an absorber and LAr as an active material, which are layered in an accordion geometry (see Figure 5.8) that allows for complete ϕ symmetry and numerous active layers. The barrel extends to $|\eta| < 1.475$, and the endcap extends in the range $1.375 < |\eta| < 3.2$. The overlapping region between the barrel and endcap is referred to as the "transition" region. The EM calorimeter is segmented in depth into four layers: a thin LAr presampler layer to correct for energy lost before the calorimeter; a pre-shower detector to precisely measure particle η for shower direction

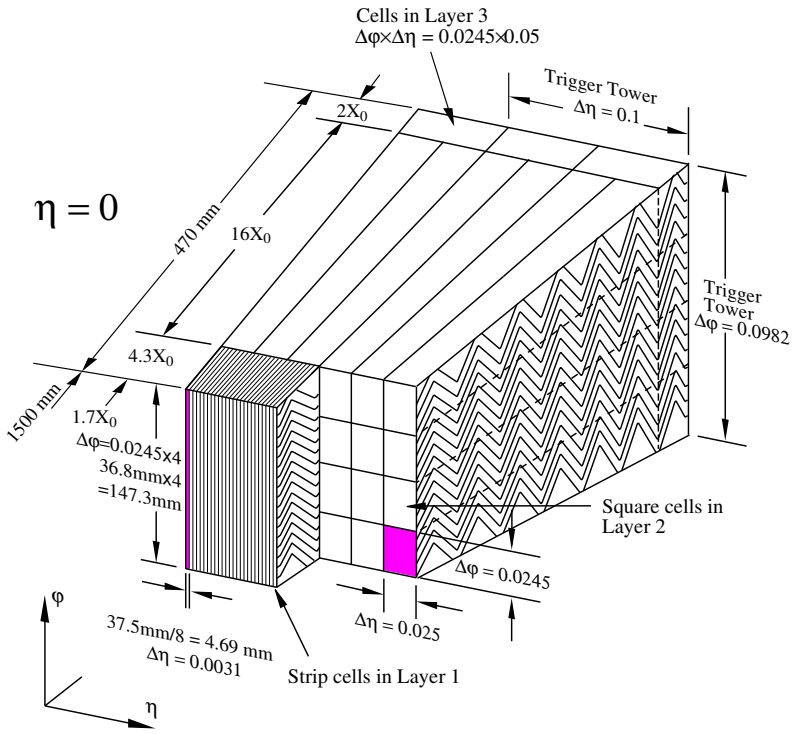


Figure 5.8: Diagram of the electromagnetic calorimeter in the barrel displaying the accordion-shaped segmentation [57].

measurement; the primary shower energy absorption layer; and a final correction layer to account for energy leakage outside the calorimeter. Its total thickness is $>$ 22 radiation lengths (X_0) in the barrel and 24 in the endcaps. Perpendicular to this segmentation, the calorimeter is divided into longitudinal cells called "towers", as shown in Figure 5.8.

5.2.3 Hadronic Calorimeter

The ATLAS hadronic calorimeter is designated for measuring the energy of hadrons and is composed of three subsystems. The first is the TileCal, which serves as the HCal in the barrel region ($|\eta|$

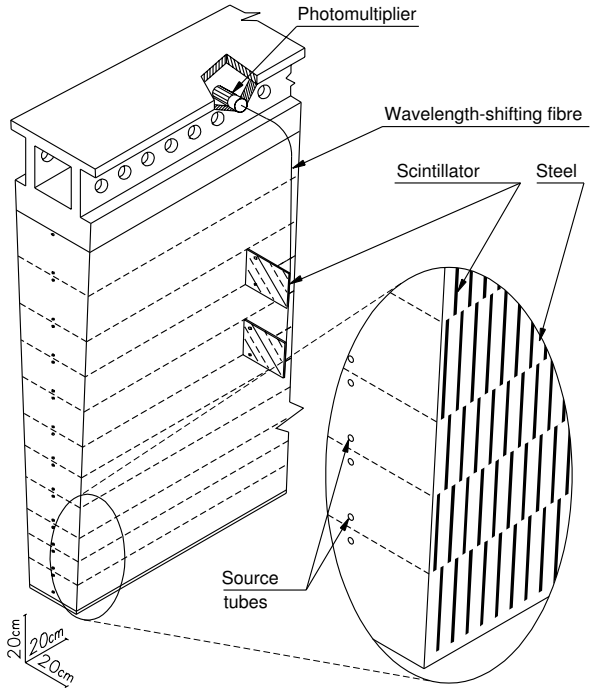


Figure 5.9: Diagram of the electromagnetic calorimeter in the barrel displaying the accordion-shaped segmentation [57].

< 1.7) immediately following the EM calorimeter. It uses scintillator tiles as an active material, alternated with steel plates that serve as the absorber material. The geometry of these layers can be seen in Figure 5.9, along with the azimuthal segmentation into modules of $\Delta\phi \approx 0.1$. The TileCal is also segmented longitudinally into three layers, altogether providing a thickness of 9.7 interaction lengths (λ) in the barrel and 10 in the endcap. This is sufficient to fully contain the large majority of hadronic showers expected from LHC collisions.

The second two subsystems supplement the TileCal in the forward region: the hadronic end cap (HEC) covers the range $1.5 < |\eta| < 3.2$, and the forward calorimeters (FCal) which consist of three modules covering $3.1 < |\eta| < 4.9$ [66]. Both the HEC and FCal use LAr as an active medium, with

either copper (HEC and first FCal module) or tungsten (outer two FCal modules) as an absorber. While the first module of the FCal is designated for EM measurements, the HEC and remaining two FCal modules primarily measure hadronic energy.

5.3 Muon Spectrometer

The outermost layer of the ATLAS detector is designated for measurement of muon position and momentum. There are four technologies used in the muon spectrometer (MS): the Muon Drift Tubes and Cathode Strip Chambers provide precision tracking in $|\eta| < 2.7$, while the Resistive Plate Chambers and Thin Gap Chambers are used for triggering in the barrel and endcap respectively, covering $|\eta| < 2.4$. A diagram of the MS and the locations of these four components can be found in Figure 5.10. The chambers of the MS are oriented between the coils of the toroid magnet (see Section 5.4), which provides a magnetic field oriented orthogonal to the muon's expected trajectory, bending the muons and allowing measurement of their momenta.

5.3.1 Monitored Drift Tubes (MDTs)

The MDTs are pressurized drift tubes that populate the barrel of the MS and contain a gas mixture that is 93% argon and 7% CO_2, with a conducting wire running along the center of the tube. In the ATLAS detector, the tubes are oriented along ϕ, providing precision measurements in η. A charged particle passing through the MDT is detected through ionization of the gas, whereby released electrons drift towards the central wire under a radial electric field. The drift time is approximately 700 ns. Detection of a particle through several nearby tubes can allow for trajectory reconstruction, pro-

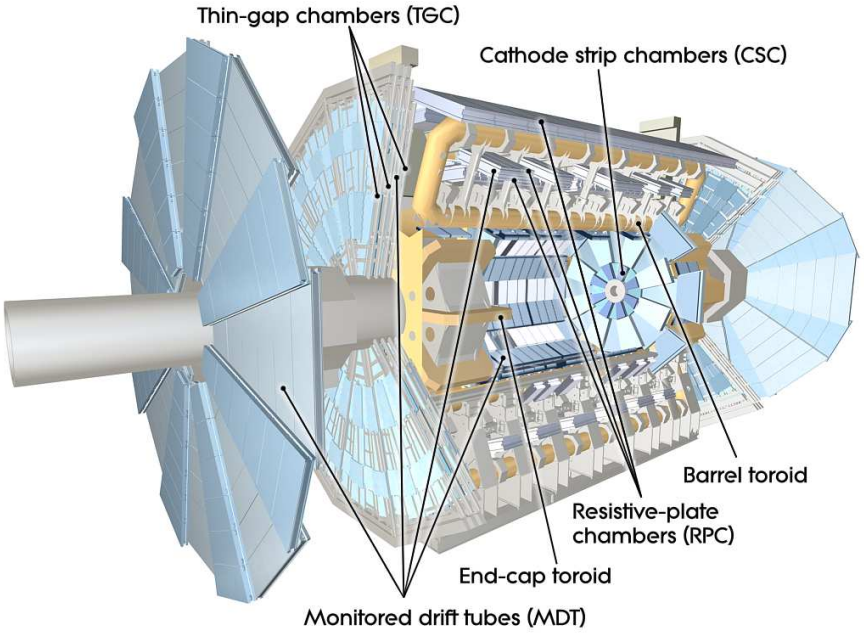


Figure 5.10: Layout of the ATLAS muon spectrometer [57]

viding a resolution in the η measurement as low as 30 μm across all three layers of MDTs [57].

5.3.2 Cathode Strip Chambers (CSCs)

CSCs are multi-wire proportional chambers with radially oriented anode wires containing a gas mixture that is 80/20% argon and CO_2 [57]. Similar to the MDTs, these chambers detect ionization released by a traversing particle, drawing released electrons to two sets of cathode readout strips with an average drift time of 40 ns. One of the cathode strip sets runs parallel to the anode wire and provides precision track measurement, and the set is perpendicular to provide the transverse coordinate. Combined these strip sets gives a resolution of 40 μm in the bending plane. With a much shorter drift time than the MDTs, the CSCs are specifically designed to handle high-rate environments, and

thus provide precision tracking in the inner endcap region at $2.0 < |\eta| < 2.7$.

5.3.3 Resistive Plate Chambers (RPCs)

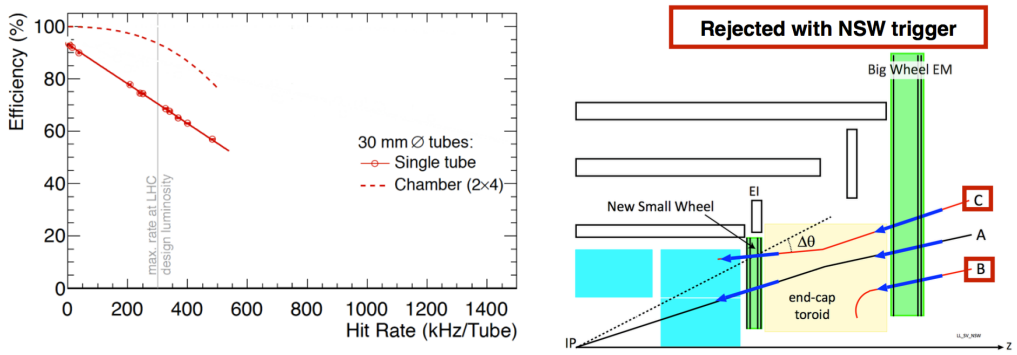
Since the drift times of both the MDTs and CSCs are longer than the LHC bunch crossing interval, triggering chambers are necessary to assign muons to specific primary interactions. RPCs provide triggering in the barrel ($|\eta| < 1.05$) and consist of two parallel resistive plates with a gas mixture of 94.7% $C_2H_2F_4$, 5% Iso-C_4H_{10}, and 0.3% SF_6 [57]. The thin plate gap of 2 mm leads to a quick response time, with an average signal width of approximately 5 ns. RPCs have a position resolution of 1 cm (providing both η and ϕ measurements), and a time resolution of 1 ns.

5.3.4 Thin Gap Chambers (TGCs)

TGCs are multi-wire proportional chambers that provide fast response times for triggering in the region $1.05 < |\eta| < 2.7$. With a similar time resolution to the RPCs, the quick response time is provided in this case by a small wire-to-cathode distance (1.4 mm), and a high electric field to give shorter drift times. The RPCs are filled with a gas mixture of CO_2 and n-pentane. The timing resolution is similar to that of the RPCs (1 ns) and the spatial resolution on the azimuthal coordinate is 2-7 mm.

5.3.5 The New Small Wheel (NSW)

Starting in 2018, the LHC entered Long Shutdown 2 (LS2), an upgrade period during which several detector subsystem improvements will be installed to cope with increased hit rates and high



(a) (b)

Figure 5.11: Left: MDT tube hit (solid) and segment (dashed) efficiency as a function of hit rate per tube, demonstrating the insufficient efficiency at high hit rate [67]. Right: diagram of NSW in the ATLAS MS showing the additional triggering capability and subsequent fake rejection improvement.

radiation exposure. The ATLAS Muon New Small Wheel (NSW) replaces the innermost endcap wheel of the muon spectrometer with new detector technologies. The motivation for this upgrade is twofold. As seen in Figure 5.11a, the MDTs will be insufficient to provide good muon efficiency for the higher hit rates expected in future LHC run conditions. Second, the NSW provides an extra trigger layer that helps reduce fake triggers from background hits, as shown diagrammatically in Figure 5.11b.

The NSW upgrade includes two new detector technologies: micromesh gaseous strip detectors (micromegas) used primarily for precision tracking, and small-strip thin gap chambers (sTGCs) used primarily for triggering [67]. The sTGCs are fundamentally similar to the existing TGCs, with a considerably smaller pickup strip pitch of 3.2 mm. The micromegas detectors reconstruct charged particle trajectories through ionized gas, using the same mixture as the existing MDTs. The released electrons traverse a maximum 5 mm drift gap towards a metallic mesh. Below this micromesh is

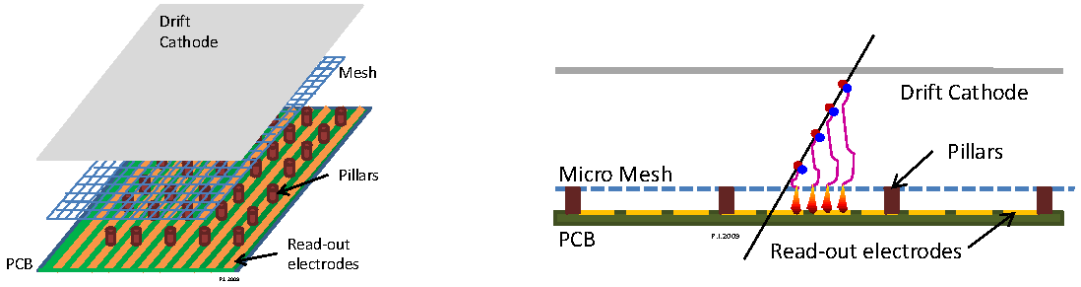


Figure 5.12: Illustrations of the geometry (left) and detection principle (right) of the micromegas detector [67].

the 128 μm amplification region, where the signal is amplified and accelerated to readout electrodes topped with resistive strips to prevent sparking. The arrival time of signals on each readout strip can be used to reconstruct the track position and incident angle. Figure 5.12 illustrates the micromegas components and their detection capability. In ATLAS, eight micromegas chambers are stacked together in an octuplet, where the four central chambers are oriented with strips at an angle of $\pm 1.5°$. This layout allows for a measurement of the ϕ coordinate while lengthening the lever arm between straight strips for triggering.

5.4 Magnet System

The magnet system of the ATLAS detector consists of two independent subsystems with four superconducting magnets in total. First, a central solenoid placed after the inner detector provides a 2 T field parallel to the beam axis, which bends charged particles in the azimuthal plane. Second, a 0.5-1 T toroidal field in the muon spectrometer provides bending in η via one barrel and two endcap magnets. Each toroidal magnet is composed of eight individual coils. The geometry of these two magnet systems can be seen in Figure 5.13. The amount of bending in the trajectory of a charged particle that

is induced by the magnets is used to measure its momentum via the Lorentz Force Law.

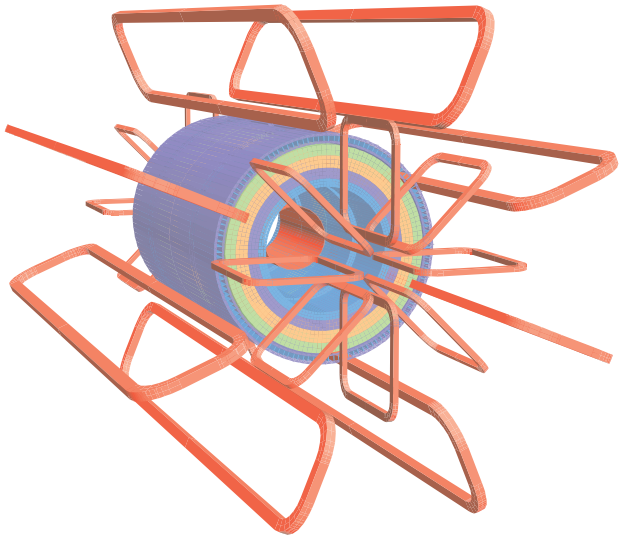
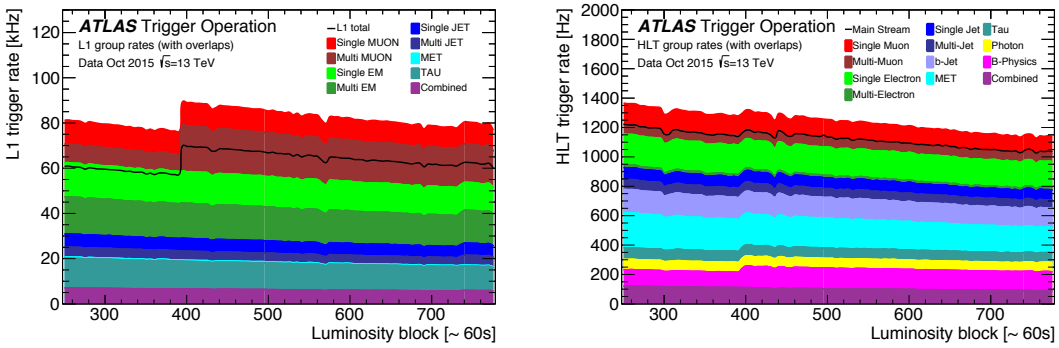


Figure 5.13: Geometry of the ATLAS magnet system [57]. The three toroids are shown in orange, while the central solenoid is shown in purple.

5.5 Trigger System

In Run II of the LHC, protons collide at the ATLAS interaction point at a rate of up to 40 MHz. Each event contains about 1 MB of information, and the data acquisition system is capable of writing this information to storage at a rate of about 100 MB/s. Therefore, the trigger system is needed to reduce the event output by about five orders of magnitude before it can be written. This system needs to be both fast and efficient at selecting events of particular interest for the search and measurement physics program of the ATLAS experiment.

The first step in the ATLAS triggering process is the hardware-based Level-1 (L1) trigger, which uses detector subcomponents to seed regions of interest (ROIs) based on generalized subsystem sig-



(a) **(b)**

Figure 5.14: L1 (a) and HLT (b) trigger rates grouped by trigger signature during an LHC fill in October 2015 [68].

natures. Events not passing any of the L1 triggers (listed in the legend of Figure 5.14a) are removed, reducing the event rate to 100 kHz. The ROIs are passed to a software-based High Level Trigger (HLT), which integrates information across the detector and provides basic object reconstruction. The legend of Figure 5.14b lists common HLT triggers, which save events containing objects of interest such as electrons, muons, jets, or missing energy, or specific combinations of multiple objects per event. After the HLT, the event rate is approximately 400 Hz, low enough to be written to disk.

5.6 Event Reconstruction

The integration of all ATLAS detector subsystems and triggering capabilities allow the reconstruction of individual objects that were created in a given proton-proton interaction. The subdetectors described in Sections 5.1 to 5.3 are designed to obtain specific identifying information about a particle, such as its mass, charge, and momentum; they can then work together to give each particle a unique signature across the entire detector. Figure 5.15 shows the passage of different Standard Model particles through the ATLAS detector and their signatures in the various subsystems. In addition to identifying objects as electrons, muons, jets and *b*-jets, or other common particles*, reconstruction determines the full kinematics of the event, including missing transverse energy. Event reconstruction can be applied to data or simulated events.

5.6.1 Electrons

The electron signature in ATLAS primarily consists of tracks in the inner detector and energy deposits in the electromagnetic calorimeter. Candidate electrons are first reconstructed from electromagnetic calorimeter cell cluster "seeds" ($p_T > 2.5$ GeV) that are matched to ID track seeds ($p_T >$ 1 GeV, with three hits in three different silicon layers). To reduce fake electron background from photon conversions or secondary particles, the track seeds are required to be compatible with the primary vertex. Algorithms for electron identification (ID) are also applied to the candidate, which use quantities related to the shower shape, track-cluster matching, TRT and inner detector properties,

*While a similar reconstruction procedure exists for particles such as photons and taus, the discussion in this treatment will be limited to particles directly used for the analyses detailed in Part IV.

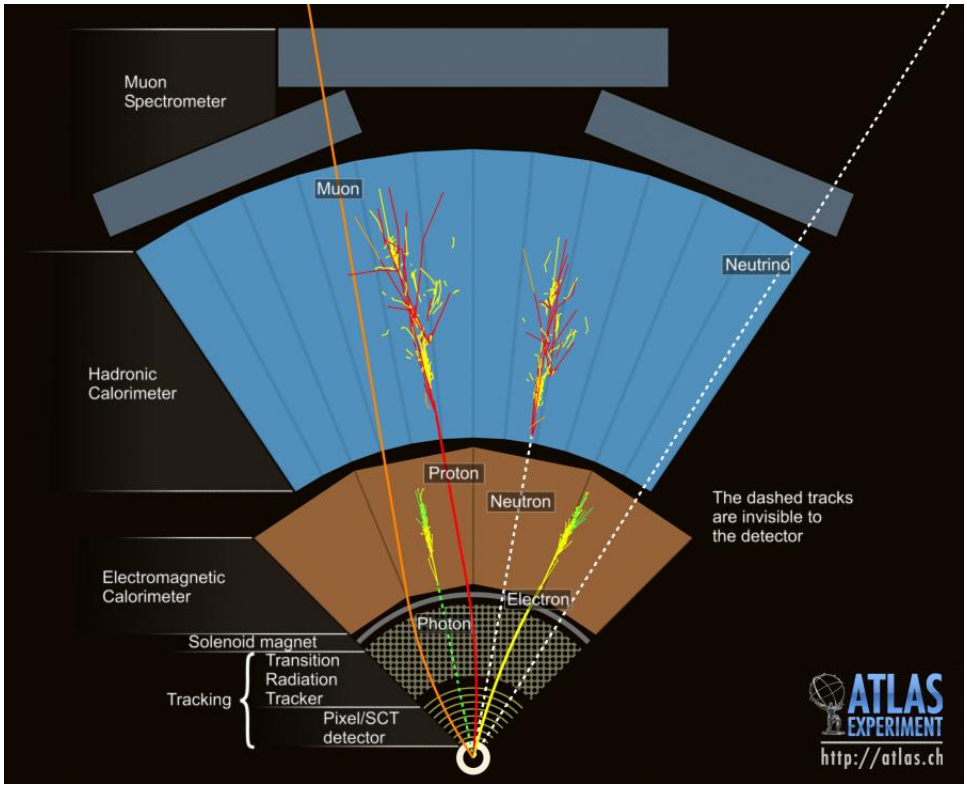


Figure 5.15: A computer-generated image of proton-proton collision decay products passing through the ATLAS detector[69].

and *bremsstrahlung* effects [70]. These algorithms are primarily based on multivariate likelihood (LH) methods [71] and optimized on Monte Carlo simulation. Three levels of electron ID are offered in Run II: *Loose*, *Medium*, and *Tight* (listed in increasing order of background rejection).

Most analyses also require electrons to pass isolation criteria, which quantify the amount of deposited energy nearby the electron candidate to discriminate between prompt electrons, from the primary hard-scatter interaction, and other non-isolated objects such as electrons from conversions or light hadrons mis-reconstructed as electrons. Two primary isolation variables are used for this assessment, one describing the electron's isolation in calorimeter energy ($E_T^{cone0.2}$), and the other

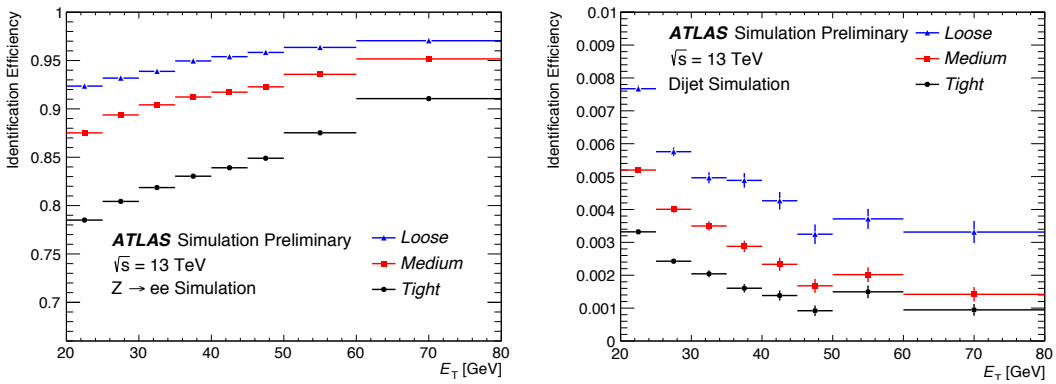


Figure 5.16: The efficiency of identifying electrons from $Z \rightarrow ee$ (left) and the efficiency for identifying hadrons as electrons (right) in dijet simulation samples. [70].

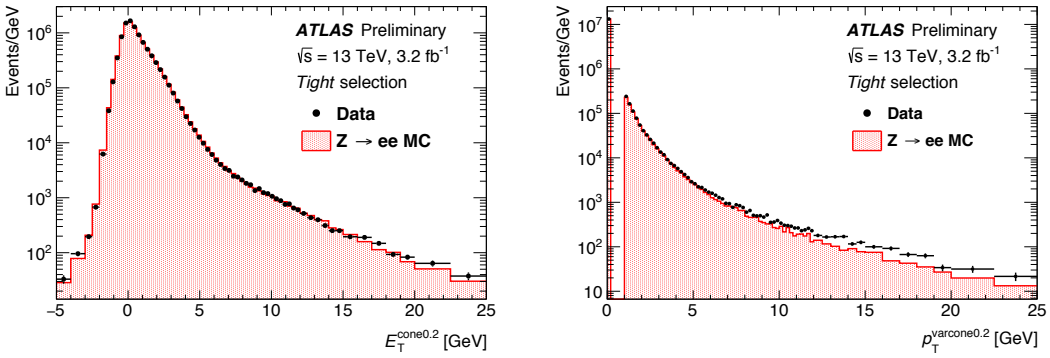


Figure 5.17: Distributions of $E_T^{cone0.2}$ (left) and $p_T^{varcone0.2}$ (right) for electrons in $Z \rightarrow ee$ data and simulation [70].

in track-based momentum ($p_T^{varcone0.2}$). Both variables sum the amount of energy or momentum in a Δ-R cone of a given size around the candidate electrons. Several isolation working points are used in Run II, which combine requirements on both energy and track-based isolation variables. Figures 5.16 and 5.17 show electron ID efficiency for primary working points and isolation variables, respectively.

5.6.2 Muons

The first step in reconstructing muon candidates is to search for patterns of hits in the muon spectrometer to form straight line segments. Tracks are first built by connecting several segments to traverse the entire MS ("standalone"), and second by matching an MS track to an ID track ("combined"). Once tracks have been made, a muon candidate can be reconstructed in one of four ways [72]:

1. Combined (CB) muon: built from combining independently-reconstructed ID and MS tracks, where the hits on the combined track must pass χ^2 matching.
2. Segment-tagged (ST) muon: built by extrapolating an MS segment to the ID and finding a suitable track candidate; used for muons with minimal information available in the MS.
3. Calorimeter-tagged (CT) muon: built by extrapolating an MS segment to a calorimeter cluster consistent with a minimum-ionizing particle; used in regions where MS is only partially available.
4. Extrapolated (ME) muon: built only with the MS segment and a loose requirement for compatibility with the interaction point; used to increase acceptance for muons in $2.5 < |\eta| < 2.7$, which is not covered by the ID.

As with electrons, identification criteria are applied to reconstructed muon candidates to reduce background, mainly from pion and kaon decays. The ID working points use information from the χ^2 match between ID and MS tracks, and compatibility of momentum measurements between the ID and MS. Four ID working points are primarily used in Run II: *Loose*, *Medium*, *Tight*, and *High-p_T*. The search described in Chapter 10 also introduces a new dedicated working point for extremely soft muons, called the *Low-p_T* working point. Several isolation working points are also available for further background rejection, using variables such as $p_T^{varcone30}/p_T$ and $E_T^{topocone20}/p_T$ that sum

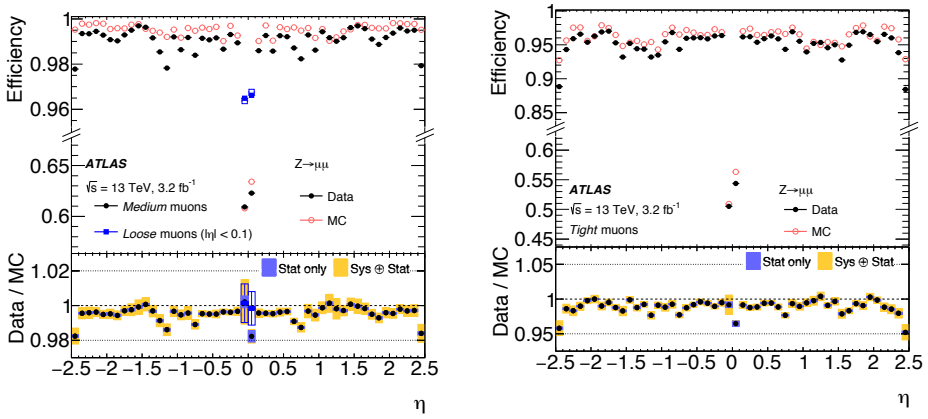


Figure 5.18: Muon reconstruction efficiency for muons with p_T > 10 GeV from $Z \rightarrow \mu\mu$ for the Loose and Medium ID working points (left) and for the Tight ID working point (right) in both data and simulation [72]. Blue squares in the left plot indicate Loose efficiency in the region $|\eta|$ < 0.1 where the Loose and Medium selections differ significantly.

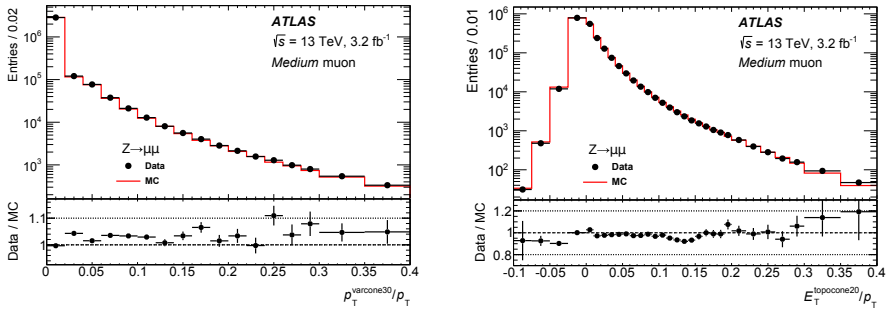


Figure 5.19: Distributions of $p_T^{varcone30}/p_T$ (left) amd $E_T^{topocone20}/p_T$ (right) for muons in $Z \rightarrow \mu\mu$ data and simulation [70].

the energy and momentum in a ΔR cone around the muon. Figures 5.18 and 5.19 show muon ID efficiency for three working points and primary isolation variables, respectively.

5.6.3 Jets

In any given proton-proton collision, many quarks and gluons are produced, but because of confinement it is not possible to individually detect them in ATLAS. Instead, colored particles undergo a branching process and subsequent hadronization, in which they create a spray of hadrons in the direction of the original parton; this spray is referred to as a *jet*. A jet signature in ATLAS consists of energy deposits in the electromagnetic and hadronic calorimeters, and tracks in the inner detector from charged particles. The process of mapping hard-scatter partons to final state hadrons is called jet reconstruction; it must be collinear and infrared safe, and yield finite and reasonable cross sections.

Jets at the LHC are made from topological clusters using calorimeter cells, known as "topoclusters". Topoclusters are built using seed cells, whose energy measurement is four times the expected noise level, and adjacent cells are recursively added to the cluster if they have sufficient large energy. Each topocluster is calibrated in one of two ways, so as to properly characterize the energy response of the calorimeter. This calibration gives the *jet energy scale* (JES), and accounts for dead calorimeter material or leakage, energy deposits below noise threshold, and pile-up. The first calibration scale option is EM, where each cluster is assumed to have come from the energy deposition of an electron or photon. The second is the local cluster weight (LCW) scale, which gives an energy correction to each cluster and allows them to be classified as electromagnetic or hadronic. Figure 5.20 shows the jet energy response (JER) for both EM- and LC-calibrated jets, where the response is defined as the ratio of reconstructed to truth jet energy.

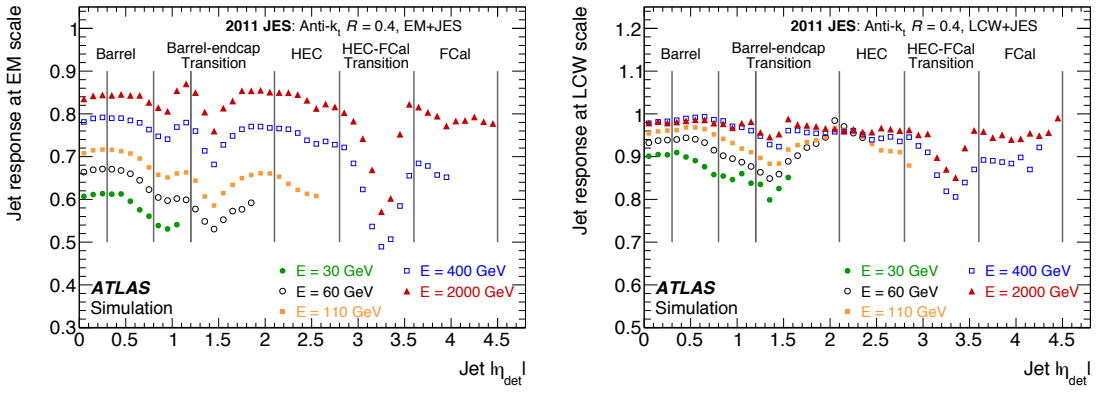


Figure 5.20: Jet energy response in simulation with the EM scale (left) and LC scale (right) as a function of η [73].

Reconstruction

Topoclusters are grouped together into jet candidates using a reconstruction algorithm. In ATLAS, sequential clustering algorithms are commonly used [74], which are based on distance measures as defined in Equation 5.6:

$$d_{ij} = \min\left(k_{ti}^{2p}, k_{tj}^{2p}\right)\frac{\Delta_{ij}^2}{R^2} \tag{5.6}$$

Here, $\Delta_{ij}^2 = (y_i - y_j)^2 + (\phi_i - \phi_j)^2$, k_{ti} is the transverse momentum of particle i, and p is a parameter that describes the relative power of energy versus Δ_{ij}^2. The clustering proceeds by identifying the smallest distance between adjacent topoclusters until the cluster is closer to the beam than it is to other topoclusters. At this point, the clustering stops and the resulting object is deemed a jet. Different values of p correspond to different distance measures and thus different algorithms: p = 1 gives the inclusive k_T algorithm, p = 0 gives the inclusive Cambridge/Aachen algorithm, and p =

-1 gives the anti-k_T algorithm, which is used to reconstruct jets in the analyses described in Part IV.

An alternate reconstruction, *particle flow*, integrates tracking and calorimeter information to construct a jet from its constituent particles [75]. For each jet, the particle flow reconstruction algorithm removes calorimeter energy deposits attributed to charged hadrons, and replaces this information with measurements of their momenta from the inner tracker. As shown in Table 5.1, the expected calorimeter and tracker resolutions are inversely related to the particle's energy/momentum; for low-energy charged particles, the resolution of the tracker is significantly better than that of the calorimeter. Therefore, particle flow reconstruction to take advantage of both charged hadron tracking information, while retaining calorimeter measurements for neutral jet components.

Given the large number of simultaneous interactions present in each ATLAS event, it is necessary to distinguish primary interaction jets from pile-up jets. A commonly used method for this discrimination is the jet vertex tagger (JVT) [76]. It uses two variables: the jet vertex fraction, defined as the ratio of tracks associated to the primary vertex to the total number of tracks in the jet, and R_{p_T}, defined as the ratio of the scalar sum of the jet track p_T to the fully calibrated jet p_T (including calibration pile-up subtraction). The JVT combines these two variables in a likelihood function developed on simulated jets, and extracts the relative probability that a jet is likely to be signal or pile-up.

b-tagging

Identifying the flavor or type of parton that originated the jet can be important information for analyses when selecting jets. Though this task is very challenging in most cases, displaced vertices from longer-lived partons can provide a useful handle on tagging jets of certain flavors. Specifically,

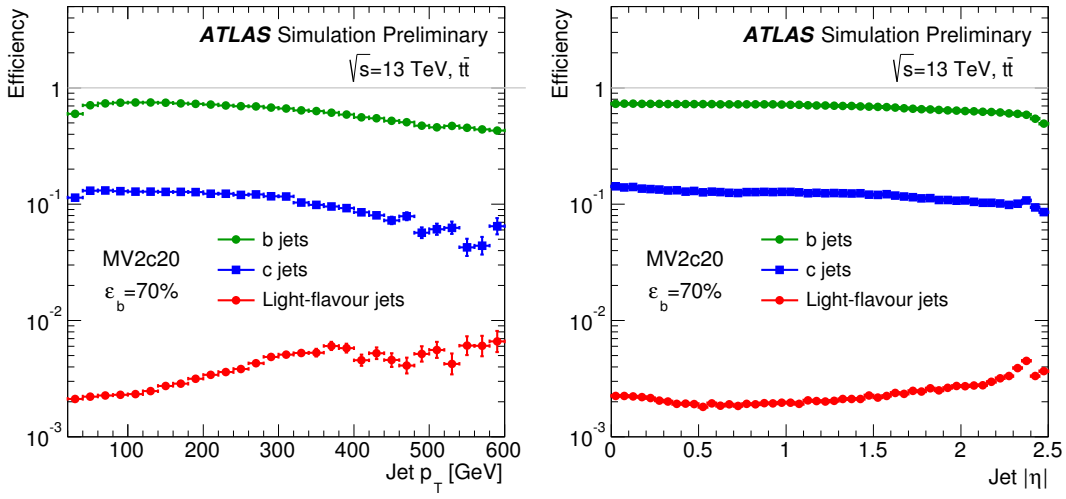


Figure 5.21: The efficiency to tag b (green), c (blue) and light-flavour (red) jets for the MV2c20 tagging algorithm with the 70% operating point as a function of p_T (left) and η (right) [77].

B mesons have a lifetime on the order of 10^{-12} seconds, corresponding to a distance travelled in the detector of about 0.5 mm [17]. This allows for b-jets to be distinguished from other jets via the presence of a secondary vertex.

Several algorithms are used in ATLAS to identify b-jets. The most commonly used b-tagger is a multivariate technique that incorporates information about the jet impact parameters, likelihood ratios between jets of different flavors, and secondary vertices. Such information is encoded in 24 variables that are fed as input to a boosted decision tree tagger known as MV2 [77]. Figure 5.21 gives the performance of the MV2c20 algorithm for one of several working points (70%), which allow customizability of good tag efficiency and fake tag rejection depending on analysis needs.

5.6.4 Missing Transverse Energy (E_T^{miss})

While most particles produced at the LHC directly interact with the detector material, certain particles such as neutrinos (or hypothetical BSM particles like the neutralinos described in Part I) do not leave any measurable trace in the detector. Instead, the presence of these particles must be inferred via momentum imbalance in the primary interaction. Since all of the momentum of the incoming protons is parallel to the beam axis, any imbalance in the transverse plane after the collision can be interpreted as momentum carried away by an invisible particle. The magnitude of this imbalance is called missing transverse energy (E_T^{miss}), and it is a crucial quantity in many searches for new physics.

E_T^{miss} is calculated as the sum of several terms as follows [78]:

$$E_{x(y)}^{miss} = E_{x(y)}^{miss,e} + E_{x(y)}^{miss,\gamma} + E_{x(y)}^{miss,\tau} + E_{x(y)}^{miss,jets} + E_{x(y)}^{miss,\mu} + E_{x(y)}^{miss,soft} \tag{5.7}$$

Each term in Equation 5.7 represents the negative vectorial sum of the momenta of the calibrated objects (in order: electrons, photons, taus, jets, and muons). The soft term represents detector signals not associated to specific objects, which can contain separately defined track (TST) and calorimeter (CST) soft terms. The total missing energy in an event is then defined in Equation 5.8:

$$E_T^{miss} = \sqrt{(E_x^{miss})^2 + \left(E_y^{miss}\right)^2} \tag{5.8}$$

E_T^{miss} can come from real sources, such as non-interacting particles, or fake sources, such as mis-

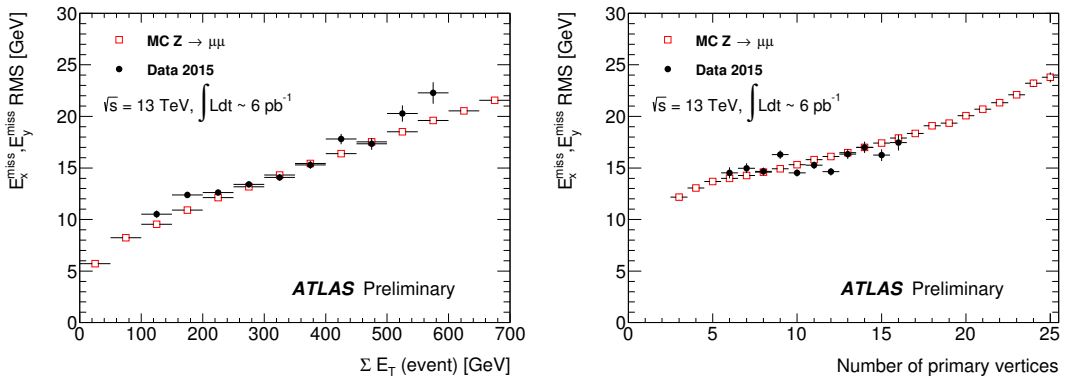


Figure 5.22: Distribution of the track soft term resolution E_T^x, E_T^y, as a function of $\sum E_T$ (left) and number of primary vertices (right), comparing data (black) and MC (red) [78].

reconstructed physics objects or dead/noisy detector regions, which can spuriously imbalance the total momentum measured in the transverse plane. As a result, the quality of the E_T^{miss} reconstruction, known as the E_T^{miss} resolution, is studied in $Z \rightarrow \mu\mu$ events, where little real E_T^{miss} is expected. Figure 5.22 shows this resolution assessment as a function of $\sum E_T$ and the number of primary vertices. Since a higher amount of signal in the detector leads to larger mis-measurements, pileup can be seen to degrade the E_T^{miss} resolution.

Part III

Strategies

As introduced in Chapter 3, compressed SUSY searches with ISR-assisted topologies are challenging. A variety of strategies must be employed to ensure that signals can be efficiently selected, while eliminating any contaminates or backgrounds that closely mimic the signal, and ultimately building an effective and correct analysis. Part III describes three essential ways in which these challenges are mitigated. Chapter 6 introduces the Recursive Jigsaw Reconstruction method, a framework designed to take advantage of event shape information, with an emphasis on the handling of difficult topologies such as those with ISR boosting. Chapter 7 details event cleaning for the ATLAS experiment in Run II, providing a motivation for the procedure, the details of its implementation, and its performance for the relevant data-taking periods. Chapter 8 describes the statistical analysis methods used to make quantitative inferences about the data, and introduces the `HistFitter` software framework used to implement these methods in searches. Together, these strategies are integral to the success of the searches performed and discussed in Part IV.

6

Recursive Jigsaw Reconstruction

One of the key challenges in a compressed SUSY search is distinguishing signal from background, due to the inherent lack of missing energy that is often the hallmark of SUSY signatures. It is therefore especially important in these searches to capture all possible information in an event, with a particular focus on crucial event shape information typically lost in traditional analysis variables. Accessing this information can be done with an event analysis strategy based on *Recursive Jigsaw Recon-*

struction (RJR), a general scheme for analyzing high energy collision events [79]. RJR has the ability to resolve combinatoric ambiguities when there are several identical objects in a final state, as well as kinematic ambiguities that arise if there is information missing in an event due to the presence of invisible particles. There are a variety of ways to implement RJR for different event topologies; in this treatment the focus is on RJR with initial state radiation (ISR), via calculation of the event thrust axis, and its application to both di-stop and di-higgsino decays.

6.1 Methodology

As discussed in detail in Chapter 3, the search for compressed signals is experimentally difficult because of the soft final state decay products and lack of missing energy. However, the fact that the daughter particle (in this case the $\widetilde{\chi}_1^0$) does not gain momentum from the parent particle decay (either $\tilde{t}$ or $\widetilde{\chi}_2^0/\widetilde{\chi}_1^\pm$) leads to other useful correlations that can be exploited.

If the pair-produced SUSY particles gain all their momentum by recoiling against a system of ISR jets, this di-sparticle system will have a strong correlation with the momenta of the ISR system. That correlation will then propagate down the decay chain, with more boost going to the more massive particle at each decay. In the parent sparticle decay, the mass difference between parent sparticle and $\widetilde{\chi}_1^0$ determines how much of the parent's energy is available to be imparted to the $\widetilde{\chi}_1^0$ as momentum. The smaller the mass splitting, the less that the $\widetilde{\chi}_1^0$ momentum's is attributable to the parent decay, therefore the stronger the correlation between $\widetilde{\chi}_1^0$ momentum (or E_T^{miss}) with ISR p_T. In this way, the correlation between E_T^{miss} and ISR is very dependent on the mass splitting in the decay chain.

Equation 6.1 demonstrates this trend quantitatively [80, 81, 82], specifically showing that the ratio of the E_T^{miss} and ISR p_T goes as the ratio of the parent and daughter sparticle masses (shown here for the example of di-stop decay.) Superscripts (subscripts) on Lorentz-transformation factors indicate the final (initial) reference frame and superscripts (subscripts) on momenta and energy indicate the reference frame (object). :wq

$$\begin{aligned} E_T^{miss} \equiv p^{lab}_{\widetilde{\chi}_1^0\widetilde{\chi}_1^0,T} \sim \gamma^{lab}_{\tilde{t}\tilde{t}}\beta^{lab}_{\tilde{t}\tilde{t}}E^{\tilde{t}\tilde{t}}_{\widetilde{\chi}_1^0\widetilde{\chi}_1^0} \sim \frac{p_T^{ISR}}{m_{\tilde{t}\tilde{t}}}2\gamma_{\tilde{t}}^{\tilde{t}\tilde{t}}m_{\widetilde{\chi}_1^0} \sim p_T^{ISR}\frac{2\gamma_{\tilde{t}}^{\tilde{t}\tilde{t}}m_{\widetilde{\chi}_1^0}}{2\gamma_{\tilde{t}}^{\tilde{t}\tilde{t}}m_{\tilde{t}}} \sim p_T^{ISR}\frac{m_{\widetilde{\chi}_1^0}}{m_{\tilde{t}}} \\ \Rightarrow \frac{E_T^{miss}}{p_T^{ISR}} \sim \frac{m_{\widetilde{\chi}_1^0}}{m_{\tilde{t}}} \end{aligned} \tag{6.1}$$

There are a few key features of compressed SUSY signatures that make this treatment especially effective. One of those is the small expected widths of the parent particles. The zeroth order treatment in Equation 6.1 describes the perfectly at rest picture; the first order correction comes from the non-trivial widths of the involved sparticles. However, since the parent sparticle widths are expected to be small (less than the top Breit-Wigner of 1.3 GeV), and the width of the $\widetilde{\chi}_1^0$ is near 0 if it is stable, the E_T^{miss}-ISR p_T correlation is strongest when the sum of the masses of the two daughter particles is almost equal to the mass of the parent particle. This is precisely the region in which traditional techniques are most difficult.

The second helpful feature is that the $\widetilde{\chi}_1^0$ is expected to be massive as compared to the Standard Model decay counterpart (top quark in the case of stop decay or off-shell W/Z boson in the higgsino case). This allows the $\widetilde{\chi}_1^0$ to absorb a significant enough fraction of the ISR-imposed boost to gen-

erate measurable E_T^{miss} in the event. Since the other Standard Model decay products are very soft, they are often not useful for triggering, making a hard LSP crucial for the use of E_T^{miss} triggers.

The first step of an RJR-based analysis is to impose a decay tree on the event. While this decay tree can in principle specify each expected final state object and all the intermediate states of the decay, a generic simpler version is applied for ISR topologies as shown in Figure 6.1. In this tree, there are three frames, or groups of final state particles: the ISR, invisible, and visible systems. The ISR frame is needed to give momentum to the system of interest. This system of interest, called the sparticle or S frame, then decays into particles that are visible in the detector (V frame), and one or more invisible particles (I frame) which escape detection, leaving only a transverse imbalance of momenta in the event. The center of mass frame (CM frame) is then the sum of the reconstructed or missing objects, sparticles and accompanying particles. Each of these four frames is identified by a four-vector sum of all particles, which can then be evaluated in any of the frames implicitly defined by the decay tree.

The decay tree is imposed on event by filling in the four vectors of the three final state frames (I, V, and ISR). The I frame requires a choice to be made regarding its missing z component. First, the vectorial E_T^{miss} reconstructed in each event as the transverse momentum of I, evaluated in the lab frame. This leaves two four-vector components unspecified: these can be expressed as the mass of I and its longitudinal momentum in the lab frame. For the former, the convention used here is to decide $m_I = 0$. While this isn't necessarily a physically correct assignment, it simplifies the problem and does not detract from any kinematic effects or correlations. For the latter, the longitudinal momentum of all objects is simply set to 0, giving an exclusively transverse view of the event.

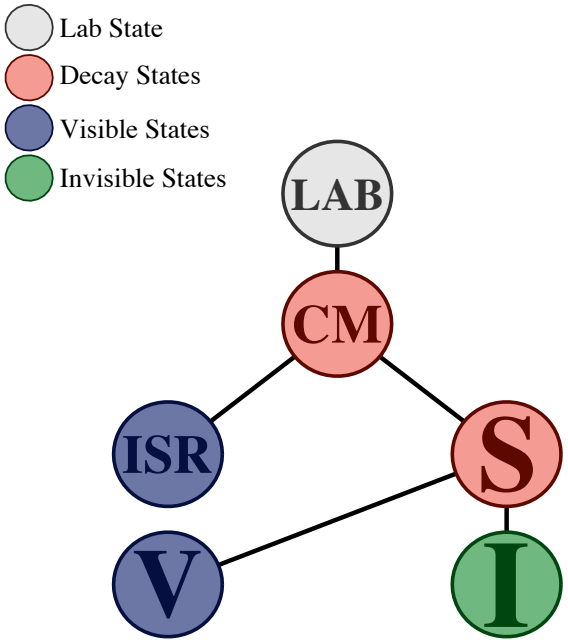


Figure 6.1: An RJR decay tree diagram for analyzing ISR-assisted signal topologies [83].

After the I frame four-vector is filled out in this way, the next step is to assign all other reconstructed objects to either the V or ISR frame. This is done using a *jigsaw rule*, which is a generic algorithm that resolves any combinatoric ambiguities associated with frame assignment. For compressed scenarios, this algorithm maximizes the back-to-back p_T of all final state objects, equivalent to calculating the thrust axis of the event.

Boosting along this axis into the center-of-mass frame allows the event to be divided into two hemispheres, revealing the back-to-back event shape consistent with ISR-assisted topologies. The only expected source of E_T^{miss} in the signal is the LSP, thus the hemisphere that contains the E_T^{miss} is the sparticle S frame, and the other hemisphere is the ISR frame. Figure 6.2 provides a diagram of this hemispherical separation along the thrust axis, showing how all of the objects in the event will

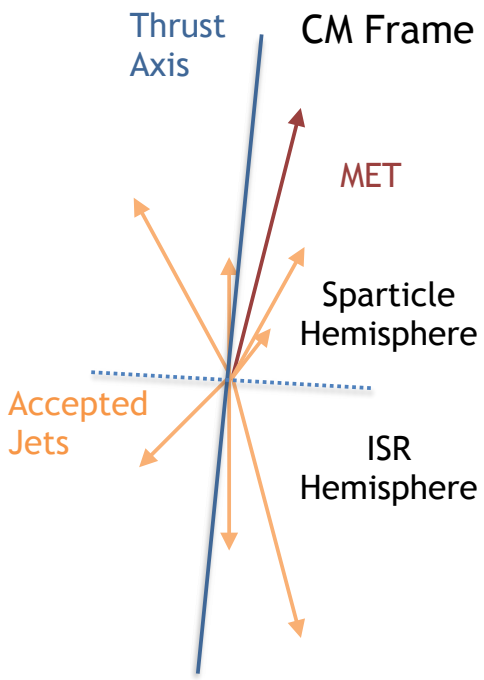


Figure 6.2: Diagram of an ISR-assisted event, where the calculation of a thrust axis allows for the designation of two distinct hemispheres. All objects can be categorized into one of these hemispheres, which become the S frame (if the E_T^{miss} vector is present) or the ISR frame.

then fall into one of the two frames.

After this frame assignment, all objects are in one of the three final state frames, and there is a full kinematic description of the decay tree in the transverse plane. From here, it is possible to analyze events by building unique jigsaw variables and using these to discriminate signal from background.

6.2 Application

The new variables that emerge from RJ reconstruction are well-equipped to perform the difficult signal to background discrimination in the compressed or diagonal area of phase space. Not only

do they contain event shape information via the thrust axis and hemisphere creation, but they also have information about whether a given final state object was more likely to come from the SUSY or ISR system. Many of these are similar in concept to traditional analysis variables, but with a more accurate understanding of the event that is gained from the reconstruction. A key example is in the ISR system; many analyses that use ISR topologies must assume that the leading jet is the ISR jet, while in RJR the ISR boost can come from a system of several jets, none of which are necessarily the leading jet.

An RJR-based analysis will utilize such novel variables, which can take the form of energy ratios, object multiplicities, or angles/momenta in the various frames, to build regions that effectively select for compressed signals while cutting away Standard Model background. Several key RJR variables are described in detail below.

R_{ISR}

The variable R_{ISR} is one of the most important variables used in compressed searches, because it encapsulates the crucial correlation between missing energy and ISR p_T described in the previous section. In fact, the variable is simply defined in Equation 6.2 as the ratio of E_T^{miss} to p_T^{ISR}. Instead of using the scalar quantity E_T^{miss}, the vector quantity $p_{I,T}$ can be used because the full four-vector for the invisible frame has been reconstructed. Recall from Equation 6.1that this ratio is also propor-

tional to the ratio of parent to daughter particle masses for the case of very compressed points.

$$R_{ISR} \equiv \frac{|\vec{p}_{I,T} \cdot \hat{p}_{ISR,T}|}{|\vec{p}_{ISR,T}|} = \frac{E_T^{miss}}{p_T^{ISR}} \sim \frac{m_{parent}}{m_{daughter}} \tag{6.2}$$

Figure 6.3 shows the distribution of R_{ISR} for several pair-produced $\widetilde{\chi}_2^0$ signals, each with a different mass splitting between the $\widetilde{\chi}_2^0$ and $\widetilde{\chi}_1^0$. For very large mass splittings, the distribution peaks at a lower value of R_{ISR} and has a broader shape, while for the very compressed points, the peak is well-resolved and at a higher value. The precise resolution of the distribution peak at the ratio of parent to daughter masses for a particular signal indicates the potential for significant sensitivity increases using a "window" cut or shape fit on R_{ISR}.

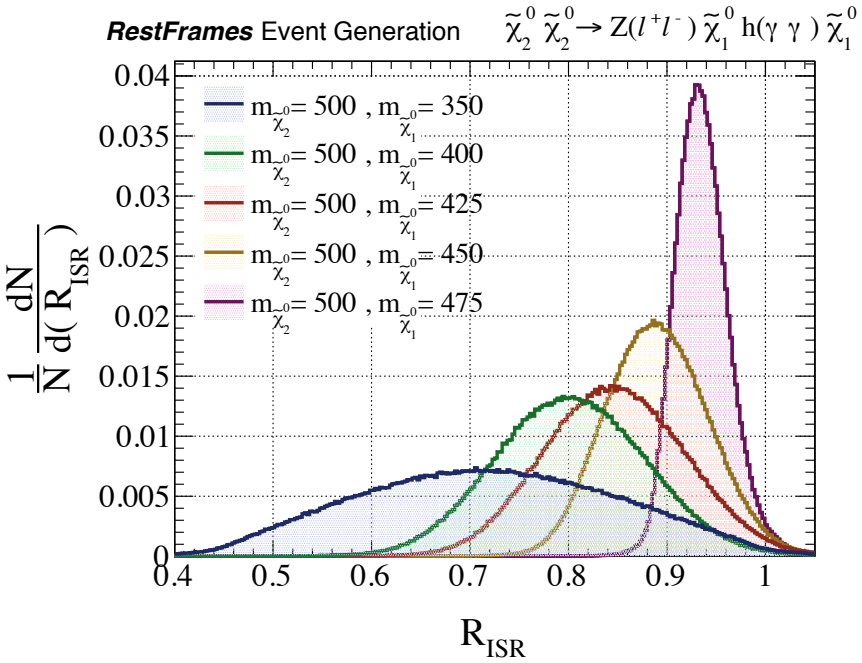


Figure 6.3: The distribution of R_{ISR} for several signals of varying ($\widetilde{\chi}_2^0$, $\widetilde{\chi}_1^0$) masses, demonstrating the correlation between R_{ISR} and decay chain mass splitting [83].

M_T^S

Due to the intentional ignorance of the longitudinal momentum in each event, the masses of all RJR states are transverse masses. Therefore, just as the transverse mass can be computed using the neutrino and lepton for a W boson, the transverse mass of the sparticle frame, M_T^S, can be computed using the Invisible and Visible frames. The length of the tail of the M_T^S distribution is determined by the characteristic scale of the process. Since this variable mimics the transverse mass of the di-sparticle system, signal events are likely to be reconstructed with M_T^S values that are consistent with the presence of the di-sparticle system upstream in the decay. Backgrounds tend to have a broader distribution, in general according to the kinematic requirements of the leading jets in the event.

Since many of the RJR variables make use of similar information relating to the event thrust axis, strong correlations exist between variables. It is particularly important to compare any new variable with R_{ISR}, as it is the direct ratio between the most correlated quantities in the reconstruction. Figure 6.4 plots the distribution of M_T^S as a function of R_{ISR} for signal, as compared to several primary backgrounds. Not only is the signal to background discrimination along M_T^S evident, but the correlation with R_{ISR} indicates potential for a diagonal cut along both variables to effectively cut away background that occurs at higher R_{ISR} (where the signal is concentrated) but low M_T^S.

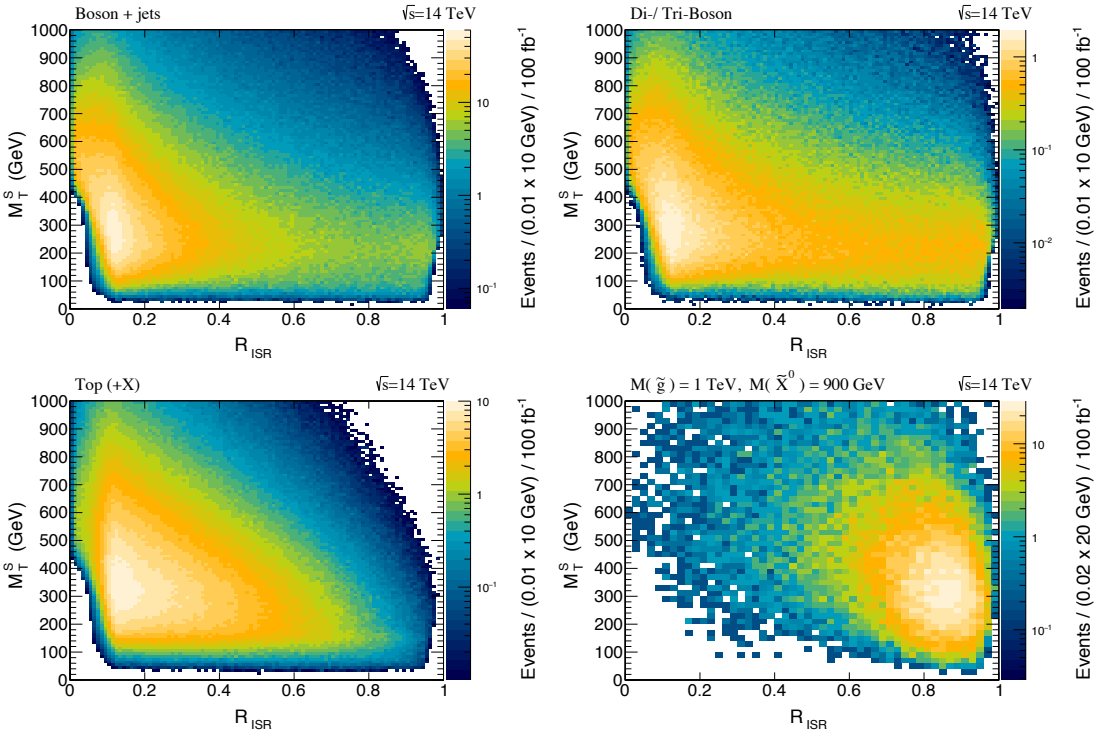


Figure 6.4: The distribution of M_T^S as a function of R_{ISR} for background as compared to signal simulations [83]. Counterclockwise from upper right: diboson, boson + jets, top + X, gluino signal.

p_T^{ISR}

One of the components of R_{ISR} is the p_T of the ISR frame. This variable on its own is found to have discriminating power, as p_T^{ISR} tends to take on higher values for the very back-to-back topologies associated to signal events. As with M_T^S, the correlations with R_{ISR} are of interest; Figure 6.5 shows 2D plots of p_T^{ISR} vs. R_{ISR} for two backgrounds and two SUSY signals. Since R_{ISR} is directly a function of p_T^{ISR}, the correlation is naturally strong, and can be used to advantage in discriminating signal from background.

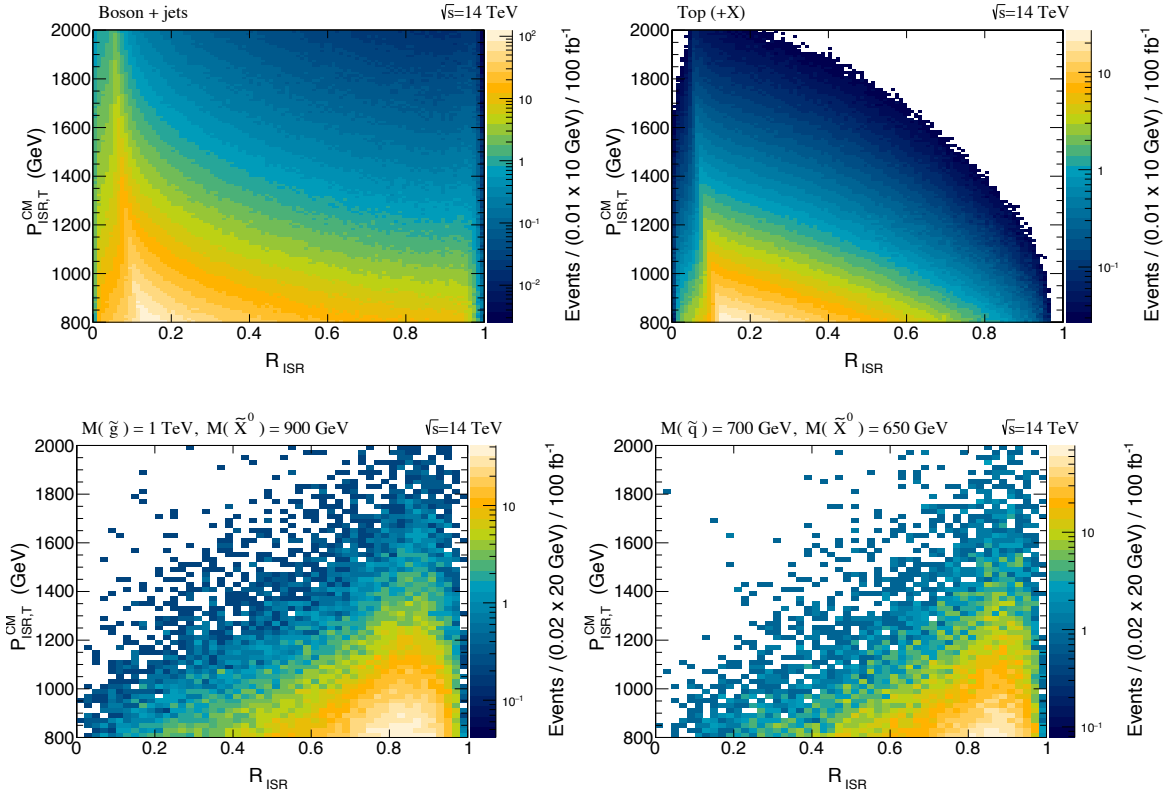


Figure 6.5: The distribution of p_T^{ISR} as a function of R_{ISR} for background (top) as compared to signal simulations (bottom) [83]. Counterclockwise from upper right: top+X, boson+jets, gluino signal, squark signal.

NjV, NlV, NbV

After the RJ reconstruction is performed, all final state objects are sorted into the ISR or Visible frames. Variables like NjV, NlV, and NbV are built by counting the number of jets, leptons, or b-jets respectively that get sorted into the Visible frame. The Visible frame is expected to come from a sparticle decay, and the expected object multiplicity in that decay is known beforehand. Thus these variables can be helpful for imposing basic expectations on the event, using the Feynman diagram of the decay of interest. Figure 6.6 shows the example of NjV as a function of R_{ISR} for several

backgrounds and a gluino signal.

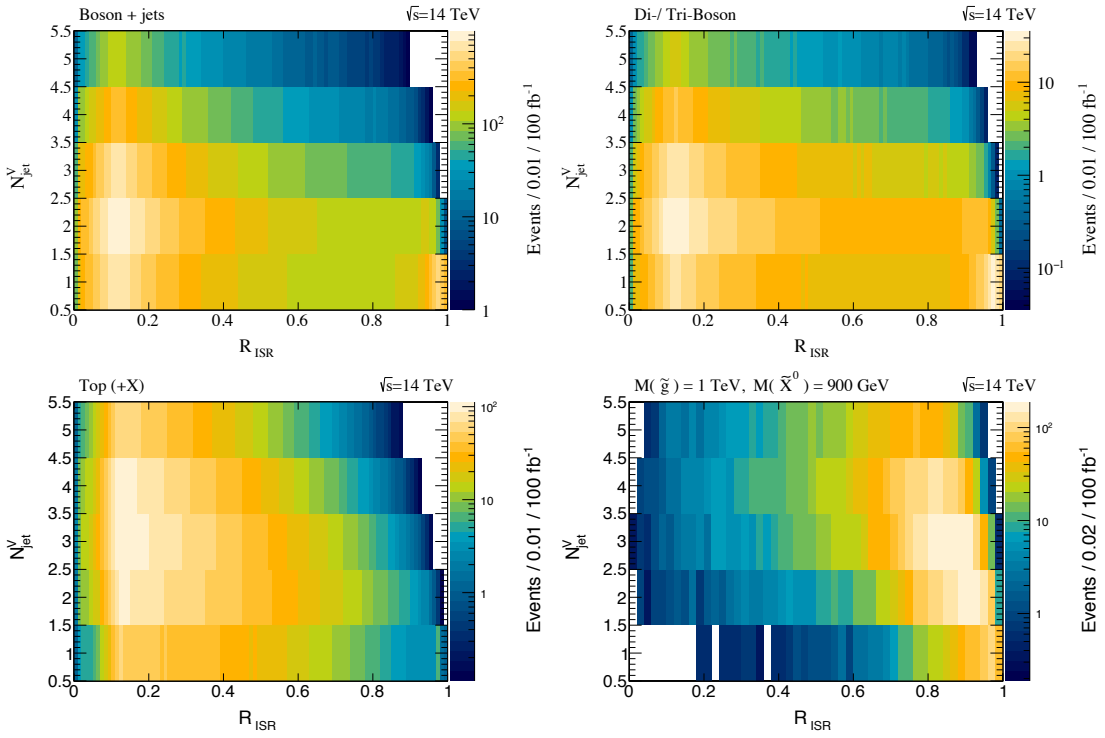


Figure 6.6: The distribution of NjV as a function of R_{ISR} for background as compared to signal simulations [83]. Counterclockwise from upper right: diboson, boson + jets, top + X, gluino signal.

$\Delta\Phi$(ISR,I)

In a scenario where the event shape is a crucial feature of the analysis, many angles between objects can be utilized to enforce the desired topology. For ISR-assisted RJ reconstruction, the difference in Φ between the ISR and Invisible frames $\Delta\Phi$(ISR,I) is used to maintain the back-to-back nature of compressed SUSY signatures. $\Delta\Phi$(ISR,I) mimics the more commonly used $\Delta\Phi$ between the leading jet and E_T^{miss}, but with a more sophisticated understanding of the ISR system (as potentially a

system of jets rather than a single jet.) Figure 6.7 shows the distribution of $\Delta\Phi$(ISR,I) for several gluino signals of different masses and several key backgrounds.

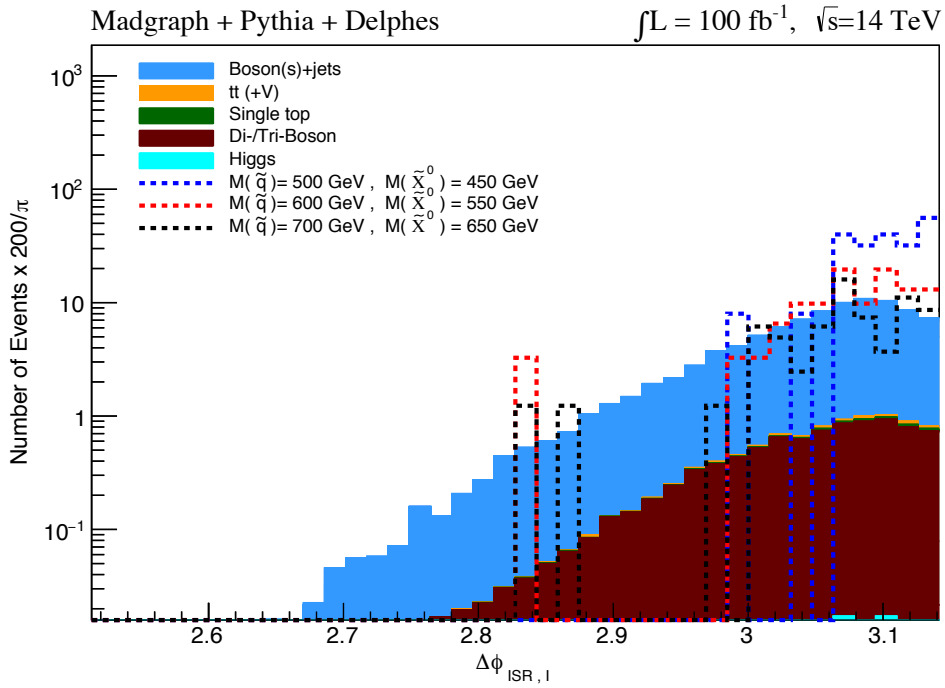


Figure 6.7: The distribution of $\Delta\Phi$(ISR,I) for background as compared to several gluino signal mass points [83].

Given the strong physics motivation and potentially powerful signal to background discrimination of these variables, they are good candidates for use in analyses that have historically struggled to gain sensitivity to compressed signals. The precise advantage provided by these variables and the RJR method overall is described further in the following part of this thesis.

7

Event Cleaning

Working with compressed mass spectra also requires precise understanding of backgrounds that may pose problems in the analysis, because they either closely mimic the signal or are difficult to estimate. In the case of compressed SUSY signatures with ISR-assisted topologies, the signal typically appears in the detector as missing energy back-to-back with energy deposited by jets and/or leptons. Because of the large transverse imbalance in the event, this final state is often contaminated by "fake" jets,

which can be coherent calorimeter noise that gets reconstructed as a jet, calorimeter energy deposition that came from a different particle such as a muon, or real hadronic activity not associated to the hard scatter collision.

The raw proton-proton data collected by the ATLAS detector must undergo several data quality procedures before it is declared usable for physics analysis [84]. Each procedure is uniquely defined to target a specific source of contamination, such as detector control conditions or subsystem effects, that can compromise an event. One of these procedures that specifically targets problematic events contaminated by fake jets is the process of *event cleaning*, which generates a decision on whether an event is "clean" by examining each jet in the event. If any of the jets are "dirty", in that they do not pass an established set of cleaning criteria, the entire event must be vetoed to avoid mismeasurement of other objects or event-level quantities such as E_T^{miss}.

The jet-level cleaning criteria targets three primary sources of jets not intended for physics.

1. Beam induced background (BIB) [85], which generally consists of muons produced from beam losses upstream of the interaction point. While there is shielding material around the beam pipe to absorb beam halo or gas, such muons often have high enough energy to pass through unencumbered, at which point their radiative energy losses in the calorimeter can be reconstructed as a jet.
2. Cosmic ray showers, which similarly produce high energy muons that can be falsely reconstructed as jets in the calorimeters.
3. Coherent calorimeter noise or pathological cells. Most of the noise from these sources is either masked in event reconstruction or rejected by data quality inspection [66]. However, in rare cases, noise can be reconstructed as a jet thats gets past these filters.

The first two of these three sources are referred to as *non-collision background*. The cleaning criteria applied to each jet consists of cut values on key variables designed to discriminate between real

jets and jets which are not associated to the primary interaction.

7.1 Jet Cleaning Variables

The Run II cleaning procedure utilizes several quality variables that are calculated for each jet [86]. These variables were selected on the basis of ability to discriminate between hard scatter (good) jets and falsely reconstructed (fake) jets. Discrimination capability is assessed in data for two dedicated regions, one enriched in good jets and the other enriched in fakes. These regions are defined in Appendix A.

The quality variables can be sorted into two categories, each of which attacks a particular source of fake jets.

7.1.1 Energy Ratio Variables

Energy ratio variables contain information about the fraction of a jet's energy that is deposited throughout the detector subsystems. They specifically target non-collision background from high energy muons, as this type of fake jet tends to traverse the detector longitudinally rather than originating from the primary interaction point, giving an anomalous pattern of energy deposition in the detector. All of these variables are computed on the electromagnetic energy scale.

- Electromagnetic Fraction (f_{EM}): ratio of the energy deposited in the electromagnetic calorimeter to the total jet energy.
- HEC Fraction (f_{HEC}): ratio of the energy deposited in the hadronic endcap calorimeter to the total jet energy.

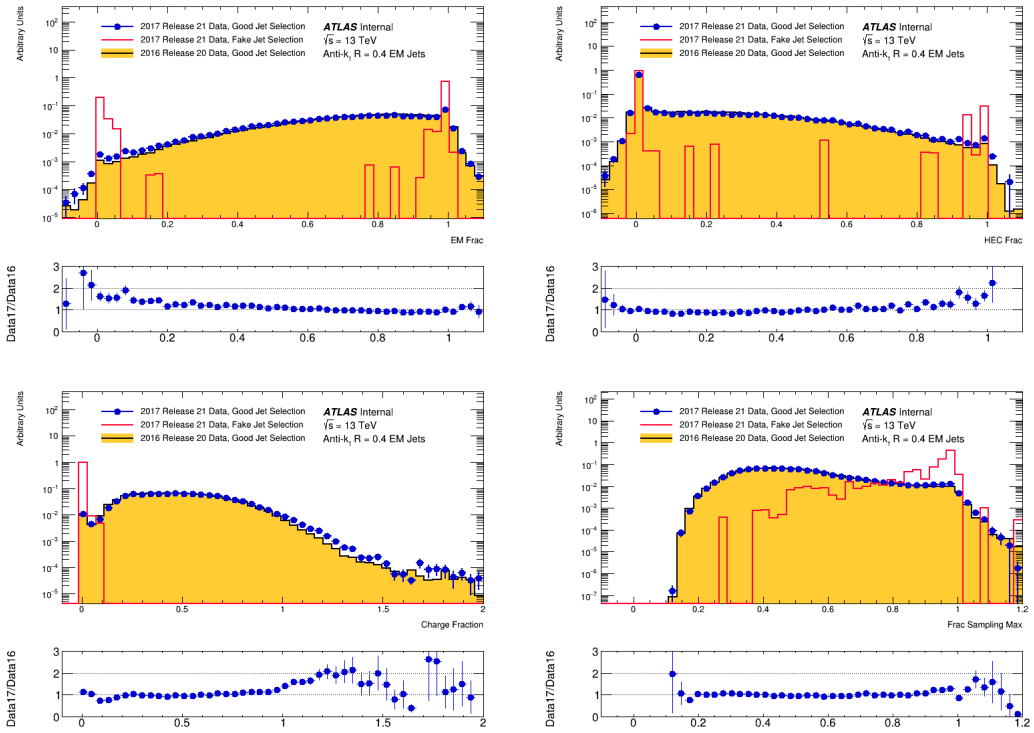


Figure 7.1: Distributions of f_{em}, f_{HEC}, f_{ch}, and f_{max} are shown in 2017 data for both good (blue) and fake (red) EMTopo jet selections. 2016 data is superimposed as a reference (yellow).

- Charge Fraction (f_{ch}): ratio of the scalar sum of p_T of primary vertex tracks associated to a jet to the total p_T of the jet.
- Maximum Energy Fraction (f_{max}): maximum fraction of a jet's energy deposited in a single calorimeter layer.

Figure 7.1 shows distributions of these four energy ratio variables using data collected by ATLAS in 2017. Good jets have a smooth distribution across all values of these variables, while fake jets tend to have very low or high values (indicating a jet with an anomalous energy deposition pattern.)

7.1.2 Calorimeter Quality Variables

Calorimeter quality variables are based on the signal shape in a LAr cell as given by Q_{cell}^{LAr} (see Equation 5.4) and are therefore used to remove coherent or isolated cell noise. For these three variables, poor signal shape quality is defined as a cell with quality variable $Q_{cell}^{LAr} > 4000$.

- Average LAr Quality $\langle Q \rangle$: Energy-squared weighted average of Q_{cell}^{LAr} for all LAr cells in the jet, normalized so that $0 < \langle Q \rangle < 1$.
- LAr Quality Fraction f_{LAr}^{Q}: Fraction of a jet's energy in the LAr calorimeter that has poor signal shape quality.
- HEC Quality Fraction f_{HEC}^{Q}: Fraction of jet's energy in the HEC calorimeter that has poor signal shape quality.

An additional calorimeter quality variable that can be used in jet cleaning is the negative energy associated to a jet, E_{neg}, which sums the energy deposited in all calorimeter cells that have negative energy. Good jets can have small amounts of negative energy coming from electronic noise or pile-up effects, while fake jets tend to have larger amounts coming from pathological cells.

Figure 7.2 shows distributions of the calorimeter quality variables using data collected by ATLAS in 2017. Good jets usually have good signal pulse shape and thus low values of these variables, while fake jets have values that differ significantly from zero as a result of problematic cell signals. Values close to one are mainly due to coherent noise or sporadically noisy cells, the primary target for discrimination, while intermediate values can come from non-collision background.

Jet quality variables are also computed in Monte Carlo simulation, and good agreement is observed with respect to data. Deviations are observed between simulation and data for the calorimeter

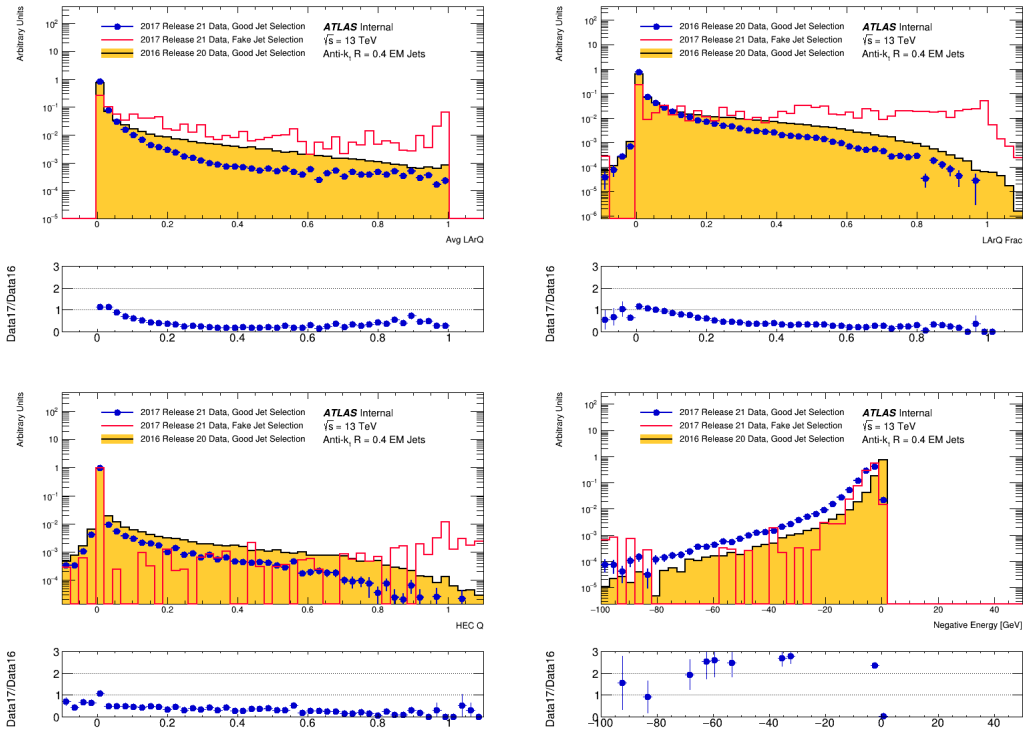


Figure 7.2: Distributions of $\langle Q \rangle$, f^{Q}_{LAr}, f^{Q}_{HEC}, and E_{neg} are shown in 2017 data for both good (blue) and fake (red) EMTopo jet selections. 2016 data is superimposed as a reference (yellow).

quality variables, which are explained by the use of a consistent pulse shape in simulation, resulting in more predicted values closer to 0 [86].

7.2 Run II Procedure & Performance

Each of the above jet quality variables are used in the full event cleaning procedure. The goal of event cleaning is to maintain good selection efficiency for good jets, while efficiently rejecting fake jets. Before event cleaning can be performed, it is necessary to perform pile-up tagging/removal with the jet vertex tagger (JVT) as described in Section 5.6.3, and overlap removal (OR) to resolve ambiguities between candidate objects.

Since different analyses have varying goals with respect to cleaning, several different quality variable cut sequences, or *working points*, are offered.

- Loose: default working point used by most analyses.
- Tight: specialized working point created for "monojet" searches with an energetic jet and large missing transverse momentum [53], which has a signal that closely mimics typical fake jet signatures and thus needs a more stringent fake jet rejection. Tight cleaning is defined only for $|\eta| < 2.4$.
- Loose/VeryLooseLLP: specialized working points created for searches with displaced vertices and missing energy [87]. As a result of the displaced vertex, the targeted signal has unique energy deposition and timing, therefore making several standard quality variables such as f_{EM} unusable.

The following cut lists define the ways in which a jet can fail the specified cleaning criteria. An events fails a particular working point if at least one of its jets is identified as "Bad" according to the cut list.

A jet is identified as LooseBad if it satisfies any of the following:

1. $f_{HEC} > 0.5$ and $|f^{Q}_{HEC}| > 0.5$ and $\langle Q \rangle > 0.8$ (HEC noise spike)
2. $f_{EM} > 0.95$ and $f^{Q}_{LAr} > 0.8$ and $\langle Q \rangle > 0.8$ and $|\eta| < 2.8$ (EM calorimeter noise)
3. $f_{max} > 0.99$ and $|\eta| < 2.0$
4. $f_{EM} < 0.05$ and $f_{ch} < 0.05$ and $|\eta| < 2.0$
5. $f_{EM} < 0.05$ and $|\eta| \geq 2.0$

A jet is identified as TightBad if it is identified as LooseBad, or if it has $f_{ch}/f_{max} < 0.1$ for $|\eta| < 2.4$. This ratio was found to be especially efficient at targeting fake jets, which preferentially have f_{ch} near 0 and f_{max} near 1. Usage of the Tight cleaning working point was found to reduce non-collision background in the monojet analysis to a negligible level as compared to other Standard Model backgrounds.

The long-lived particle (LLP) working points are defined separately as they do not build on the LooseBad decision. A jet is identified as VeryLooseBadLLP if it has $f_{max} > 0.8$ or $f_{EM} > 0.96$. A jet is identified as LooseBadLLP if it satisfies LooseBad cut strings 1, 2, or 3 (above), or if it has $E_{neg} > 4$ GeV and $f_{max} > 0.85$. This procedure was found to remove 90% of beam-induced background in the displaced vertex plus missing energy searches, with < 1% effect on signals.

Recall that the event-level cleaning decision is determined by examination of all the jets in an event; if one jet is dirty, the entire event is vetoed. Calculation of this decision for the Loose working point, along with preliminary JVT and OR procedures, was added at derivation level in 2018. Doing so allows the removal of all jet quality variables from the derivations and replacing them with a single event-level decision, saving space and simplifying the application of the cleaning procedure.

7.2.1 Tag-and-Probe Efficiency

The efficiency of the event cleaning procedure is measured with a "tag-and-probe" method using the good dijet region defined in Appendix A. One of the two leading jets in the event is required to pass the Tight working point criteria; this is known as the tag jet. The probe jet is then by default the other leading jet, and is required to be back-to-back with the tag jet. Since the event is well-balanced and "good" according to the region definition, it is expected that if one of these two jets passes the Tight criteria, it is very unlikely that the other is a fake jet. The cleaning efficiency can therefore be defined as the fraction of probe jets that are not rejected by the cleaning criteria for the working point of interest. This efficiency is measured as a function of p_T and η of the probe jets, as seen in Figure 7.3.* Good agreement is observed between efficiencies calculated with data and simulation.

7.2.2 Particle Flow Jets

The recent increase in usage of Particle Flow (PF) jets (as defined in Section 5.6.3) in ATLAS analyses throughout Run II generated the need for a dedicated PF jet cleaning procedure. Since PF jets add information from the tracker to reconstruct jets from particle level, it is expected that some of the ratio variable shapes may be different than those of EM jets. As the event cleaning decision is based on cutting away parts of these variable distributions, such reconstruction differences could compromise its effectiveness. Thus it was necessary to quantify the ability of standard EM cleaning to select good

*Some variations in efficiency across p_T and η bins can be attributed to the use of JVT to remove pile-up jets, which is implemented for jets with $p_T < 60$ GeV and $|\eta| < 2.4$. In particular, the jets rejected by this tagger have a large overlap with those rejected by the f_{ch}/f_{max} Tight cleaning cut, resulting in a heightened Tight efficiency for jets with $p_T < 60$ GeV. This cut also results in lower efficiency in the central-$|\eta|$ region.

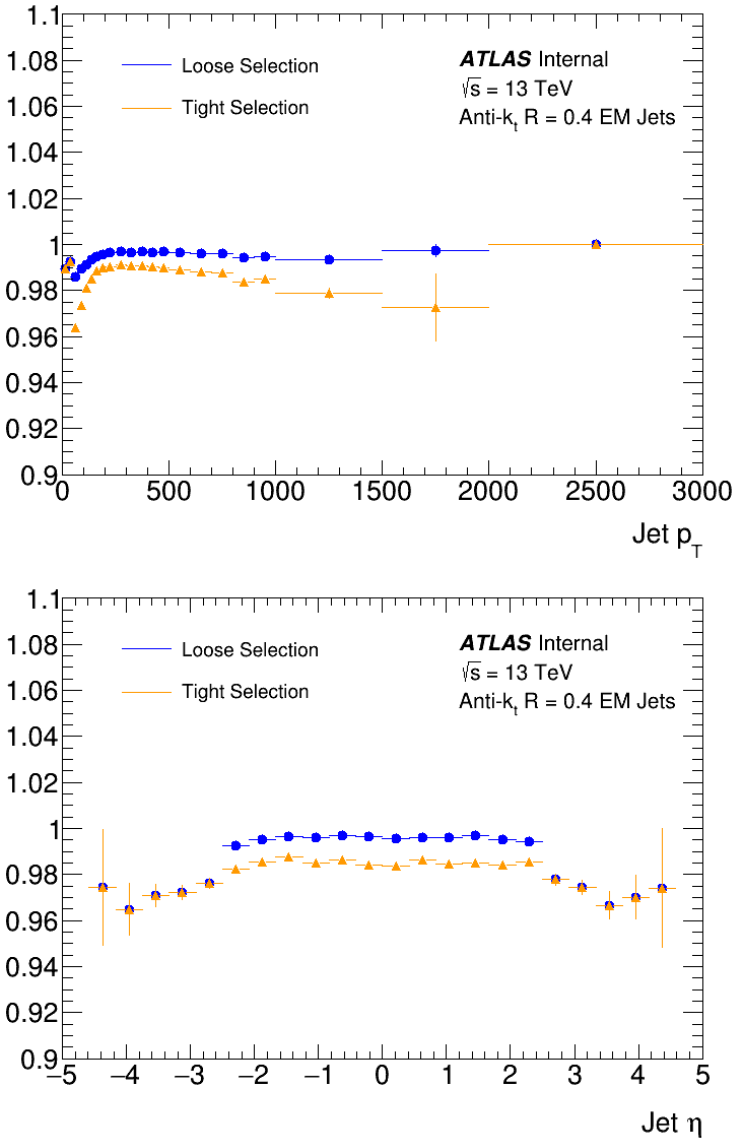


Figure 7.3: EM jet quality selection efficiency for anti-k_T EM jets with R = 0.4 measured with a tag-and-probe technique as a function of p_T and η (p_T > 100 GeV), for the Loose and Tight selection criteria. Only statistical uncertainties are shown.

PF jets and reject fake ones.

Producing the tag-and-probe efficiency plots for PF jets is not possible, since large shape differences between EM and PF jet variables were observed, leading to the conclusion that the EM cut sequences could not sensibly be applied to PF jet variables.[†] However, since the cleaning procedure using EM jets outputs an event-level decision, the cleaning performance can be assessed by examining populations of PF jets that pass EM scale cleaning requirements, and through their characteristics the extent of the fake jet contamination can be determined. This is done with histograms of PF jet p_T and η, before and after cleaning, in both good and fake enriched selections.

Figure 7.4 demonstrates the capability of the EM scale Loose and Tight cleaning working points to preserve selection efficiency for good jets, while effectively cutting away fake jet sources in PF jets. Estimates of cleaning efficiency from these yields show minimal loss of good jets and sufficient removal of fakes, demonstrating that event cleaning using EM jets could be used to clean populations of PF jets as well. Therefore, the cleaning recommendation for analyses using PF jets does not need to be modified from the standard event-level decision.

In conclusion, event cleaning constitutes an important and well-maintained procedure in the chain of tests that ensure good data quality. Such confidence in the quality of jets enables precise description of the physics processes present in a given collision, which is necessary for a robust analysis of the data. The following chapter describes methods that are commonly used to make such statements.

[†]A similar study was performed to assess shape differences in the quality variables between EM and LCW jets, which were deemed small and negligible for cleaning purposes. This comparison can be found in Appendix A.

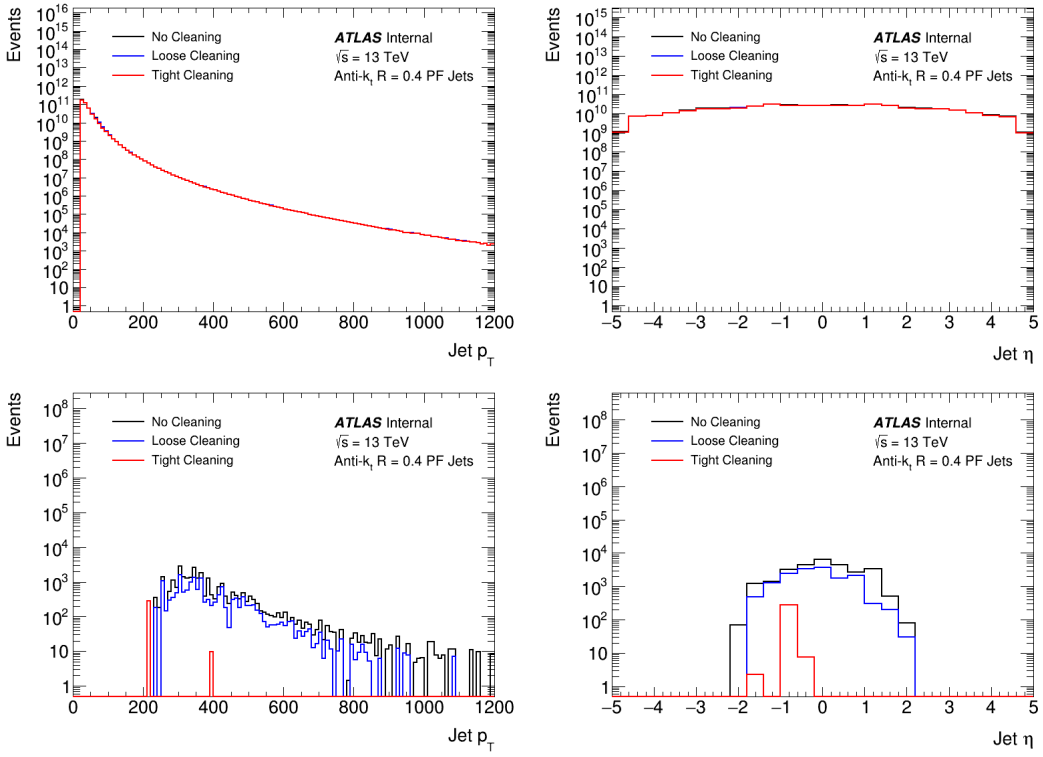


Figure 7.4: Histograms of jet p_T (left) and η (right) shown after application of Loose (blue) and Tight (red) cleaning working points, in data samples enriched in good dijet events (top) and fake jets (bottom).

8

Statistical Methods

In a search for new physics, any statement about the presence or absence of a feature in the data must be quantifiable. This is done via statistical analysis methods. In this chapter, the primary statistical tools and methodologies used in LHC data analysis are discussed. Section 8.1 describes the use of hypothesis testing, and Section 8.2 describes likelihood minimization and fitting procedures. More information can be found in several references [88, 89].

8.1 Hypothesis Testing

To claim discovery or exclusion of a physics model, it is first necessary to define the assumptions made. Hypothesis testing in particle physics makes use of two primary hypotheses. The first describes the background, or the expectation of the data from the Standard Model alone (also called the null hypothesis). The second describes the signal scenario, which necessarily includes some BSM components. The compatibility of the observed data with either of these hypotheses is used to make a statement about the validity of the model.

Several parameters are defined to quantitatively define the test. The signal strength μ is defined to separate the two scenarios as the ratio of signal cross sections found in Equation 8.1:

$$\mu = \frac{\sigma_{obs}}{\sigma_{exp}} \tag{8.1}$$

Here, $\mu = 1$ corresponds to the signal hypothesis, and $\mu = 0$ gives the background-only hypothesis, with varying values giving different multiplicative factors to the signal cross section. The probability that the observed data originates from either of the two hypotheses is defined as a p-value, where p_0 gives the probability that the data is consistent with the Standard Model expectation and p_μ gives the same probability for the signal model expectation.

The obtained p-value is used as a test statistic to determine whether the data agrees with either hypothesis. It can be converted into the significance Z, which is defined as the number of standard deviations of the data from the expectation of a Gaussian-distributed variable. Particle physicists

define a Z of 5σ to mark the discovery of the given process. Figure 8.1 demonstrates the relationship between probability and significance for a Gaussian distribution. A 5σ significance for a signal hypothesis corresponds to a probability of 2.9×10^{-7} that, assuming the null hypothesis is correct, the data fluctuated to produce the observation. Evidence for new physics is chosen to occur at $Z = 3\sigma$.

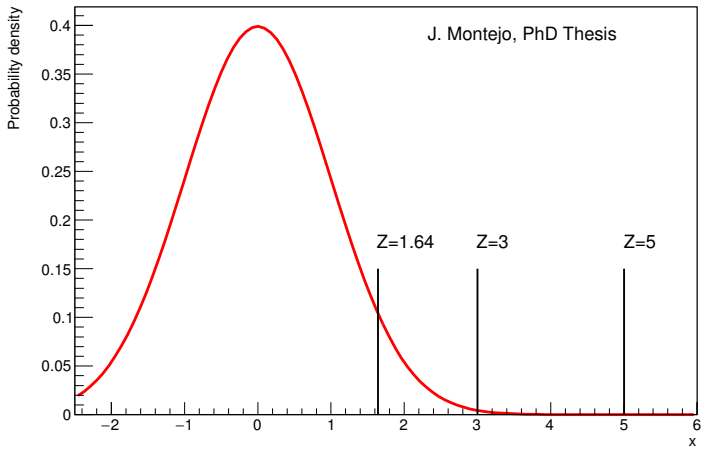


Figure 8.1: Significance thresholds on a Gaussian-distributed variable, indicating exclusion of a process (Z = 1.64), evidence for a new process (Z = 3), and discovery (Z = 5) [90].

The p-value prescription can also be used to determine that a particular signal process has been excluded. If the p-value is less than 5%, the Z value is 1.64, and the signal hypothesis is determined to be rejected. This convention is referred to as the 95% confidence level (CL). In particle physics, the CL_s method is used [91], which defines a new statistics that combines the null p_0 and signal hypothesis p_μ values to reduce the impact of statistical fluctuations in the data. Equation 8.2 defines this ratio of probabilities:

$$CL_s = \frac{p_\mu}{1 - p_0} \tag{8.2}$$

For searches at the LHC, the CL_s method is used in place of the regular signal p-value to set upper limits. The same numerical threshold for exclusion then holds: if $CL_s < 0.05$, the signal hypothesis with signal strength μ is excluded at 95% confidence.

8.2 Likelihood Fitting

The likelihood method extrapolates the quantification of signal and background hypothesis probabilities to a scenario with multiple variables. It builds a likelihood function which can be globally maximized to fit the signal strength μ, the expected yields in various bins, and the uncertainties on those yields, modeled by nuisance parameters. The likelihood maximization allows the simultaneous consideration of hypotheses across multiple regions of phase space. This process relies on *Bayesian probabilities*, which makes statements based on degree of certainty, rather than on repeated experiments (*frequentist probabilities*).

The likelihood function for the observed data to be produced by the model can be written as follows in Equation 8.3:

$$L(\mu, \theta) = \prod_{i=1}^{N} \frac{(\mu s_i + b_i)^{n_i}}{n_i!} e^{-(\mu s_i + b_i)} \prod_{k=1}^{M} \rho(\theta_k) \tag{8.3}$$

Here, N is the number of independent measurements; s_i and b_i are the expected number of signal and background events in the ith bin respectively; n_i is the number of observed events in the ith bin; μ is the signal strength defined in Equation 8.1; θ are the nuisance parameters (NPs) representing statistical and systematic uncertainties; $\rho(\theta)$ is the probability distribution function (PDF) of

the NP; and the data is assumed to follow a Poisson distribution. The likelihood function can be globally maximized, where both μ and θ are fit and assigned given values defined as $\hat{\mu}$ and $\hat{\theta}$. It can also be conditionally maximized for a fixed value of μ, giving only values for the systematics as $\hat{\hat{\theta}}$.

When maximizing the likelihood, the NPs are adjusted in the fit to improve the agreement of the expectation with the observation. The PDF of the uncertainty encodes information about the size and shape of the uncertainty, determined beforehand by dedicated studies. Often, the PDF for a systematic is assumed to be Gaussian. A key benefit of the likelihood fitting procedure is that adding information from data to the prediction can in turn provide additional information on the systematics. Specifically, when the NP is pulled in the fit, certain values within the initial uncertainty window are found to be inconsistent with the data, and thus the overall uncertainty can be reduced. This is referred to as "profiling" the uncertainty.

As with the CL_s method described in the previous section, a dedicated test statistic is defined specifically for use in LHC analyses as the ratio of absolute to conditional maximal likelihoods. This ratio is called the *profile likelihood* λ, given in Equation 8.4. It ranges from $0 < \lambda < 1$, where larger values indicate good agreement between data and the model with a given value of μ.

$$\lambda(\mu) = \frac{L(\hat{\mu}, \hat{\hat{\theta}}(\mu))}{L(\hat{\mu}, \hat{\theta})} \tag{8.4}$$

8.3 Analysis Strategy & HistFitter

In many ATLAS searches, including the ones described in Part IV, the aforementioned likelihood fitting is performed using a statistical analysis software package called HistFitter [92]. HistFitter provides a framework for likelihood fitting that incorporates several common features of an LHC analysis, such as the profile likelihood metric and the presence of multiple uncertainties. It also allows for the *blinding* of signal regions during analysis construction, meaning that the data in the signal region is removed from consideration during analysis design to minimize bias.

For the SUSY searches described in Chapters 9 and 10, where a specific signal model is used, several statistically independent regions are used in the likelihood fit that are each enriched in particular processes of interest. A *signal region (SR)* is used to isolate the characteristics of the signal model in the phase space of proton collisions. To make a background prediction, a *control region (CR)* is designed to be kinematically similar but orthogonal to the signal region, and enriched in an SM background process, with minimal contamination from signals or other backgrounds. Often a *validation region (VR)* is defined as well, to verify the accuracy of the background prediction given by the control region, before the signal regions are unblinded. Figure 8.2 diagrammatically demonstrates the relationship between these regions as a function of different dataset features.

The ratio of observed to expected events in a CR is referred to as its *normalization factor*, and can be used to make background estimations obtained from Monte Carlo simulation more precise in the signal regions. The final expected yield of a particular background in a SR is given by the normalization factor times the number of expected MC events of the process of interest in the SR.

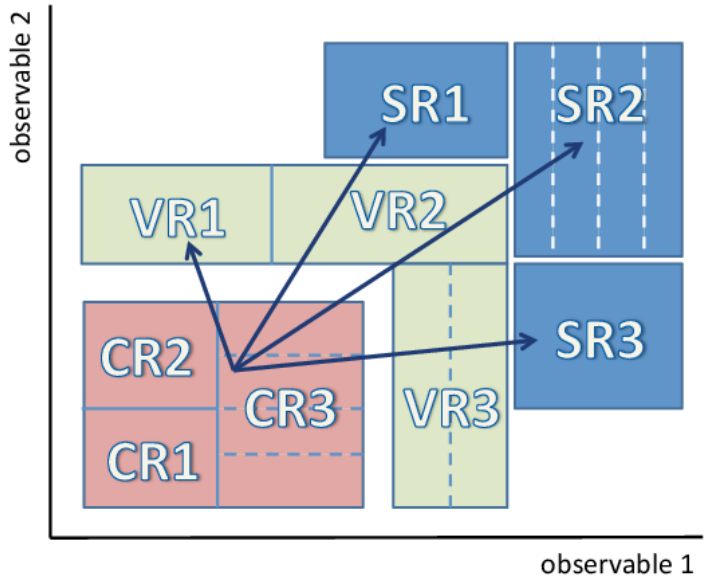


Figure 8.2: A schematic view of an analysis strategy with multiple control, validation and signal regions (multiple bins illustrated by dashed lines). The extrapolation from the control to the signal regions is verified in the validation regions [92].

Equivalently, this can be defined as:

$$N(SR, scaled) = N(CR, obs) \times \left[\frac{N(SR, unscaled)}{N(CR, unscaled)}\right] \tag{8.5}$$

The quantity in brackets in Equation 8.5 is hereafter called the *transfer factor*. A transfer factor is computed for every region-to-region extrapolation, and used as a constraint in the likelihood fit when adjusting the predicted background components in all regions. In the full analysis, where there are several CRs and SRs, the likelihood fit can determine all normalization and transfer factors and generate internally consistent SM background estimates for each SR. This makes the analysis more robust against potential mismodeling effects in simulated events, and reduces the correlations

between CRs.

`HistFitter` can be used to perform three types of fits, given below in typical analysis order. The analysis flow is depicted diagrammatically in Figure 8.3, where the normalization factors extracted from the fit to CR data can be seen to be used in validation and the SR background prediction.

1. Background-only fit: extract normalization factors and estimate background in SRs and VRs using only data in the CRs.
2. Model-independent ("discovery") fit: using data in the SRs and CRs, sets an upper limit on the number of observed events beyond the SM expectation. This can be thought of as quantifying the agreement of the data with the background-only hypothesis, without any assumptions about the signal model.
3. Model-dependent ("exclusion") fit: in the absence of an excess in the SRs as revealed by the background-only fit, exclusionary power for a particular signal strength μ can be determined using data in both SRs and CRs. This can be thought as quantifying the agreement of the data with a particular signal model.

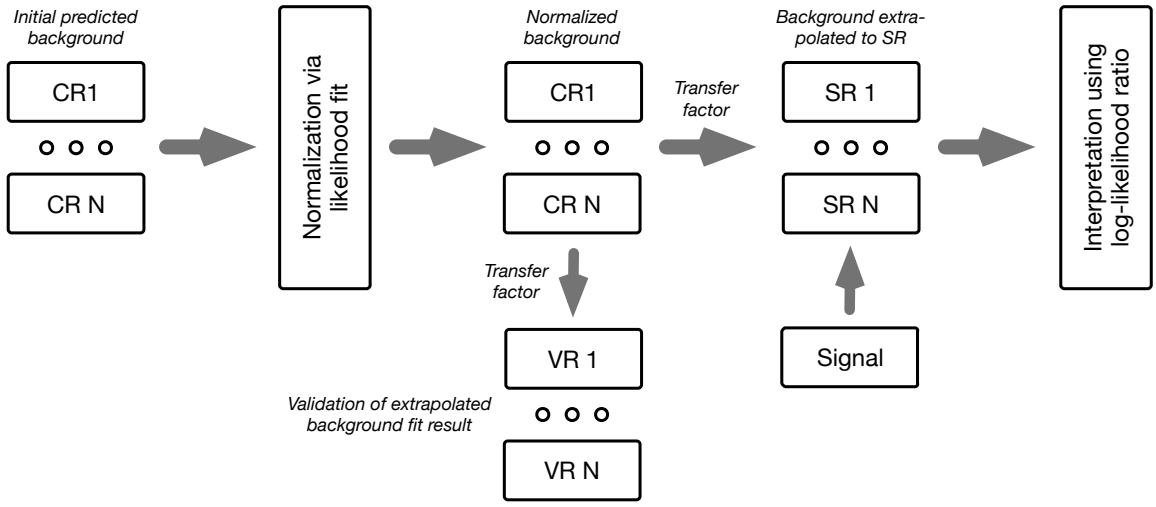


Figure 8.3: Overview of an analysis flow using SRs, CRs, and VRs in `HistFitter` [92].

A background-only fit is necessarily performed in an analysis that uses control regions to estimate background, while the choice of model-independent or dependent fits varies per analysis team. In either case, because of the statistical techniques discussed in this chapter, the level of confidence in the final result is consistently defined across different papers, and can be precisely described outside of an LHC context. Therefore, such methods are a mainstay of modern high energy physics analyses, and provide a foundation for the sharing of results across physics subfields. Both hypothesis testing and likelihood fitting, along with the `HistFitter` software framework, are used to describe the results discussed in the following chapters.

Part IV

Searches

Armed with a well-motivated signal, a detector, a dataset, and a method, the searching can begin. Searches for supersymmetry have constituted a cornerstone of the ATLAS experimental program since it was first commissioned. Models of natural SUSY such as the ones described in Chapter 3 have long predicted new particles at the weak scale, first sparking excitement at the discovery potential for SUSY in the Tevatron datasets [93, 94]. With the advent of the LHC, promising even higher energies and larger luminosities, the exploration of SUSY possibilities was an even grander priority.

In this chapter, two searches for natural supersymmetry are discussed, one for stop quarks and the other for higgsinos. Despite having very different production mechanisms and final states, these two searches have several features in common. Both analyses start with the pair production of the sparticle of interest, using a simplified model of R-parity conserving supersymmetry [95, 96] where the only light sparticles are the ones involved in the decay. Both use $\sqrt{s}$ =13 TeV proton-proton collision data delivered by the LHC and collected by the ATLAS detector (see Chapter 5). The general strategy is fundamentally the same: build signal regions that efficiently select for signal while rejecting background, carefully estimate the backgrounds in these regions, and ultimately look at the qualifying data for an excess of events. The Recursive Jigsaw Reconstruction technique introduced in Chapter 6 is applied to both analyses in the context of ISR-assisted topologies, and its utility is discussed.

Chapter 9 describes the search for top squarks in a one lepton final state, using 36.1 fb^{-1} of data collected in 2015 and 2016. Chapter 10 describes the search for higgsinos in a two lepton final state, with the full Run II dataset of 139.5 fb^{-1}.

9

For Third Generation SUSY

Searches for stop quarks at ATLAS rely on evidence of di-stop production in a proton-proton collision, by way of the stop decay products. Each pair-produced stop can decay in one of several ways, as described in Section 3.1. Given this treatment's emphasis on compressed mass spectra, the focus will be on the $\tilde{t} \to t\widetilde{\chi}_1^0$ decay.* A Feynman diagram of the decay of interest is shown in Figure 9.1. Along

*Examinations of several other signatures and models are described in detail in Reference [38], coverage of which will be omitted in this text.

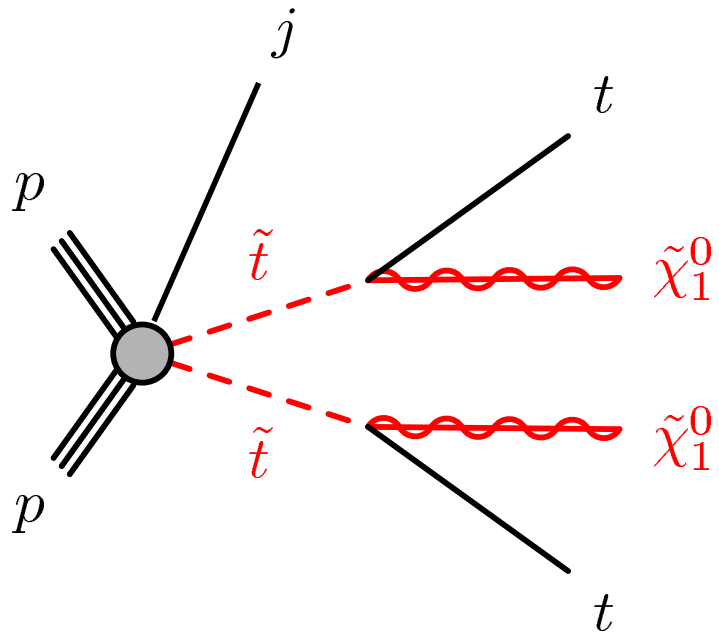


Figure 9.1: Diagrams illustrating stop pair production into the typical two-body signature: $\tilde{t} \rightarrow t\widetilde{\chi}_1^0$ [38].

with the byproducts of the di-stop decay, there is a jet (or system of jets) attributable to the initial state radiation (ISR) that kicks the di-stop system and boosts the $\widetilde{\chi}_1^0$s.

In this particular analysis, the $t\bar{t}$ decays semi-leptonically, giving a final state of one lepton, at least four jets (two of which are b-jets), and E_T^{miss} coming from one neutrino and two $\widetilde{\chi}_1^0$s. This is hereafter referred to as the *"stop 1L"* analysis. In the simplified model used to describe this scenario, the $\widetilde{\chi}_1^0$ is composed entirely of the bino weak eigenstate.

The compressed area of phase space that will be the focus of this discussion was introduced in Section 3.1 as the diagonal region, where the sum of the t and $\widetilde{\chi}_1^0$ masses is close to (but necessarily less than) the mass of the $\tilde{t}$. Because of the small mass splittting, the total p_T of the $\widetilde{\chi}_1^0$s is expected to come almost entirely from the magnitude of the ISR boost. This strategy relies on a massive $\widetilde{\chi}_1^0$ so

that it can be more boosted by the ISR system with respect to the top quark. Thus, the discussion is further narrowed to the high-mass end of the diagonal, where the $\tilde{t}$ mass is $\gtrapprox$ 400 GeV.

The analysis overview and section organization is as follows, focusing exclusively on the high-mass diagonal region. Section 9.1 describes the data and simulated samples used in the analysis. Section 9.2 describes the event reconstruction and object requirements. Section 9.3 describes the study of new discriminating variables and signal region design for the high-mass compressed signals. These signal regions are utilized in two analysis techniques: *cut-and-count* for discovery, and *shape-fit* for exclusion. The shape-fit analysis here uses a boosted decision tree trained on several traditional and RJR variables, with the cut-and-count regions providing a cross-check of the results.

The background estimation strategy is described in Section 9.4. The largest backgrounds are estimated with dedicated control regions to extract a normalization of data to Monte Carlo simulation, while the estimates of smaller backgrounds are taken directly from simulation. The estimation and incorporation of systematic uncertainties is discussed in Section 9.5. Finally, all regions are used in a simultaneous fit as discussed in Section 9.6 to determine the amount of expected background in the signal regions and constrain the number of data events that could be attributed to a stop signal. Section 9.6 also presents the results and conclusions of the search.

9.1 Data/MC Samples

This analysis uses the full 2015-2016 ATLAS dataset, corresponding to an integrated luminosity of 36 $\text{fb}^{-1} \pm$ 3.2%, with a collision energy of $\sqrt{s}$ = 13 TeV and a mean pileup of 23.7. Events were primarily

collected using a E_T^{miss} trigger, which is fully efficient for $E_T^{miss} > 230$ GeV, with a secondary use of single lepton triggers with E_T^{miss} below this threshold. Thresholds for the single lepton triggers are set such that constant efficiency as a function of lepton p_T is obtained, the value of which is approximately 90% for electrons and 80% for muons. Each event is required to satisfy beam, detector, and data quality checks, as described by the Good Run Lists, which ensure the accelerator and detector were operating correctly when the data was recorded. Additionally, events were required to have a primary vertex, with two associated tracks with $p_T > 400$ MeV.

Simulated event samples are generated using Monte Carlo (MC) simulation to model the SM background processes and SUSY signals of interest. Both signal and background simulations were produced with varying numbers of minimum-bias interactions added to the primary interaction to simulate the effect of pileup, and with μ reweighting to match the distribution in data.

Background samples were processed with a full simulation of the ATLAS detector [97]. The nominal $t\bar{t}$ and single top samples [98] were generated with `POWHEG` [99] interfaced to `PYTHIA 6` [100] for parton showering (PS) and hadronization. W/Z+jets [101] and diboson [102] samples were generated and showered with Sherpa [103]. The $t\bar{t}$ + W/Z samples [104] were generated with MG5_aMC@NLO [105] interfaced to `PYTHIA 8` [106]. The signal $\tilde{t} \to t\widetilde{\chi}_1^0$ samples used a fast ATLAS simulation [97]. They were generated at leading order (LO) with MG5_aMC@NLO including up to two extra partons, and decayed using only phase space considerations in `PYTHIA 8`. A list of all simulation samples and the corresponding event generators and PS/hadronization models used can be found in Table 9.1.

Process	MC Generator
$t\bar{t}$	POWHEG + PYTHIA 6
Single top Wt	POWHEG+ PYTHIA 6
W/Z + jets	Sherpa
Diboson	Sherpa
$t\bar{t}$ + W/Z	MG5_aMC@NLO + PYTHIA 8
SUSY signal	MG5_aMC@NLO + PYTHIA 8

Table 9.1: Overview of simulated samples.

9.2 Object Requirements

The final state of the analysis contains jets, missing energy, and one lepton, which can be a electron or a muon. The reconstruction of these objects is discussed in detail in Section 5.6. Two classes of reconstructed physics objects are used in the analysis. *Baseline* objects are used to perform overlap removal and reconstruct E_T^{miss}, while *signal* objects have tighter kinematic and quality requirements, and are used to define regions of interest. In this section, the analysis specific requirements are described.

9.2.1 Leptons

In addition to typical kinematic requirements, there are three primary factors that determine whether a lepton is deemed usable for the analysis. The details of these metrics are introduced and detailed in Section 5.6.

1. Likelihood-based identification (ID) [71].
2. Impact parameter, which can distinguish between prompt and non-prompt leptons by taking into account the proximity of the track to the beam axis, measured in both transverse d and longitudinal z distances. Cuts on impact parameter involve both the measurement of

		Electron	Muon
Baseline	p_T	> 5 GeV	> 4 GeV
	$\|\eta\|$	< 2.47	< 2.47
	ID	VeryLoose	Loose
Signal	Isolation	LooseTrackOnly/FixedCutTight	FixedCutTightTrackOnly
	Impact Parameter	$\|d_0\|/\sigma_{d0} < 5$	$\|d_0\|/\sigma_{d0} < 3$, $\|z_0 sin\theta\| < 0.5$ mm
	ID	LooseAndBLayer/Tight	Medium

Table 9.2: Overview of baseline and signal lepton requirements for the stop1L analysis.

the point of closest approach of the track (d_0 or z_0) and its uncertainty (σ_{d_0} or σ_{z_0}, respectively).

3. Isolation, which gives an additional handle on whether a lepton is prompt or nonprompt, using information about the transverse energy not attributable to the lepton that is deposited in a cone with size ΔR around it.

Minor mismodelling of leptons in MC is corrected for by dedicated scale factors for each of the above three requirements, as derived from data events with Z or J/$\psi \to \ell\ell$ [70, 72]. Table 9.2 gives an overview of all kinematic, ID, impact parameter, and isolation requirements for both flavors of baseline and signal leptons used in the analysis.

9.2.2 Jets & E_T^{miss}

The jets used in this analysis are anti-k_t R = 0.4 jets. They are calibrated for detector response and *in situ* jet energy scale. Baseline jets are required to have p_T > 20 GeV, while signal jets have the more stringent requirement of p_T > 25 GeV and $|\eta| < 2.5$. Jets containing b-hadrons are identified using the MV2c10 b-tagging algorithm, at a working point that provides 77% selection efficiency in $t\bar{t}$ simulation.

Pile-up contamination is mitigated in each jet using the jet area subtraction methods; furthermore, signal jets with $p_T < 60$ GeV and $|\eta| < 2.4$ have to satisfy JVT requirements. The event cleaning procedure as described in Chapter 7 is applied to suppress fake jet contamination.

The E_T^{miss} in the event is defined as the negative vector sum of the transverse momenta of baseline leptons and jets. A soft term is added as well to account for primary vertex tracks but not to any baseline object [78].

9.2.3 Overlap Removal

In certain scenarios, a single pattern of energy deposition can be reconstructed as two distinct physics objects. To ensure that no detector signature is duplicated in the final set of reconstructed objets, an overlap removal procedure is applied to each event. An "overlap" between two objects can be a shared track, ghost-matching [107], or a minimum ΔR. Each possible combination of objects, i.e. electron and muon, electron and jet, jet and jet, has a certain criteria that determines an overlap, and a precedence that determines which of the two objects is kept and which is discarded. The specific priority ordering of this procedure is described in detail in Ref. [38].

9.3 Signal Regions

The kinematic features of stop decays near the diagonal are crucial to effective signal region design. In Section 6.1, the correlation between E_T^{miss} and ISR p_T was shown to be important when working with ISR topologies. Furthermore, the variable R_{ISR} was shown to aptly exploit this correlation for ultra-compressed signals, where all of the E_T^{miss} in the event comes from the ISR momentum

imparted to the di-$\widetilde{\chi}_1^0$ system.

This is promising for compressed stop sensitivity. However, there is a key complication in the stop 1L search; there is another source of E_T^{miss} in the event, the neutrino from the leptonic W boson decay. The neutrino adds to the total E_T^{miss} in the event, smearing the R_{ISR} resolution. This effect must be taken into account when designing optimal signal regions with R_{ISR} and other variables, the process of which is described in the following subsections for the cut-and-count and BDT signal regions.

9.3.1 Cut-and-Count SR Development

The cut-and-count analysis strategy is based on counting the number of events in a single region of phase space and comparing the result to prediction. It is therefore model-independent and best suited for discovery limits.

The first step undertaken in cut-and-count SR construction was to compare signal to background distributions for a set of key analysis variables. This set includes standard variables, such as E_T^{miss}, jet multiplicity, lepton p_T, and transverse mass m_T (defined in Equation 9.1). Other variables commonly used in analyses with tops were also used, such as *topness* and am_T2.[†]

$$m_T\left(p_T^\ell, p_T^{miss}\right) = \sqrt{m_\ell^2 + 2\left(E_T^\ell E_T^{miss} - p_T^\ell \cdot p_T^{miss}\right)} \tag{9.1}$$

Several RJR variables were examined in the optimization, specifically R_{ISR}, M_T^S, p_T^{ISR}, NjV,

[†] *topness* is a χ-squared fit based variable to identify and suppress partially reconstructed dileptonic $t\bar{t}$ events. am_T2 is a form of asymmetric m_T2 for dileptonic $t\bar{t}$ events with a lost lepton.

NlV, and $\Delta\phi$(ISR,I), as defined in Section 6.2. Additionally, the RJR variable $p_T bV1$ was incorporated, defined as the p_T of the highest momentum b-jet in the event. The signal region is expected to be made by imposing cuts on these variables, the values of which are optimized to both maximize signal yield and kill Standard Model backgrounds.

To quantify this process of finding optimal cut values, histograms known as "N-1 plots" were made for each variable, including both expected backgrounds and a few key signal points. The defining feature of these histograms is that the cut on the variable displayed is not applied. A second panel below each histogram displays the Z_n sensitivity as defined in Section 8.1 and calculated using the `RooStats NumberCountingUtils` method [108], for a few representative signal points as a function of the potential cut value. This can provide a clear indication of which cut value gives maximum performance.

Multiple iterations of these histograms were made in the optimization procedure. For the first, only a general preselection was applied to enforce the desired topology. The most powerful cut, i.e. the value of the variable that gives the maximal Z_n sensitivity for that preselection, is chosen and added to the selection. This procedure repeats, with each subsequent iteration adding the most powerful possible cut for the current selection.

In an event that is kinematically very close to the diagonal, where the decay chain has a very small mass splitting, all of the E_T^{miss} is provided by the p_T^{ISR}. However, moving slightly off this diagonal line in phase space, corresponding to slightly larger mass splittings, weakens this correlation, as larger mass splittings allow for some of the $\tilde{t}$ mass energy to go to the $\widetilde{\chi}_1^0$ as momentum. This "off-diagonal" region is still sufficiently compressed, and far from the standard bulk search region, that

the RJR method still proves useful. Moreover, the difference between on- and off-diagonal kinematics is significant enough to merit two separate but identical optimization procedures, allowing their kinematic features to be fully utilized.

Four canonical signal points, defined by ($m_{\tilde{t}}$ [GeV], $m_{\tilde{\chi}_1^0}$ [GeV]), were used in the optimization procedure. Two of these were chosen to capture the kinematic features of the on-diagonal region; these are (400, 227) and (450, 277). The two points that represent the off-diagonal region are (450, 200) and (500, 250). Figures 9.2 through 9.4 show N-1 plots of E_T^{miss} (MET), m_T, jet multiplicity, NjV, NlV, leading lepton p_T, R_{ISR}, p_T^{ISR}, M_T^S (MS), and $\Delta\Phi$(ISR,I) for the diagonal signal topology. An arrow indicates the optimal cut value determined from the optimization. Figures 9.5 to 9.6 similarly show the results of N-1 optimization using the variables of jet multiplicity, NjV, NlV, leading lepton p_T, R_{ISR}, p_T^{ISR}, M_T^S (MS), and $p_T bV1$ for the off-diagonal topology.

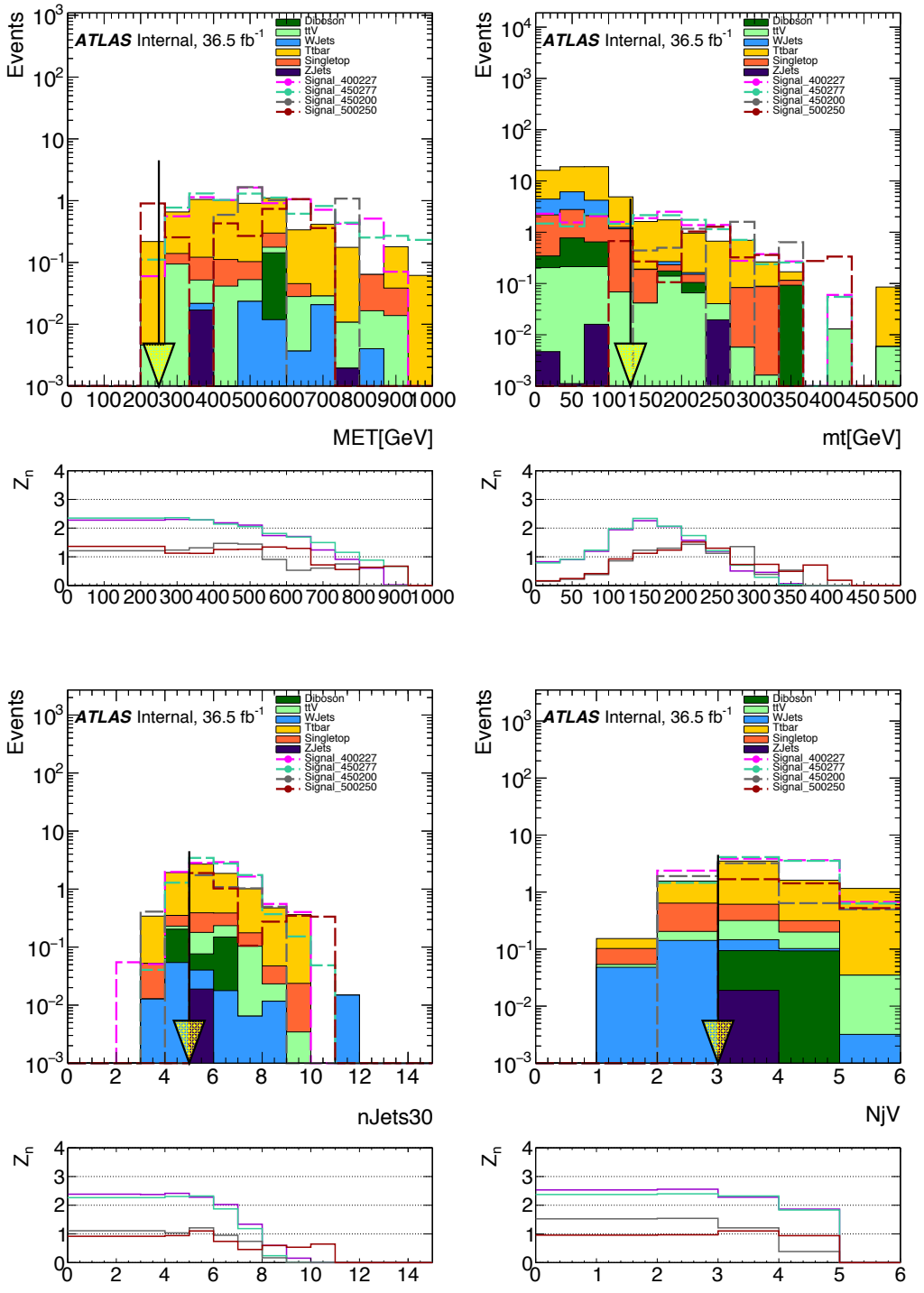


Figure 9.2: Distribution of variables after applying all on-diagonal SR cuts, except the one on the displayed distribution.

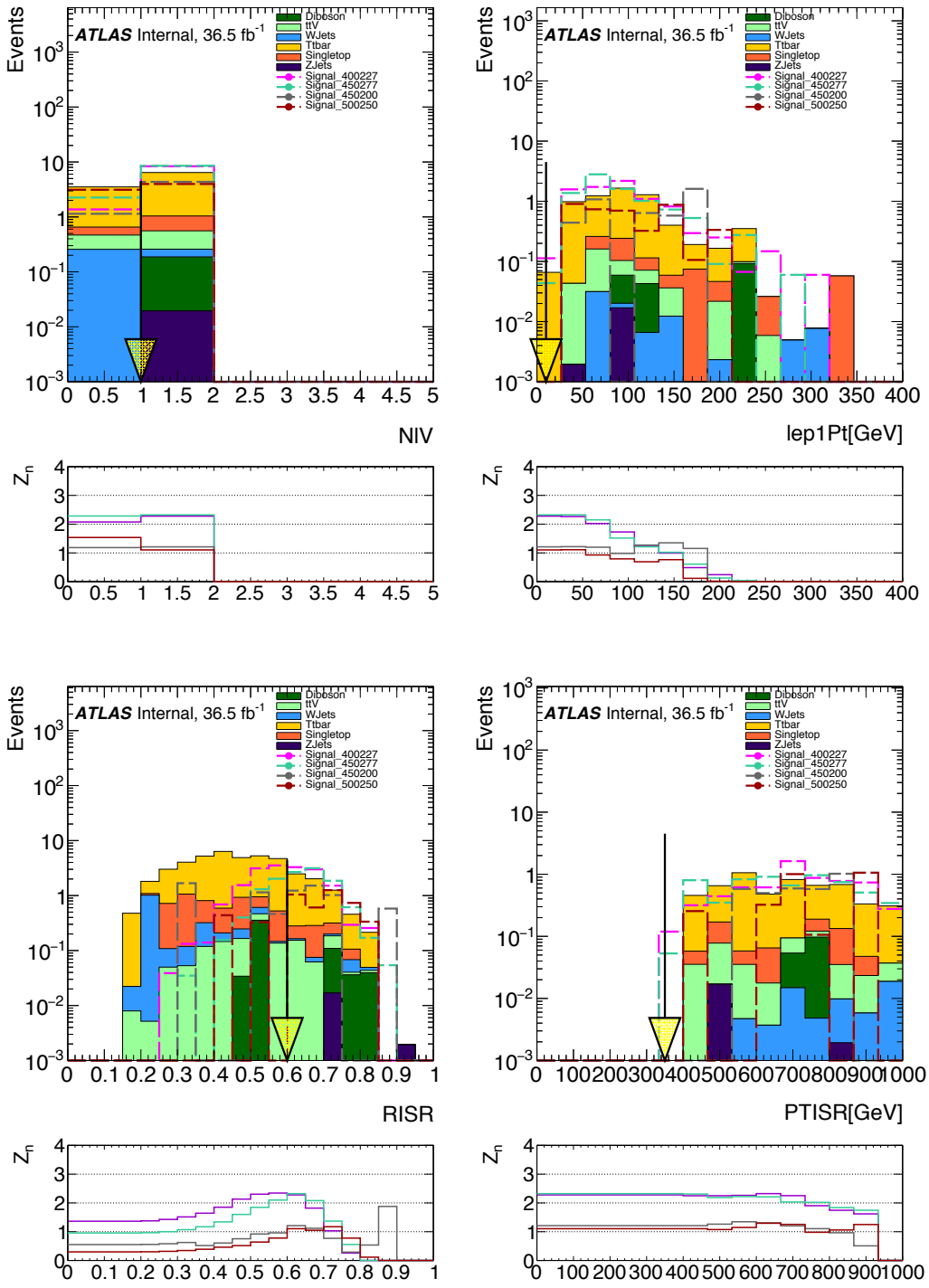


Figure 9.3: Distribution of variables after applying all on-diagonal SR cuts, except the one on the displayed distribution.

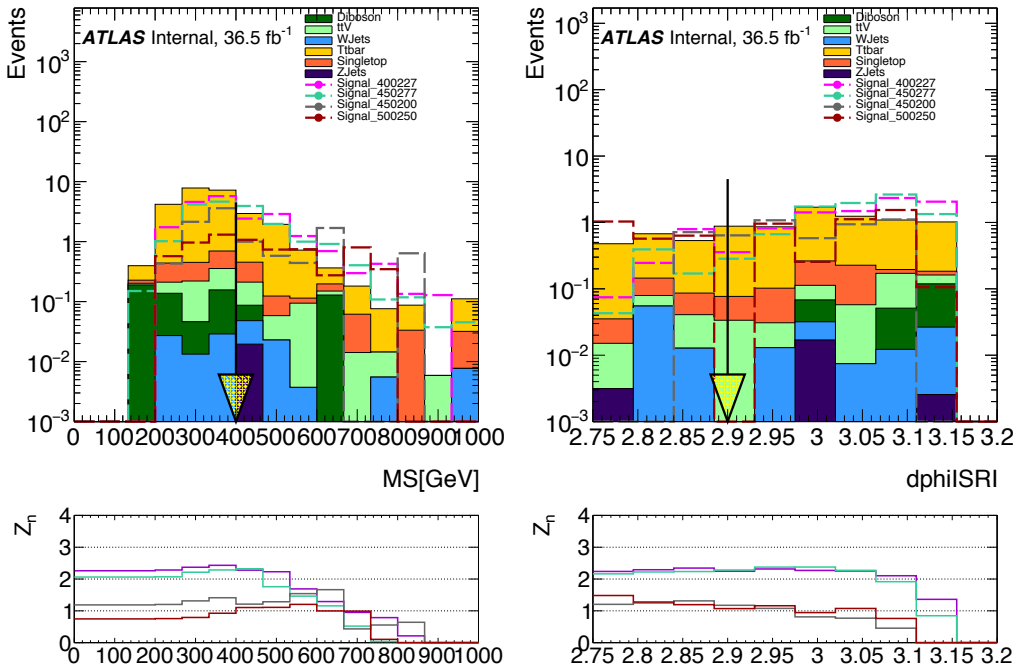


Figure 9.4: Distribution of variables after applying all on-diagonal SR cuts, except the one on the displayed distribution.

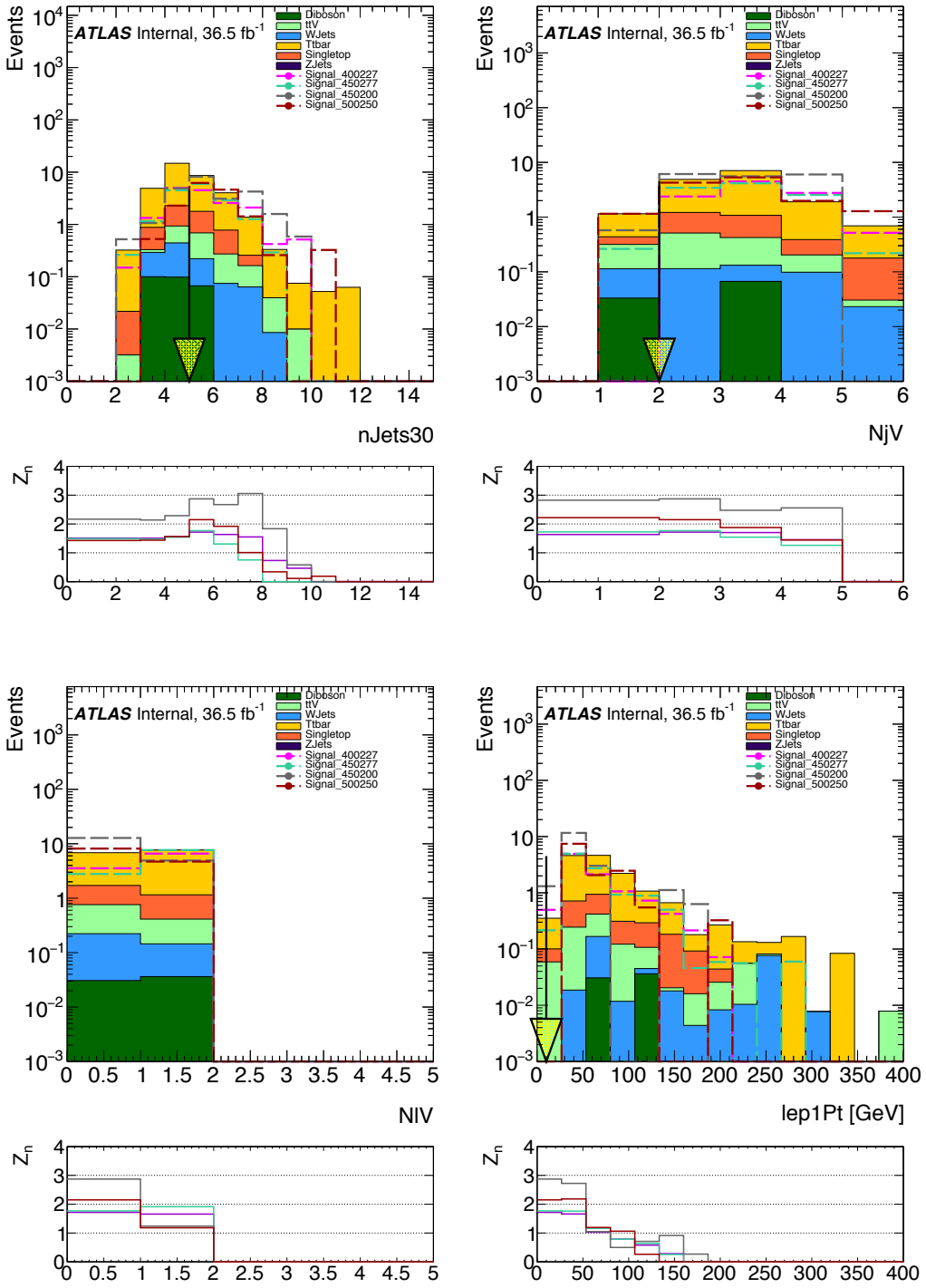


Figure 9.5: Distribution of variables after applying all off-diagonal SR cuts, except the one on the displayed distribution.

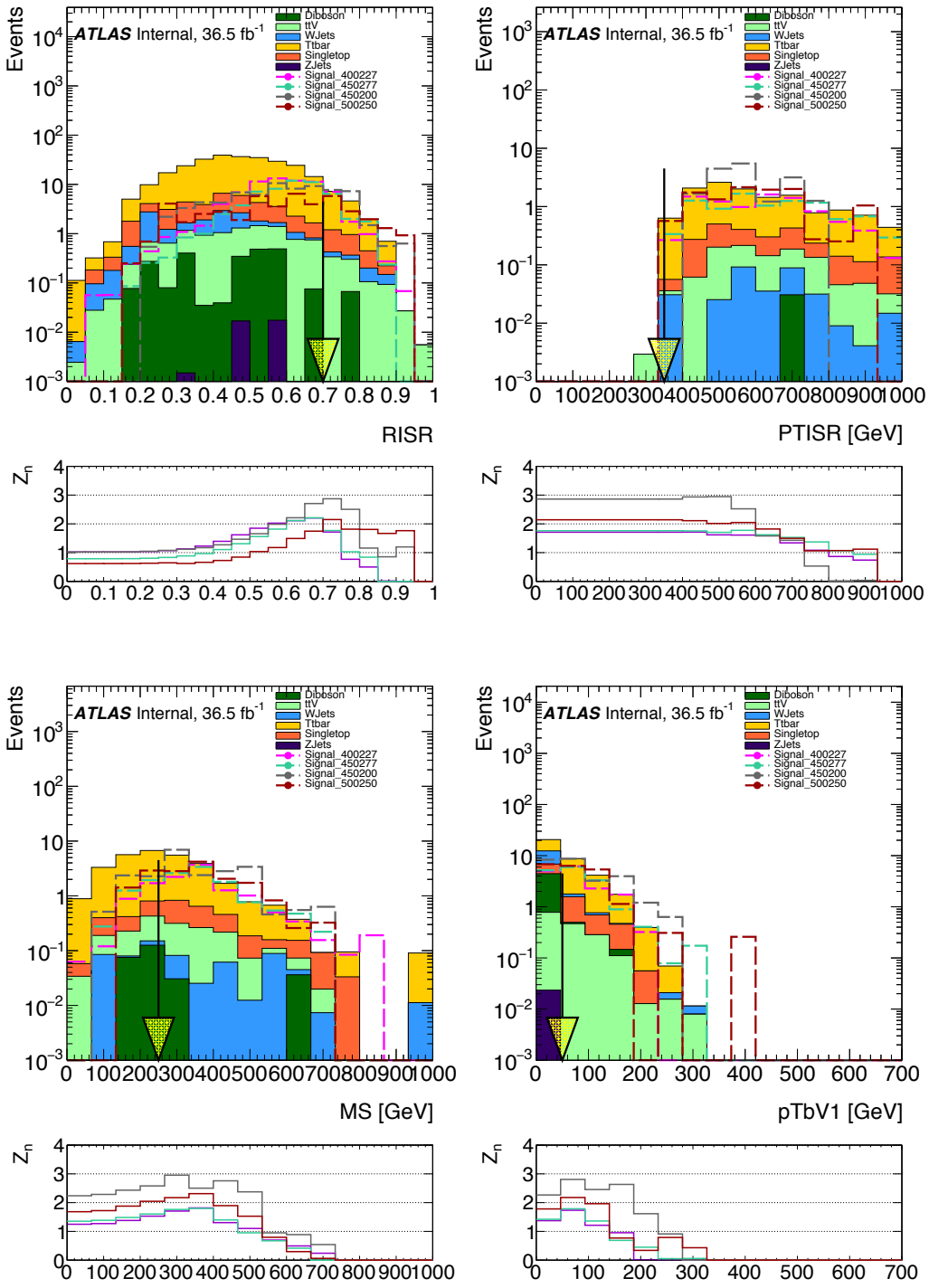


Figure 9.6: Distribution of variables after applying all off-diagonal SR cuts, except the one on the displayed distribution.

Variable	Preselection	Diagonal	Off-Diagonal
E_T^{miss}	230 GeV	-	-
N_{jets}	≥ 5	-	-
Leading lepton p_T	> 25 GeV	-	-
p_T^{ISR}	> 350 GeV	-	-
m_T	> 130 GeV	-	-
M_T^S	-	≥ 400 GeV	≥ 250 GeV
R_{ISR}	-	≥ 0.6	≥ 0.7
NjV	-	≥ 1	≥ 2
NbV	-	≥ 1	-
NlV	-	≥ 1	-
$\Delta\Phi(ISR, I)$	-	≥ 2.9	-
Leading jet p_T	-	-	> 300 GeV
$p_T bV1$	-	-	≥ 50 GeV

Table 9.3: Table of selection criteria for high-mass compressed cut-and-count signal regions.

The cut values obtained in the N-1 optimization procedure were subsequently implemented into two distinct diagonal and off-diagonal signal regions. A common preselection for these regions, along with their individual definitions, is shown in Table 9.3.

Because of the relative novelty of the RJR method with regard to SUSY analyses, careful study of the new variables was necessary to ensure that they were well-modeled by simulation. Figure 9.7 shows two primary RJR variables, R_{ISR} and M_T^S, at preselection, to demonstrate good data vs. MC agreement. Such studies give confidence to potential extrapolation across these variables, that is, the selection of different ranges of values of a given variable in different analysis regions. To keep data vs. MC inconsistencies from sculpting the analysis regions, generally it is desirable for the data/MC ratio to be flat across a given variable of interest.

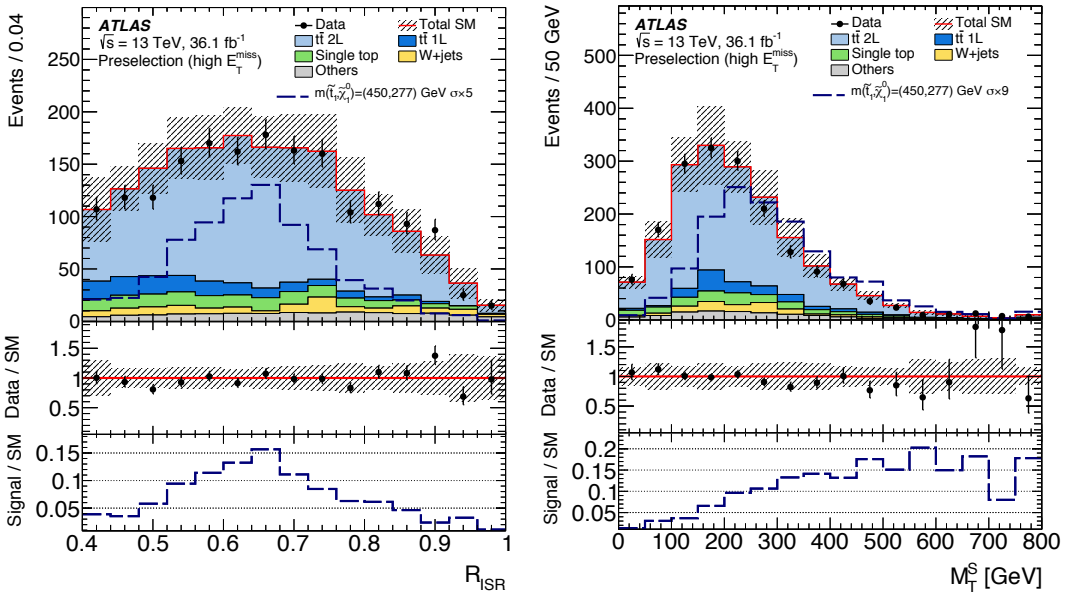


Figure 9.7: Distributions of key RJR variables, including data to simulated SM background agreement and the ratio of expected signal to total SM background. [38].

9.3.2 BDT SR Development

To help perform the difficult signal-to-background discrimination on the high-mass diagonal, a *boosted decision tree* (BDT) was trained and used to build a supplemental diagonal signal region. Inherently the training of the BDT to discriminate stop signal from background is model-dependent, so in this analysis, the BDT-based signal region was used for exclusion limits.

A decision tree is a multivariate classification method that learns a set of discriminating features, and splits an input dataset recursively based on those features. Each *node* in the tree represents a boolean decision; in the case, whether the input data event looks more signal-like or more background-like. The tree begins with a training sample at the root node, which is then split at each node based on the cut in a variable of choice that gives the best separation gain. The number of decisions that are made on the input creates a number of levels that make up the *depth* of the tree. The last level consists of *leaves* that provide the final classification, which assigns a "score" from 0 to 1, where 0 is most background-like and 1 is most signal-like (see Figure 9.8).

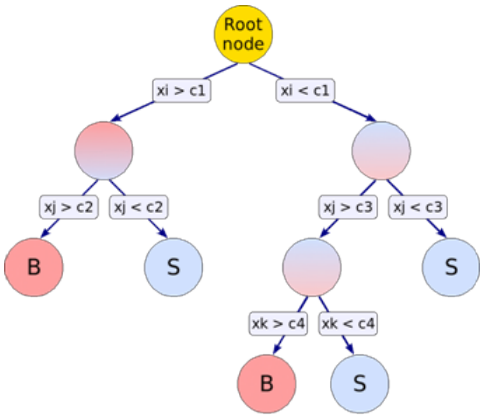


Figure 9.8: Diagram of a decision tree [109].

TMVA Setting	Value	Description
`BoostType`	Grad	Boosting type for all tree in forest.
`NTrees`	200	Number of trees in forest.
`MinNodeSize`	10	Minimum percentage of training events required in a leaf node.
`UseRandomisedTrees`	True	At each node splitting, choose a random set of variables from which the best variable is selected.
`UseNvars`	10	Size of the subset of variables used with RandomisedTree option.
`MaxDept`	4	Maximum allowed depth of the decision tree.
`UseBaggedBoost`	True	Use a random subsample of all events for growing the trees in each iteration.
`BaggedSampleFraction`	0.6	Relative size of bagged event sample to original size of the sample.

Table 9.4: High-mass compressed BDT settings in TMVA.

Boosting combines many individual trees into a *forest*, where each tree has a weight that is assigned based on its achieved accuracy in the final classification. Data samples are also assigned a weight, which gets larger if the sample is frequently misclassified. This method helps to reduce bias and strengthen the correlations exploited in the classification.

Implementation for training and testing of the BDT was done with the Toolkit for Multivariate Analysis (TMVA) framework [110], which provides a environment for building multivariate classifiers that integrates with ROOT. TMVA has a variety of settings that can be specified by the user, which affect how the BDT is generated. For this analysis, the setting choices as shown in Table 9.4 were made to maximize signal to background separation while avoiding *overtraining*, or teaching the BDT to classify based on fluctuations or inauthentic features, leading to a classifier that is specific to the input data set and thus has degraded performance overall.

Variable	Cut Value	Motivation
E_T^{miss}	230 GeV	Trigger threshold
# (jets, b-tags)	$(\geq 5, \geq 1)$	Enforce expected final state
$p_T(\text{jet}_i)$ [GeV]	$> (25, 25, 25, 25, 25)$	Kinematic expectation
m_T	> 120 GeV	Suppress multijet/$t\bar{t}$
R_{ISR}	≥ 0.4	Remove uninterestting events

Table 9.5: Table of preselection criteria for the high-mass compressed BDT training.

The BDT for the high-mass compressed analysis was trained to select four benchmark signals again $t\bar{t}$ and W+jets backgrounds.[‡] As with the cut-and-count optimization procedure, the signal points were selected to encompass a variety of stop masses, as well as diagonal and off-diagonal kinematic features. Those four points are ($m_{\tilde{t}}$ [GeV], $m_{\tilde{\chi}_1^0}$ [GeV]) = (400, 227), (450, 262), (450, 277), and (500, 327). To ensure that all signals were assigned equal weight in the training, they were not normalized by cross section. The preselection of events used for training the BDT was selected to enforce basic topological and kinematic expectations, and eliminate any background events that would easily be removed by other cuts. This preselection is shown in Table 9.5.

In order to minimize overtraining, the set of events on which the BDT is trained and tested cannot be the same. It is possible to split the input set of simulated events in half (by even and odd numbered events), giving two equal sized but nonintersecting sets that can be used for these two purposes. However, this results in a 50% loss of MC statistics from entering the training. A solution to this problem was found in training two BDTS, each with identical settings and input variables. The only difference between them is that the even numbered events are used to train the first BDT and test the second, and vice versa for the second BDT. This method reduces overtraining while

[‡]The complete analysis in ref. [38] contains three BDTs, for the low, middle, and high mass regions of the diagonal.

ensuring usage of the full MC statistics.

The set of variables given to each BDT were chosen to maximize signal to background separation, while carefully avoiding correlations between variables that may lead to overtraining. Many of the discriminating variables from the cut-and-count optimization were considered, along with some new variables like ΔR(b,ℓ) or $\Delta\phi(t_{lep}, t_{had})$ being constructed out of lower level variables. Also added was the hadronic top mass $m_t\chi$.[§]

Potential input variable modeling was validating through data vs. MC agreement, as shown for R_{ISR}, M_T^S, $\Delta\Phi(ISR, I)$, NjV, the 3rd & 4th jet p_T (to capture information about softer event activity), $m_t\chi$, $\Delta\phi(t_{lep}, t_{had})$, ΔR(b,ℓ), m_T, E_T^{miss}, and jet multiplicity in Figures 9.9 and 9.10. This ensures that only well-modeled variables are used to train the BDT discriminator. E_T^{miss} and jet multiplicity, while shown in this validation study, were ultimately not used in training. All input variables that were used in training, ranked by their importance to the BDT performance, can be seen in Table 9.6.

The resulting signal and background distributions as a function of BDT score, for both even- and odd-trained BDTs, can be seen in Figure 9.11. The Kolmogorov-Smirnov check as implemented by TMVA was also performed, to ensure there is no significant overtraining. Comparisons of the signal and background distribution shapes for each BDT confirm that there is no fundamental difference between even- and odd-numbered events that would have affected the training or performance between the two BDTs.

[§]The hadronic top mass is defined by minimizing the function $\chi^= \frac{(m_{j1,j2,bi}-m_t)^2}{m^2_{j1,j2,bi}(r^2_{j1}+r^2_{j2}+r^2_{bi})} + \frac{(m_{j1,j2}-m_W)^2}{m^2_{j1,j2}(r^2_{j1}+r^2_{j2}}$, where i=1 or 2, b1 and b2 are the two jets with the highest b-tagging weights, j1 and j2 are the two highest p_T jets in the event (excluding b1 and b2), and r_i is the fractional jet energy uncertainty of the p_T of jet i.

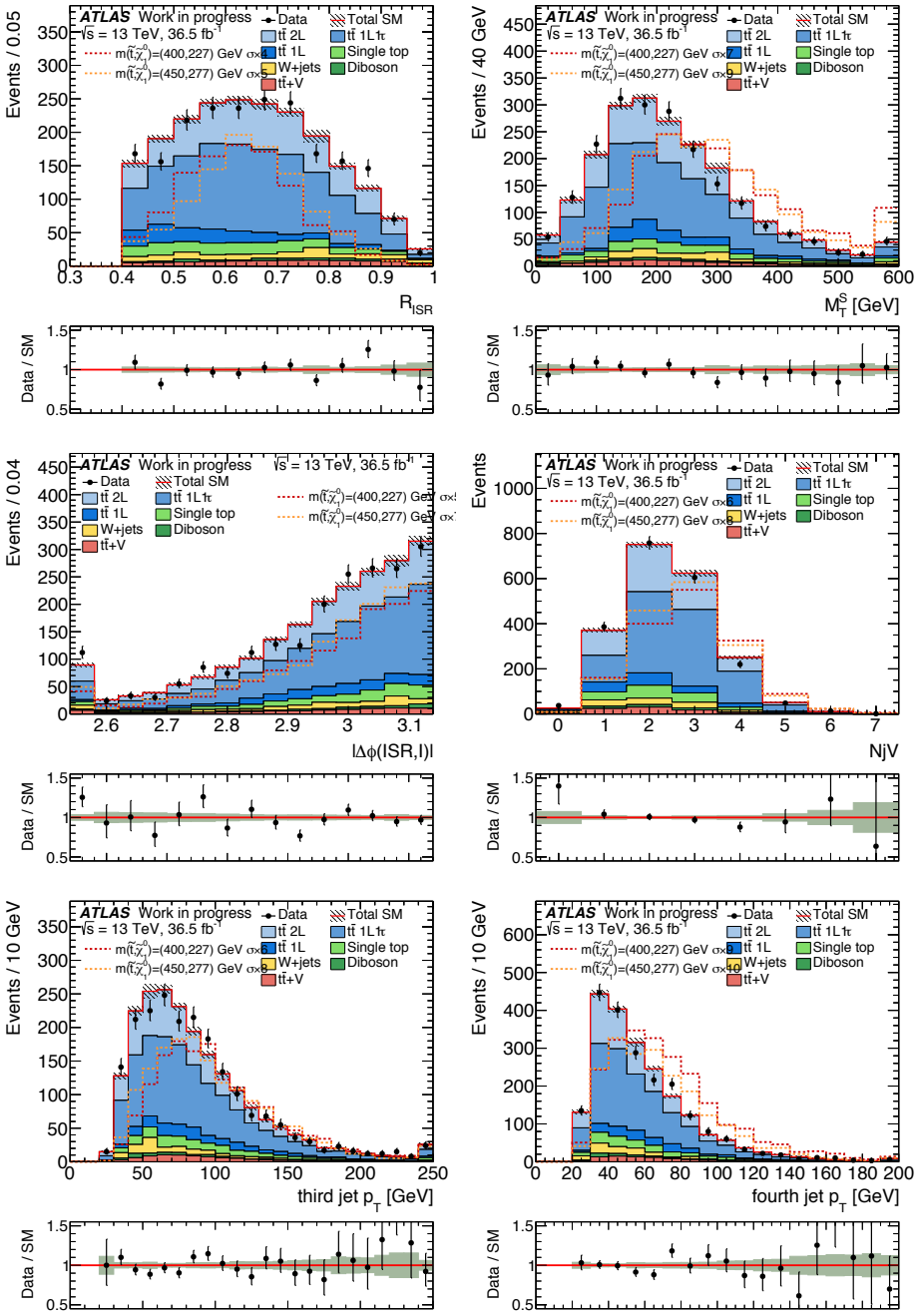


Figure 9.9: Comparison of data and simulation at preselection level for input variables to the BDT, before the fit to data.

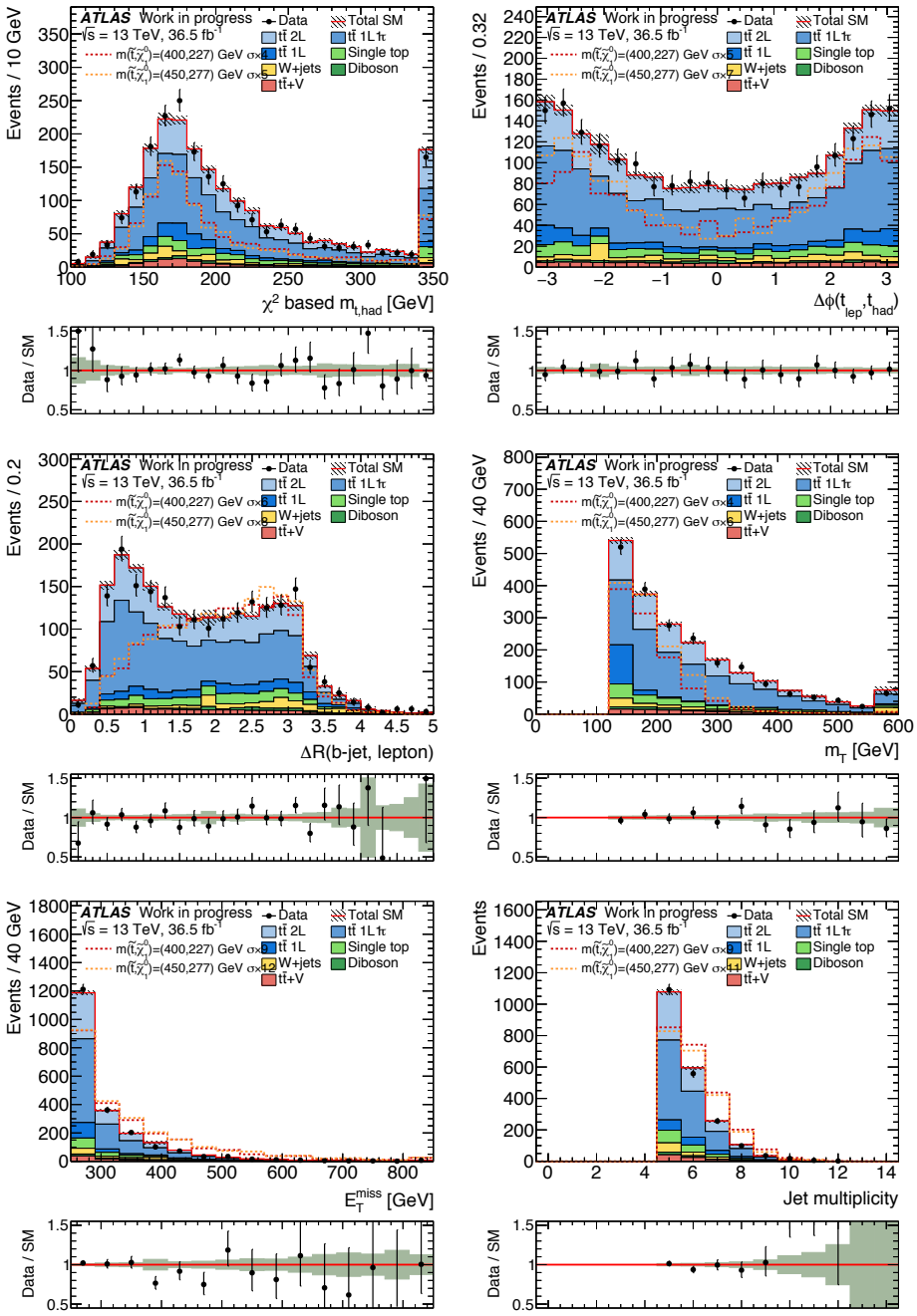


Figure 9.10: Comparison of data and simulation at preselection level for input variables to the BDT, before the fit to data. E_T^{miss} and jet multiplicity were ultimately not used.

Variable	BDT Ranking (even training events)	BDT Ranking (odd training events)
R_{ISR}	0.123	0.111
$\Delta\phi$(ISR,I)	0.117	0.100
ΔR(b,ℓ)	0.116	0.112
$\Delta\phi(t_{lep}, t_{had})$	0.113	0.111
m_T	0.108	0.124
M_T^S	0.095	0.102
Fourth jet p_T	0.094	0.092
$m_t\chi$	0.082	0.080
Third jet p_T	0.080	0.088
NjV	0.074	0.077

Table 9.6: Input variables for the high-mass compressed BDT, with the rankings assigned to each variable based on their importance in the BDT performance.

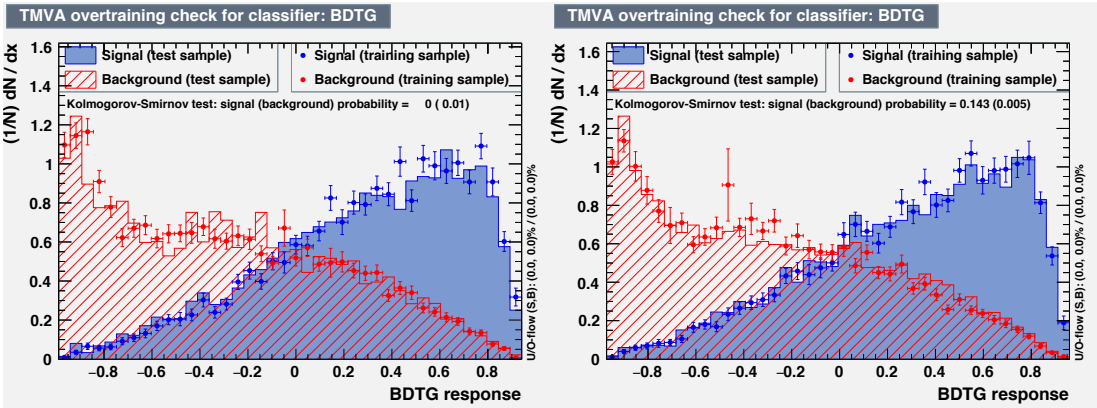


Figure 9.11: Signal vs. background discrimination capability and TMVA Kolmogorov-Smirnov overtraining check; for the first BDT, trained on even events and test on odd events (left), and for the second BDT, trained on odd events and tested on even events (right).

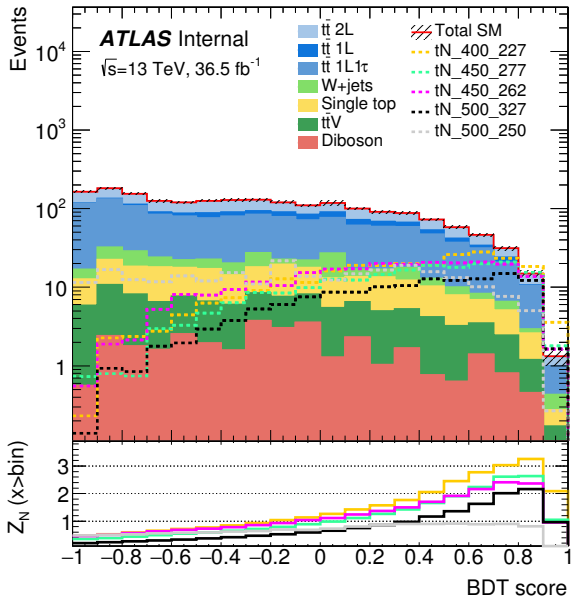


Figure 9.12: The distribution of the final BDT score for primary background processes and the benchmark signals. The ratio plot shows the cumulative significance after a rectangular cut corresponding to the x-axis bin position. The one-sided Z_n significance is estimated using the `RooStats NumberCountingUtils` BinomialExpZ formula [108], assuming a flat 20% systematic uncertainty. The signal region is defined as events with BDT score greater than 0.6.

The final performance of the BDT can be seen in Figure 9.12, in the form of signal vs. background distributions as a function of final per-event assigned BDT score. Here, -1 is the most background-like score, and +1 is the most signal-like. and good discrimination is demonstrated. The signal region is thus defined as the events where the BDT score is greater than 0.6. A shape fit is also performed over this region, using three signal region bins defined as [0.6, 0.7], [07, 0.8], and [0.8,1.0] (referred to as SR1, SR2, and SR3, respectively.) This strategy uses model information and accounts for the shape of the signal across analysis variables, thereby improving the exclusion sensitivity.

With a variety of signal regions in hand and ensured to be robust, the next step in the analysis is to develop a solid estimation of the non-signal processes in these regions.

9.4 Background Estimation

The background estimation strategy for the analysis is to use dedicated control regions (CRs) to estimate all significiant SM processes in the signal regions. The data in the CR is used to extract a *normalization factor* for the background process, defined in Section 8.3 as the ratio of observed to expected events in the CR. The normalization factor can then be used to scale the MC prediction of that background in the SR, which gives a more precise estimate of the process yield accounting for modeling discrepancies in the phase space of interest.

While the Standard Model backgrounds for the stop1L search can include $t\bar{t}$, single-top Wt, tt+Z$\rightarrow \nu\nu$ (irreducible), QCD, and W+jets, the largest contributors in the high-mass diagonal signal regions are the top backgrounds. To pass signal region selections, the $t\bar{t}$ background must have exactly one lepton. This occurs if the decay is either semileptonic, or dileptonic where one of the leptons is either lost (i.e. not reconstucted, not identified, or removed by overlap removal) or a hadronically decaying tau. The fraction of semileptonic and dileptonic $t\bar{t}$ events vary across regions. The high-mass compressed analysis uses only one CR, to normalize the $t\bar{t}$ and single-top backgrounds. The multijet background is estimated from data using a fake-factor method [111], and is found to be negligible in all regions.

Validation regions (VRs) are defined to validate the CR predictions, with one VR built for every CR. Similarly, the VR is designed to be enriched in a background process of interest, but is kinematically closer to the SR. It is not used to extract or constrain any normalization factors, but rather to provide a statistically independent check of background estimates as provided by the normalization

factor extracted from the CR. Signal contamination in the VRs can be higher than in the CRs, but generally kept small to ensure goodness of normalization. Different CRs are defined for cut-and-count and BDT SRs, as defined below.

9.4.1 Cut-and-Count Estimation Strategy

To design control region selections for the cut-and-count analysis, key signal region cuts that eliminate SM background are inverted. This allows the CR to satisfy all design requirements: non-overlapping with the signal region, but otherwise kinematically similar, and enriched in a single background. Other signal region cuts can be loosened to enhance statistics. Validation regions also need to be orthogonal, but even closer in phase space, to the signal region. These requirements impact the choice of SR cuts that are inverted or loosened. Since there are two distinct cut-and-count signal regions, diagonal and off-diagonal, each one must have a dedicated control and validation region.

Diagonal Control & Validation Regions

In both control and validation regions for the diagonal SR, the chosen cut to invert was that on M_T^S. This was selected because out of the primary SR cuts, it provided the best background purity and smallest contamination of benchmark signal points. Additionally, the requirement on NlV was loosen to allow primarily background in to the region and increase purity.

Simulation studies of $t\bar{t}$ in the SR showed that for low values of m_T (primarily CR-like), the dominant $t\bar{t}$ decay was semileptonic, while at higher m_T values (primarily SR-like), the decays

Variable	Common		
E_T^{miss}	$\geq$ 230 GeV		
N_{jets}	$\geq$ 5		
Leading lepton p_T	$>$ 25 GeV		
p_T^{ISR}	$>$ 350 GeV		
m_T	$>$ 130 GeV		
R_{ISR}	$\geq$ 0.6		
NbV	$\geq$ 1		
$\Delta\Phi(ISR, I)$	$\geq$ 2.9		
	Signal	Control	Validation
M_T^S	$\geq$ 400 GeV	$<$ 300 GeV	$<$ 300 GeV
NjV	$\geq$ 3	$\geq$ 1, $<$ 3	$\geq$ 3
NlV	$\geq$ 1	$\geq$ 0	$\geq$ 0

Table 9.7: Table of signal, control, and validation region selections for high-mass compressed cut-and-count diagonal regions.

tended to be dileptonic with a hadronically decaying tau. Since the latter decay likely has more jets in the final state, this distinction impacts the number of jets expected in the CR as compared to the SR. To ensure approximately similar numbers of ISR jets across both regions, the NjV cut was inverted for the CR, but remained the same between the VR and SR. Table 9.7 shows the selection for the diagonal CR and VR with respect to the signal region.

It is important for the validity of the final background estimate as obtained from the likelihood fit that the data is well-modeled in these regions, and that the region is pure in the background of interest, in particular free from signal. To verify the modeling of the key analysis variables, Figures 9.13 to 9.14 show data vs. MC plots of p_T^{ISR}, R_{ISR}, |$\Delta\Phi$(ISR,I)|, M_T^S, m_T, E_T^{miss}, lepton p_T, jet multiplicity, b-jet multiplicity,NjV, and NbV for the diagonal CR.

In order to verify the background predictions given by the CRs, variables of interest are plotted in the validation region, both before and after the background fit to data. Pre-fit data vs. MC plots for

the diagonal validation region can be found in Figures 9.15 to 9.16. Though the primary purpose of the VR is to validate the overall normalization of MC to data, the pre-fit plots (without NFs applied) are still a valuable way to build confidence in the chosen variables and the estimation process. In this way, the good agreement in these figures reflects a robust background estimation for the analysis.

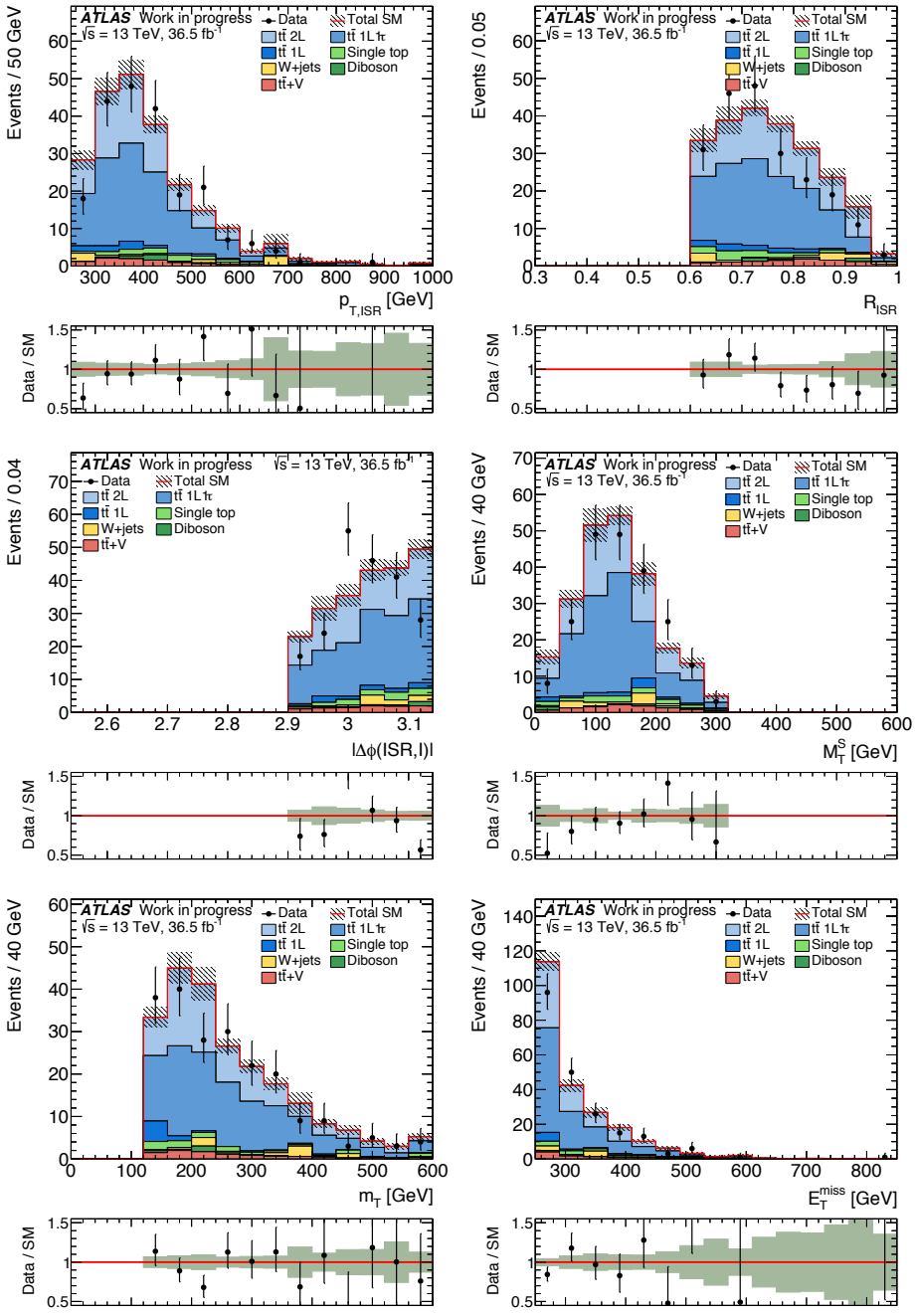


Figure 9.13: Comparison of data and simulation in the cut-and-count diagonal control region, before the fit to data.

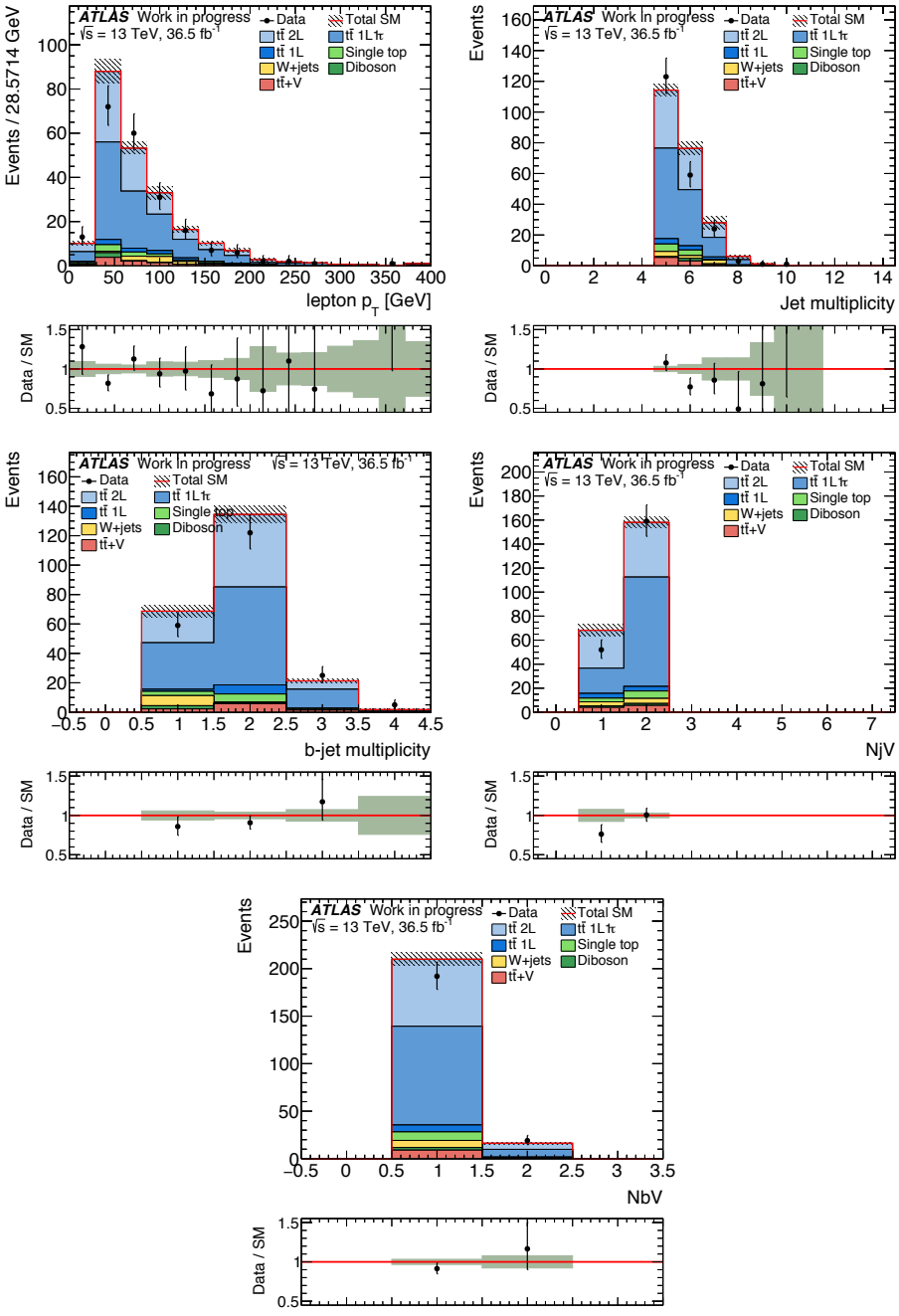


Figure 9.14: Comparison of data and simulation in the cut-and-count diagonal control region, before the fit to data.

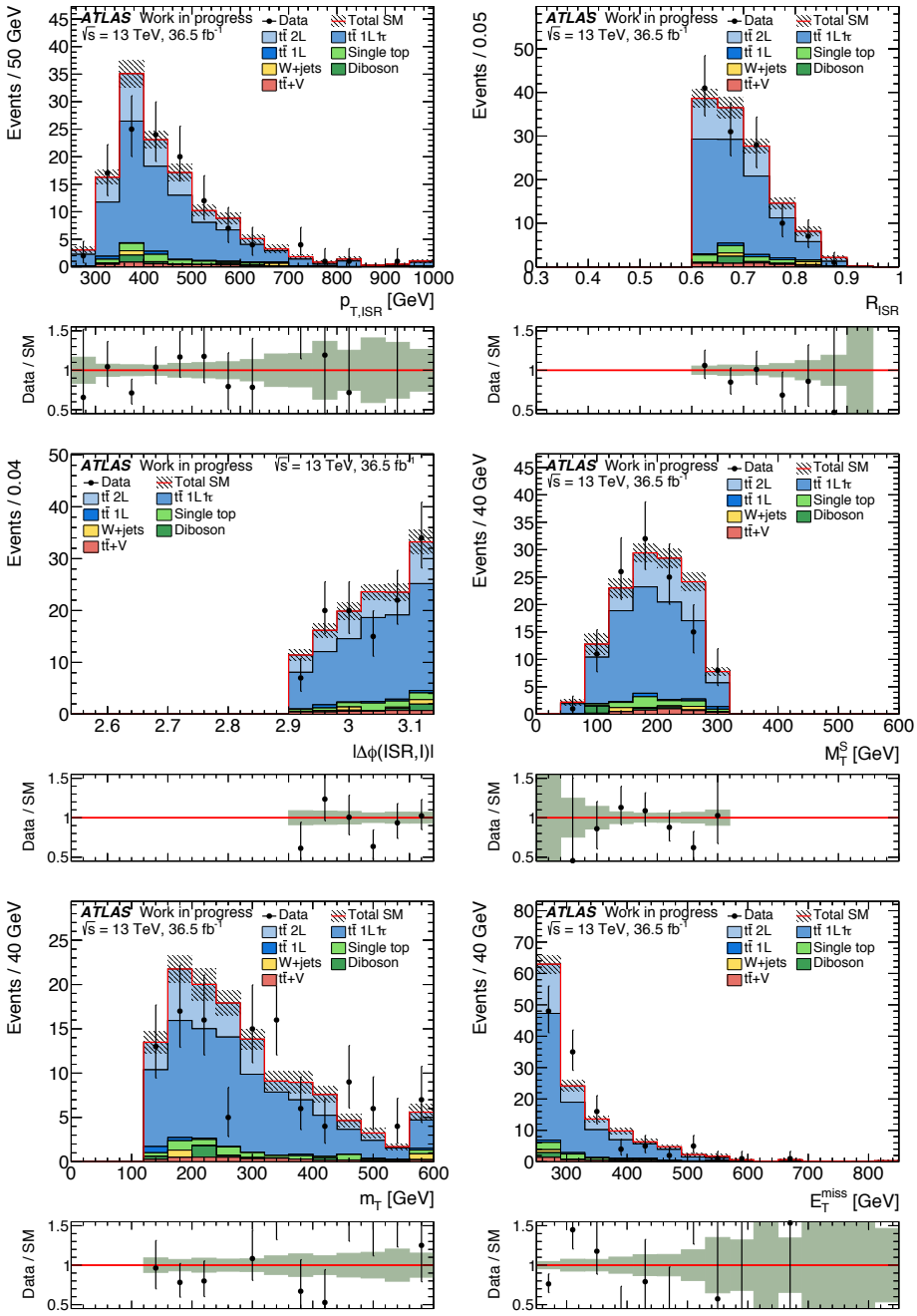


Figure 9.15: Comparison of data and simulation in the cut-and-count diagonal validation region, before the fit to data.

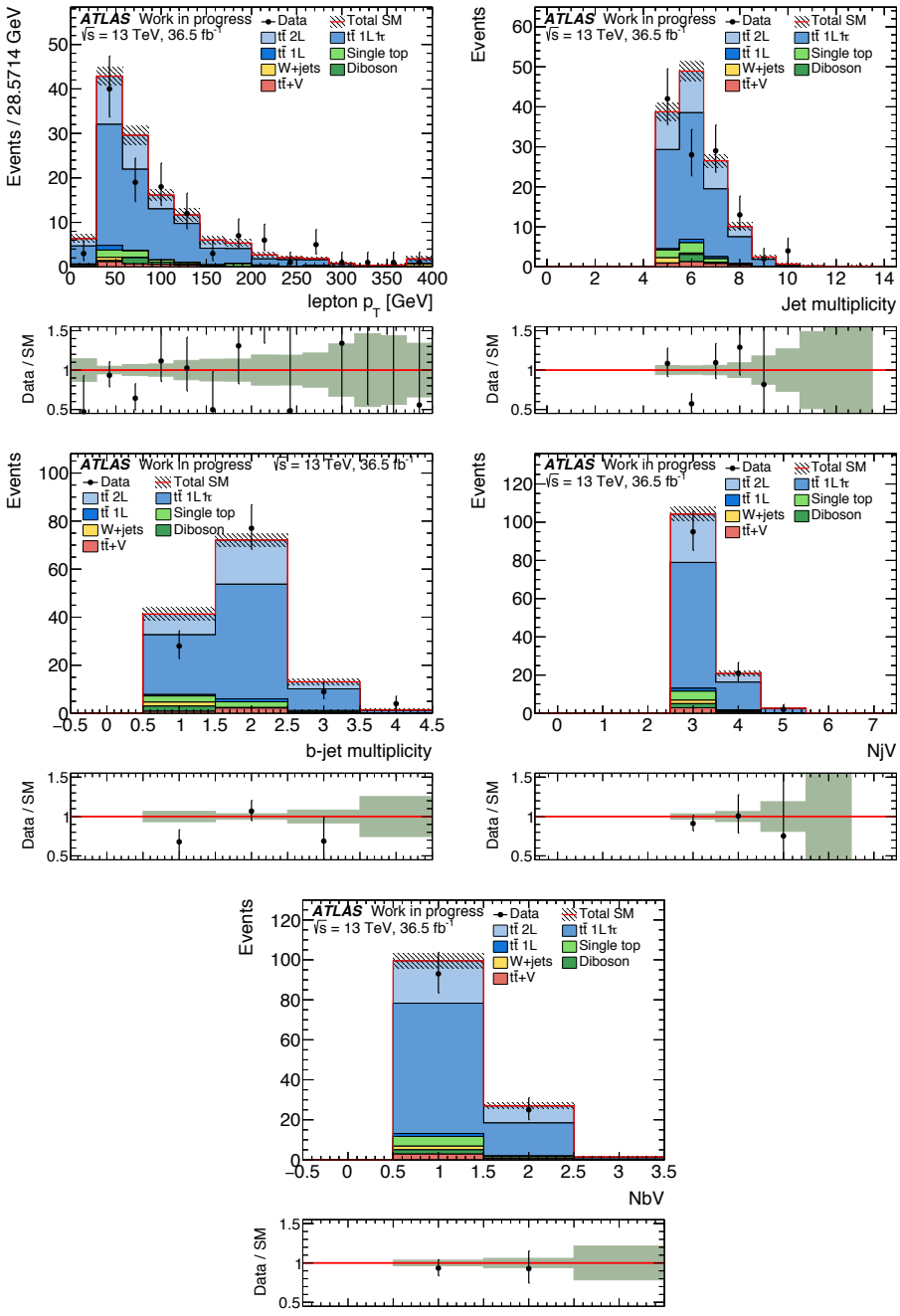


Figure 9.16: Comparison of data and simulation in the cut-and-count diagonal validation region, before the fit to data.

Variable	Common		
E_T^{miss}		$\geq$ 230 GeV	
N_{jets}		$\geq$ 5	
Leading lepton p_T		$>$ 25 GeV	
Leading jet p_T		$>$ 300 GeV	
p_T^{ISR}		$>$ 350 GeV	
m_T		$>$ 130 GeV	
$p_T bV1$		$\geq$ 50 GeV	
NjV		$\geq$ 2	
	Signal	Control	Validation
M_T^S	$\geq$ 250 GeV	$<$ 250 GeV	$<$ 250 GeV
R_{ISR}	$\geq$ 0.7	$<$ 0.6	$\geq$ 0.6
$\Delta\Phi(ISR, I)$	-	$<$ 3.1	$<$ 3.1

Table 9.8: Table of signal, control, and validation region selections for high-mass compressed cut-and-count off-diagonal regions.

Off-Diagonal Control & Validation Regions

Compared to the on-diagonal region, the off-diagonal phase space tends to have a slightly weaker ISR topology and thus looks more like SM background in the detector. As a result, care must be taken when designing background estimation regions, particularly in terms of keeping signal contamination to a minimum.

As with the diagonal regions, the inverted variable used to define the off-diagonal CR and VR is M_T^S. Additionally, R_{ISR} is inverted in the CR definition and loosened in the VR definition to enhance background contribution. A cut on $\Delta\phi$(ISR,I) was added to minimize signal contamination, inverting and loosening the cut with respect to the SR. Table 9.8 shows the selection for the off-diagonal control and validation regions with respect to the off-diagonal signal region.

Data vs. MC plots for the off-diagonal control region are shown in Figures 9.17 to 9.18, and for

the off-diagonal validation region in Figures 9.19 to 9.20. As with the diagonal case, all variables have good agreement between data and simulation, with no slope in the data/MC ratio, and the estimation can be deemed suitable.

To ensure that there is no significant contamination of any signal in either the diagonal or off-diagonal CR, a full scan of the signal grid is performed, checking the yield of each signal in the diagonal and off-diagonal CRs. As shown in Figure 9.21, the contamination is below 20% for all signal points not already excluded in previous iterations of the search.

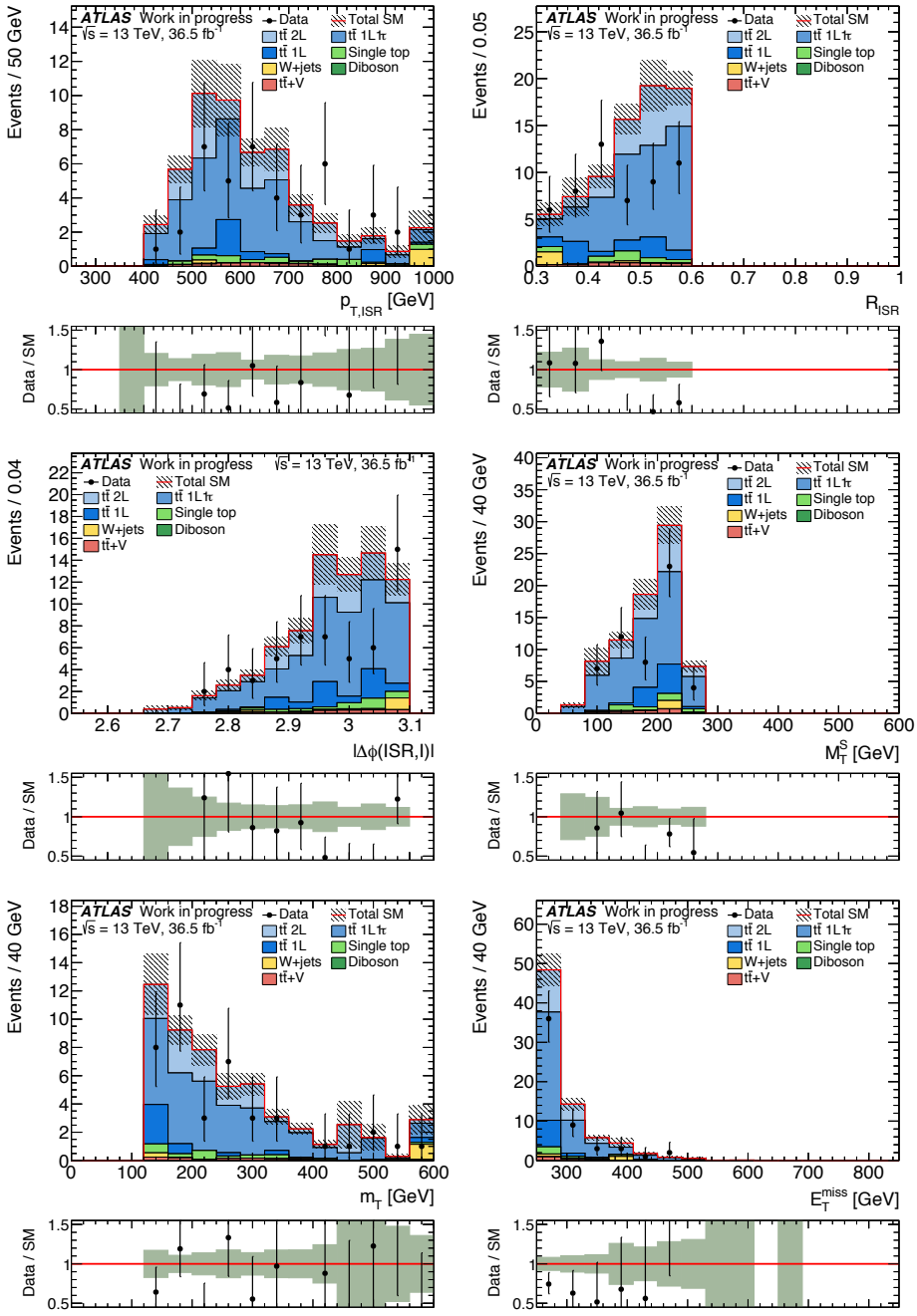


Figure 9.17: Comparison of data and simulation in the cut-and-count off-diagonal control region, before the fit to data.

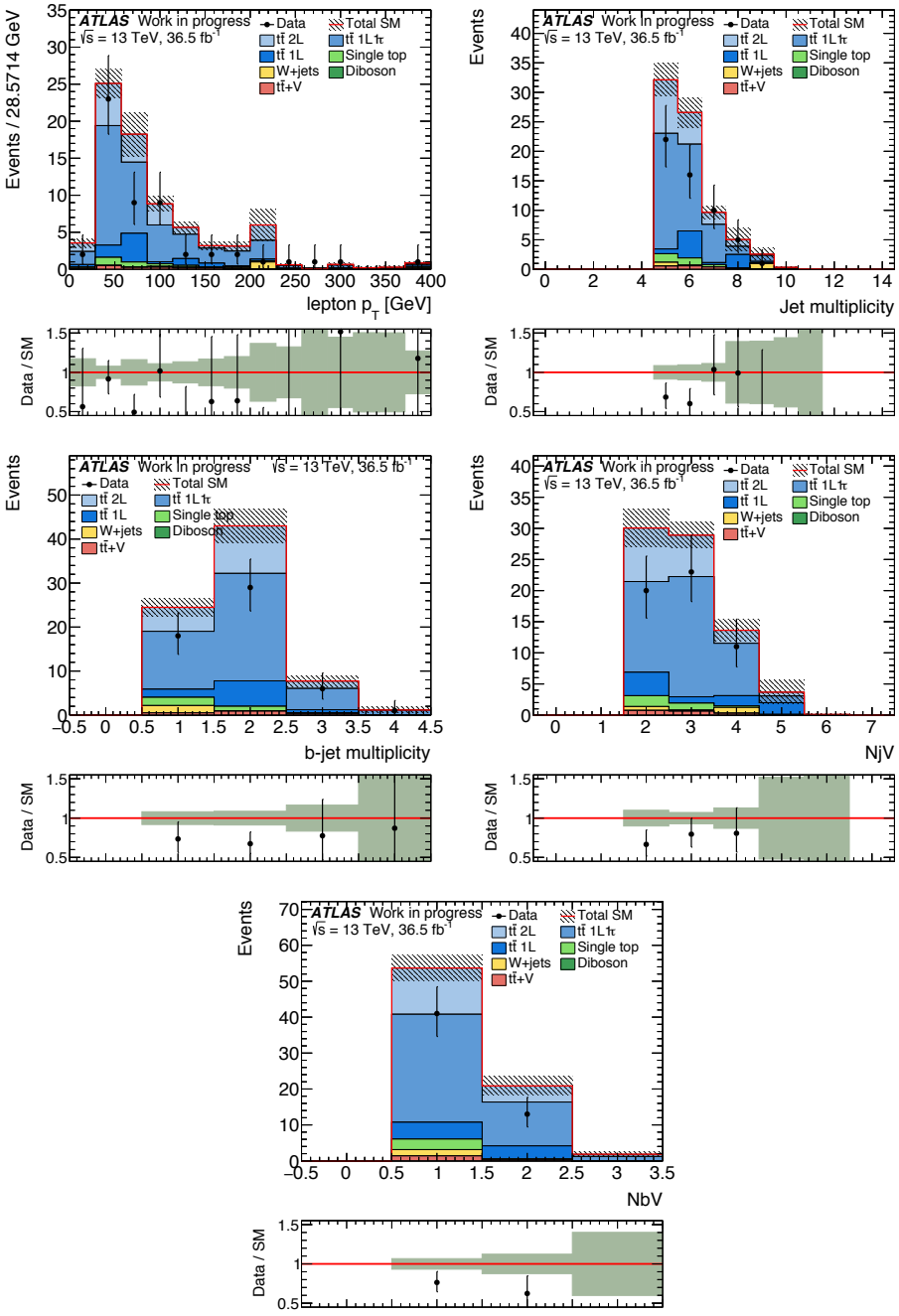


Figure 9.18: Comparison of data and simulation in the cut-and-count off-diagonal control region, before the fit to data.

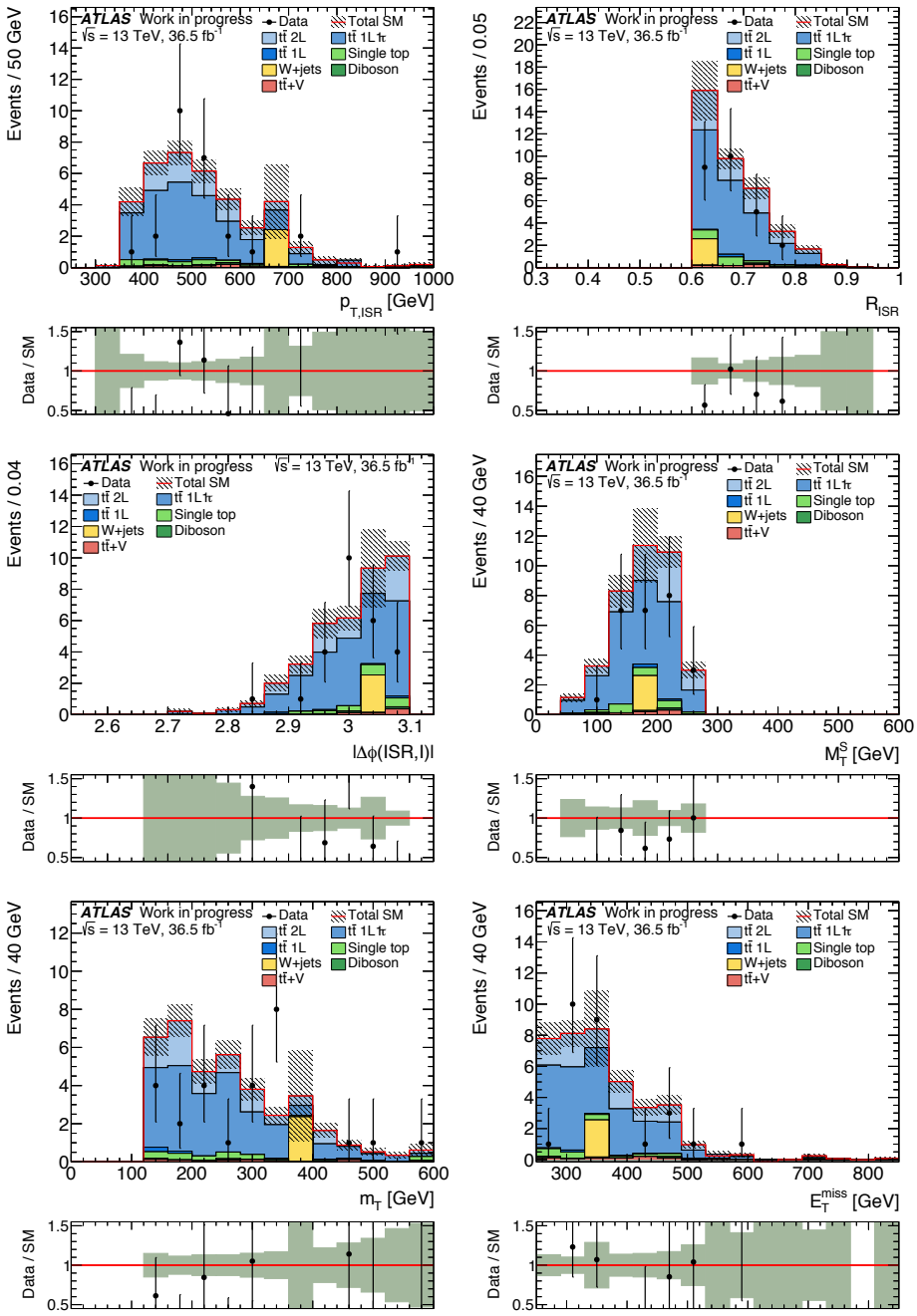


Figure 9.19: Comparison of data and simulation in the cut-and-count off-diagonal validation region, before the fit to data.

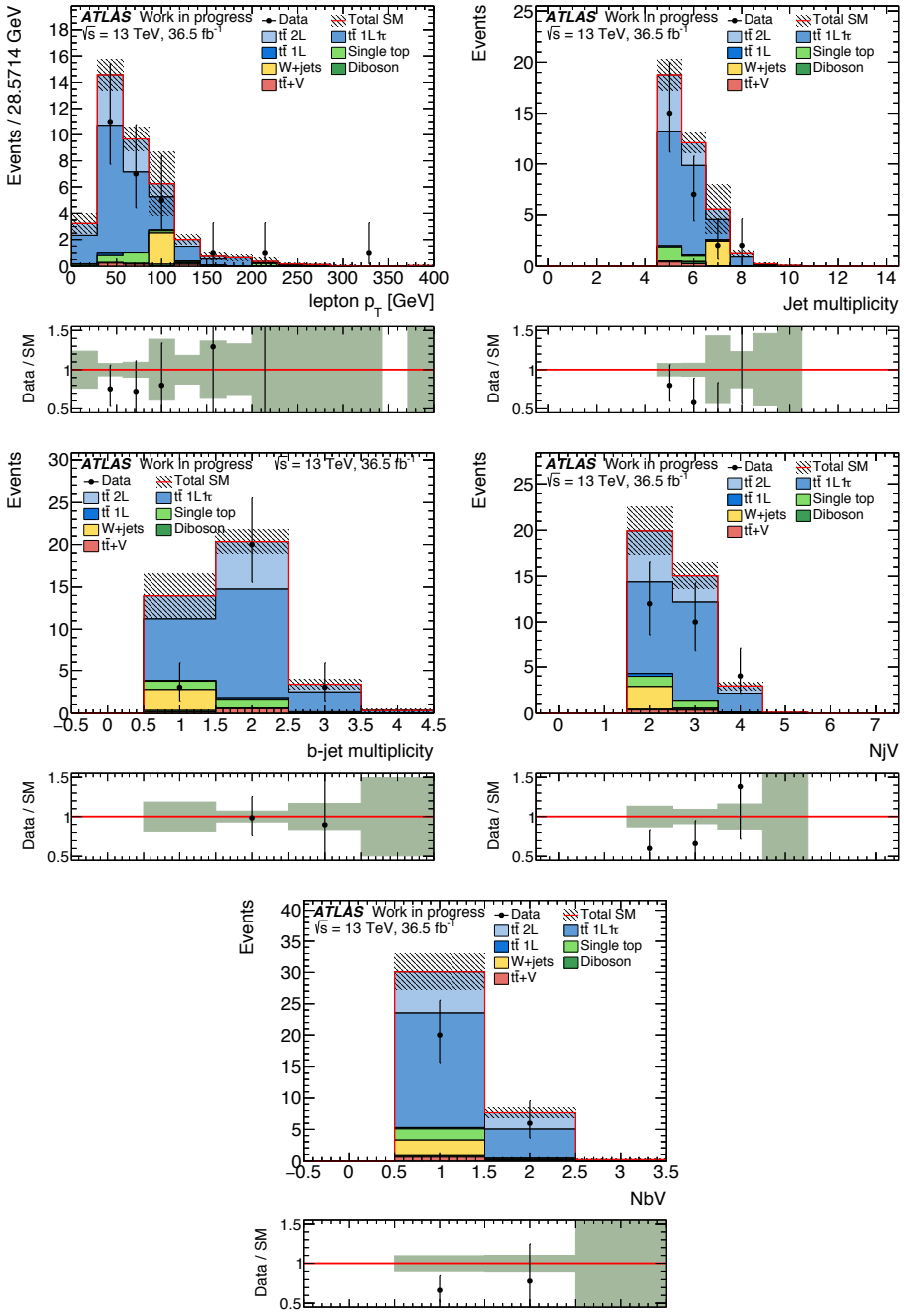


Figure 9.20: Comparison of data and simulation in the cut-and-count off-diagonal validation region, before the fit to data.

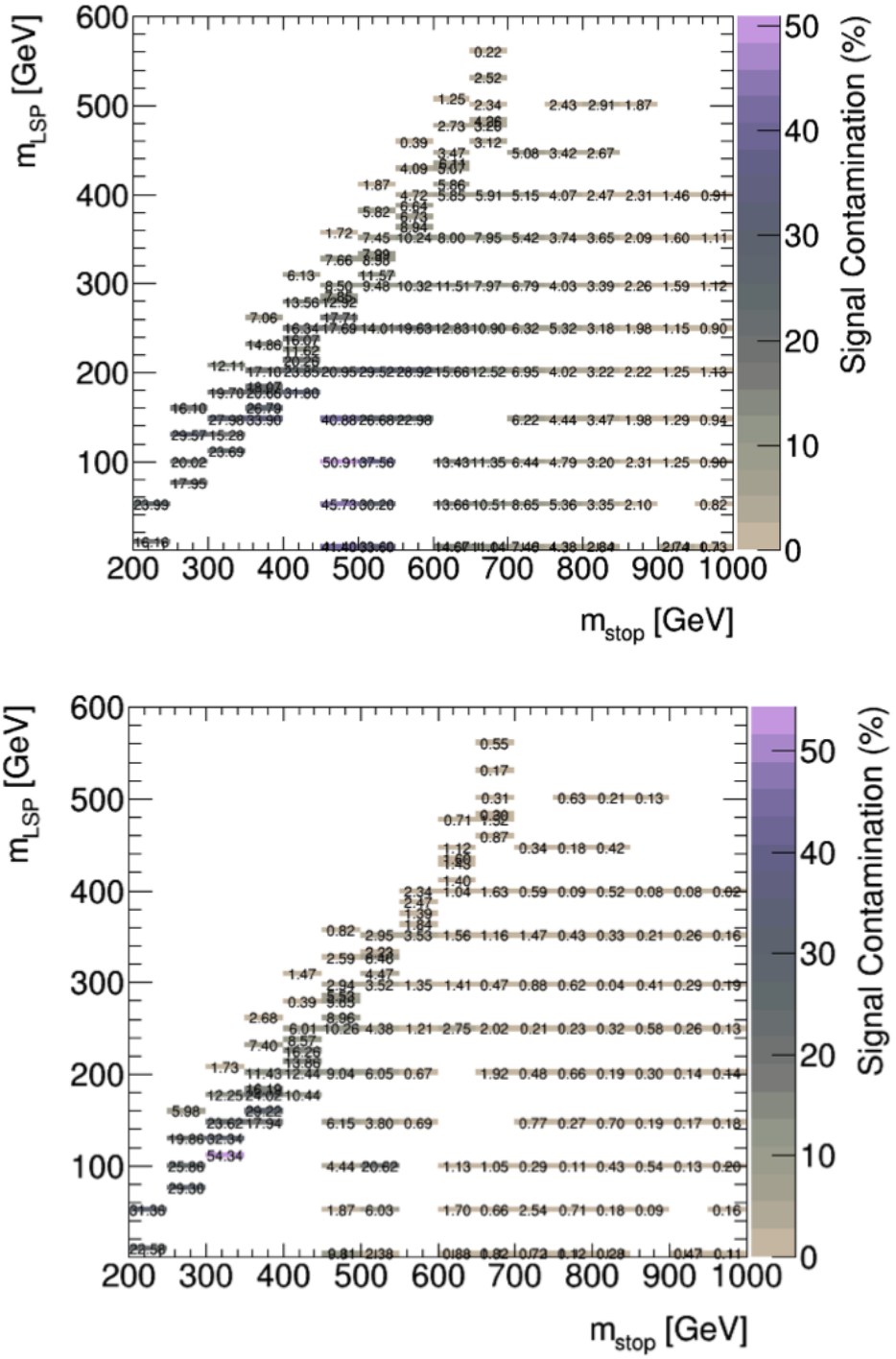


Figure 9.21: Signal contamination in the control region for the diagonal phase space (top) and off diagonal phase space (bottom).

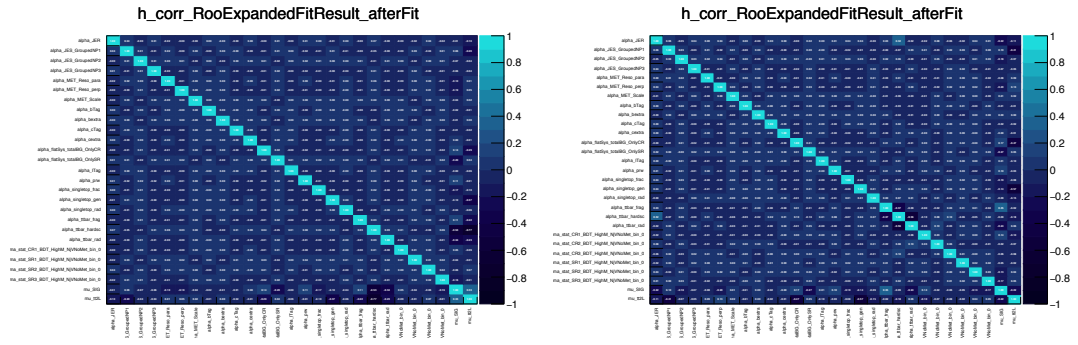


Figure 9.22: Correlation matrix for the high-mass compressed BDT using 1 CR bin (left) or 3 CR bins (right). The correlation between $t\bar{t}$ modeling systematics and the significance of the signal or $t\bar{t}$ background is greatly reduced when considering the three bin scenario.

9.4.2 BDT Estimation Strategy

The backgrounds in the BDT-based signal region are similarly estimated with control regions to normalize the dominant top backgrounds. However, for the BDT SR three CRs are used, each with an identical selection to the SRs, but with a different requirement on the BDT output score. Each of the three CRs corresponds to a given bin in BDT score, specifically [-1.0, -0.5], [-0.5, 0.0], and [0.0, 0.4] (recall that -1 is the score corresponding to the most background-like event.) These three bins are used to break correlations between signal and background. Figure 9.22 demonstrates this advantage over a single bin CR approach, which has correlations between μ parameters of up to 77%.

Table 9.9 shows the final binning of BDT score used for all regions in the analysis. The range [0.4,0.6] was chosen as a pseudo-validation region, to validate the normalization factors extracted from the CRs, but was vetoed in the final likelihood fit.

Region	BDT Score
SR1	[0.6, 0.7]
SR2	[0.7, 0.8]
SR3	[0.8, 1.0]
CR1	[-1.0, -0.5]
CR2	[-0.5, 0.0]
CR3	[0.0, 0.4]
VR	[0.4, 0.6]

Table 9.9: Full shape fit information for BDT analysis. Square brackets denote intervals in BDT score.

Though a formal validation using a VR was not included in the fit, the validity of the background prediction must still be verified. To do this, plots were made of all BDT input variables, comparing two selections: the full non-SR BDT range ([-1.0, 0.6]), and a slightly less inclusive selection closer to SR ([0.0, 0.6]). These plots are used to ensure good agreement of simulation and data in the CR bins, look for significant shape differences in variables across BDT score, and to validate the normalization factors across different regions of phase space. Figures 9.23 to 9.26 demonstrate these validation checks for all BDT training variables, showing good agreement.

This wide variety of cross checks on the background estimation and validation regions is conducive to a robust likelihood fit, which is instrumental in generating confidence in the final result. However, the likelihood fit also contains a term for nuisance parameters, which represent the systematic uncertainties on the yield estimates. Building and estimating these uncertainties is the next step in the analysis construction.

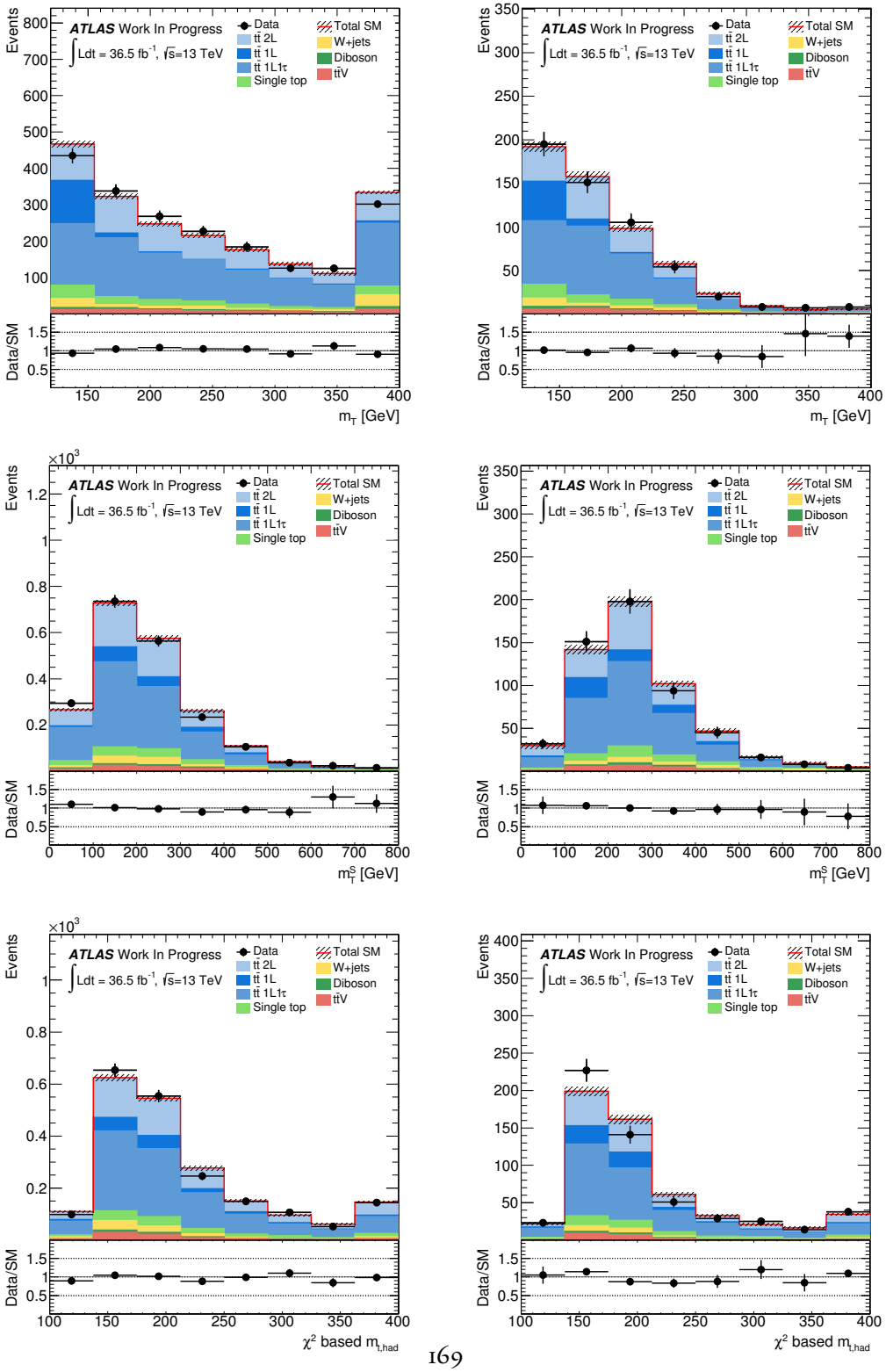


Figure 9.23: Comparison of the BDT score range [-1.0,0.6] (left) and [0.0, 0.6] (right) in the m_T, M_T^S, and $m_{top}\chi$ distributions, with normalization factors applied.

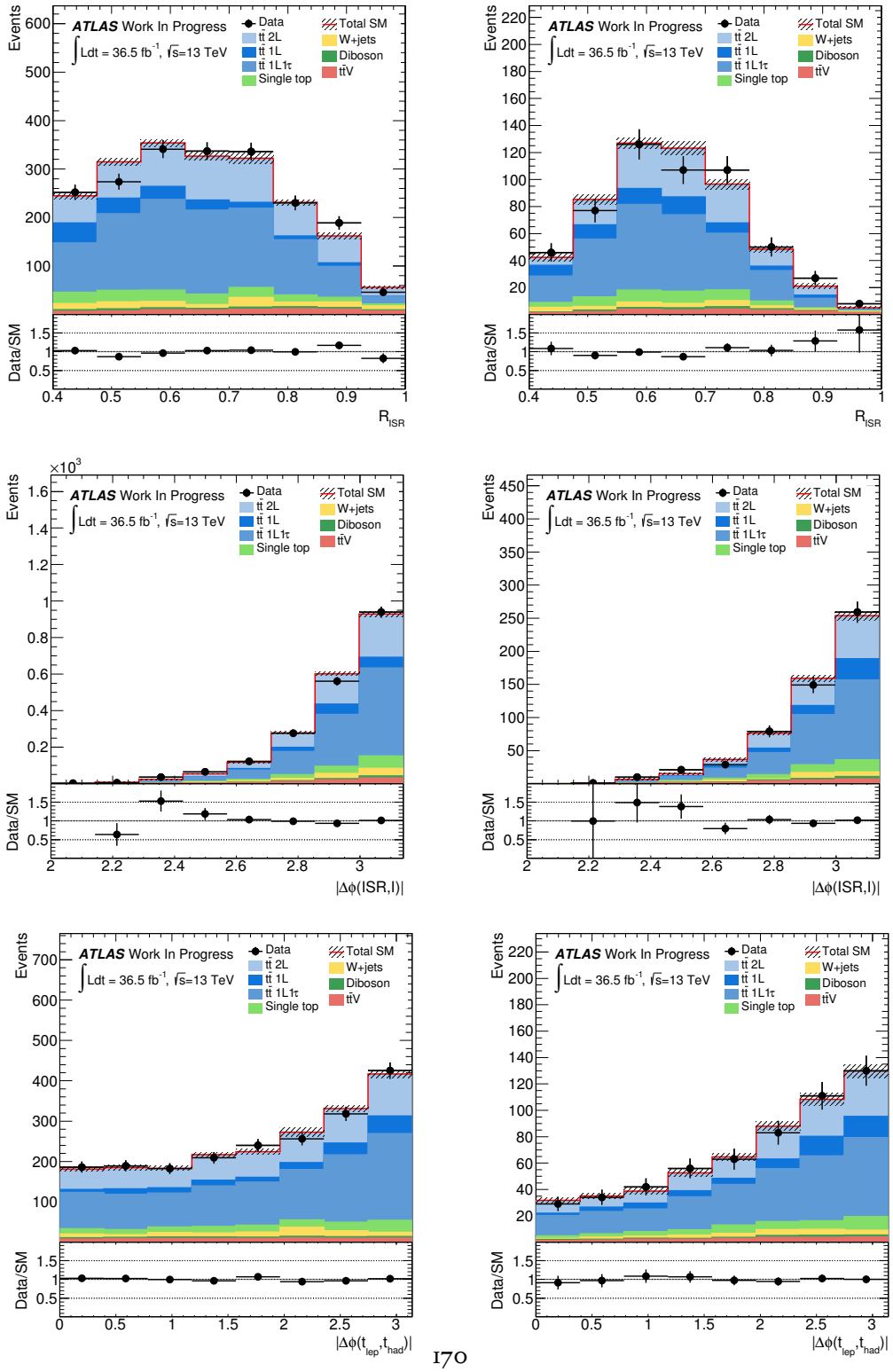


Figure 9.24: Comparison of the BDT score range [-1.0,0.6] (left) and [0.0, 0.6] (right) in the R_{ISR}, $\Delta\phi$(ISR,I), and $\Delta\phi(t_{lep}, t_{had})$ distributions, with normalization factors applied.

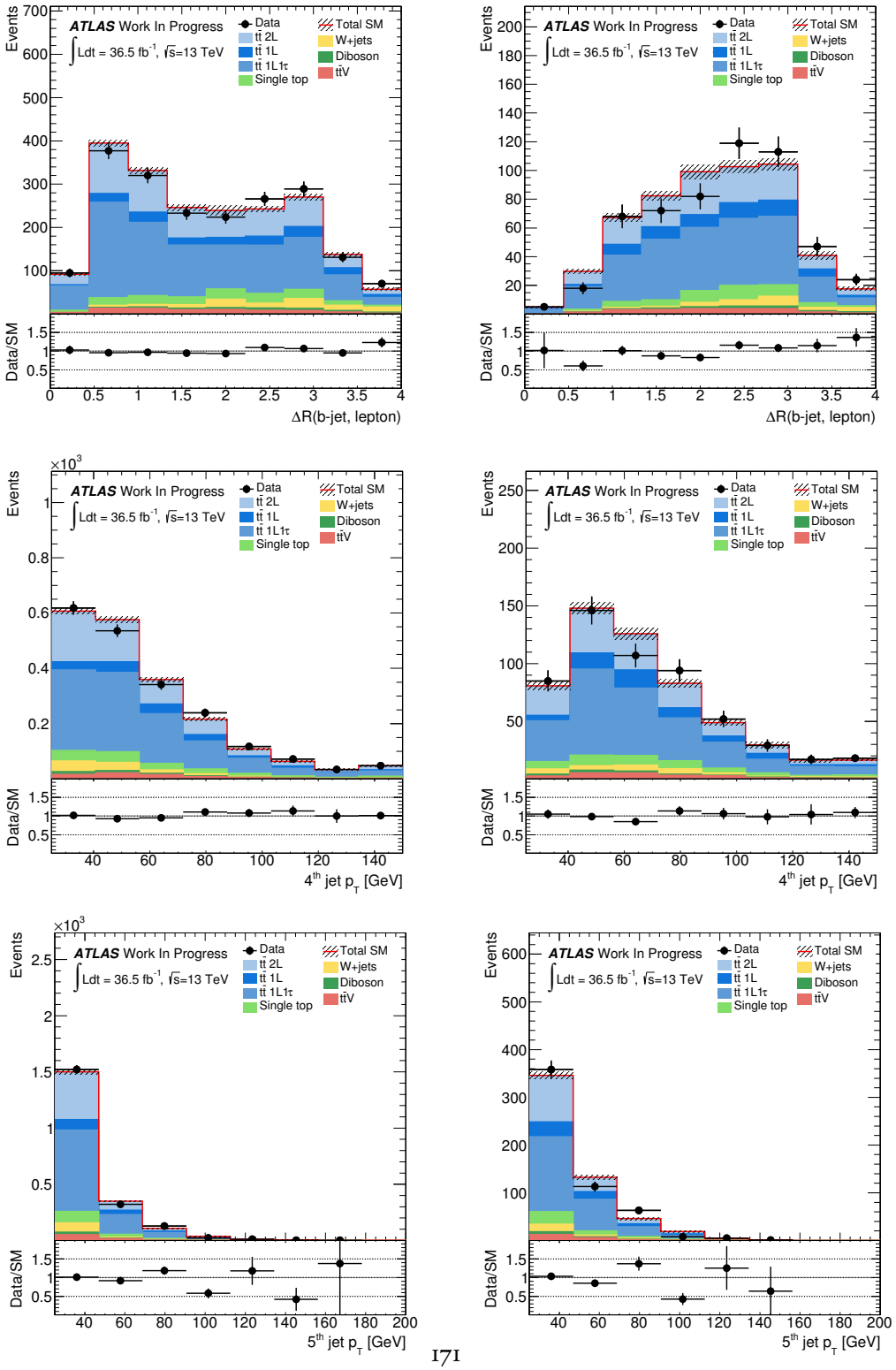


Figure 9.25: Comparison of the BDT score range [-1.0,0.6] (left) and [0.0, 0.6] (right) in the ΔR(b,ℓ), fourth jet p_T, and fifth jet p_T distributions, with normalization factors applied.

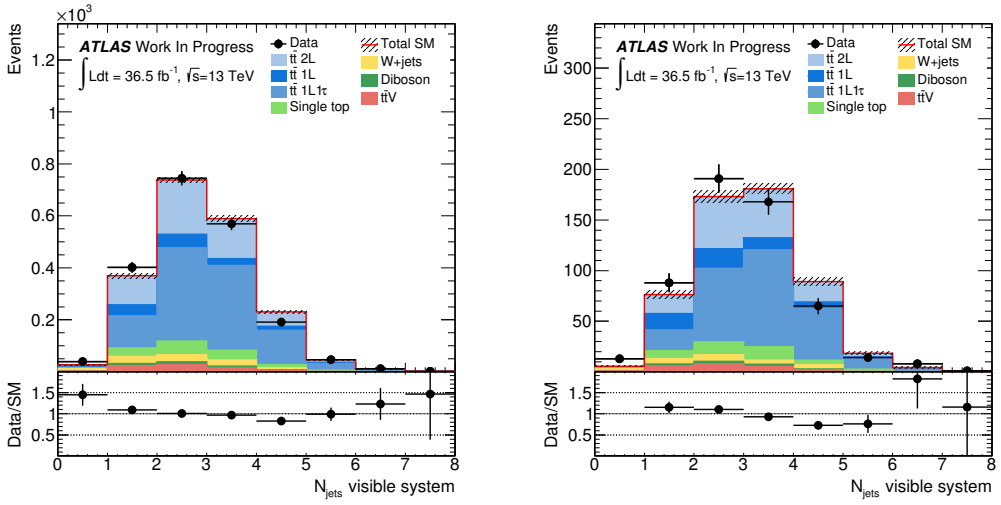


Figure 9.26: Comparison of the BDT score range [-1.0,0.6] (left) and [0.0, 0.6] (right) in the NjV distribution, with normalization factors applied.

9.5 Systematic Uncertainties

Systematic uncertainties refer to the level of confidence that can be ascribed to the event yields in the analysis regions. This level of knowledge must be estimated in size and accounted for in the final result. Systematics exist on both signal and background estimates, and fall into two primary categories. The first, experimental systematics, arise from features of the detector or event reconstruction. The second source is from uncertainty in theoretical predictions and modeling. Each systematic uncertainty is described by a nuisance parameter with a Gaussian constraint that is profiled in the likelihood fit.

9.5.1 Experimental

The source of experimental uncertainty are ranked in terms of size below, with dominant uncertainties listed first. These systematics are not specifically evaluated in the analysis; rather, numbers are calculated by the combined performance groups and applied in the final fit.

- Jet energy scale (JES) and jet energy resolution (JER). Binned in p_T and η, values are provided by the jet/E_T^{miss} combined performance group [112, 113], and estimated based on both Monte Carlo studies and *in situ* measurements. The uncertainty arises on knowledge of the scales used, and the size is 1.4-7% for JES and 1.5-7% for JER on total predicted background yield in SRs.
- B-tagging, specifically efficiency and mis-tag estimates [114, 115]. The uncertainty ranges from 1.6-13% on total predicted background yield in SRs.
- Modeling of lepton energy scales and resolutions (negligible in fit.)
- Reconstruction and identification efficiencies (negligible in fit).

- Trigger efficiencies (negligible in fit).
- Pileup and luminosity modeling (negligible in fit).

9.5.2 Theoretical

There are many potential sources of theoretical uncertainty on simulation, which vary from sample to sample depending on generator and other simulation settings. Systematics are evaluated by plotting variations in MC modeling methods overlaid with the nominal sample, and determining the size of the discrepancy attributable to that modeling choice. In the high-mass compressed analysis, the largest backgrounds are $t\bar{t}$ and single-top Wt, which are both generated by Powheg + Pythia6 (see Sec. 9.1). Therefore only systematics 1-5 in the list below are evaluated and discussed in further detail [98].

1. Hadronization and fragmentation: compare different hadronization choice (i.e. Herwig to Pythia6).
2. MC generator/hard scatter: compare choices of event generator (i.e. Powheg to Sherpa or MG5_aMC@NLO). Evaluated using truth samples to remove effects from hadronization.
3. Additional radiation: compare various amounts of parton shower radiation in the generator and hadronization method, i.e Powheg+Pythia6 samples with differing NLO radiation and modified factorization/renormalization scales.
4. Cross section: uncertainties on the $t\bar{t}$ cross section come from generator features, such as scale, PDF, or α_s. Since the $t\bar{t}$ background is normalized with a control region in this analysis, this uncertainty is negligible.
5. Interference: specifically with $t\bar{t}$, evaluated only for single-top backgrounds [98]. There are several diagrams that can contribute to the $t\bar{t}$ and Wt final states, and these interfere with one

	Systematic	$TF_{CR \to VR}$	$TF_{CR \to SR}$
Diagonal	Had/Frag	-5.2 $\pm$ 14.7	-29.8 $\pm$ 59.7
	Hard Scatter	10.9 $\pm$ 14.3	42.9 $\pm$ 38.5
	Radiation	5.7 $\pm$ 35.1	15.5 $\pm$ 7.9
Off Diagonal	Had/Frag	-18.8 $\pm$ 23.1	-11.7 $\pm$ 59.7
	Hard Scatter	2.5 $\pm$ 21.4	-17.0 $\pm$ 33.4
	Radiation	2.1 $\pm$ 8.6	-1.0 $\pm$ 6.5

Table 9.10: Theoretical systematic uncertainties on transfer factors for the $t\bar{t}$ background in the high-mass compressed analysis, for both diagonal and off-diagonal cut-and-count SRs. Hard scatter uncertainty is sum in quadrature of systematic and statistical errors.

another in such a way that the final yield can be different than expected. The interference systematic is evaluated at truth level.

6. Parton distribution function (PDF) variations: evaluated only for aMC@NLO generated samples.

7. Scale variations: renormalization, factorization, resummation of soft gluon emissions (QSF): evaluated for Sherpa generated samples only.

8. Matrix element matching scale (CKKW) variations in calculating the overlap between jets from matrix element and parton shower: evaluated for Sherpa generated samples only.

Tables 9.10 and 9.11 provides the theory systematics estimates for the diagonal and off-diagonal cut and count signal regions, and the uncertainties on those estimates, for the $t\bar{t}$ and single-top backgrounds respectively. Since the background yields are obtained from normalization in the CR, there is no uncertainty on the CR yield, only on the extrapolation between regions. For the cut-and-count regions this method of determining systematic uncertainties was sufficient, but a more in-depth procedure was needed for the BDT estimates.

	Systematic	$TF_{CR \to VR}$	$TF_{CR \to SR}$
Diagonal	Had/Frag	-23.6 $\pm$ 14.4	51.6 $\pm$ 15.9
	Radiation	7.3 $\pm$ 11.5	9.2 $\pm$ 10.3
	Interference	84.9 $\pm$ 1.8	85.5 $\pm$ 1.4
Off Diagonal	Had/Frag	-26.2 $\pm$ 36.7	-29.3 $\pm$ 31.0
	Radiation	16.6 $\pm$ 25.7.	-14.6 $\pm$ 22.7
	Interference	81.3 $\pm$ 0.6	90.0 $\pm$ 3.2

Table 9.11: Theoretical systematic uncertainties on transfer factors for the single-top background in the high-mass compressed analysis, for both diagonal and off-diagonal cut-and-count SRs.

9.5.3 BDT Smoothing Procedure

The BDT signal regions ultimately are very tight; this results in extremely limited MC statistics, in particular for the alternate samples used to estimate generator and hadronization/fragmentation systematics. To mitigate these issues, a smoothing procedure is implemented to estimate the theory uncertainties for the dominant $t\bar{t}$ and single-top Wt processes, based on smoothing with a Gaussian kernel.

For each input variable to the BDT (in addition to jet multiplicity and E_T^{miss}), the average value of the variable is found in each BDT bin listed in Table 9.9, using profile plots of each variable as a function of BDT score. Figures 9.27 and 9.28 show these average per-bin values for all twelve variables in the smoothing process. These values are used to assign an uncertainty on the extrapolation from the CR bins to each SR bin for a given variable.

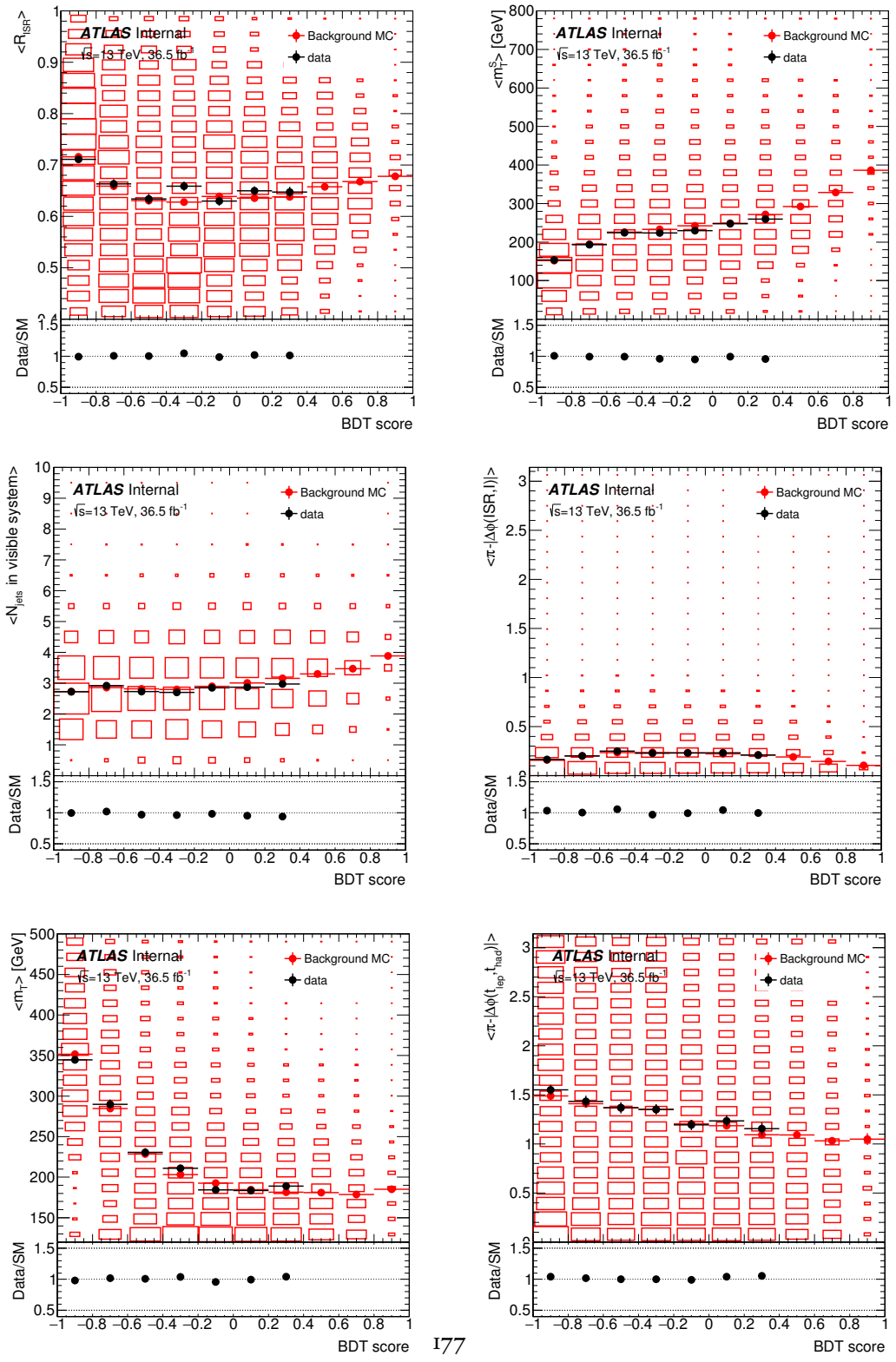


Figure 9.27: Average value of variables used in the smoothing procedure to estimate BDT systematic uncertainties.

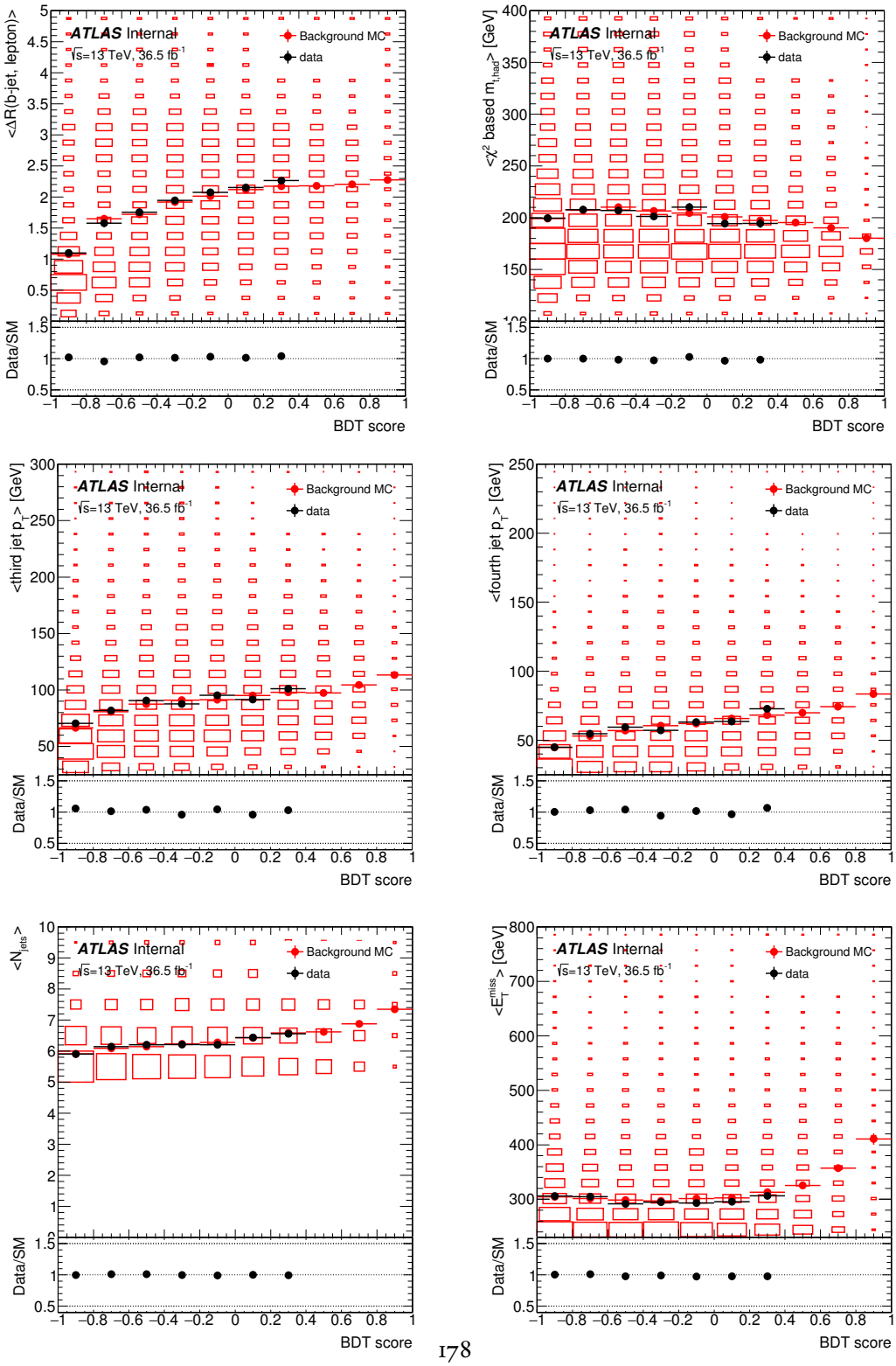


Figure 9.28: Average value of variables used in the smoothing procedure to estimate BDT systematic uncertainties.

Systematic	CR1	CR2	CR3	$TF_{CR\to SR1}$	$TF_{CR\to SR2}$	$TF_{CR\to SR3}$
Had/Frag	-3%	1%	3%	9%	17%	20%
Hard Scatter	1%	-1%	2%	9%	20%	21%
Radiation	-4%	3%	1 %	6%	9%	18%

Table 9.12: Theoretical systematic uncertainties on the relative fraction of events in each CR bin, and on transfer factors for the CR to SR extrapolation, for the $t\bar{t}$ background in the high-mass compressed BDT-based CRs and SRs.

The final uncertainty estimate for the extrapolation is found by summing all the per-variable values in quadrature. This procedure minimizes the effect of statistical fluctuations by effectively merging statistically insignificant bins and smoothing the result with a Gaussian kernel. The obtained systematic uncertainties for the dominant $t\bar{t}$ background can be found in Table 9.12, given as the relative fraction of events in each CR bin, as well as the extrapolation from the CR to each SR bin.

9.6 Results

The first step in obtaining analysis results is to unblind the signal regions and determine the number of observed events in each SR. The agreement of this yield with the SM background hypothesis is quantified via a profile-likelihood fit, giving a p-value for each SR. If no significant excess is observed, an exclusion limit is calculated using the CLs prescription. All of the statistical methods used are discussed in detail in Chapter 8.

The first fit performed is the background-only fit, which constrains the normalizations of each background in its dedicated CR. The fit procedure then diverges for the two sub-analyses discussed here: the cut-and-count regions are used in a discovery fit, while the BDT signal and control region bins are used in an exclusion fit.

9.6.1 Unblinded Yields & Background-Only Fits

Once the signal regions are unblinded, the observed events can be compared to the background prediction, which is scaled using a normalization factor extracted from the unblinded CRs. This is called the background-only fit. The predicted number of SM background events, the expectation from the background-only fit, and the number of events observed in the cut-and-count signal and control regions can be found in Table 9.13. The background estimation is broken down by SM process. In all SRs, the agreement between data and the simulation is good, with no significant excess of data over fitted background expectation.

	Diagonal CR	Off-Diagonal CR	Diagonal SR	Off-Diagonal SR
Observed total background	138	57	6	12
Fitted background	136.66 ± 11.42	55.36 ± 6.90	7.43 ± 1.63	13.89 ± 2.57
Fitted single top	5.89 ± 1.05	2.89 ± 0.95	0.54 ± 0.21	1.84 ± 0.34
Fitted ttV	5.25 ± 0.73	1.47 ± 0.20	0.23 ± 0.08	0.96 ± 0.17
Fitted diboson	1.15 ± 0.31	$0.31^{0.34}_{-0.31}$	0.07 ± 0.02	0.31 ± 0.09
Fitted W+jets	3.62 ± 1.71	1.41 ± 1.19	0.09 ± 0.08	0.43 ± 0.09
Fitted $t\bar{t}$	120.75 ± 11.75	49.27 ± 7.04	6.51 ± 0.87	10.35 ± 1.72
MC expected	125.01	67.99	7.93	17.83
MC single top	5.95	2.84	0.56	1.88
MC ttV	5.30	1.48	0.23	0.96
MC diboson	1.14	0.29	0.07	0.31
MC W+jets	3.61	1.32	0.10	0.43
MC $t\bar{t}$	109.01	62.06	5.97	13.24

Table 9.13: Expected (pre- and post-fit) and observed event yields in the cut-and-count diagonal and off-diagonal regions.

The shape fit over the full BDT distribution utilizes the bins listed in Table 9.9, where the region [0.4, 0.6] in BDT score is vetoed. The multiple bins for both CRs and SRs allow for the $t\bar{t}$ normalization and determination of best fit signal strength to occur simultaneously. Normalization factors for all backgrounds, including semileptonic and dileptonic $t\bar{t}$, are in good agreement with 1. The expected and observed event yields in the BDT CR bins can be found in Table 9.14, both before and after the background-only fit. Table 9.15 shows the same pre- and post-fit yields in the SR bins. As with the cut-and-count regions, no significant excess is observed in any of the three BDT SR bins.

The unblinded post-fit distribution of data and background estimation for the full BDT score distribution can be seen in Figure 9.29. The p-value (p_0) from the profile-likelihood test for the highest SR BDT bin, the one that is most expected to contain the signal, is 0.44. This corresponds to a σ value of 0.14. Both the expected and observed 95% CL upper limits on the number of beyond

	CR1	CR2	CR3
Observed total background	762	694	399
Fitted background	763.95 ± 26.54	678.92 ± 21.82	408.42 ± 16.45
Fitted single top	54.85 ± 33.92	54.84 ± 35.70	32.22 ± 19.67
Fitted ttV	28.65 ± 8.83	25.62 ± 7.69	16.93 ± 5.29
Fitted diboson	11.34 ± 3.81	11.75 ± 4.00	7.15 ± 2.58
Fitted W+jets	44.24 ± 34.81	44.73 ± 23.89	16.74 ± 12.91
Fitted $t\bar{t}$	624.86 ± 58.35	541.96 ± 45.72	335.39 ± 31.12
MC expected	745.64	626.93	396.04
MC single top	49.58	49.71	29.50
MC ttV	27.72	24.79	16.62
MC diboson	10.77	11.15	6.96
MC W+jets	35.84	38.48	17.81
MC $t\bar{t}$	621.73	502.80	325.16

Table 9.14: Expected and observed events in the control regions of the BDT shape fit.

	SR1	SR2	SR3
Observed total background	40	41	19
Fitted background	47.26 ± 3.62	37.52 ± 3.48	18.34 ± 2.17
Fitted single top	3.36 ± 2.20	3.30 ± 1.64	1.54 ± 1.15
Fitted ttV	2.31 ± 1.27	1.43 ± 0.80	0.68 ± 0.37
Fitted diboson	0.94 ± 0.53	0.45 ± 0.27	0.21 ± 0.11
Fitted Wjets	1.59 ± 0.97	1.15 ± 0.65	0.70 ± 0.56
Fitted $t\bar{t}$	39.06 ± 4.62	31.18 ± 4.21	15.21 ± 2.41
MC expected	43.88	33.02	15.94
MC single top	3.11	2.97	1.48
MC ttV	2.42	1.46	0.70
MC diboson	1.03	0.47	0.22
MC W+jets	1.58	0.99	0.59
MC $t\bar{t}$	35.74	27.14	12.95

Table 9.15: Expected and observed events in the signal regions of the BDT shape fit.

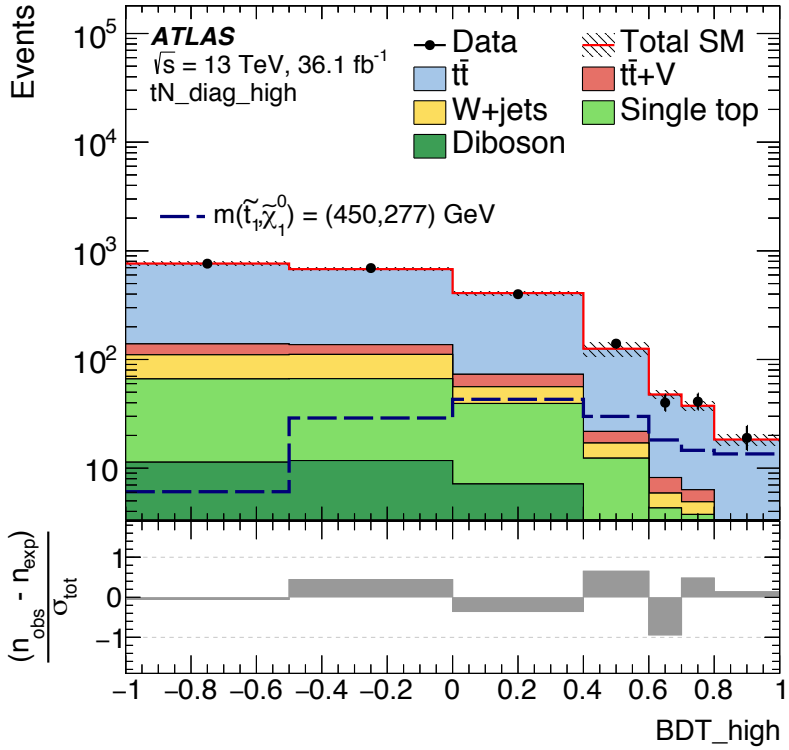


Figure 9.29: Distributions of BDT score for the tN diag high signal regions. The SM background predictions are obtained using the background-only fit configuration, and the hatched area around the total SM background prediction includes all uncertainties. [38].

the Standard Model events is 11 for this bin. Cumulatively, these metrics indicate that there is no significant evidence for the presence of new physics in the data.

9.6.2 Exclusion Limits

Given that no significant excess is observed in either cut-and-count or BDT-based signal regions, model-dependent exclusion limits can be set at at 95% confidence using the stop pair production simplified model. Exclusion contours are drawn in the $(m_{\tilde{t}}, m_{\tilde{\chi}_1^0})$ plane by interpolating the CLs val-

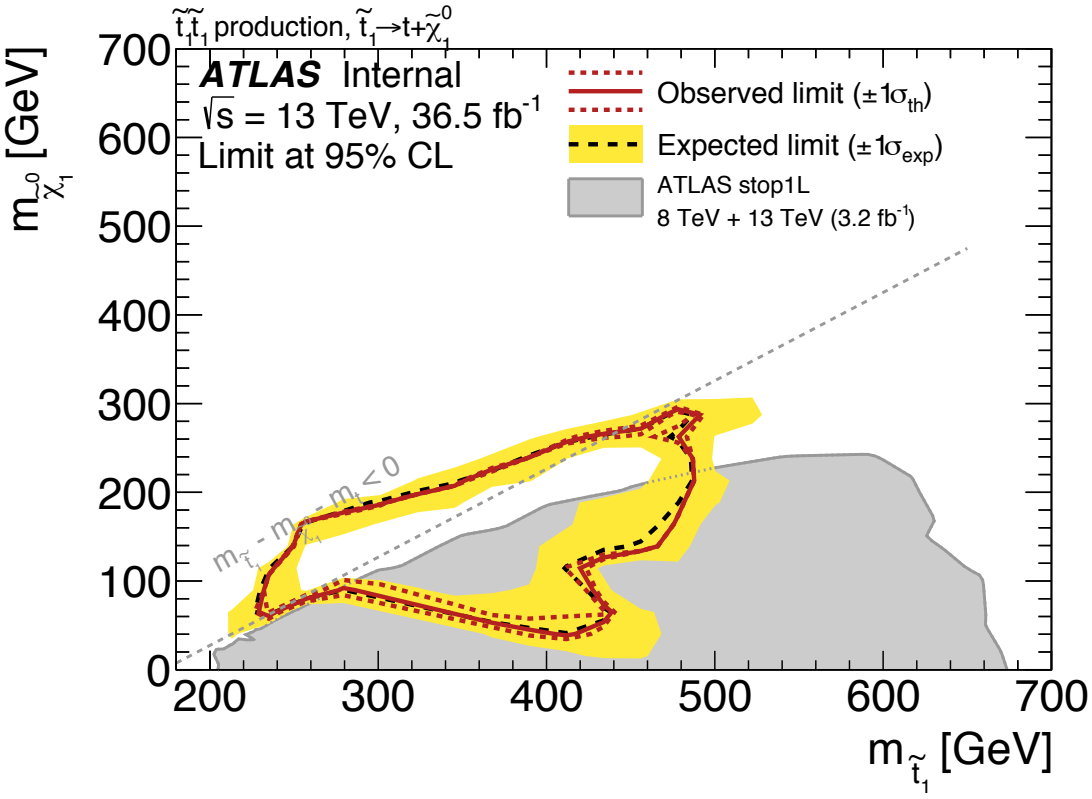


Figure 9.30: Expected and observed exclusion contours for the high-mass compressed BDT signal regions. All detector systematics and $t\bar{t}$ systematic uncertainties are included, with flat 30% uncertainties assumed for all other background sources.

ues obtained by the fit for each signal point. Figure 9.30 shows the expected ($\pm\sigma_{exp}$) and observed ($\pm\sigma_{th}$)contours from the high-mass compressed BDT analysis. The previous best exclusion from the ATLAS stop search using 3.2 fb^{-1} is overlaid in gray, revealing the large increase in excluded mass range along the diagonal.

Figure 9.31 shows the combined exclusion for all of the $\tilde{t} \to t\tilde{\chi}_1^0$ signal regions, covering the pure bino LSP scenario in the stop 1L analysis. For a massless $\tilde{\chi}_1^0$, and assuming a 100% branching ratio of the $\tilde{t}$ to a top and $\tilde{\chi}_1^0$, a stop quark with a mass below 940 GeV is excluded at 95% confidence.

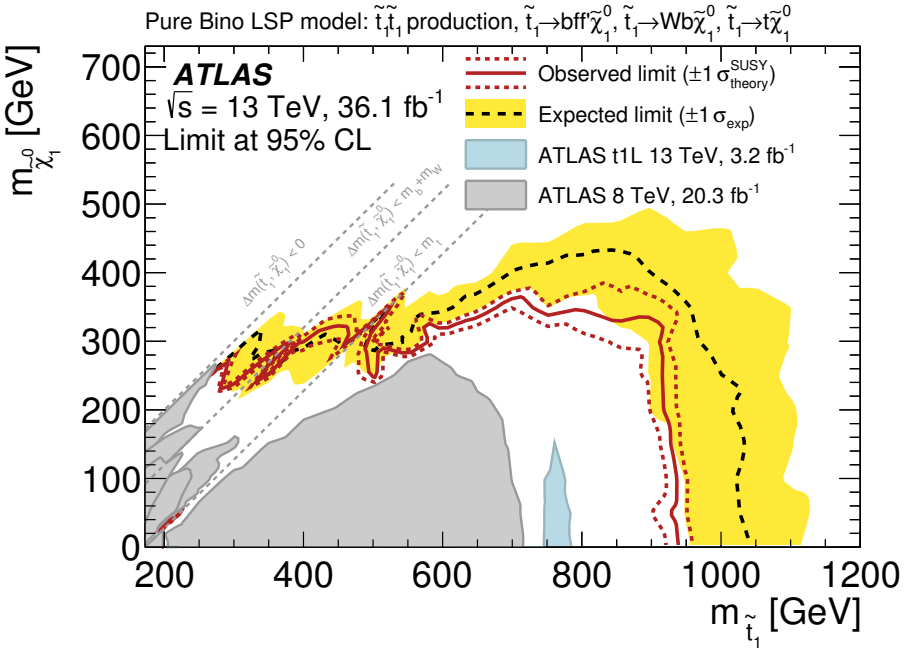


Figure 9.31: Expected combined exclusion contour for the $\tilde{t} \to t\tilde{\chi}_1^0$ signal regions.

For each signal point in the grid, the lowest expected CLs value (best exclusion) is chosen across all signal regions, which includes regions off the diagonal area of phase space, and those targeting lower stop masses. Figure 9.32 shows the results of this scan, combining information from seven bino LSP SRs, covering the two, three, and four body stop decays. Each marker on the grid indicates which signal region in the analysis is responsible for sensitivity for that point. Such a breakdown highlights that the high-mass compressed BDT region, shown in blue diamond markers, is driving sensitivity primarily for points in the diagonal area of phase space. This is expected from both the physics motivation of the region and the optimization strategy, and is consistent with the single region exclusion shown in Figure 9.30.

The results of this stop search in the 1 lepton final state are combined with other concurrent

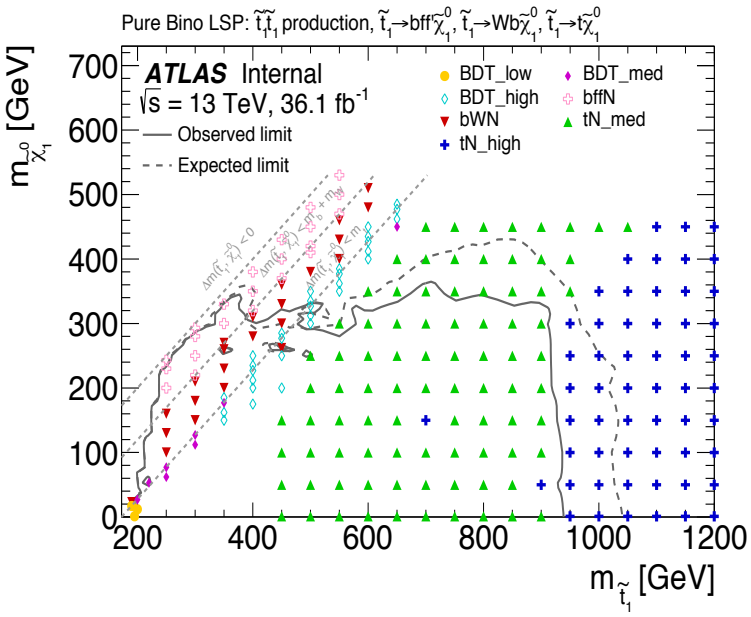


Figure 9.32: Exclusion curve for the stop1L analysis, broken down by dominant signal region. The high-mass compressed BDT corresponds to the light blue diamond markers, which show that this SR is primarily responsible for sensitivity on the $\tilde{t} \to t\tilde{\chi}_1^0$ diagonal.

stop pair production searches at ATLAS, decaying to different final states and covering a variety of mass spectra and kinematic scenarios. Figure 9.33 shows the combined total exclusion for stop searches at ATLAS as of May 2018, representing the full exclusion for stop masses at the end of Run II. Comparison to Figure 3.2 demonstrates the success of the dedicated diagonal signal regions and the Recursive Jigsaw Reconstruction technique for compressed signal points. Specifically, two analyses contribute strongly on the diagonal: the stop 1L analysis described here, and the 0-lepton final state version of the search (referred to as "stop 0L"). This 0L search similarly built a dedicated compressed SR in Run II, and utilized the RJR variables to do so [116]. The confluence of these two successful analyses, working with different final states but the same phase space and methodology, further confirms the generalizable utility of the RJ technique for compressed SUSY searches.

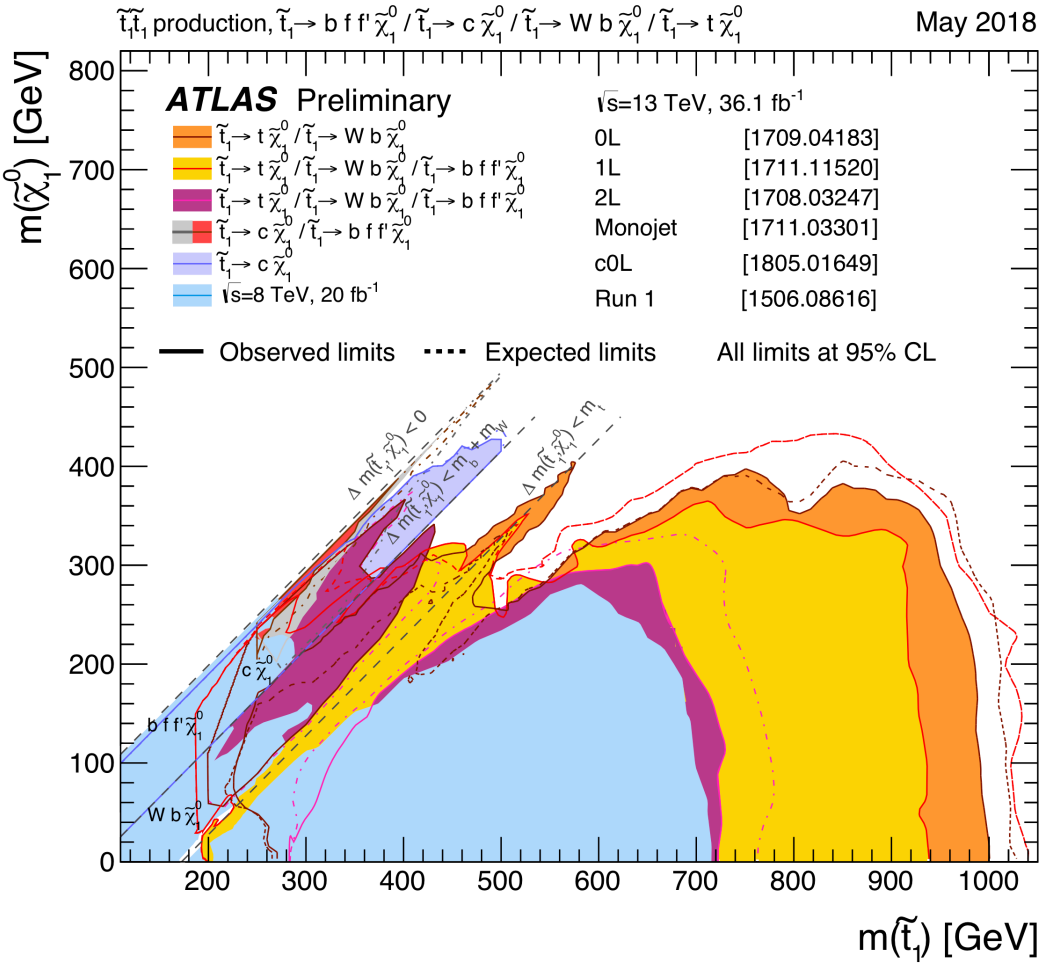


Figure 9.33: Combined exclusion curve for all stop analyses at ATLAS, as a function of $\tilde{t}_1$ and $\tilde{\chi}_1^0$ masses [51].

10

For Electroweak SUSY

Electroweak SUSY production is at the core of naturalness, and searches for these sparticles are especially exciting given their expected light masses. However, this theoretical excitement is countered in practice by the significant difficulties of such searches at the LHC, in large part due to their low expected cross sections (see Figure 2.4). In spite of this, a significant component of the electroweakino search program at ATLAS relies on direct pair production of the lightest chargino and lightest two

neutralinos, which are the three sparticles most constrained in natural models.

The mixing of electroweak eigenstates into charginos and neutralinos was discussed in Chapter 2. In this search, several simplified models are used to impose valuable simplifications: each electroweakino decays with 100% branching fraction to the SM weak boson of the same charge, and only the mass parameters relevant to the electroweakino spectrum are considered. The focus here will be on the naturalness scenario, where $\mu \ll$ M1, M2 and the LSP is dominantly higgsino, which gains momentum via boost from an initial state radiation jet or jets.

Recall that the natural mass parameter hierarchy yields a compressed mass spectrum, similar to that of the stop search described in the previous chapter. This restricts the phase space to a scenario where the mass splitting between $\widetilde{\chi}_2^0$ and $\widetilde{\chi}_1^0$ (or $\widetilde{\chi}_1^\pm$ and $\widetilde{\chi}_1^0$) is sufficiently small to force the $W^\pm$ or Z^0 boson off its mass shell. All of the characteristics of a compressed electroweakino decay as discussed in Section 3.2 apply: the quarks from the $W^\pm$ are too soft to be reconstructed, the leptons from the Z^0 have a small amount of p_T, and the E_T^{miss} in the event is attributable to the boosted LSPs. Feynman diagrams showing these processes can be seen in Figures 10.1 and 10.2. The final state of all decays is E_T^{miss}, two soft opposite sign same flavor leptons, and at least one jet from initial state radiation.

Three orthogonal regions target this scenario: high-E_T^{miss}, low-E_T^{miss}, and one lepton + track (in which the subleading lepton is too soft to be reconstructed). While this treatment will only discuss the high-E_T^{miss} regions, all three are combined in the final higgsino results, therefore low-E_T^{miss} and 1L+track analysis material can be found in Appendix B*. The small production cross

*Several other subanalyses are performed in this result, including a pair-produced slepton model decaying

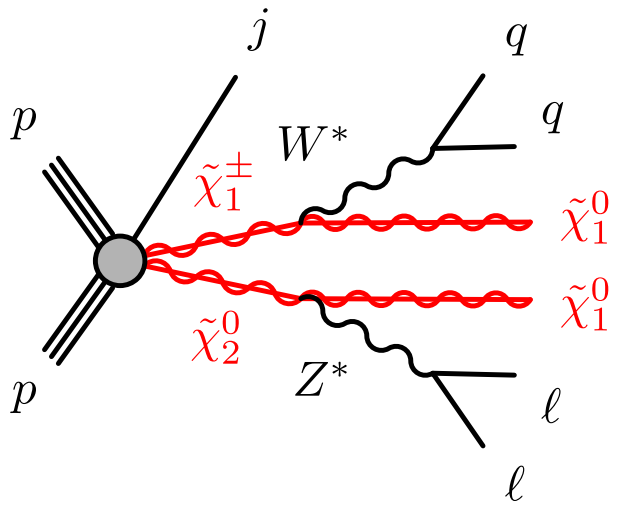


Figure 10.1: Diagrams illustrating electroweakino simplified model $\widetilde{\chi}_2^0\widetilde{\chi}_1^+$ pair production in association with a jet radiated from the initial state (labeled j) [48].

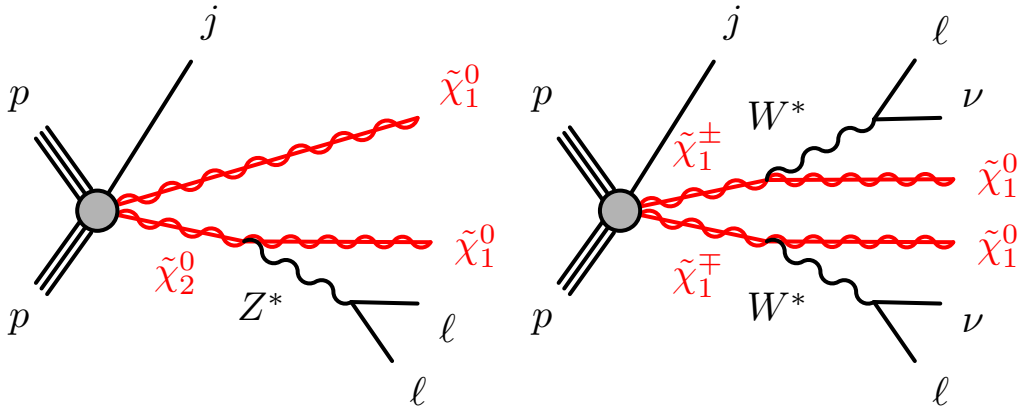


Figure 10.2: Other electroweakino pair production modes considered in the analysis, specifically $\widetilde{\chi}_2^0\widetilde{\chi}_1^0$ and $\widetilde{\chi}_1^+\widetilde{\chi}_1^-$ [48].

sections, extremely soft final state objects, and low amount of missing energy all contribute to the difficulty of such a search, and motivate careful analysis structure and selections.

This chapter describes the setup, procedures, and results of the full Run II high-E_T^{miss} direct higgsino search. Section 10.1 and Section 10.2 give technical details, specifically on the data/MC samples and reconstructed objects used, respectively. Section 10.3 describes the optimization of the primary higgsino signal regions and the addition of the Recursive Jigsaw Reconstruction variables. Section 10.4 gives information on the background estimation, including control and validation region definitions, and a description of the data-driven fake factor method to estimate the dominant fake lepton background. Systematic uncertainties are discussed in Section 10.5. Finally, results of the search are given in Section 10.6, and interpreted in the context of electroweak SUSY mass exclusions.

10.1 Data/MC Samples

This search is performed using 140.45 fb^{-1} of pp collision data at $\sqrt{s}$ = 13 TeV collected by the ATLAS detector throughout Run II of the LHC (see Chapter 5 for more details). Events were primarily collected using the lowest unprescaled E_T^{miss} trigger[†], and required to pass all Good Run Lists requirements. Candidate events must further have at least one pp interaction vertex with a minimum of two associated tracks, each with $p_T > 400$ MeV.

to the same final state of two soft leptons + E_T^{miss}; a VBF-assisted EWKino signal; a wino NLSP/bino LSP interpretation; and an NUHM2 interpretation [117]. None of these will be described in the following text as they are less connected to the naturalness scenario.

[†]Other searches for electroweak SUSY at ATLAS use single lepton triggers, functional in the scenario where the $W^{\pm}$ or Z^0 is on-shell. The lepton p_T thresholds of these triggers severely restrict the phase space of interest in the compressed case, and thus are not used.

The higgsino LSP signal samples are generated at leading order with MG5_aMC@NLO, decayed with `MadSpin`, and showered with `PYTHIA 8`. To account for the required ISR boost, each process is generated with up to two additional parton emissions in the matrix element, with a minimum required p_T of 50 and 10 GeV respectively. Signals are then filtered to require two leptons with p_T > 2 GeV and E_T^{miss} > 75 GeV. The matrix element must be matched to a parton shower, which was performed with the CKKW-L scheme [118] with a merging scale of 15 GeV.

For each signal as defined by the mass splitting, four production modes were produced: $pp \rightarrow \widetilde{\chi}_2^0\widetilde{\chi}_1^+$, $pp \rightarrow \widetilde{\chi}_2^0\widetilde{\chi}_1^-$, $pp \rightarrow \widetilde{\chi}_2^0\widetilde{\chi}_1^0$, and $pp \rightarrow \widetilde{\chi}_1^+\widetilde{\chi}_1^-$. The branching ratio of $\widetilde{\chi}_2^0 \rightarrow Z^{0*}\widetilde{\chi}_1^0$ and $\widetilde{\chi}_2^\pm \rightarrow W^{\pm *}\widetilde{\chi}_1^0$ is assumed to be 100%. However, the branching ratio of $Z^{0*} \rightarrow \ell\ell$ or $W^{\pm *} \rightarrow \ell\nu$ was specifically computed to account for the masses of the b quark and τ lepton, in order to accurately reflect the smaller phase space available for decay into heavier particles. The resulting branching fractions vary from 0.5% to 5.3% for $Z^{0*} \rightarrow \ell\ell$ depending on flavor, and 11% to 20% for $W^{\pm *} \rightarrow \ell\nu$.

The mass splitting of the signal Δm is defined to be the difference between the masses of the $\widetilde{\chi}_2^0$ and $\widetilde{\chi}_1^0$, with the chargino mass set to be halfway between neutralino masses as a convention. Signal cross sections for this simplified model are calculated using `RESUMMINO` at NLL+NLO precision. Though mass splittings above the MeV scale are only achieved via weak eigenstate mixing, the calculated cross sections assume pure Higgsino states for all mass combinations. All signal samples in the analysis use `ATLFAST2` detector simulation [97].

Three different campaigns of background simulation were used to appropriately model differences in run conditions across data-taking years. Unless otherwise specified, all samples with pro-

cessed with a full simulation of the ATLAS detector [97] using GEANT4 [119]. Processes involving single or multiple $W^{\pm}$ or Z^0 bosons plus jets [101, 102] were modeled with Sherpa [103], with dedicated extensions for low statistic phase space areas of importance in the analysis. The nominal $t\bar{t}$ and single top samples [104] (excluding tZ), as well as single Higgs production processes, were generated with `POWHEG` [99] interfaced to `PYTHIA8` [106] for parton showering/hadronization. tZ production used `MadGraph5` [105] for the matrix element and `PYTHIA6` [100] for showering. Additional soft QCD interactions were generated by `PYTHIA8` to simulate the effects of pileup.

10.2 Object Requirements

Three primary classes of event features are relevant for this analysis: leptons, jets, and missing energy. Since processes with fake leptons are a dominant background for the analysis, the selection and reconstruction of the two soft leptons is of particularly fundamental importance. The only expected jets in the final state are from the ISR boost, but the details of the selected jets are also a key feature in determining the E_T^{miss} resolution. In this section, details specific to the analysis are discussed for all three categories.

10.2.1 Leptons

The reducible fake lepton background is estimated using a data-driven fake factor method (described in more detail in Section 10.4). Special care must be taken to avoid double counting in this scenario, given that certain SM processes that produce one prompt lepton and one non-prompt lepton may be predicted by both the fake factor method and MC simulation. A solution to this problem is to

subtract the prompt lepton background as predicted by MC. This prediction requires truth matching leptons utilizing the `MCTruthClassifier` [120], which classifies truth particles according to their origin (prompt, non-isolated from meson decays, conversions, and other background sources.) The truth matching decision is then incorporated into the signal, control, and validation region definitions.

Final state leptons can be electrons or muons, and both baseline and signal leptons are defined for use, where signal leptons satisfy more stringent quality requirements and constitute a subset of baseline leptons. The likelihood, isolation, and impact parameter cuts defined in Section 5.6 are all employed in making these distinctions. Baseline electrons and muons are reconstructed using inner detector tracks matched to electromagnetic calorimeter energy clusters and muon spectrometer tracks, respectively. Electrons are required to satisfy VeryLoose likelihood identification criteria at baseline level, and Medium ID at signal level. They additionally must pass Gradient isolation requirements and impact parameter cuts. A cut on electron author (at truth level) is applied to reject electron candidates seeded by photon conversion reconstruction algorithms.

A novel feature of this analysis is the inaugural use of muons down to 3 GeV in p_T. A dedicated working point for these very soft muons was developed, referred to as *LowPt* [121], which gives improved signal efficiency and background rejection for muon candidates with $p_T < 10$ GeV. Both baseline and signal muons are required to pass the LowPt ID criteria; signal muons must additionally pass FixedCutTightTrackOnly isolation and impact parameter requirements.

Due to the low p_T of the leptons, a small angular separation between them is expected. As a result, such "nearby" leptons can land in each other's isolation cones, resulting in a loss of efficiency.

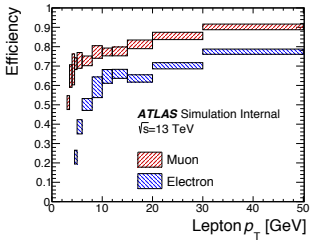


Figure 10.3: Signal lepton efficiencies for electrons and muons within detector acceptance, averaged over a mix of higgsino and slepton simulated samples, with uncertainty bands reflecting the range of observed efficiencies across all samples.

This primarily affects the softest leptons and thus the smallest mass splitting samples. To avoid this, a dedicated nearby lepton isolation correction is performed, which removes nearby lepton tracks from the track isolation sum (and similarly, nearby lepton topoclusters are removed from the calorimeter isolation sum if the nearby lepton is an electron.) The definition of nearby in this context is determined by ΔR and having p_T matching within a given margin of error.

Table 10.1 lists all selection criteria of electrons and muons used in the analysis, for both baseline and signal categories. The efficiency for selection of signal electrons and muons binned in lepton p_T can be found in Figure 10.3, where the dependence on η is consistent with ATLAS combined performance paper results.

10.2.2 Jets & E_T^{miss}

The jets used in this analysis are anti-k_t R = 0.4 jets calibrated using the EM scale. Baseline and signal jets are both required to have $p_T > 20$ GeV, with signal jets required to have $|\eta| < 2.8$ and baseline jets $|\eta| < 4.5$. Jets containing b-hadrons are identified using the MV2c10 b-tagging algorithm, at a working point that provides 85% selection efficiency in $t\bar{t}$ simulation. Pileup mitigation is per-

formed with the jet vertex tagger (JVT), with cuts applied to jets with p_T < 60 GeV and $|\eta|$ < 2.4. Event cleaning is applied to remove jets originating from non-collision processes or calorimeter noise.

The E_T^{miss} in the event is defined as the negative vector sum of the transverse momenta of all identified physics objects (electrons, muons, and jets.) It is reconstructed using the Tight working point. The soft term is constructed from all primary vertex tracks not associated to any baseline object, to allow adjustments for the best calibrations of jets and other objects, while remaining agnostic to pileup conditions.

Table 10.1 gives an overview of all kinematic, ID, impact parameter, and isolation requirements for baseline and signal jets and *b*-jets used in the analysis. Small corrections are applied to objects in simulated samples to better match reconstruction efficiencies in data.

10.2.3 Overlap Removal

Baseline objects undergo an overlap removal (OR) procedure to prevent the double counting of signal objects. This procedure uses collections of electrons, muons, and jets, and removes overlapping objects based on ΔR matching (or shared inner detector tracks). Fat jets, photons, and taus are not used in the OR procedure of this analysis, while boosted electrons and *b*-tagging are included.

The order of overlaps removed between collections is as follows. To remove muon bremsstrahlung where a photon converts into an electron-positron pair, electrons sharing an inner detector track with muons are removed first. Next, jets that do not have a *b*-tag are removed if they are within ΔR < 0.2 of the remaining electrons. Jets within ΔR < 0.4 of a muon with less than three tracks of p_T

Property	Signal	Baseline
Electrons		
Kinematic	$p_T > 4.5$ GeV, $\|\eta\| < 2.47$	$p_T > 4.5$ GeV
ID	Medium	VeryLoose
Isolation	Gradient	-
Impact Parameter	$\|d_0\|/\sigma_{d_0} < 5$, $\|z_0 sin\theta\| < 0.5$ mm	$\|z_0 sin\theta\| < 0.5$ m
Muons		
Kinematic	$p_T > 3$ GeV, $\|\eta\| < 2.5$	$p_T > 3$ GeV
ID	LowPt	LowPt
Isolation	FixedCutTightTrackOnly	-
Impact Parameter	$\|d_0\|/\sigma_{d_0} < 3$, $\|z_0 sin\theta\| < 0.5$ mm	$\|z_0 sin\theta\| < 0.5$ mm
Jets		
Kinematic	$p_T > 30$ GeV, $\|\eta\| < 2.8$	$p_T > 20$ GeV, $\|\eta\| < 4.5$
Pileup mitigation	JVT Medium for $p_T < 60$ GeV, $\|\eta\| < 2.4$	-
b-jets		
Kinematic	$p_T > 20$ GeV, $\|\eta\| < 2.5$	$p_T > 20$ GeV, $\|\eta\| < 4.5$
Pileup mitigation	JVT Medium for $p_T < 120$ GeV, $\|\eta\| < 2.5$	-
b-tagging	MV2c10 85% eff WP	-

Table 10.1: Overview of baseline and signal object requirements for the compressed electroweak analysis.

> 500 MeV are then removed. Finally, electrons or muons within ΔR < 0.4 of the remaining jet candidates are removed, to suppress heavy flavor hadron decays.

10.3 Signal Regions

The signal regions must be optimized so as to maximize sensitivity to an elusive compressed higgsino signal, while cutting away backgrounds from fake leptons and other SM processes. Below all discriminating variables are defined, and the selection for the high-E_T^{miss} higgsino signal region is provided.

10.3.1 Discriminating Variables

A helpful feature in the SR optimization effort is the kinematic endpoint in the invariant mass of the two leptons m_{ll}, which is exploited via a shape fit across bins of this variable. Additionally, the Recursive Jigsaw Reconstruction method, which is described in Chapter 6 and applied to compressed stop scenarios in Chapter 9, can also be of use to produce powerful discriminating variables. These and other discriminating variables used in the signal region construction are listed and described below (excluding basic event quantities such as E_T^{miss} and object multiplicities).

- Event Shape Variables
  - $|\Delta\phi(j_1, p_T^{miss})|$: angular separation between the leading jet and E_T^{miss}; larger values of this variable can ensure the ISR-assisted topology and remove QCD background.
  - min $\Delta\phi(anyjet, p_T^{miss})$: angular separation between all jets and E_T^{miss}; larger values can help eliminate events with fake E_T^{miss} contributions from jet mis-measurements.

- Leptonic Variables
  - ΔR_{ll}: angular distance between leptons, defined as $\sqrt{(\eta_{\ell 1} - \eta_{\ell 2})^2 + (\phi_{\ell 1} - \phi_{\ell 2})^2}$; soft leptons tend to have smaller values.
  - m_{ll}: invariant mass of the two leptons, correlated to the mass splitting of the higgsino signal.
  - $m_T^{\ell 1}$: transverse mass of the leading lepton, defined in Equation 9.1.
  - m_{T2}: "stransverse" mass, defined as $\min_{q_T}(\max[m_T(p_T^{\ell 1}, q_T, m_\chi), m_T(p_T^{\ell 2}, p_T^{miss} - q_T, m_\chi)])$, where m_χ is the hypothesized mass of the invisible particles, and q_T is chosen to minimize the larger of the two transverse masses (defined above).
  - E_T^{miss} / H_T^{lep}: the ratio of the E_T^{miss} to the scalar sum of lepton momenta H_T^{lep}, defined as $\sum_i^{leps} p_T^{\ell i}$; backgrounds tend to have harder leptonic activity and thus lower values of this variable.

- $m_{\tau\tau}$: di-tau invariant mass, which fully reconstructs the fully leptonic $Z \rightarrow \tau\tau$ decay with associated jets. It is defined as the signed square root of $m^2_{\tau\tau} \equiv 2p_{\ell 1} \cdot p_{\ell 2}(1+\xi_1)(1+\xi_2)$, where p_ℓ are the lepton four-momenta and the ξ parameters are determined by solving $p_T^{miss} = \xi_1 p_T^{\ell 1} + \xi_2 p_T^{\ell 2}$. Negative values of $m_{\tau\tau}$ are associated to events where one of the lepton moment is smaller in magnitude than the E_T^{miss} and points in the hemisphere opposite to the p_T^{miss} vector (see Figure 10.4).

- RJR Variables, which are calculated using a variation on the standard ISR-assisted decay tree as shown in Figure 10.5, to remove the two leptons from the calculation of the thrust axis.
  - R_{ISR}, as defined in Section 6.2.
  - M_T^S, as defined in Section 6.2.

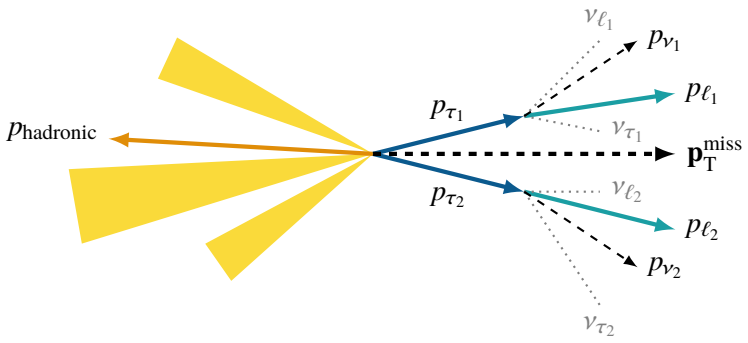


Figure 10.4: Diagram of the fully leptonic $Z \rightarrow \tau\tau$ + jets system, motivating construction of the $m_{\tau\tau}$ variable.

10.3.2 Event Selection

All regions in the analysis share a common event preselection, defined in Table 10.2. This preselection serves to enforce basic requirements of the signal events, such as two opposite-sign same-flavor soft leptons. It also imposes the expected ISR-assisted topology, by way of requiring a hard leading

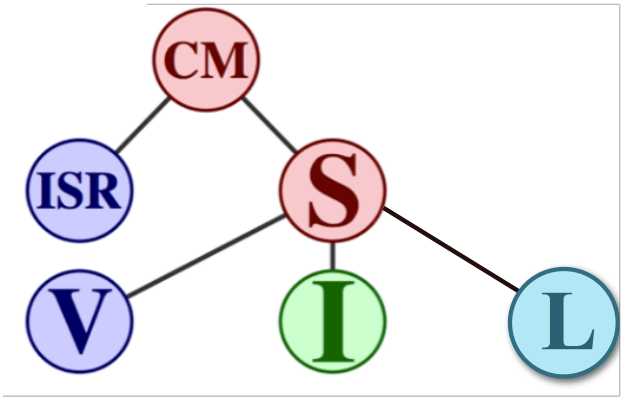


Figure 10.5: Decay tree corresponding to the ISR-assisted E_T^{miss} strategy for the compressed higgsino analysis.

jet that is back-to-back with the missing energy. Other requirements on the number of b-jets, $m_{\tau\tau}$, leading lepton p_T, and min $\Delta\phi(anyjet, p_T^{miss})$ serve to cut away common backgrounds from SM processes ($t\bar{t}$, $Z \rightarrow \tau\tau$, fake/non-prompt lepton, and jet energy mismeasurements, respectively). Contributions from J/ψ decays are removed with a veto on [3.0, 3.2] GeV in m_{ll}, while other resonances such as the Υ states are expected to be negligible. The upper bound on $m_{ll} < 60$ GeV reduces contributions from on-shell Z^0 boson decays, and the lower bound $m_{ll} > 1$ GeV removes events with collinear lepton pairs from a photon conversion (aided by the various cuts on ΔR_{ll}.)

The optimization strategy in building the high-E_T^{miss} higgsino SR utilized N-1 plots of the discriminating variables. Scanning possible cut values of each variable and examination of the corresponding Z_n significance (with a flat 20% background uncertainty) reveals the most powerful variables for signal to background discrimination, as well as an optimal cut value for each variable. The N-1 plots in Figures 10.6 to 10.7 use five benchmark compressed Higgsino signal points, as well as SM background simulation and a data-driven fake estimation. Variables displayed include all

Variable	Preselection Requirement
Number of leptons	= 2
Lepton charge & flavor	$e^{\pm}e^{\mp}$ or $\mu^{\pm}\mu^{\mp}$
Leading lepton p_T [GeV]	> 5
ΔR_{ll}	$\Delta R_{ee} > 0.30$; $\Delta R_{\mu\mu} > 0.05$; $\Delta R_{e\mu} > 0.20$
E_T^{miss} [GeV]	> 100
Number of jets	≥ 1
Leading jet p_T [GeV]	≥ 100
min $\Delta\phi(anyjet, p_T^{miss})$	> 0.4
$\lvert\Delta\phi(j_1, p_T^{miss})\rvert$	≥ 2.0
J/ψ invariant mass [GeV]	veto $3 < m_{ll} < 3.2$
Lepton invariant mass [GeV]	$1 < m_{ll} < 60$
Number of b-jets	= 0
$m_{\tau\tau}$ [GeV]	< 0 or > 160

Table 10.2: Table of common event preselection criteria for the high-E_T^{miss} higgsino regions.

aforementioned analysis variables, as well as E_T^{miss}, actual interactions per crossing μ, leading and subleading lepton p_T, leading jet p_T, and jet/b-jet multiplicity. Arrows indicate the presence of an optimized cut position, if a cut exists on the displayed variable.

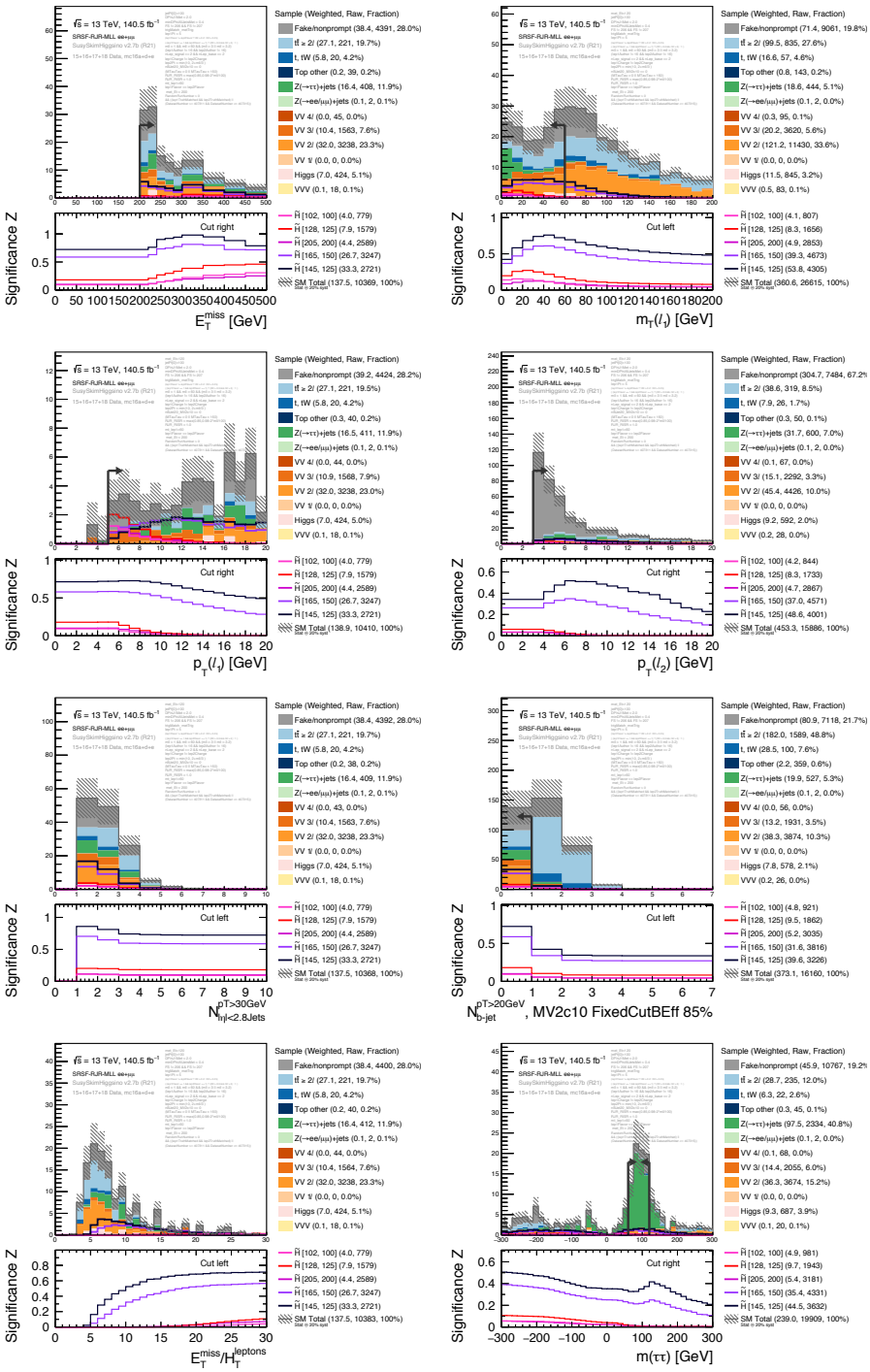


Figure 10.6: N-1 plots of analysis variables for the high-E_T^{miss} higgsino regions inclusively in m_{ll}. The legend includes the relative contribution of each background. Statistical uncertainties and a flat 20% background systematic uncertainty are included. Arrows indicate the cut value chosen for the SR.

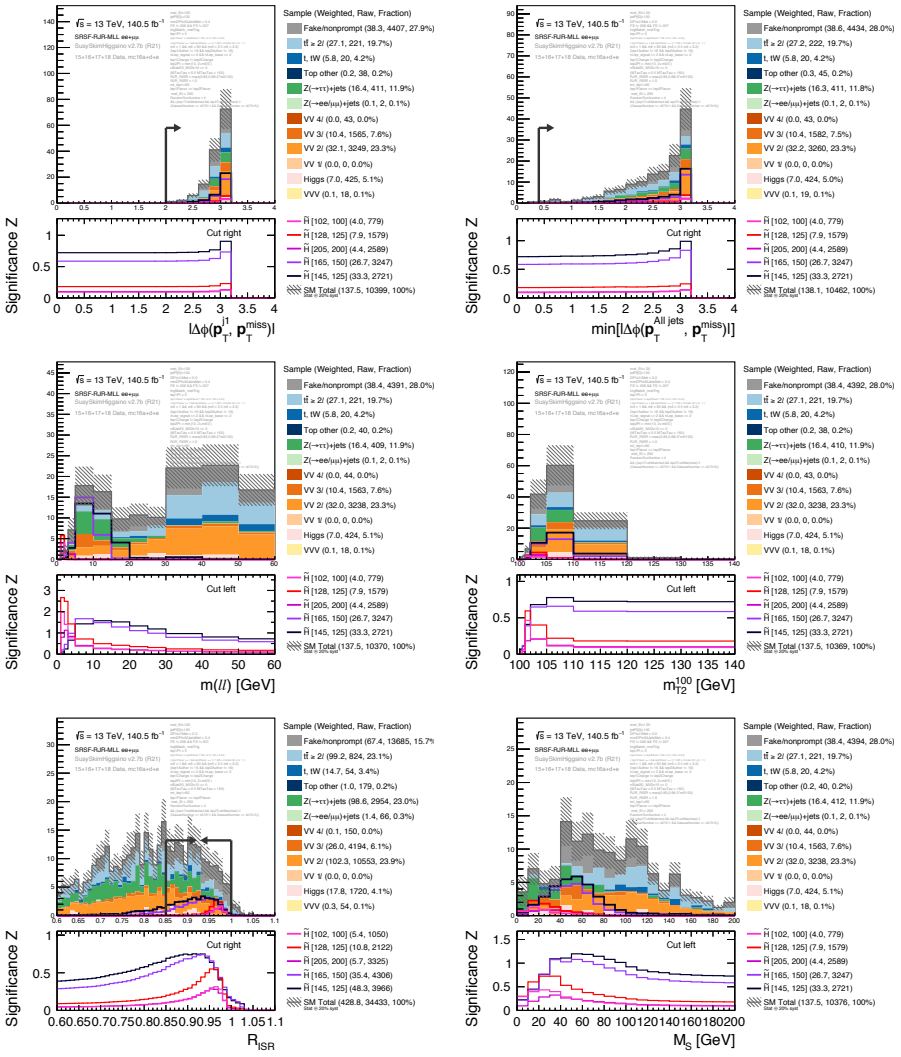


Figure 10.7: N-1 plots of analysis variables for the high-E_T^{miss} higgsino regions inclusively in m_{ll}. The legend includes the relative contribution of each background. Statistical uncertainties and a flat 20% background systematic uncertainty are included. Arrows indicate the cut value chosen for the SR.

In Figure 10.7, the localization of the data-driven fake lepton background at low m_{ll} is evident. This presents a difficulty for some signals more than others. The strong correlation between signal mass splitting and m_{ll} means that different signals have a variety of distributions across the full m_{ll} spectrum, with smaller mass splitting samples concentrated in the very lowest bins. This feature can also be seen in Figure 6.3, demonstrating that the R_{ISR} variable can exploit this feature given its natural correlation to the mass splitting.

To further optimize the removal of the fake background in conjunction with the preservation of signal, "sliding" cuts on key variables were developed, to allow cut value to vary as a function of m_{ll}. Such cut functions were determined by linearly fitting the optimal cut placement in N-1 plots of all m_{ll} bins. R_{ISR} and $p_T(\ell_2)$ distributions were specifically studied for this purposes, since both variables are especially powerful for eliminating the fake lepton background. Figures 10.8 to 10.9 show the variation of signal sensitivity across bins of m_{ll}, thereby motivating the use of sliding cuts on R_{ISR} and $p_T(\ell_2)$, and indicating the linear scaling of the optimal cut value. Arrows on the histograms do not reflect this sliding cut, and rather show the absolute bounds on the variable in the SRs.

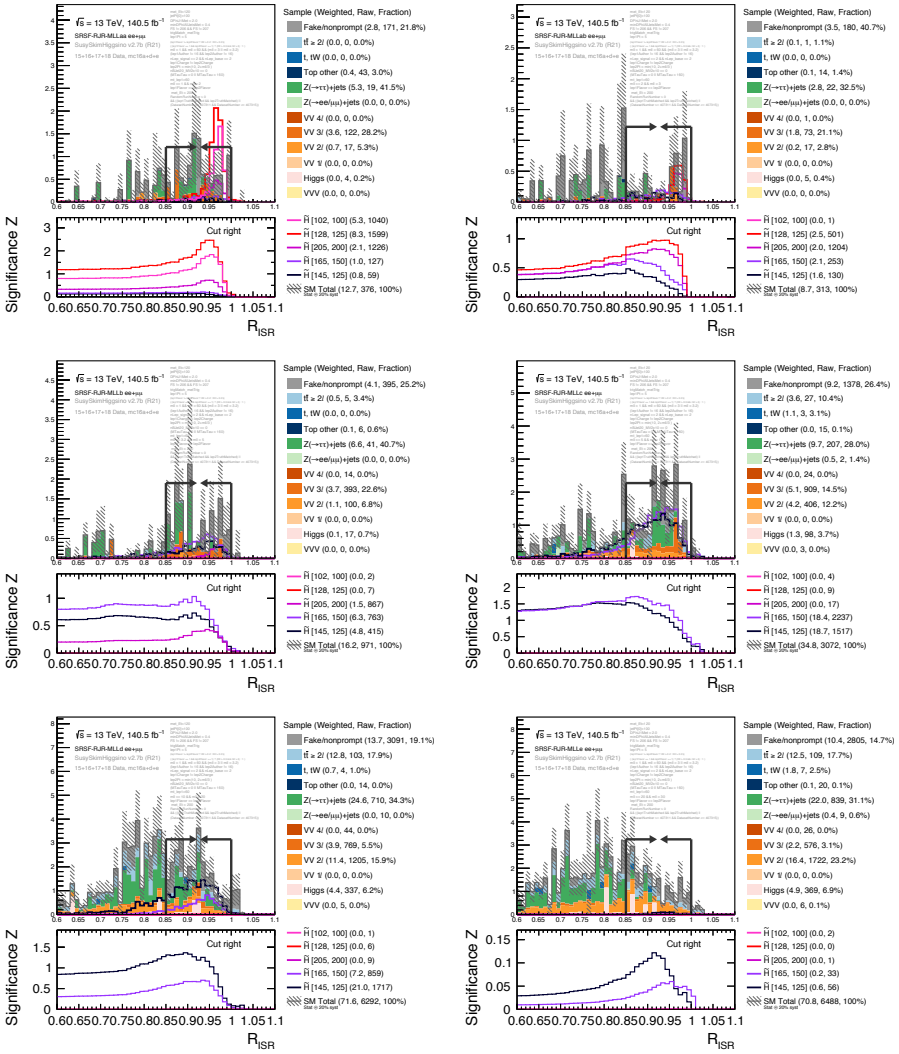


Figure 10.8: N-1 plots of R_{ISR}, in the lowest six bins of m_{ll}, demonstrating the efficacy of a sliding cut. Arrows indicate upper and lower bounds on R_{ISR} in the signal regions.

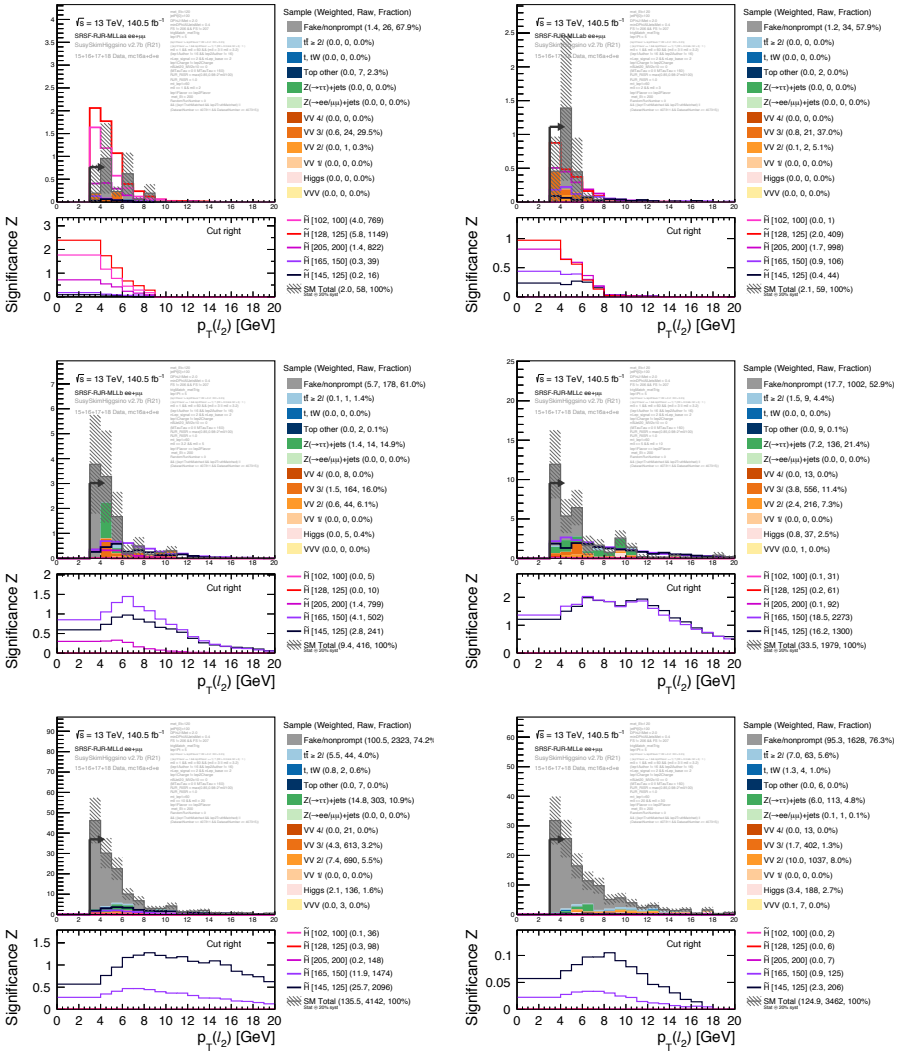


Figure 10.9: N-1 plots of $p_T(\ell_2)$, in the lowest six bins of m_{ll}, demonstrating the efficacy of a sliding cut. Arrows indicate the lower bound on $p_T(\ell_2)$ in the signal regions.

Variable	Selection Requirement							
E_T^{miss} [GeV]	> 200							
$m_T^{\ell 1}$ [GeV]	< 60							
$p_T(\ell_2)$ [GeV]	$> \min(10, 2 + m_{ll}/3)$							
R_{ISR}	$> \max(0.85, 0.98 - 2 \cdot m_{ll} / (100\ \text{GeV}))$ and < 1.0							
	eMLLaa	eMLLab	eMLLb	eMLLc	eMLLd	eMLLe	eMLLf	eMLLg
$m(ee)$ [GeV]	-	-	[3.2,5]	[5,10]	[10, 20]	[20,30]	[30,40]	[40,60]
$m(\mu\mu)$ [GeV]	[1,2]	[2,3]	[3.2,5]	[5,10]	[10, 20]	[20,30]	[30,40]	[40,60]
	iMLLaa	iMLLab	iMLLb	iMLLc	iMLLd	iMLLe	iMLLf	iMLLg
m_{ll} [GeV]	< 2	< 3	< 5	< 10	< 20	< 30	< 40	< 60

Table 10.3: Table of common event selection criteria for the high-E_T^{miss} higgsino signal regions. Exclusive SRs ("eMLL") are used for Higgsino model-dependent limits, while inclusive bins ("iMLL") are used to set model-independent limits. ee and $\mu\mu$ channels are statistically independent and fit separately.

The selection criteria defining the high-E_T^{miss} higgsino signal regions can be found in Table 10.3, provided as a list of cuts applied in addition to the preselection. This criteria incorporates optimal cut information from N-1 plots of all analysis variables, and the sliding cuts on R_{ISR} and $p_T(\ell_2)$ as a function of m_{ll}. The shape fit binning for m_{ll} is also given, with different bins for different flavors due to the lower muon p_T threshold, and both exclusive and inclusive bins.

10.4 Background Estimation

The discussion of background estimation strategies is divided into two categories: first, for the data-driven estimation of the fake lepton background; and second, for the Monte Carlo-estimated backgrounds, including those that are normalized via control regions and further verified in validation regions.

10.4.1 Fake Lepton Background & Fake Factor Method

The fake lepton background consists of both non-leptonic objects falsely reconstructed as leptons, and real leptons that are non-prompt or originating from decays other than the process of interest (for example, semi-leptonic decays of heavy-flavor hadrons or photon conversions, the former being found to be the dominant component in the SRs). Monte Carlo simulation tends to poorly model these backgrounds, so a data-driven *fake factor method* is employed to ensure accurate estimation.

In the fake factor method, two lepton definitions are established: one called *ID* defined by the standard signal leptons, and the second referred to as *anti-ID* criteria which is designed to be enriched in fake leptons. The anti-ID leptons are selected by relaxing or inverting the standard lepton ID, isolation, and/or impact parameter requirements, as shown in Table 10.4. Flavor differences in the anti-ID definitions exist; anti-ID electrons are not allowed to simultaneously fail the isolation and ID requirements, while anti-ID muons may not simultaneously fail the isolation and d_0 significance requirements.

Variable	Anti-ID Electrons	Anti-ID Muons
p_T [GeV]	> 4.5 GeV	> 3 GeV
$\|\eta\|$	< 2.47	> 2.5
$\|z_0 \sin\theta\|$	< 0.5 mm	< 0.5 mm
ID	LooseAndBLayer	LowPt
Requirement	(! Medium ID || $\|d_0/\sigma_{d_0}\|$ > 5 || ! Gradient Isolation) && (Medium ID || Gradient Isolation)	($\|d_0/\sigma_{d_0}\|$ > 3 || ! FCTightTrackOnly Isolation) && ($\|d_0/\sigma_{d_0}\|$ < 3 || FCTightTrackOnly Isolation)

Table 10.4: Table defining anti-ID leptons for the fake factor method.

The *fake factor (F)* is thus defined in Equation 10.1 as the ratio of ID lepton multiplicity to anti-ID lepton multiplicity, where N is the number of events and i is the p_T bin number.

$$F(i) = \frac{N_{ID}(i)}{N_{anti-ID}(i)} \tag{10.1}$$

Conceptually this is not a fake rate; rather, it is a probability that, given the CR construction, a fake lepton will be present in the SR. The fake factor is measured in a region of data that is both enriched in fake leptons and kinematically close to the signal region, to ensure reasonability of extrapolation of the estimate. This region primarily consists of multijet events collected by a prescaled low-p_T single lepton trigger, with an additional requirement of $m_T^{\ell 1} < 40$ GeV to minimize the contribution of events with prompt leptons. Dependences of the fake factors on lepton flavor and b-jet multiplicity were observed in initial studies. Therefore, fake factors are calculated separately for electrons and muons, and for samples with exactly zero and at least one b-tagged jet.

Next, an anti-ID control region is created, with identical selection to the signal region except replacing one of the ID leptons with an anti-ID lepton. Each event in the control region is then

multiplied by the fake factor, and to first order the yield in the signal region can then be calculated as in Equation 10.2. Prompt lepton yields as predicted by MC are subtracted from $N_{anti-IDCR}$ so as to not double-count the prompt lepton backgrounds, and to ensure that only the fake lepton background (and not other single anti-ID lepton processes) is estimated.

$$N_{SR}^{fake} = \sum_{i} N_{anti-ID\,CR}^{fake,i} \cdot F(i) \tag{10.2}$$

The expression in Equation 10.2 is overly simplified, leaving out one important contribution. Since the SR has two leptons in it, the fake factor method must be able to account for events with two anti-ID leptons, even though only one is required for the anti-ID CR. Specifically, the contribution from events with two anti-ID leptons must be subtracted off, as inherently in the method, the single anti-ID lepton terms will have some events with two anti-ID leptons, and thus this contribution would be counted twice. The total number of events with fake leptons can therefore be expressed as follows in Equation 10.3, where a subscript I indicates the presence of an ID lepton and a subscript A indicates an anti-ID lepton. Each N term in Equation 10.3 includes the prompt MC subtraction of real lepton events.

$$N_{SR}^{fake} = [N_{IA}] \cdot F_1 + [N_{AI}] \cdot F_2 - [N_{AA}] \cdot F_1 F_2 \tag{10.3}$$

Figure 10.10 gives a diagrammatic explanation of the fake factor method, demonstrating the location of the ID/anti-ID regions in phase space.

An important assumption made in the fake factor method is that the composition of non-prompt

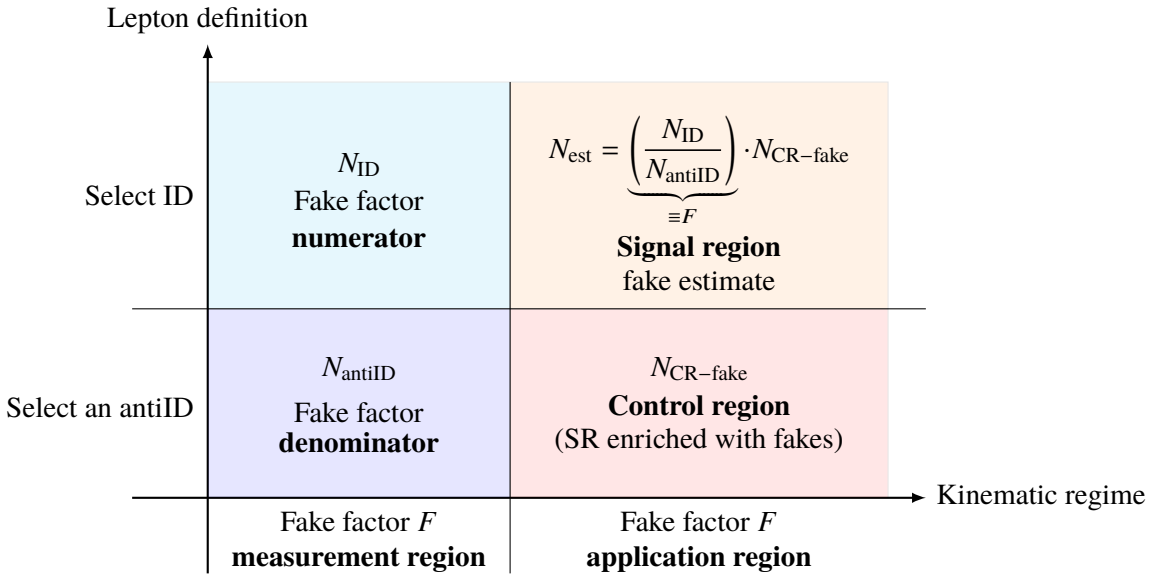


Figure 10.10: Schematic illustrating the fake factor method to estimate the fake lepton contribution in the signal region.

leptons is consistent across measurement and signal regions. Discrepancy in composition is taken as a systematic uncertainty on the estimation. Furthermore, since the minimum p_T of electrons and muons considered in the analysis is lower than the threshold for single electron/muon triggers, the fake factors cannot be measured for the lowest p_T leptons and must be extrapolated. This is done by fitting the p_T distributions and using the fit to obtain reasonable estimations for leptons with p_T below trigger thresholds.

10.4.2 Control Regions

Three control regions are used in the analysis to normalize the three (non-fake) dominant backgrounds. CR-top normalizes the $t\bar{t}$ and singletop backgrounds, CR-tau normalizes the Z$\rightarrow \tau\tau$

+ jets background, and CR-VV normalizes the diboson background (in zero to four lepton final states.) CR-top is enriched in top background by inverting the SR requirement on the number of *b*-tags. CR-tau is separated from the SR by selecting events with a di-tau invariant mass consistent with a Z decay, specifically selecting events with 60 < $m_{\tau\tau}$ < 120 GeV, whereas the SR has a veto on 0 < $m_{\tau\tau}$ < 160 GeV. CR-VV is created by inverting the R_{ISR} cut, selecting events with 0.7 < R_{ISR} < 0.85.

By way of these cut inversions, all CRs are orthogonal to the SR and have a purity of their dedicated background process that is greater than 70%. The only exception is CR-VV, which has a purity of approximately 45% of the diboson background; however, the largest contaminants in CR-VV are top and Z$\rightarrow \tau\tau$ + jets backgrounds, which are already appropriately normalized in their dedicated CRs. The signal region cut on $m_T^{\ell 1}$ is not included to enhance background statistics and purity. Similarly, the R_{ISR} cut is loosened with respect to the SR to $R_{ISR} > 0.7$. Since all three normalized processes are flavor symmetric, all lepton flavor combinations are allowed to enhance statistics.

Table 10.5 gives a summary of the selections for the high-E_T^{miss} higgsino control regions, including the orthogonality to the SR and flavors included. To minimize extrapolation across different kinematic regions, selection criteria are identical to those given in Table 10.3 except for the changes listed here.

To ensure good modeling of data in the control regions, plots overlaying data to Monte Carlo simulation are made for all key analysis variables. Figures 10.11 and 10.12 show data to MC comparisons in CR-top. Figures 10.13 and 10.14 shows data to MC comparisons in CR-tau. Figures 10.15 and 10.16 shows data to MC comparisons in CR-VV. All plots include statistical uncertainties summed in

Region	SR Orthogonality	Additional Requirements	Flavor
CR-top	Number of b-jets ≥ 1	$R_{ISR} > 0.7$, no cut on $m_T^{\ell 1}$	$ee + \mu\mu + e\mu + \mu e$
CR-tau	$60 < m_{\tau\tau} < 120$ GeV	$R_{ISR} > 0.7$, no cut on $m_T^{\ell 1}$	$ee + \mu\mu + e\mu + \mu e$
CR-VV	$R_{ISR} < 0.85$	$R_{ISR} > 0.7$, no cut on $m_T^{\ell 1}$	$ee + \mu\mu + e\mu + \mu e$

Table 10.5: Table of criteria for the high-E_T^{miss} higgsino control regions, provided as differences from the signal region definitions in Table 10.3. All regions also include the preselection requirements listed in Table 10.2.

quadrature with a flat 20% background systematic. Good modeling is shown for all regions across all variables, ensuring that the regions are well-defined for the likelihood fit.

The amount of signal contamination in CR-top, CR-tau, and CR-VV is shown in Figures 10.17, 10.18, and 10.19 respectively, given as percentages of the total CR yield attributable to the given signal point. The contamination is below 14% across the full higgsino signal grid, ensuring that the background estimate in the SRs is robust and will not accidentally account for signal in the data.

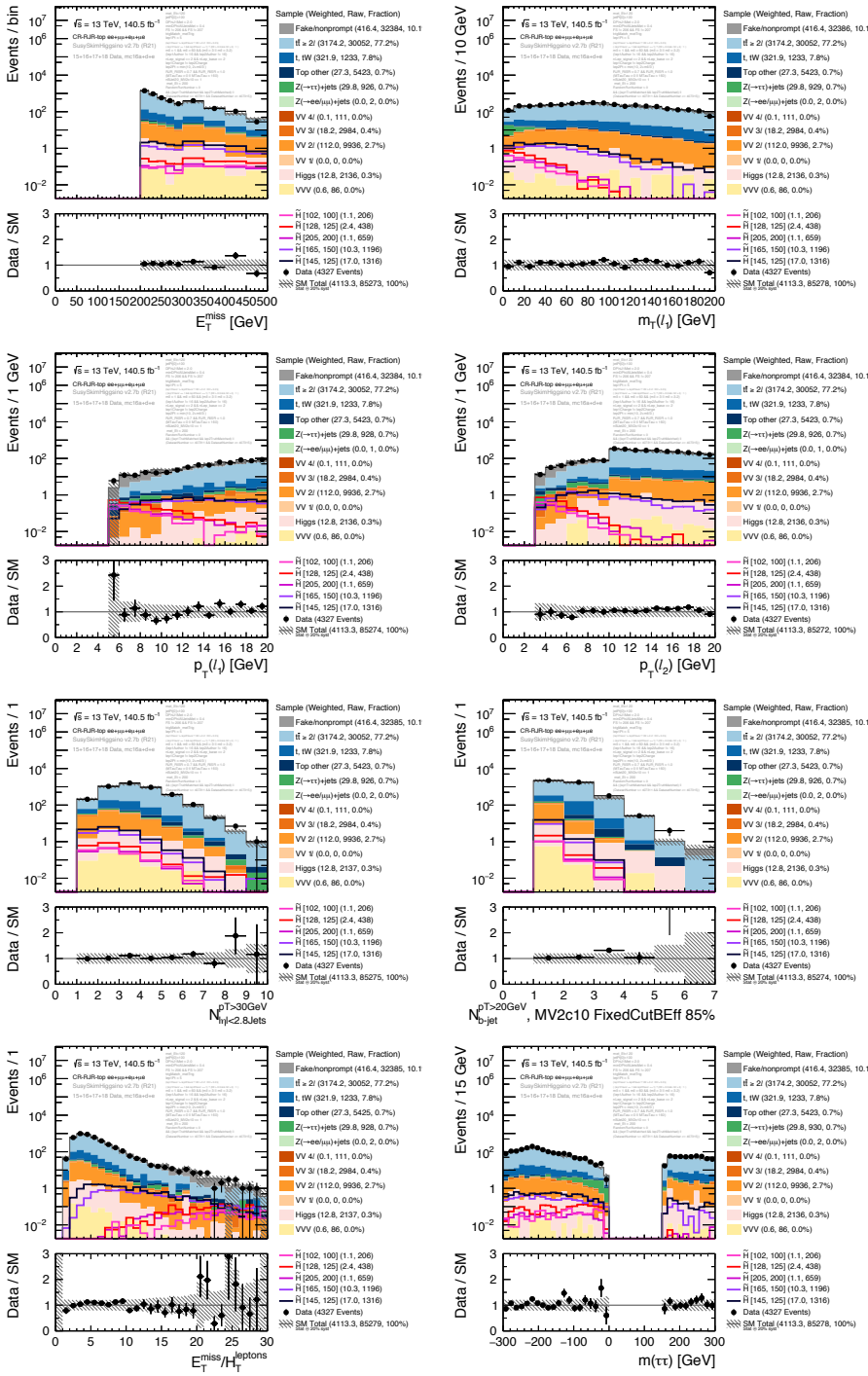


Figure 10.11: Distributions of analysis variables in high-E_T^{miss} higgsino top control region.

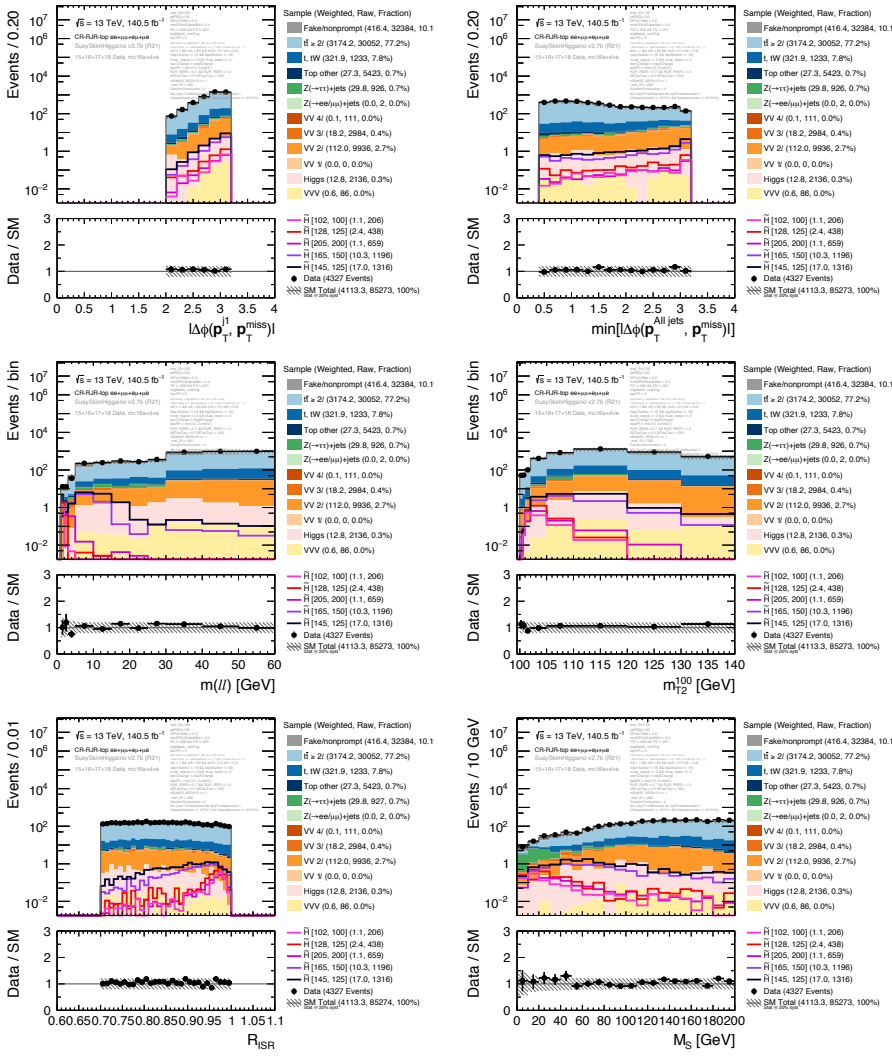


Figure 10.12: Distributions of analysis variables in high-E_T^{miss} higgsino top control region.

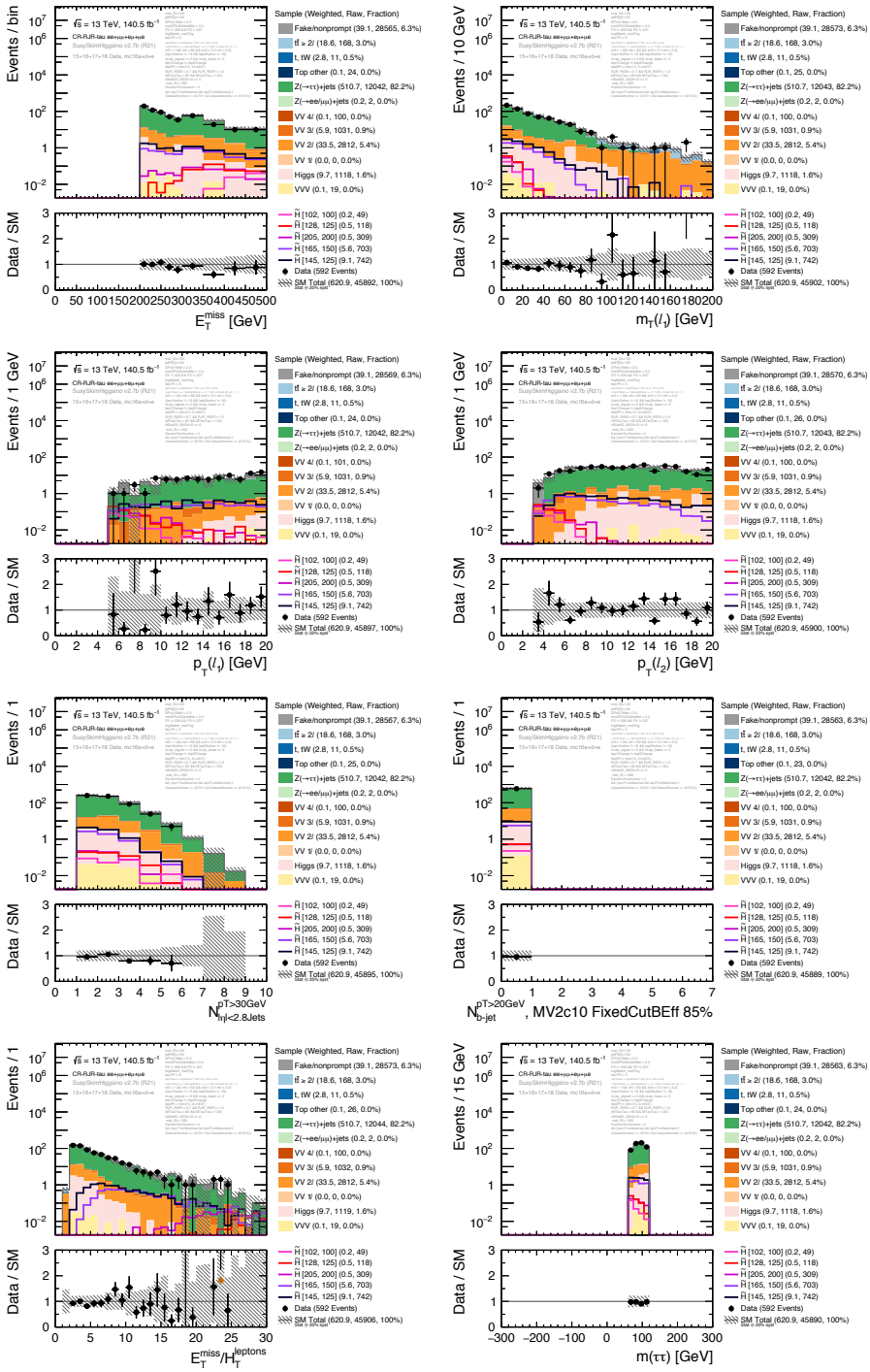


Figure 10.13: Distributions of analysis variables in high-E_T^{miss} higgsino Z$\rightarrow \tau\tau$ + jets control region.

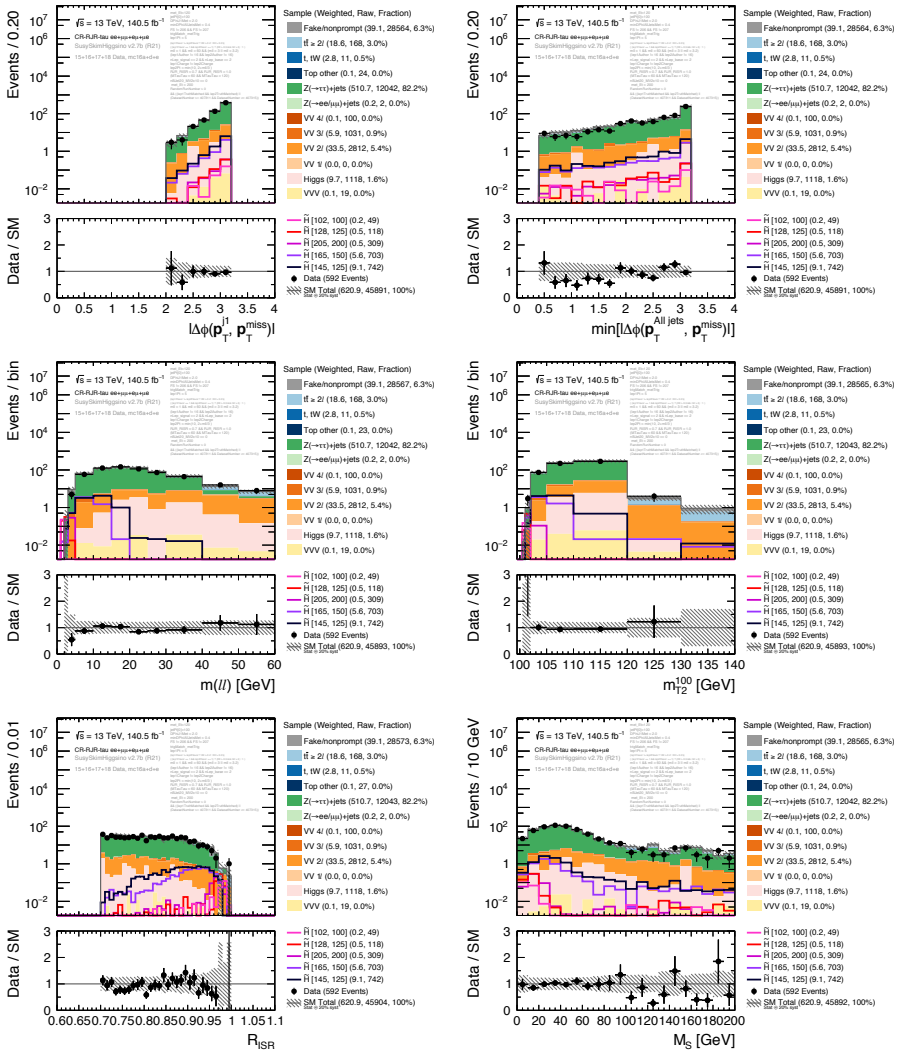


Figure 10.14: Distributions of analysis variables in high-E_T^{miss} higgsino Z$\rightarrow \tau\tau$ + jets control region.

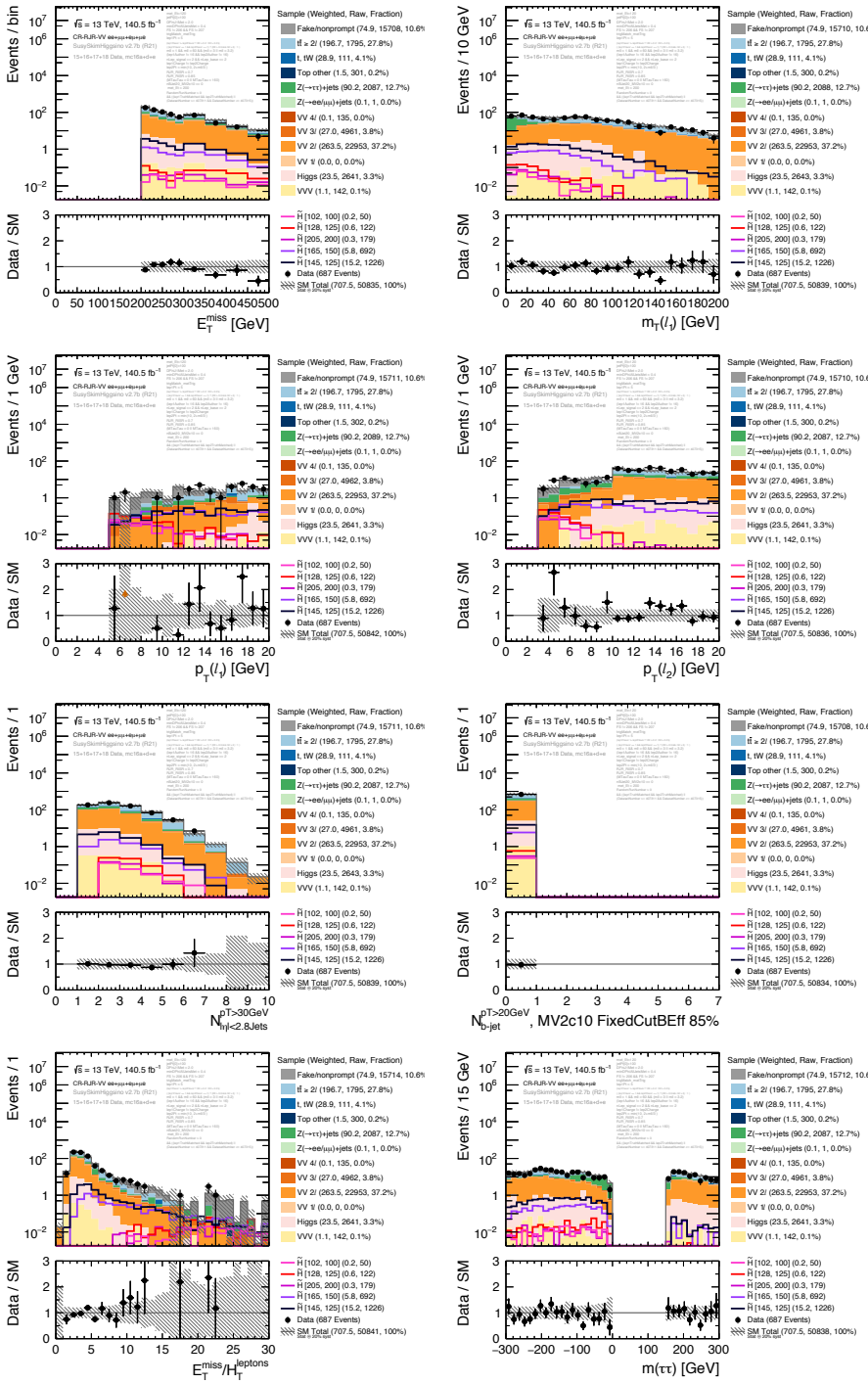


Figure 10.15: Distributions of analysis variables in high-E_T^{miss} higgsino diboson control region.

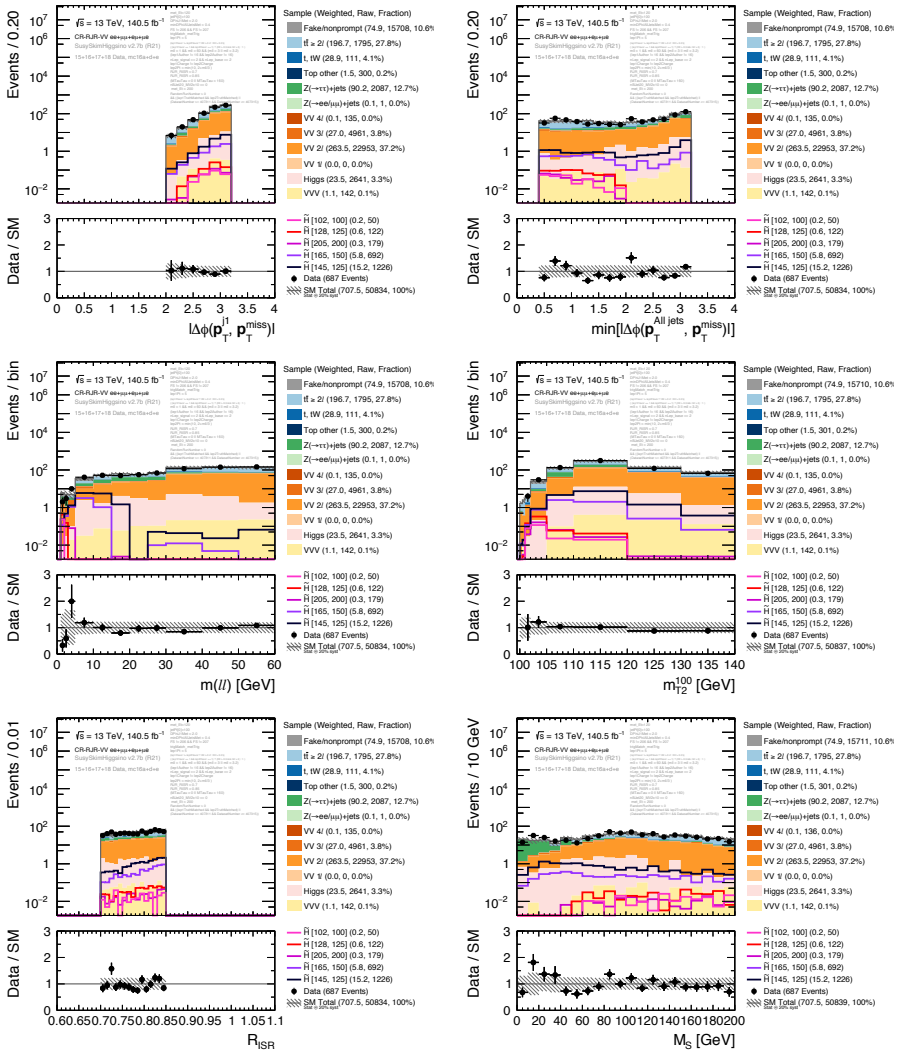


Figure 10.16: Distributions of analysis variables in high-E_T^{miss} higgsino diboson control region.

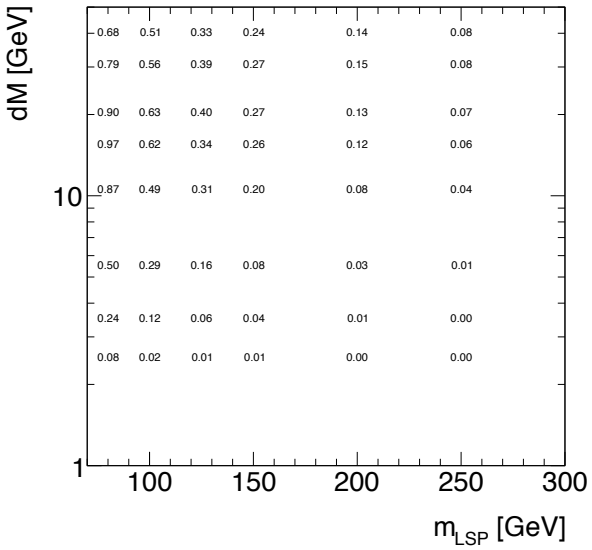


Figure 10.17: Contamination of signal in CR-top across full higgsino signal grid.

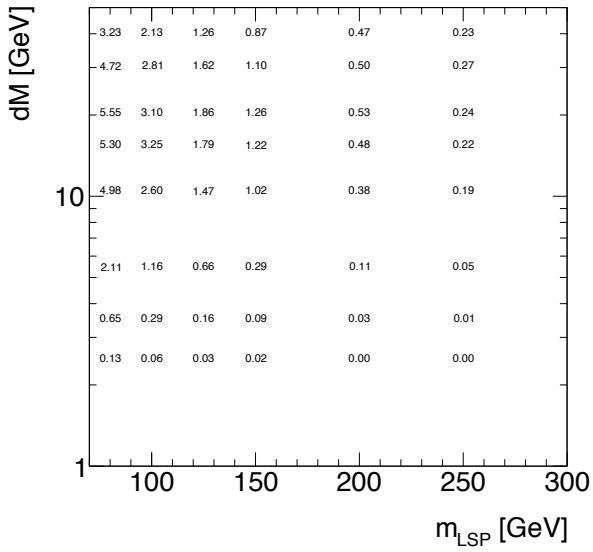


Figure 10.18: Contamination of signal in CR-tau across full higgsino signal grid.

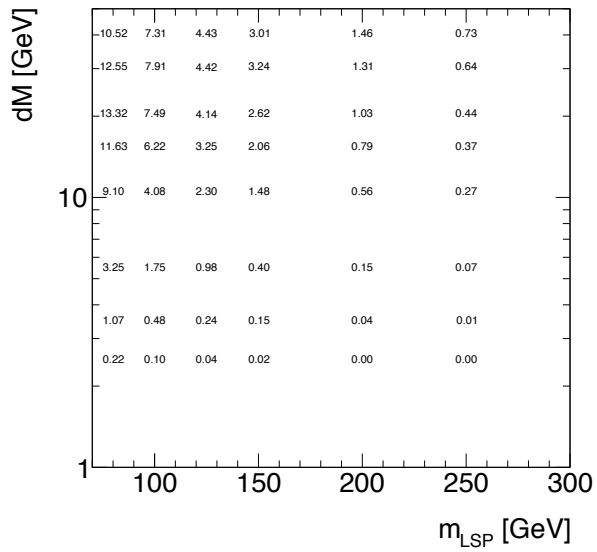


Figure 10.19: Contamination of signal in CR-VV across full higgsino signal grid.

Region	SR Orthogonality	Additional Requirements	Flavor
VR-DF	$e\mu + \mu e$	-	$e\mu + \mu e$
VR-SS	Same-sign $\ell^{\pm}\ell^{\pm}$	$R_{ISR} > 0.7$, no cut on $m_T^{\ell 1}$ or $p_T(\ell_2)$	$ee + \mu e$, $\mu\mu + e\mu$

Table 10.6: Table of criteria for the high-E_T^{miss} higgsino validation regions, provided as differences from the signal region definitions in Table 10.3. All regions also include the preselection requirements listed in Table 10.2.

10.4.3 Validation Regions

Two validation regions are implemented for the high-E_T^{miss} higgsino analysis. Both share identical criteria to the signal region, except for the inversion of a cut that maintains orthogonality. The different flavor validation region VR-DF is constructed by selecting two leptons of different flavor, which separates the region from the SR. Such a change does not affect the ability of the region to estimate the irreducible SM backgrounds normalized by the CRs, which are all symmetric in $ee + \mu\mu$ and $e\mu + \mu e$. It validates the normalization factors extracted from the control regions, and verifies good quality of background prediction in a region kinematically close to the SR.

The same-sign validation region VR-SS validates the fake factors and the predictions made by the method. The region is constructed to be enriched in fake leptons by selecting two leptons that have the same electric charge ("same-sign"), and thus are not likely to come from a Z^0 boson decay. VR-SS similarly verifies that the data-driven fake estimation is predictive in an SR-like region.

Table 10.6 gives a summary of the selections, orthogonality to the SR, and flavors utilized for the high-E_T^{miss} higgsino validation regions, provided as changes with respect to the preselection.

Data vs. Monte Carlo plots for all key analysis variables can be found in the following figures. Figures 10.20 and 10.21 show data to MC comparisons in VR-DF, with statistical and flat 20% sys-

tematic uncertainties overlaid. Given that the SM estimation is suitably predictive of the data, and no significant slopes in the data/MC ratio exist, the estimation regions are further confirmed for use in background modeling and the likelihood fit.

VR-SS plots are sorted by the flavor of the sub-leading lepton, which is more likely to be fake than the harder lepton. Figures 10.22 and 10.23 shows data to MC comparisons in the $ee + \mu e$ channel, while Figures 10.24 and 10.25 shows data to MC comparisons in the $\mu\mu + e\mu$ channel, including statistical and flat 20% systematics summed in quadrature. The data-driven fake background is found to provide good modeling in these fake-enriched regions.

The signal contamination in VR-DF is shown in Figures 10.26, and for VR-SS in Figure 10.27 for all flavor combinations. The signal contamination can be acceptably higher in the VRs than the CRs, since they do not directly provide a background estimate for the SRs. Therefore, the observed maximum contamination of 27% in VR-DF and 14% in VR-SS is within reason for the analysis. Along with the data vs. MC plots, these checks confirm the validity of proceeding with the background estimation as established in this section.

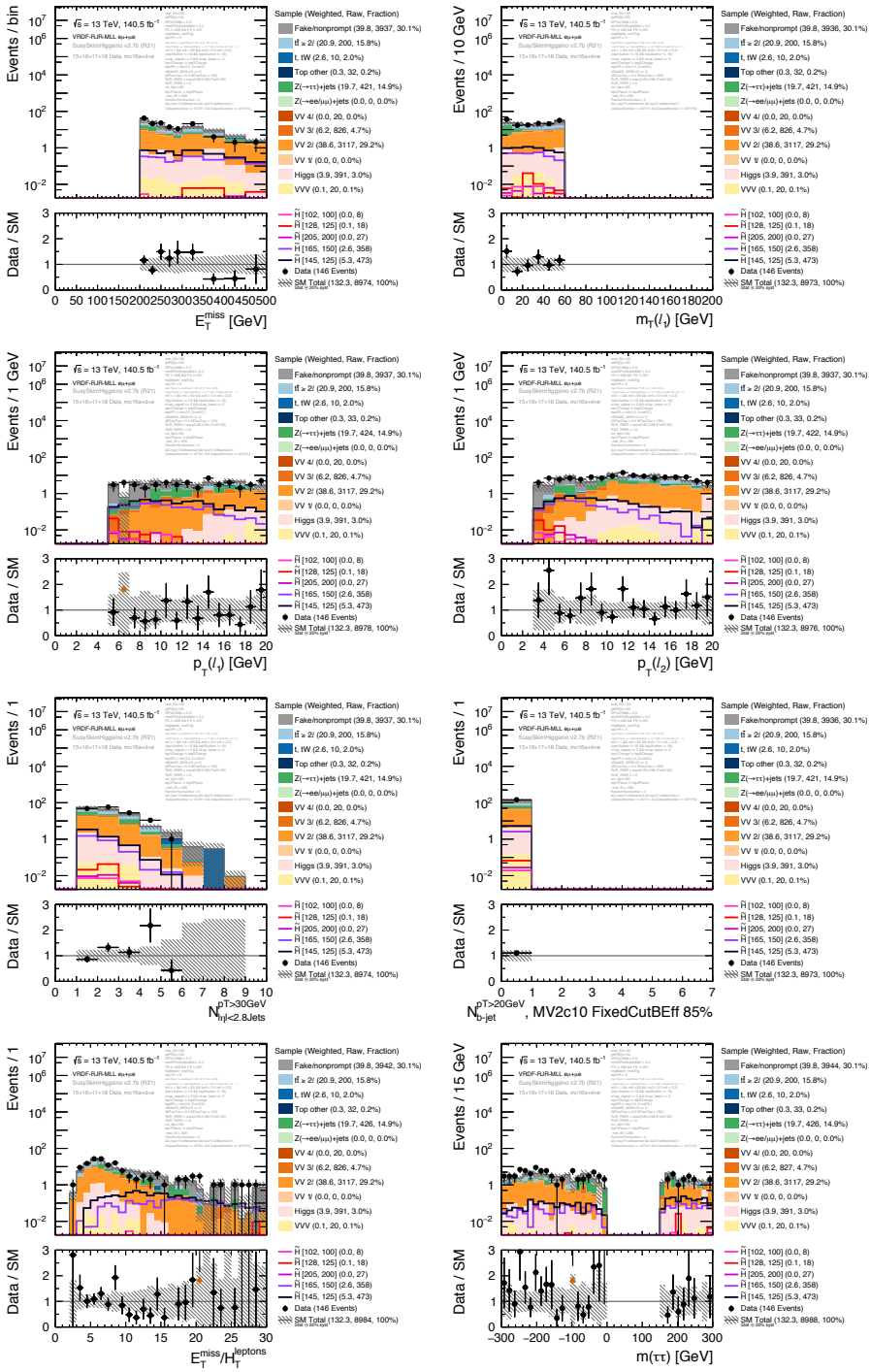


Figure 10.20: Distributions of analysis variables in high-E_T^{miss} higgsino different flavor validation region.

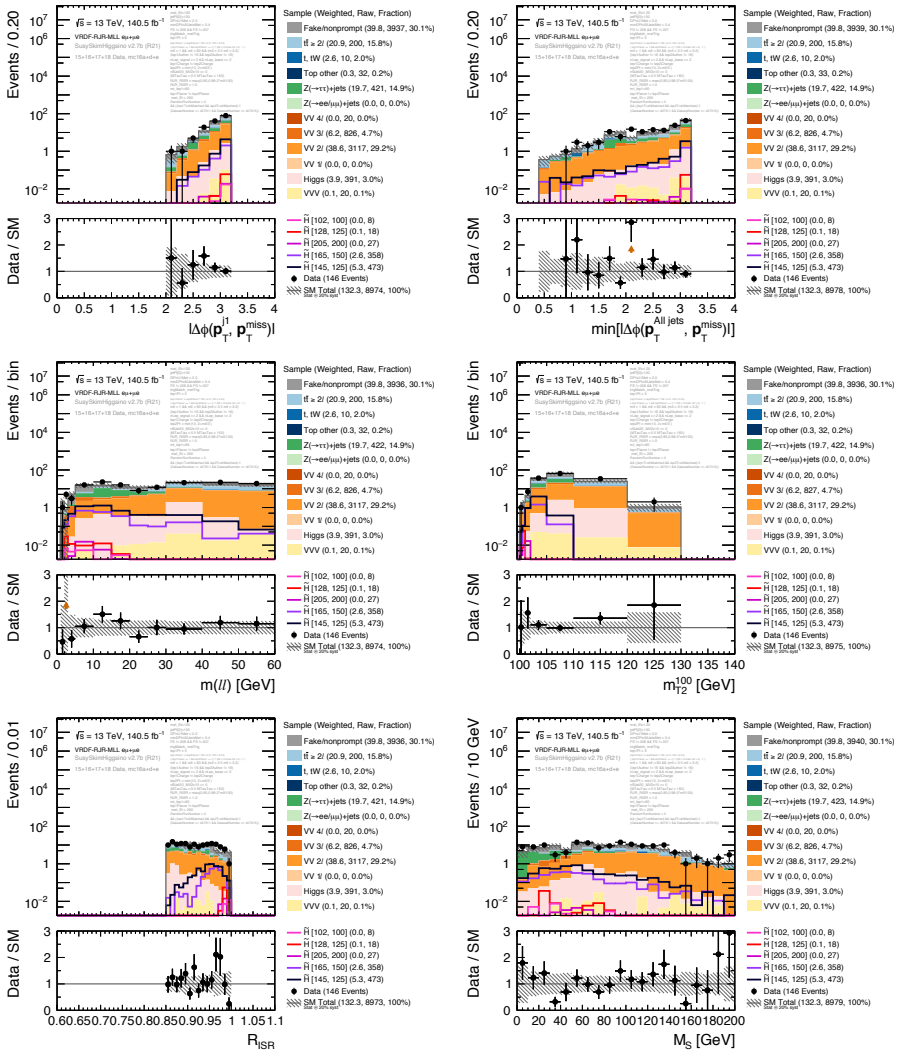


Figure 10.21: Distributions of analysis variables in high-E_T^{miss} higgsino different flavor validation region.

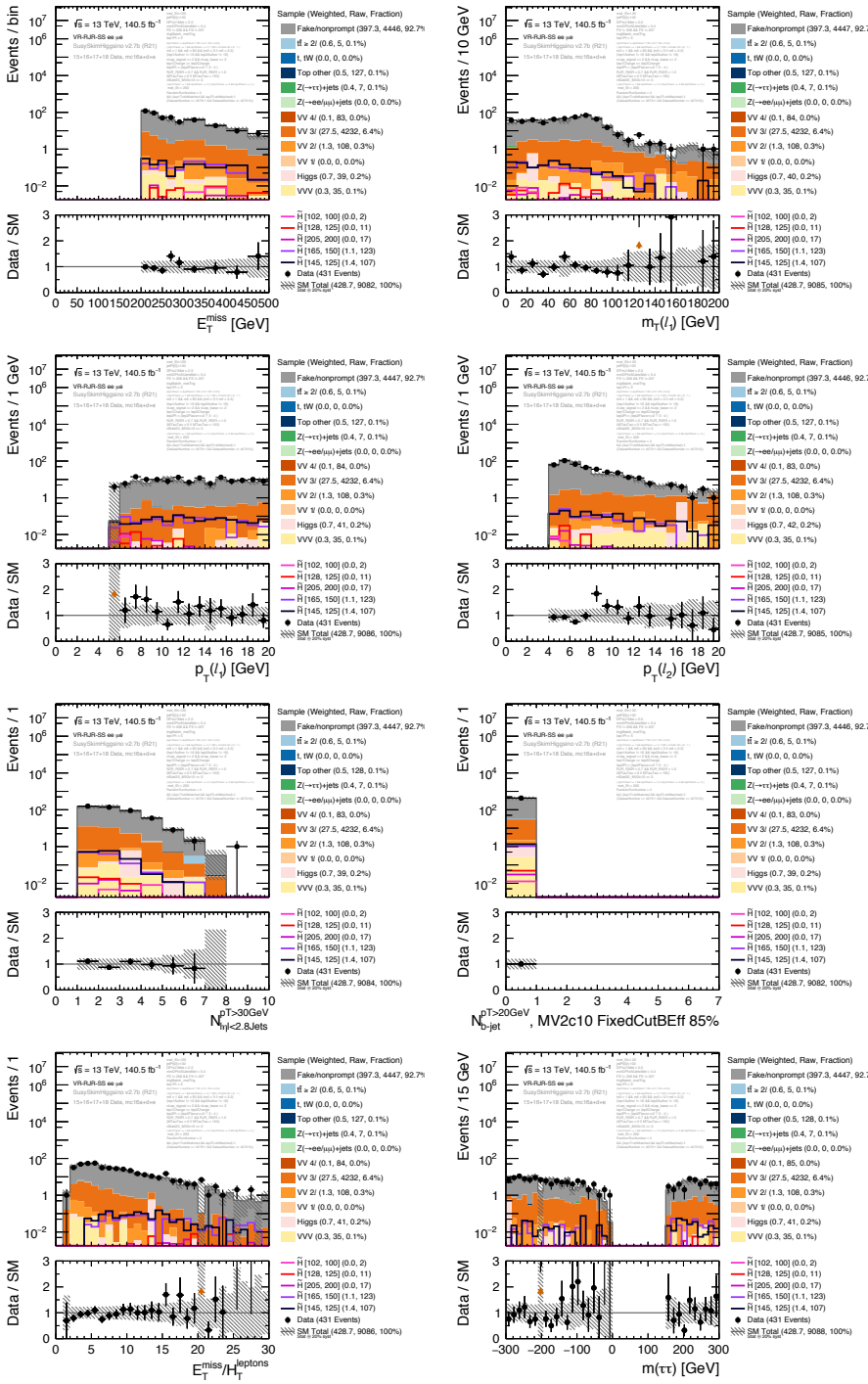


Figure 10.22: Distributions of analysis variables in the $ee + \mu e$ channel of the high-E_T^{miss} higgsino same-sign validation region.

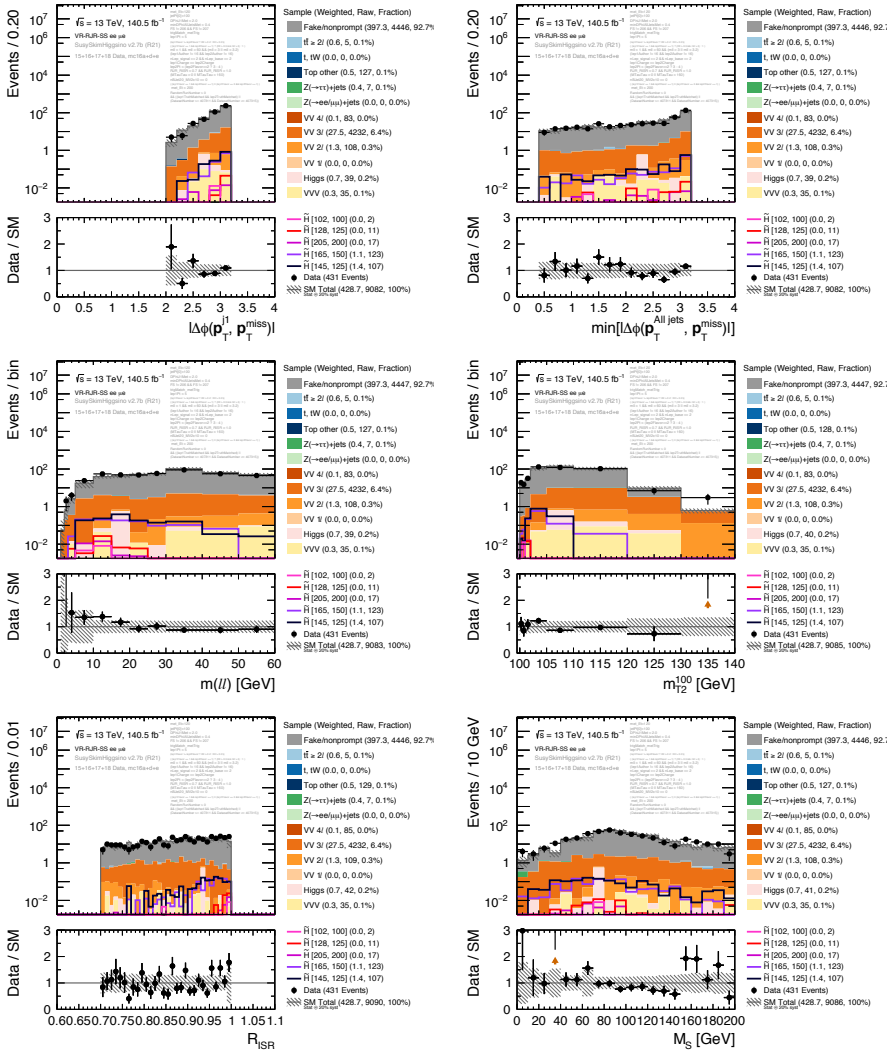


Figure 10.23: Distributions of analysis variables in the $ee + \mu e$ channel of the high-E_T^{miss} higgsino same-sign validation region.

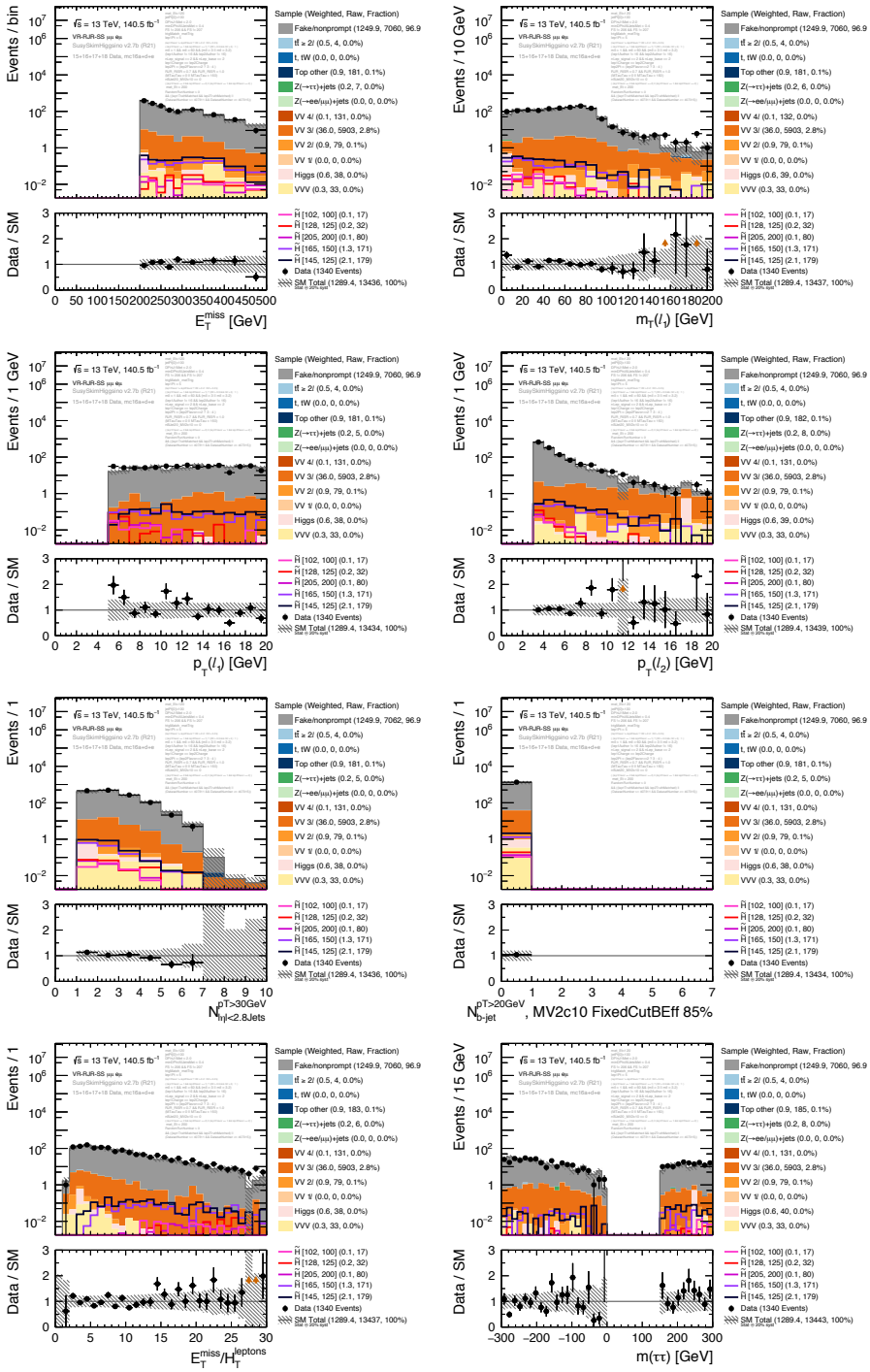


Figure 10.24: Distributions of analysis variables in the $\mu\mu + e\mu$ channel of the high-E_T^{miss} higgsino same-sign validation region.

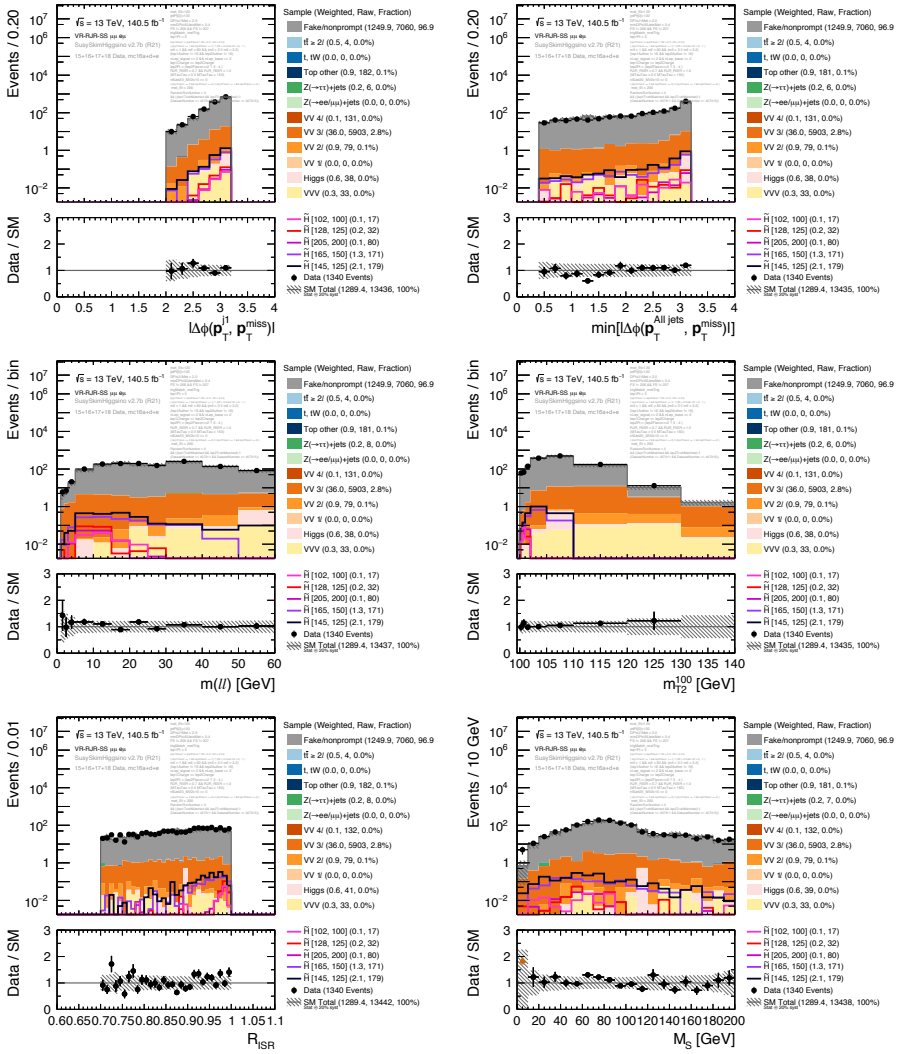


Figure 10.25: Distributions of analysis variables in the $\mu\mu + e\mu$ channel of the high-E_T^{miss} higgsino same-sign validation region..

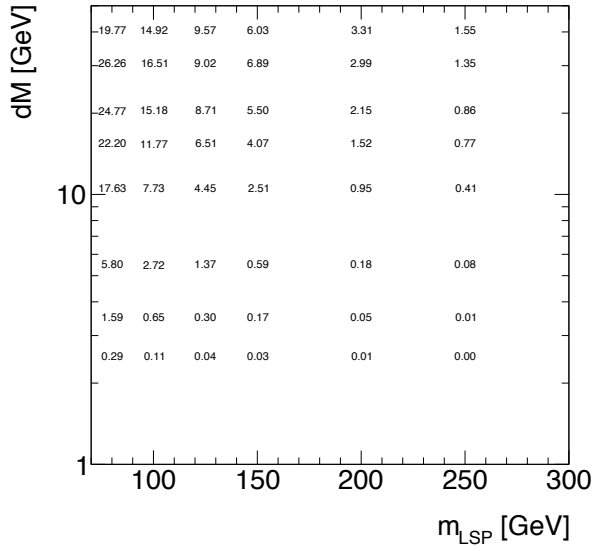


Figure 10.26: Contamination of signal in VR-DF across full higgsino signal grid.

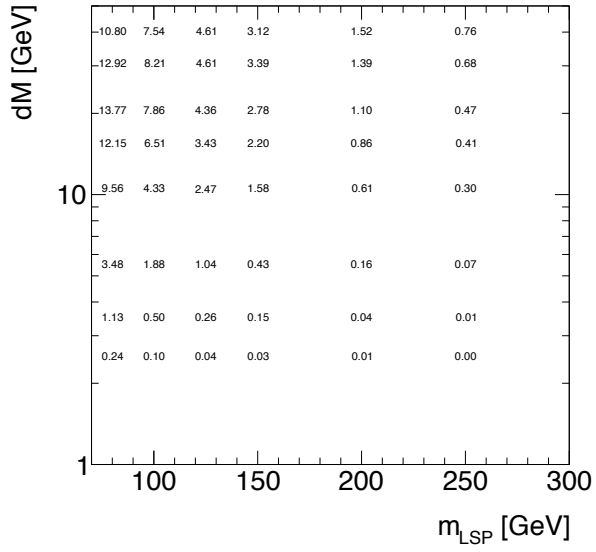


Figure 10.27: Contamination of signal in VR-SS across full higgsino signal grid.

10.5 Systematic Uncertainties

As with the stop analysis, two categories of systematic uncertainties are estimated in the analysis: experimental (from detector simulation, accelerator conditions, and data-driven estimate effects) and theoretical (pertaining to Monte Carlo simulation features). Theoretical uncertainties can further be sorted into those that affect the background and signal samples. Since predictions for the main SM backgrounds are normalized in control regions, the systematic uncertainties only affect the extrapolation to the signal region for these processes.

10.5.1 Experimental

Experimental uncertainties are provided by dedicated working groups in ATLAS, which divide the uncertainties based on their origin from the various detector subsystems. The list of considered systematics provided by these groups and considered in this analysis, categorized by source, are as follows:

- Uncertainty on the pileup re-weighting procedure, which is performed on the simulation to ensure that the distribution of $\langle\mu\rangle$ (average number of interactions per bunch crossing) is consistent to that of data.
- Jet energy scale and resolution (JES/JER) uncertainties [73], with additional uncertainties estimated for the effects of the JVT pileup mitigation procedure, and the efficiency of the b-tagging identification algorithm.
- Electron/muon scale and resolution uncertainties, and uncertainties on the scale factors on simulation that match soft lepton characterization efficiencies achieved in data.
- E_T^{miss} uncertainties, which come from propagating the uncertainties on momenta of hard objects considered in the missing energy calculation, as well as uncertainties on the scale and

resolution of the soft term.

- Uncertainty on the total luminosity for the Run II dataset [122], which is derived via luminosity scale calibration to be 1.7%.

Systematics from the fake factor method also constitute a large source of uncertainty in the analysis. The following sources are considered:

- Statistical uncertainty on the measured fake factors, arising from the potentially limited samples sizes of single lepton-triggered dijet data used for measurement.
- Uncertainties due to kinematic dependencies of the fake factors.
- Non-closure in VR-SS, which accounts for slight inexact features of the fake modeling in the same-sign validation region.
- Uncertainties from the prompt lepton MC subtraction, which are found to be negligible.

10.5.2 Theoretical

Systematics on background sources include uncertainty on the value of the strong coupling constant α_s, the choice of QCD renormalization and factorization scales, and the choice of parton distribution functions (PDFs). These are estimated using variations in the Monte Carlo samples, by either symmetrizing the difference between high and low variations on the nominal, or taking the envelope of several variations corresponding to different generator parameter choices. Estimates are made for the largest SM processes measured from simulation in the analysis, that is, the top, $Z\rightarrow\ \tau\tau$ + jets, and diboson backgrounds. Variations can be studied and the uncertainty can be estimated on each background in its dedicated CR, and additionally in the VRs and SRs.

Figures 10.28, 10.29, and 10.30 show the m_{ll} distribution in CR-top and the high-E_T^{miss} higgsino SR, with variations overlaid on α_s, QCD renormalization/factorization scales, and PDF scales, respectively. Analogous plots for the Z$\rightarrow \tau\tau$ + jets background can be found in Figures 10.31 to 10.33, and Figures 10.34 to 10.36 for the diboson background. Both electrons and muons are allowed in these plots (including in the signal region selections), because the uncertainties are not expected to be flavor-dependent. The impact of the variation is evaluated directly on the prediction of the background on a bin-by-bin basis, and added to the final likelihood fit as nuisance parameters.

Since the signature of the SUSY signal is fully reliant on boosting from an ISR system, modeling of ISR in MC is a dominant theoretical uncertainty for the signals. Other theoretical uncertainties such as those on cross section and PDF acceptance are also evaluated, and are typically small.

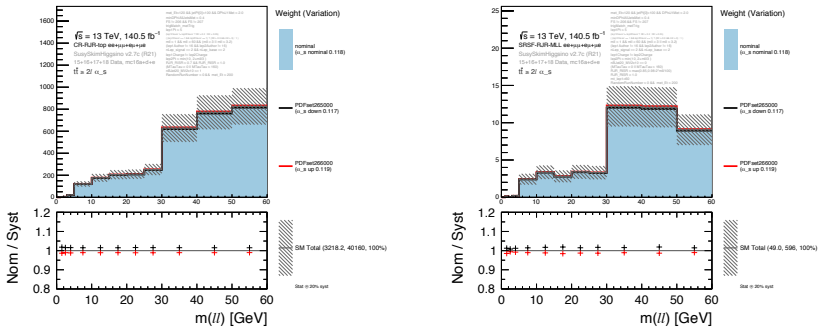


Figure 10.28: Variations of α_s for the $t\bar{t}$ background, in CR-top (left) and the high-E_T^{miss} all flavor higgsino SR (right).

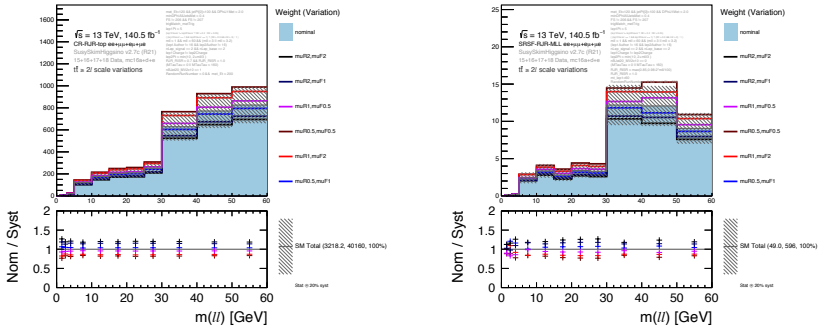


Figure 10.29: Variations of QCD renormalization/factorization scales for the $t\bar{t}$ background, in CR-top (left) and the high-E_T^{miss} all flavor higgsino SR (right).

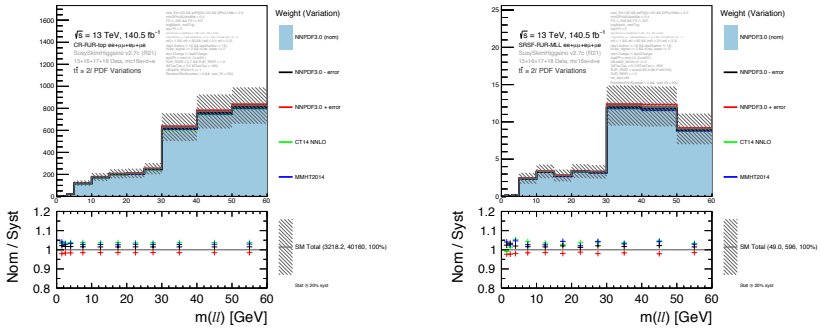


Figure 10.30: Variations of PDFs for the $t\bar{t}$ background, in CR-top (left) and the high-E_T^{miss} all flavor higgsino SR (right).

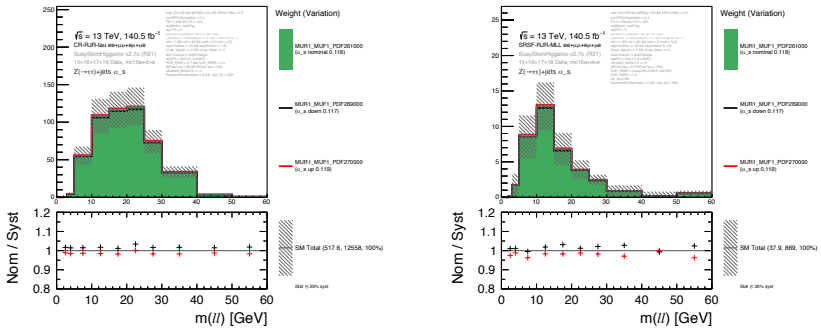


Figure 10.31: Variations of α_s for the Z$\to\ \tau\tau$ + jets background, in CR-tau (left) and the high-E_T^{miss} all flavor higgsino SR (right).

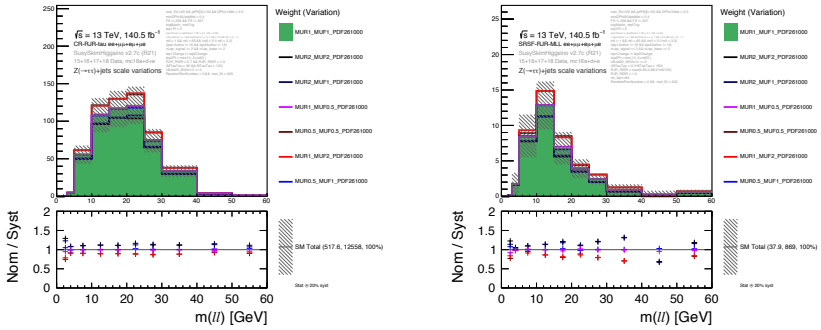


Figure 10.32: Variations of QCD renormalization/factorization scales for the Z$\to\ \tau\tau$ + jets background, in CR-tau (left) and the high-E_T^{miss} all flavor higgsino SR (right).

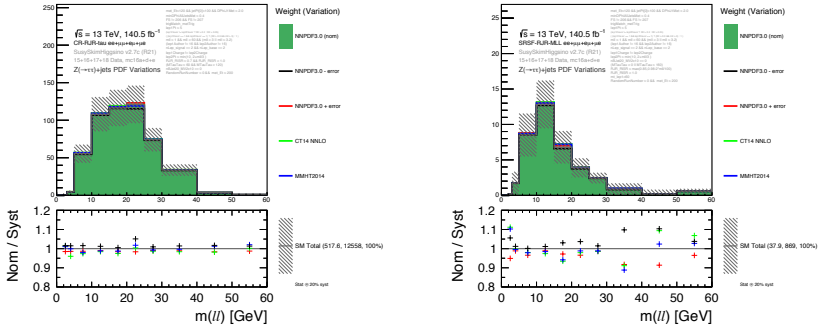


Figure 10.33: Variations of PDFs for the Z$\to\ \tau\tau$ + jets background, in CR-tau (left) and the high-E_T^{miss} all flavor higgsino SR (right).

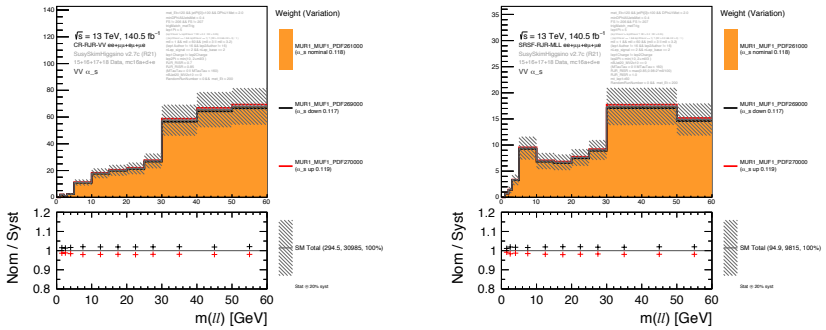


Figure 10.34: Variations of α_s for the diboson background, in CR-VV (left) and the high-E_T^{miss} all flavor higgsino SR (right).

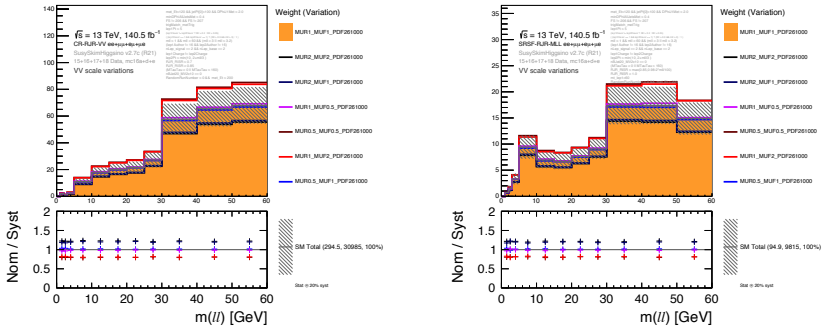


Figure 10.35: Variations of QCD renormalization/factorization scales for the diboson background, in CR-VV (left) and the high-E_T^{miss} all flavor higgsino SR (right).

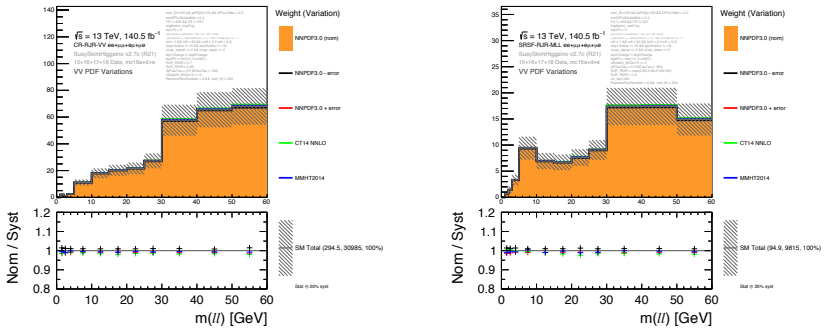


Figure 10.36: Variations of PDFs for the diboson background, in CR-VV(left) and the high-E_T^{miss} all flavor higgsino SR (right).

To determine if the choice of generator (`Powheg+Pythia` vs. Sherpa) for the diboson background constitutes a considerable systematic, the direct ratio of diboson control region to all-flavor signal region yields is assessed as a function of m_{ll}. Figure 10.37 shows this SR to CR ratio across all m_{ll} bins, along with the ratio of nominal to alternate generator in the lower panel. General agreemen between the two generators, in particular across the m_{ll} spectrum, indicates that no further determination of a generator systematic is required.

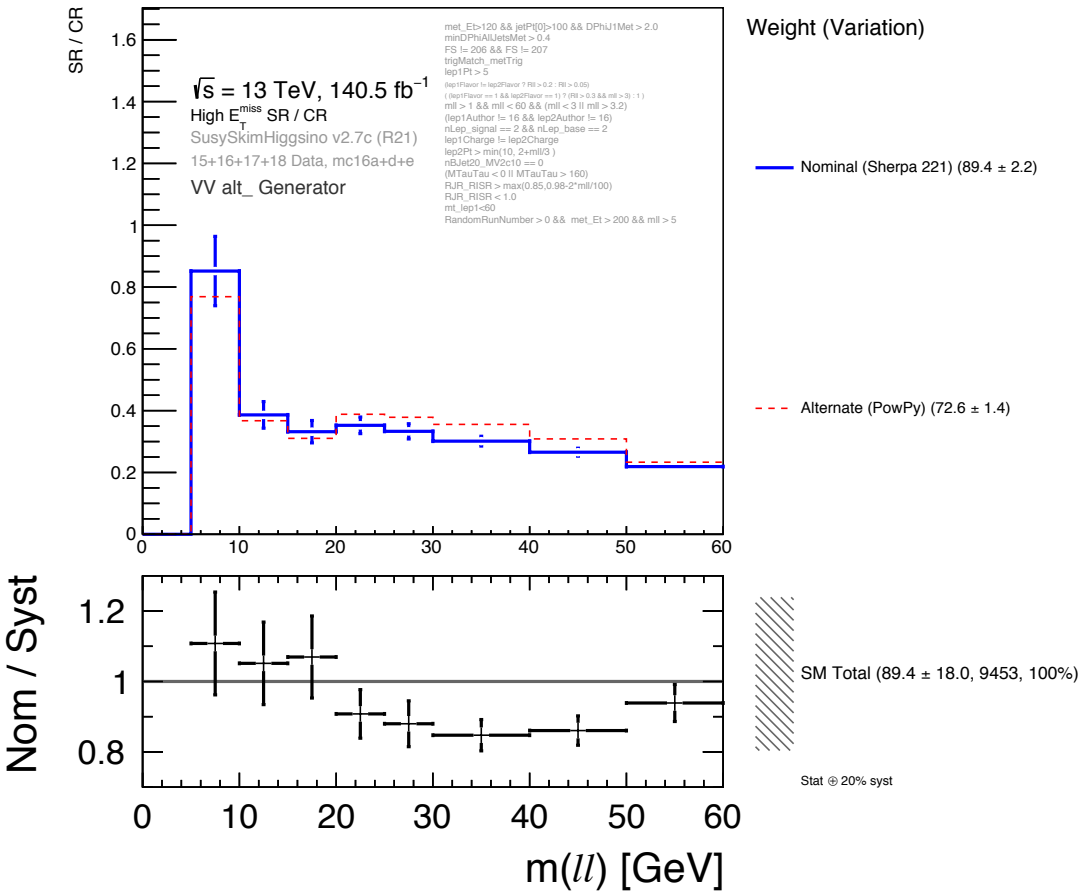


Figure 10.37: Variations of PDFs for the diboson background, in CR-VV(left) and the high-E_T^{miss} all flavor higgsino SR (right).

10.5.3 Summary

Figure 10.38 provide a condensed breakdown of the systematics in all three higgsino SRs, for each m_{ll} bin. Experimental uncertainties are grouped into those associated to the fake factor method, statistical, experimental (including jet uncertainties), normalization, modeling, and same-sign (SS) data extrapolation uncertainties for the opposite-sign (OS) 1L+track analysis (see B.2 for details.) It is evident from this figure that the fake/non-prompt background estimation is the primary source of uncertainty.

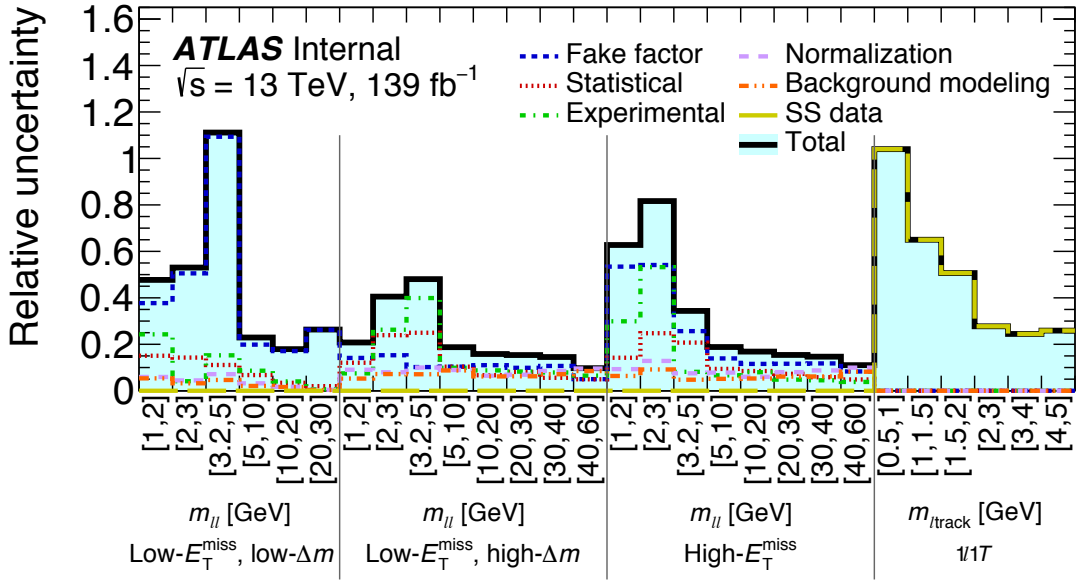


Figure 10.38: Relative systematic uncertainties as obtained from background-only fits on the background prediction in the electroweakino SRs. Individual uncertainties can be correlated and do not necessarily add up in quadrature to the total uncertainty.

10.6 Results

The results of the analysis are organized as follows. Several cross-checks from the background-only fit with blinded SRs are shown first, to validate the fit setup and constrain fit parameters. Next the SRs are unblinded in the background-only fit, and results are shown in the form of signal region data vs. MC distributions and pull plots, to determine compatibility of data to background prediction in the SRs. Finally, model-dependent exclusions are shown for higgsino simplified models, using a shape fit in m_{ll}. Definitions and details of all profile likelihood fits as performed by `HistFitter` can be found in Chapter 8.

All fits in the analysis were performed using a pruned setup, in that any variation that deviates less than 3% from the nominal is removed from the likelihood. A simultaneous fitting of the high-E_T^{miss} higgsino regions is performed with orthogonal low-E_T^{miss} and 1L+track regions, which have analogous construction of signal, control, and validation regions. Additional material on the low-E_T^{miss} and 1L+track regions can be found in Appendix B.

Low statistics in MC background predictions for some SR bins led to unwanted effects of the jet uncertainties, and large unphysical increases of the background prediction after the fit. This motivated the use of an extended set of jet uncertainties, ultimately considering 35 independent sources. Additionally, a systematics smoothing procedure was implemented, in which the jet systematics are removed from samples with a very large statistical uncertainty in affected bins. They are replaced by a flat 30% uncertainty, which is roughly the size of a single jet uncertainty in this phase space. The affected bins and samples are the low-H_T $Z\rightarrow\ \tau\tau$ + jets sample for all m_{ll} bins, and the top and

Normalization Factor	Value
$\mu_{t\bar{t}}$	1.07 ± 0.04
$\mu_{Z\to\tau\tau+jets}$	0.95 ± 0.09
μ_{VV}	0.88 ± 0.19

Table 10.7: Normalization factors of the high-E_T^{miss} higgsino control regions, in a CR-only fit.

Z$\to \tau\tau$ + jets samples in bin eMLLc of the ee channel, corresponding to [5, 10] GeV in m_{ll}.

10.6.1 Background-Only Fits

Before unblinding the signal region, it must be verified that the fit configuration is functional and providing reasonable results. Several validation checks are performed using only data in the CRs ("background-only") to do so. Normalization factors μ for the top, Z $\to \tau\tau$ + jets, and diboson backgrounds are determined at this stage, using data in the corresponding control regions. These factors are then used to normalize their respective samples in the signal regions. Table 10.7 provides the obtained μ values for these three backgrounds and their uncertainties. No unusual values are found that deviate significantly from 1, and no significant constraints or correlations are found on the nuisance parameters.

The values of the normalization factors and nuisance parameters as determined by the background-only fit can be further validated by extrapolating to the VR-DFs. This is done by testing the ability of the obtained background normalization to predict the data in the VR-DFs. Discrepancies are quantified by the magnitude of the *pull* χ, defined in Equation 10.4:

$$\chi = \frac{n_{observed} - n_{predicted}}{\sigma_{tot}} \tag{10.4}$$

Here, $\sigma_{tot} = \sqrt{\sigma^2_{predicted} + \sigma^2_{stat,exp}}$ is the sum in quadrature of the total systematic uncertainty on the background prediction and the expected statistical uncertainty on the background prediction (taken as the Poissonian variation on the expected number of background events). Figure 10.39 shows the data and MC prediction in all higgsino VR-DF m_{ll} bins (both high- and low-E_T^{miss}), as well as the pulls (significance) for each bin. No general misestimation of the data is present. Therefore, the background estimation is found to be reliable in the relevant phase space.

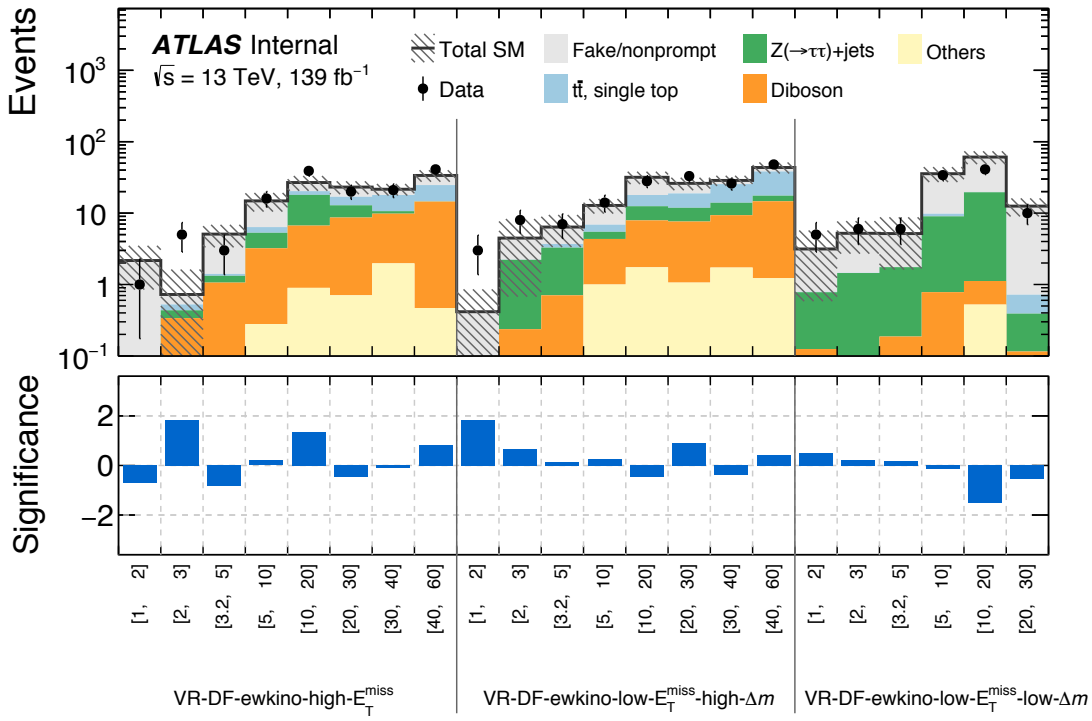


Figure 10.39: Data vs. MC in the higgsino different flavor validation regions & corresponding pulls per bin.

Once the signal regions are unblinded, the background prediction from the background-only fit is then extrapolated to the SRs in a similar manner as the check for VR-DFs. Figure 10.40 shows the data and MC prediction and pulls in all higgsino SR m_{ll} bins (both high- and low-E_T^{miss} and

1L+track). Deviations of data from background prediction have a significance less than 2σ. The largest deviation is observed in the eMLLc bin of the high-E_T^{miss} ee channel, corresponding to [5, 10] GeV in m_{ll}; this is interpreted as a statistical fluctuation.

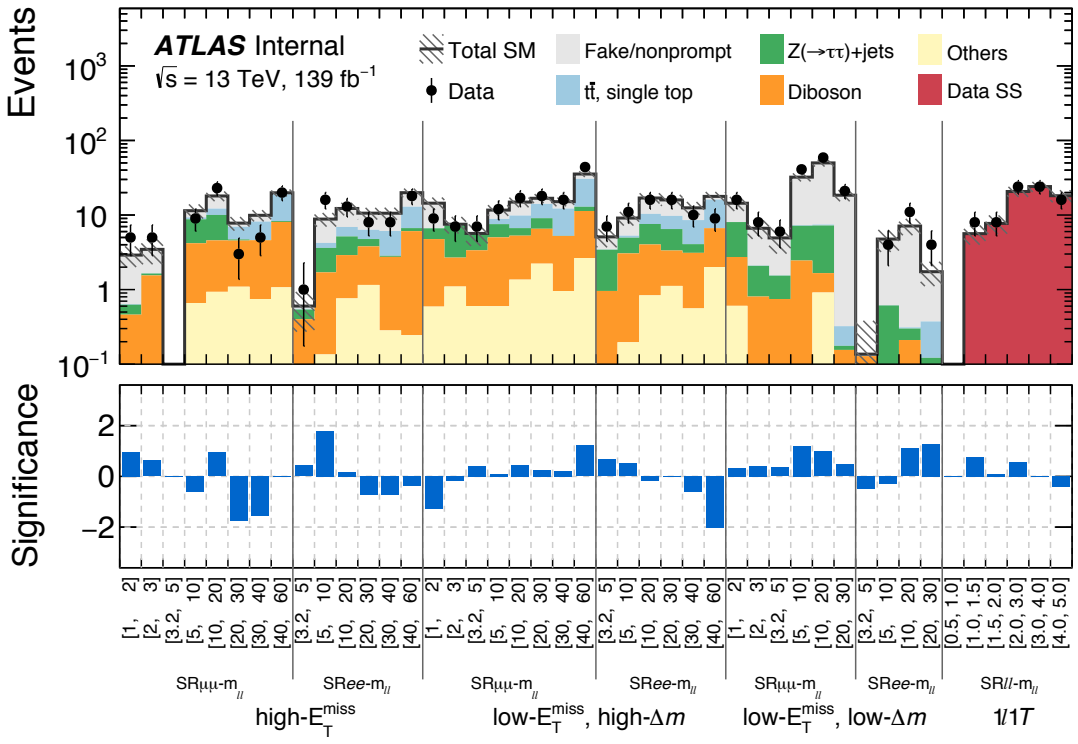


Figure 10.40: Data vs. MC in the unblinded higgsino signal regions & corresponding per-bin significance of the deviation of observed from expected yield. Uncertainties shown include both statistical and systematic uncertainties.

Kinematic distributions in the SRs are also examined to further study the agreement of data to background prediction. Figures 10.41 to 10.43 show unblinded distributions of key analysis variables (inclusive in m_{ll}) in the high-E_T^{miss} higgsino SR. Good agreement is seen between data and background predictions in both shape and normalization of the analysis variables.

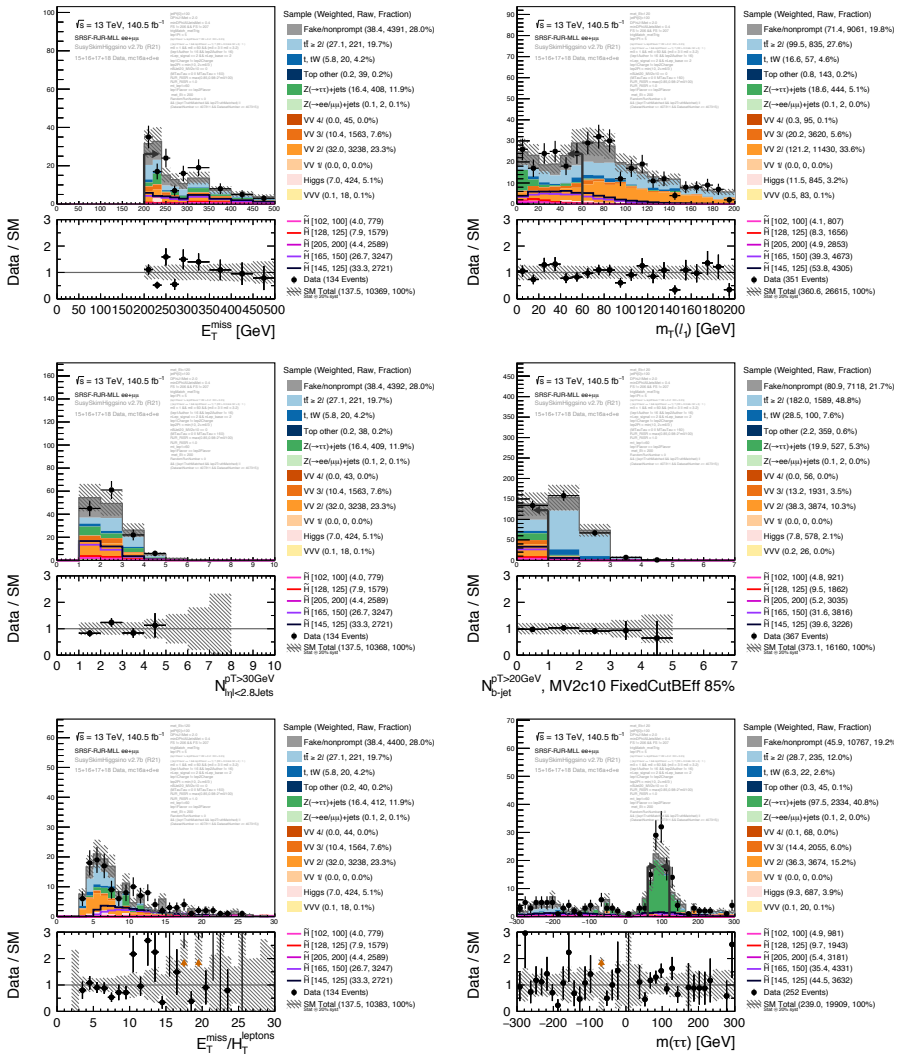


Figure 10.41: Unblinded distributions in the high-E_T^{miss} higgsino SR.

10.6.2 Model-Dependent Results

Interpretations of the results in the context of higgsino simplified models are performed combining the high- and low-E_T^{miss} and 1L+track regions. These model-dependent results are generated via exclusion fits, which perform hypothesis tests to determine the confidence of the exclusion for each

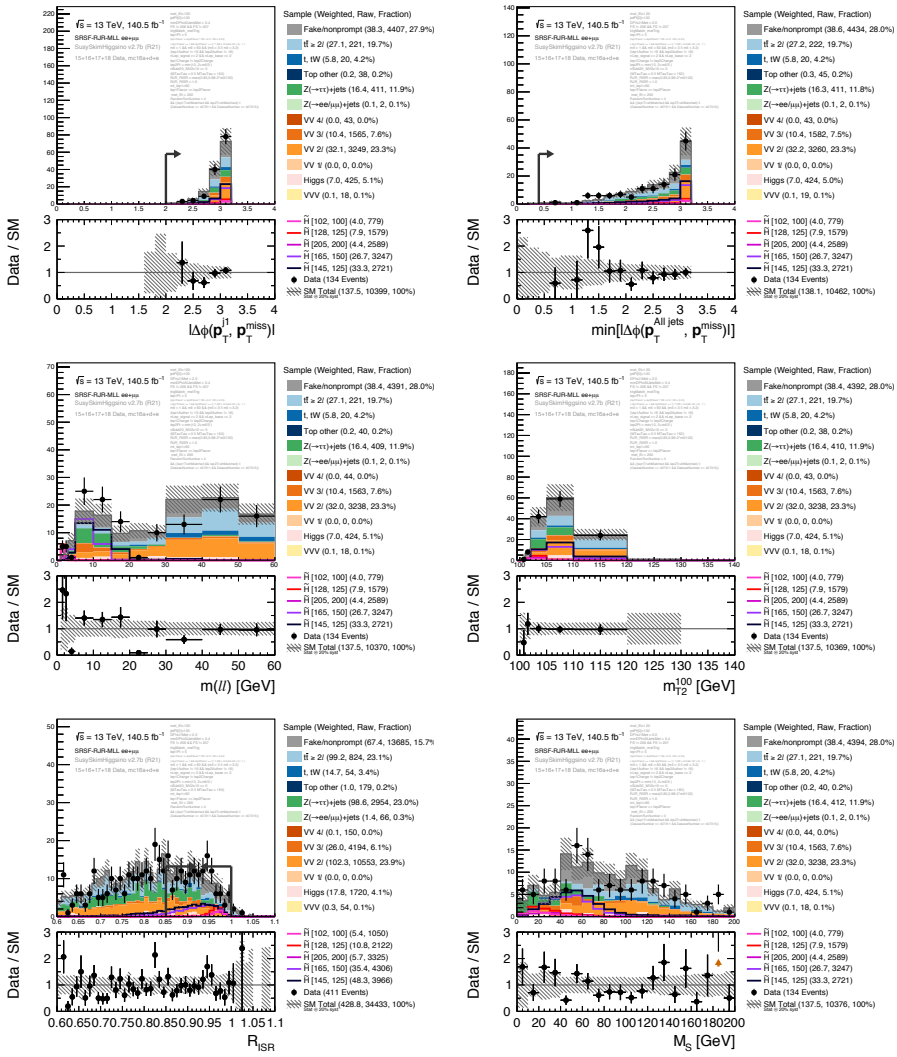


Figure 10.42: Unblinded distributions in the high-E_T^{miss} higgsino SR.

signal point using the CLs prescription. Exclusion fits are run with the asymptotic approximation in `HistFitter` rather than pseudo-experiments to improve performance [92].

Figure 10.44 shows the 95% confidence level exclusion contours for the $\widetilde{\chi}_2^0$-$\widetilde{\chi}_1^0$ mass splitting as a function of $\widetilde{\chi}_2^0$ mass. This exclusion combines all three dedicated higgsino analysis. The observed

limit is seen to be weaker than the expected, due to the presence of upward fluctuations in the SRs.

The choice of exclusion shown for $\widetilde{\chi}_2^0$ masses differs from that of the LEP exclusion for $\widetilde{\chi}_1^\pm$ masses, shown in Figure 3.3. Given the dependence of the analysis on the decay products of the off-shell Z^0, this search is more sensitive to the $\widetilde{\chi}_2^0$-$\widetilde{\chi}_1^0$ splitting. However, given the set convention of the $\widetilde{\chi}_1^\pm$ mass being halfway between $\widetilde{\chi}_2^0$ and $\widetilde{\chi}_1^0$ masses, these limits can be translated between one another. Excluded mass ranges are presented here for charginos to generate easy comparison to previous limits.

Lower limits on chargino mass range from 162 GeV to 205 GeV (depending on the simplified model used) for moderate mass splittings, and extend down to mass splittings of approximately 2 GeV at the LEP chargino bounds. With respect to the previous result shown in Figure 3.4, this represents an increase of about 20-40 GeV in excluded chargino mass range. This illustrates the added sensitivity achieved from the addition of 1L+track and low-E_T^{miss} regions in the fit. The exclusion given here represents the first full Run II ATLAS result for direct higgsino production, and constitutes the best ATLAS constraint on this process to date.

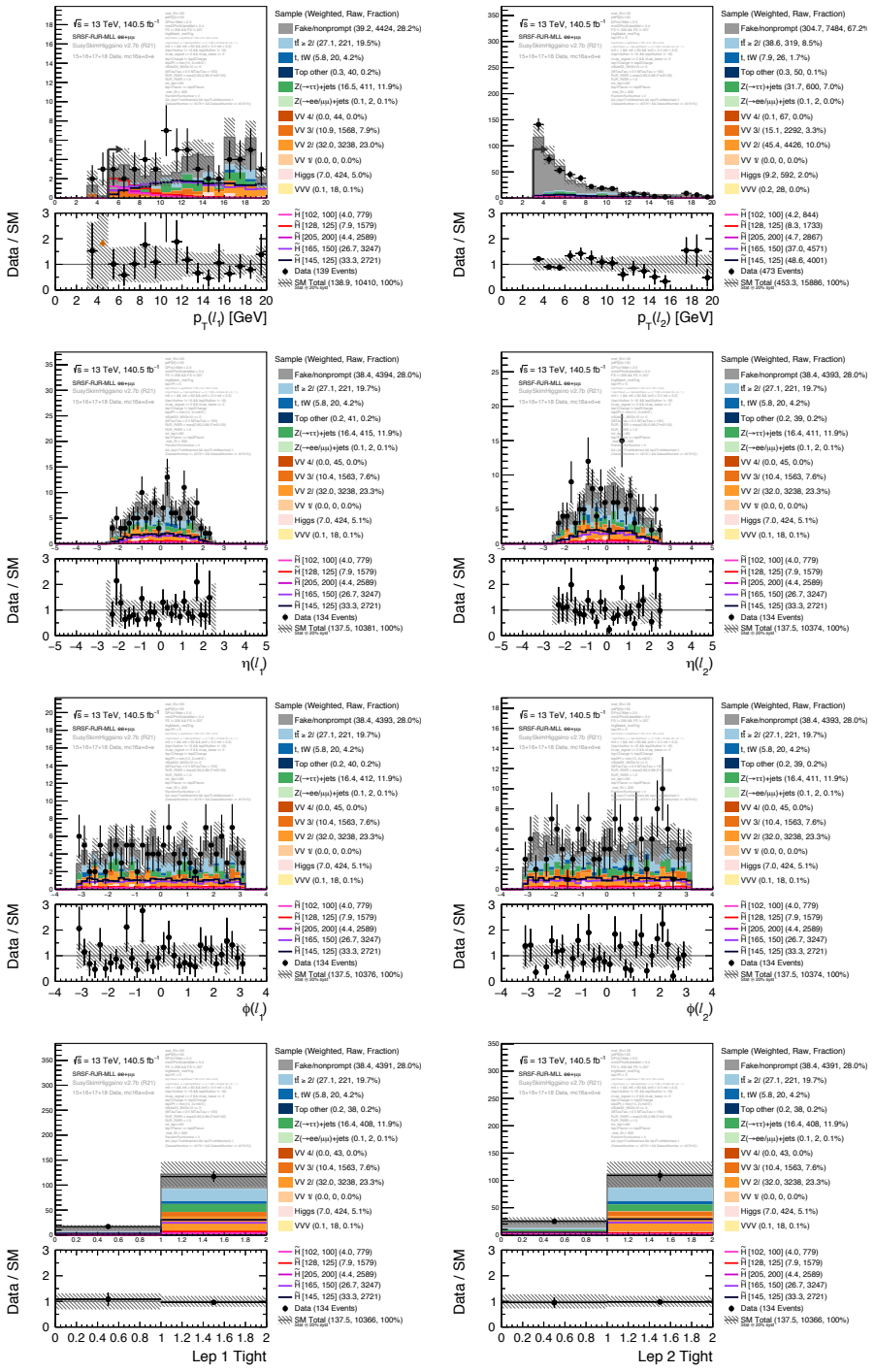


Figure 10.43: Unblinded distributions in the high-E_T^{miss} higgsino SR.

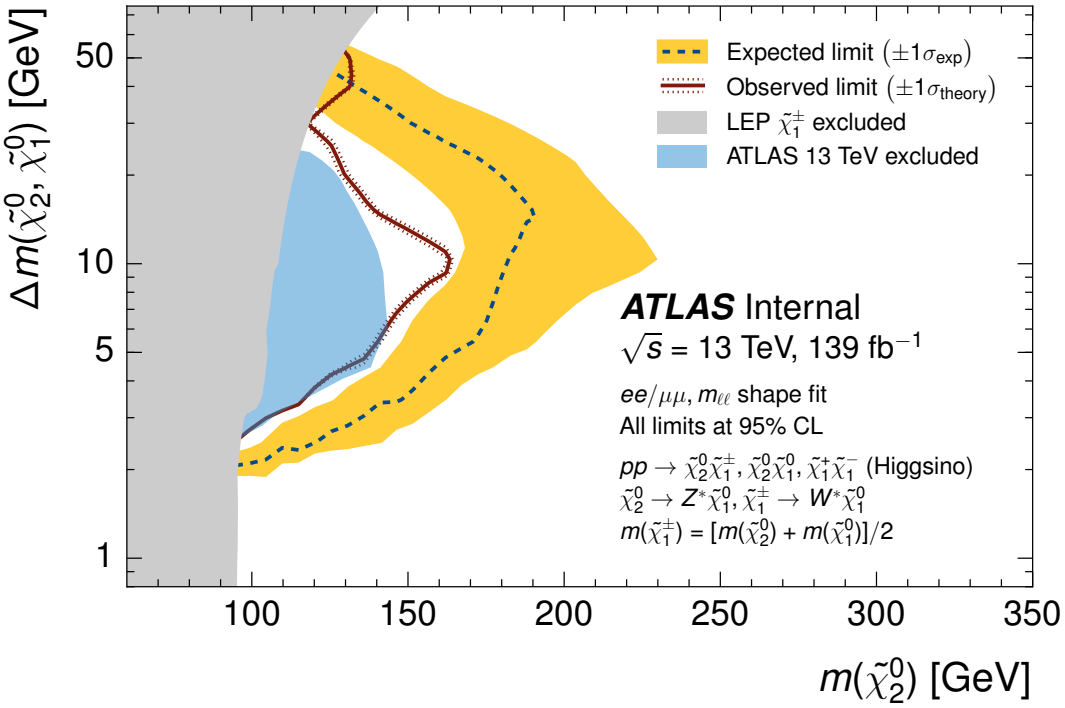


Figure 10.44: Expected and observed exclusion contours for the higgsino signal grid as a function of mass splitting and $\tilde{\chi}_2^0$ mass, combining low- and high-E_T^{miss} SRs. The CLs value obtained from the hypothesis test is shown for each signal point.

Part V

Outlook

11

Future Efforts

As discussed earlier in this thesis, the next several decades of high energy collider physics have already been outlined. After the conclusion of the Phase-I upgrade during Long Shutdown 2 (LS2), Run III of the LHC will begin. Though the increase in collision energy is relatively modest, going from $\sqrt{s}$ = 13 TeV to 14 TeV, the total integrated luminosity of the LHC proton collision

dataset will approximately double, making the next several years promising for search prospects of natural SUSY.

Additionally, subsystem upgrades installed during LS2 will enhance the detection capability of the ATLAS experiment, aiding reconstruction and enabling more sophisticated analysis development. For example, new proposed triggers that make use of the L1Calo and FTK Phase-I upgrades aim to boost search sensitivity beyond the inherent gains from added luminosity.

After Run III, another shutdown (LS3) is scheduled, followed by Run IV, which marks the official beginning of the HL-LHC. The dataset gains from this undertaking are impressive; estimates of the integrated luminosity delivered by the HL-LHC are currently at 3000 fb^{-1}, a nearly twenty-fold increase with respect to the full Run II dataset. For the processes discussed in this thesis with very low production cross sections, this huge new dataset is especially valuable.

Sensitivity studies are already underway to determine the potential mass reach of SUSY searches with this large amount of data. To establish expectations for the discovery (or eventual invalidation) of natural SUSY, the stop and higgsino mass reaches are especially compelling. Figure 11.1 provides an estimated exclusion for the $\tilde{t} \to t\widetilde{\chi}_1^0$ process with 3000 fb^{-1} of data in a zero lepton final state, at both 95% confidence and at 5σ discovery level. Figure 11.2 shows the expected exclusion for the soft dilepton higgsino search at the same luminosity, including the expectation from the disappearing track analysis. Both stop and higgsino exclusions utilize similar construction to the existing versions of the relevant searches, with only slight re-optimizations.

On the stop diagonal defined in Chapter 9, the potential exclusion is as high as 850 GeV in this projection, increasing the current mass reach by almost 300 GeV. The soft dilepton analysis has the

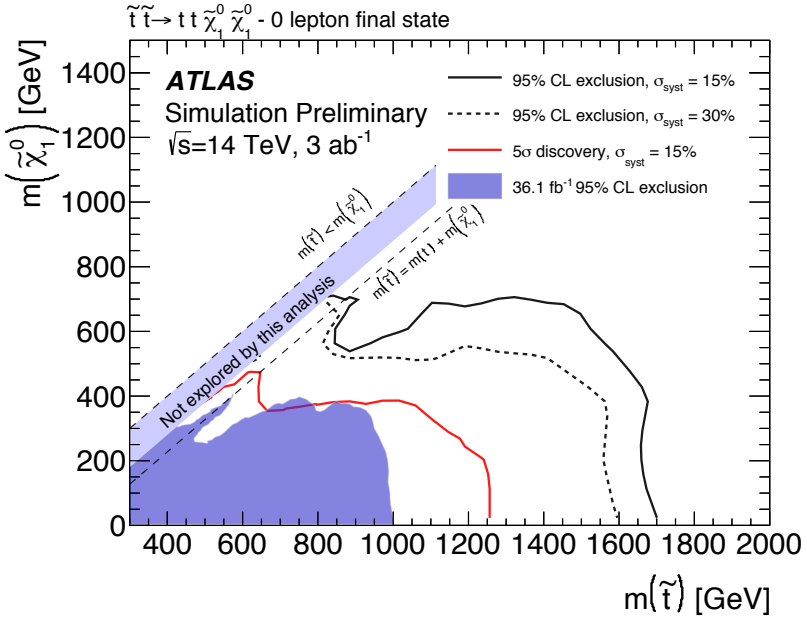


Figure 11.1: Projected 95% CL exclusion reach and 5σ discovery contour utilizing 3000 fb^{-1} of proton-proton collisions collected by ATLAS at the HL-LHC [123].

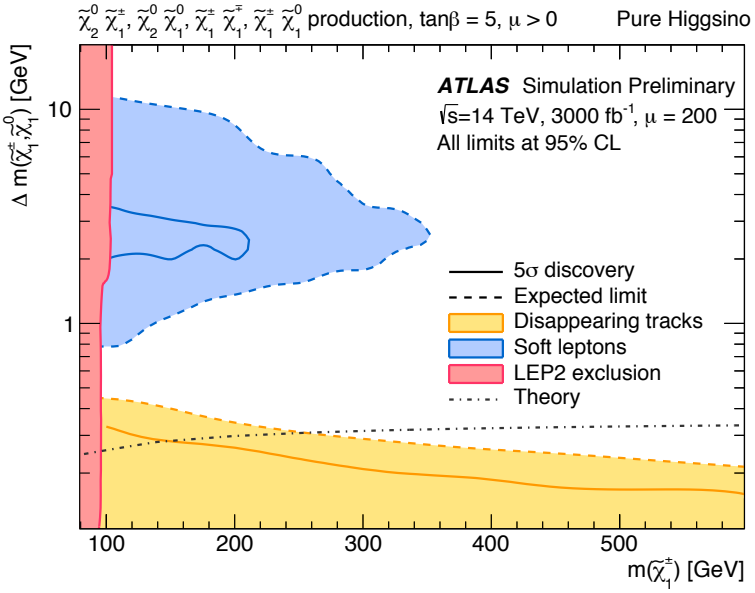


Figure 11.2: Projected exclusions from the disappearing track (yellow) and dilepton (blue) searches, as a function of $\widetilde{\chi}_1^{\pm}$ mass and $\Delta(\widetilde{\chi}_1^{\pm}, \widetilde{\chi}_1^0)$, assuming 3000 fb^{-1} of data [124].

potential to exclude $\widetilde{\chi}_1^{\pm}$ masses up to 350 GeV, more than doubling the upper bound of the current exclusion provided here. Recall that the original naturalness paradigm established in Chapter 2, with an upper bound of 10% fine tuning, predicted viable natural SUSY manifestations up to 1.5 TeV in stop mass and up to a few hundreds of GeV for the higgsino. It is interesting to note that while the full HL-LHC potential will forge significantly into this territory, carrying with it large potential for discovery, it may not be sufficient to fully rule out the natural regime of the theory.

Taken together, these stop and higgsino search expectations constitute a significant knowledge reach promised by the HL-LHC. Combined with the similarly increased observation power of other sparticle searches, such as for squarks/gluinos and long-lived particles, it is certain that the next decade of particle physics will be crucial in the hunt for new physics. The natural cohesion of LHC higgsino searches with dark matter searches, both direct detection and astrophysical, creates even more assurance that the phase space in which these particles could hide is quickly narrowing.

Lastly, these prospects only describe the experimental advances which are known and scheduled. Proposals for the next international collider experiment are proliferating, including the High Energy LHC (HE-LHC) [125] at CERN, the International Linear Collider (ILC) [126] in Japan, and the Circular Electron-Positron Collider (CEPC) [127] in China, along with several other smaller scale experiments focused on specific new physics signatures. Regardless of the ultimate outcome of each novel experimental proposal, the momentum of collider physics at present is sure to carry into the next century, bringing with it a never-ending flow of new ideas and results.

12

Conclusion

Run II of the Large Hadron Collider was unequivocally a triumph. The ATLAS Collaboration has, at the time of this writing, released over two hundred publications over this four year data-taking period, with even more results guaranteed to follow. These include several milestones for the field such as the observation of the Higgs boson decaying to two bottom quarks [128] and the first high-precision measurement of the $W^{\pm}$ boson mass made at the LHC [129].

The story for supersymmetry, once the subject of early Run I excitement, has remained open-ended. In fact, all beyond the Standard Model physics still remains elusive. This serves as an important reminder that the aim of physics research is not necessarily to make discoveries, but simply to determine the truth. In this regard, while the analyses conducted at ATLAS are performed in separate corners by independent groups of researchers, their outcomes taken together are representative of the vast achievements of the field in recent years, in terms of null results as well as observations.

This thesis presents the status of searches for stops and higgsinos, held up as cornerstones of natural SUSY models, from the ATLAS experiment at the conclusion of Run II. Individual analyses for each particle are presented in detail: the stop decaying to a one lepton plus jets final state, and the higgsino decaying to two soft leptons. Both final states also include E_T^{miss} carried away by the lightest supersymmetric particle. The compressed areas of phase space for these two particles are specifically motivated using naturalness arguments, and initial state radiation is found to be useful for boosting a compressed signal, thereby gaining sensitivity. The Recursive Jigsaw Reconstruction method is introduced as a novel way to utilize such a boost for these mass scenarios, and its application is described.

The analysis strategy is common to both stop and higgsino searches. Signal regions are built for the expected signatures, by applying constraints on a variety of kinematic variables in such a way that is consistent with the signal. Dominant Standard Model backgrounds are estimated using data-driven methods, Monte Carlo simulation, or hybrid methods that constrain simulated predictions with data via control regions. All regions enter into a simultaneous likelihood fit to examine agreement of observation with prediction, and produce mass exclusions for the particles of interest. The

contributions of the compressed search regions to the total exclusion are documented and discussed. Both of these results constitute the most sensitive searches to date for the given particles and channels at ATLAS.

No excess of events consistent with the presence of either particle is observed. Combining all ATLAS searches, stops masses up to 1 TeV are excluded for a massless $\widetilde{\chi}_1^0$. For the compressed case, where the mass of the $\tilde{t}$ is approximately equal to the sum of the masses of the t and $\widetilde{\chi}_1^0$, stops are excluded between 235 and 590 GeV [116]. On the electroweak side, the combined exclusion is up to 162 GeV for the mass of the $\widetilde{\chi}_1^{\pm}$ at a mass splitting of 10 GeV, in a simplified model of direct Higgsino production. Mass splittings down to 2.6 GeV are excluded at the LEP chargino mass limit.

These searches will be continually revisited and improved throughout the lifetime of the ATLAS Experiment, and for future experimental generations to come. Given the small production cross section associated to both particles, the expected increase in integrated luminosity from the HL-LHC is especially promising.

Whether future efforts result in a discovery or a series of null results, high energy physics is entering a period of rapid knowledge acquisition. The experimental strategies developed in this thesis will serve as a launching point for more powerful searches in Run III and beyond. Moreoever, various other areas of innovation on the luminosity and astrophysical frontiers are sure to act coherently with collider data, furthering the progress of an increasingly interdisciplinary field marked by boldness and perserverance. It has been, and will continue to be, an exciting time for particle physics.

A

Jet Quality Variables

A.1 Good and Fake Jet Regions

There are several features of a jet that are associated to its origin and can therefore help determine whether it is a hard-scatter (good) or falsely reconstructed (fake) jet. To build an event cleaning procedure that can maintain both a high selection efficiency for good jets and a high rejection rate of fake jets, two regions are defined in data. These regions make use of such discriminating jet features

so that one region is enriched in good jets and the other in fake jets.

A.1.1 Good-Enriched Sample

The good jet region estimates a dijet topology, where both leading jets are balanced and back-to-back in the transverse plane. This is achieved by requiring the following:

- At least two jets with p_T > 20 GeV (JVT > 0.59 for jets with 20 < p_T < 60 GeV and $|\eta|$ < 2.4)
- $\Delta\phi$ > 3.0 between the two leading jets
- Two leading jets balanced in p_T ($(p_T^1$ - $p_T^2)/(p_T^1$ + $p_T^2)$ < 0.3)
- Primary vertex
- Single jet trigger

A.1.2 Fake-Enriched Sample

The fake jet region captures a scenario where a jet is unbalanced or out of time, two key characteristics of jets that come from coherent noise or non-collision background. The requirement that the jet be out of time also helps reduce contamination in this sample from physics processes such as $Z \to \nu\nu$ + jets.

The imbalance is characterized by the missing transverse energy from hadronic activity: H_T^{miss} = $-\Sigma_{jets}\vec{p_T}$, where all jets with p_T > 20 GeV are considered. The timing of a jet t_{jet} is defined as the difference between the calorimeter time (as measured by the trigger) and the energy-squared weighted average of the signal timing in each calorimeter cell: $t_{jet} = \Sigma E_{cell}^2 t_{cell}/\Sigma E_{cell}^2$, where

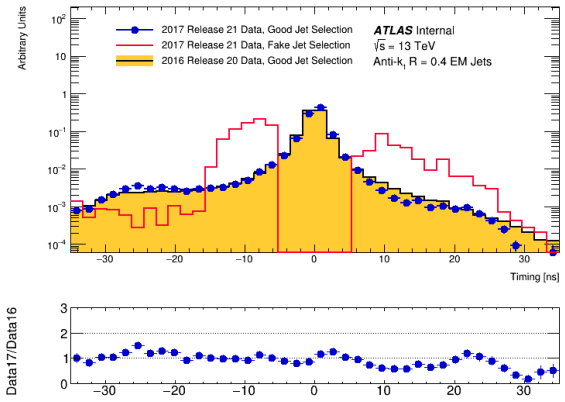


Figure A.1: The distribution of t_{jet} is shown for 2017 release 21 data for good (blue) and fake (red) EM jet samples. 2016 release 20 data is superimposed as a reference (yellow).

all cells with energy from the jet of interest are considered. While good jets are expected to arrive at a time consistent with the primary interaction ($t_{jet} = 0$), in practice good jets can also arrive in adjacent bunch crossings, leading to populations of good jets at $t_{jet} = \pm 25$ ns. Figure A.1 shows the distribution of t_{jet} using data collected by ATLAS in 2017.

The fake-enriched region is defined as follows:

- At least 1 jet with $p_T > 250$ GeV and $|\eta| < 2.4$ (JVT > 0.59 for jets with $20 < p_T < 60$ GeV and $|\eta| < 2.4$)
- $H_T^{miss} > 250$ GeV
- $\Delta\phi > 3.0$ between the leading jet and H_T^{miss}
- $|t_{jet}| > 6$ ns
- E_T^{miss} trigger

A.2 EM Jet Kinematic Variables

Figure A.2 shows kinematic distributions of both good and fake jets. There is no significant shape difference in the p_T spectrum of good and fake jets, so the fake jet distribution is not shown, but comparison of good and fake jets in η and ϕ reveal useful discrepancies. For example, fake jets accumulate at $\phi = 0$ and $\pm\phi$ as a result of material gaps in the cavern that allow more beam-induced background or cosmic muons to reach the calorimeter. Additionally, the beam-induced background peaks at low $|\eta|$ values due to the requirements on the jet transverse momentum and the jet timing as provided in the fake-enriched sample defintion [86].

Figure A.3 shows correlations between kinematic variables in EM jets, as well as timing. Over the course of Run II, increasing populations of hard-scatter jets were noticed in adjacent bunch crossings, that is, at $\pm$ 25 ns. This can be observed in the 2D plot of leading jet timing vs. subleading jet timing. These jets were studied and concluded to be good jets from the cleaning perspective.

A.3 LCW Jet Quality Variables

Analyses that use LCW jets (discussed in Section 5.6) are similarly affected by coherent calorimeter noise and non-collision backgrounds. Investigation of the jet quality variables calculated for LCW jets and tag-and-probe efficiency estimates indicate that the Run 2 cleaning procedure as defined for EM scale jets is sufficient for use in LCW-based analyses.

Figures A.4 and A.5 show all jet quality variable distributions, comparing EM to LCW jets. No significant discrepancies are observed. Figure A.6 shows the tag-and-probe efficiencies for LCW jets,

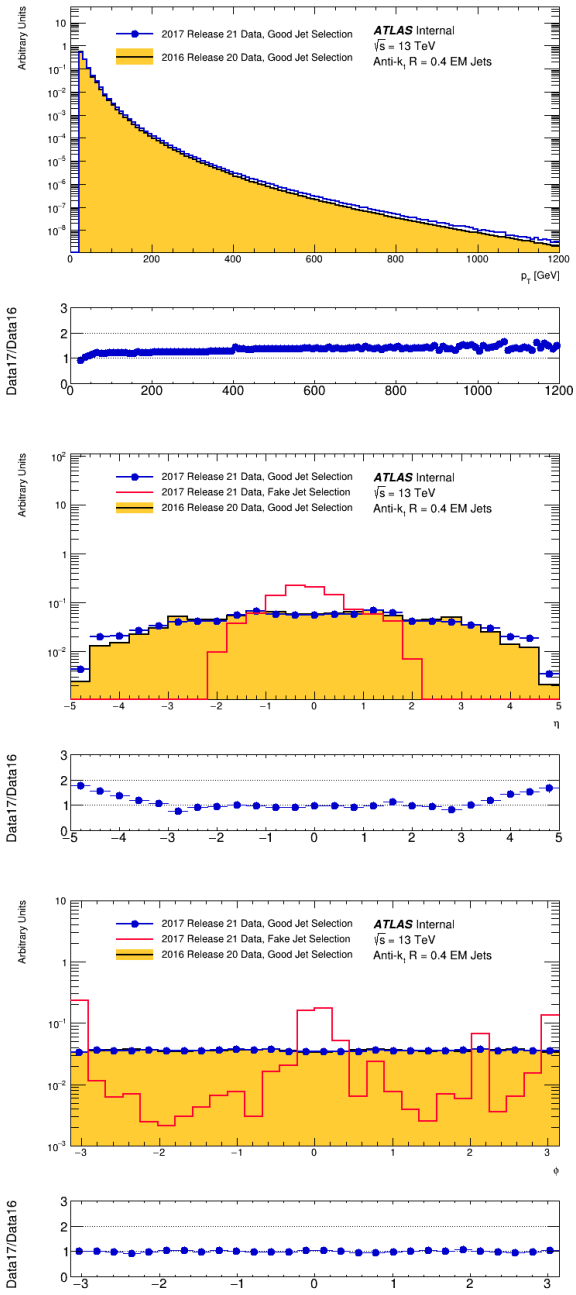


Figure A.2: Distributions of p_T, η, and ϕ are shown for 2017 release 21 data for good (blue) EM jet selections, with fake (red) jets superimposed for η, and ϕ. 2016 release 20 data is superimposed as a reference (yellow).

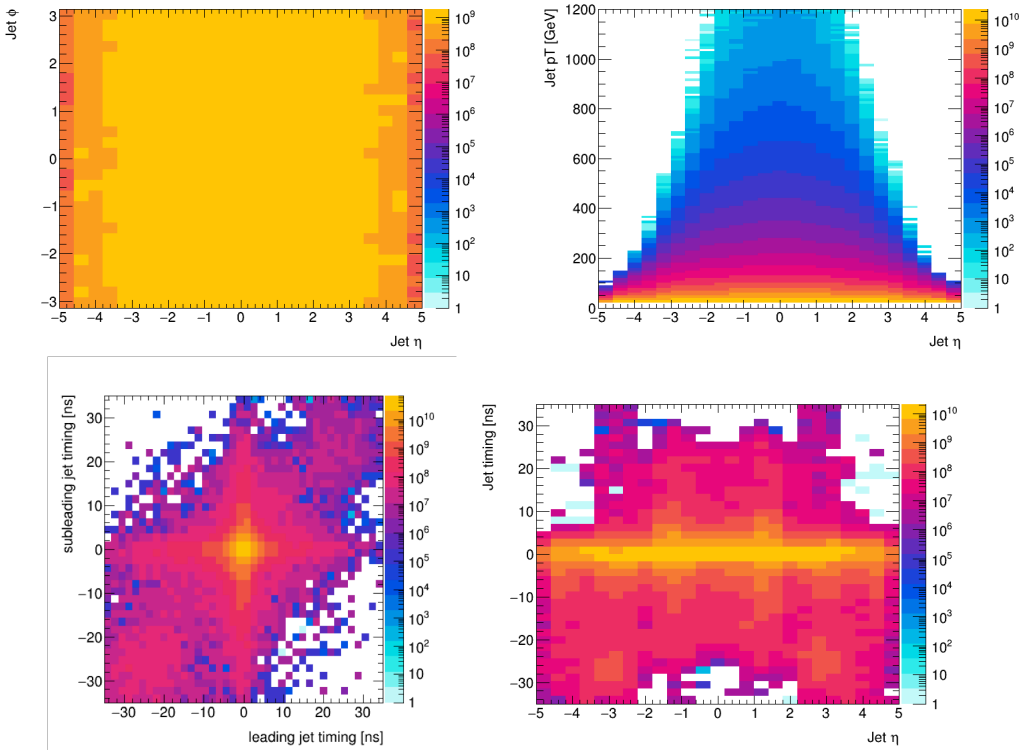


Figure A.3: 2D histograms showing correlations between key jet quality variables in good jet data.

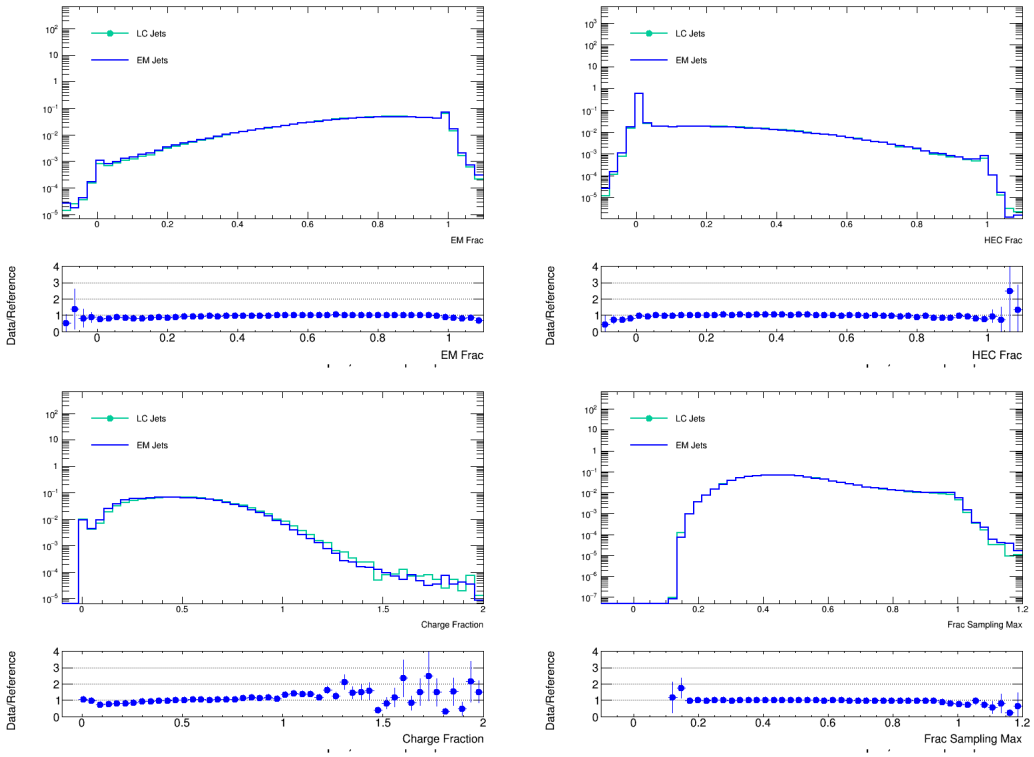


Figure A.4: Distributions of f_{em}, f_{HEC}, f_{ch}, and f_{max} are shown in 2016 data for both LC and EM jets.

for both Loose and Tight cleaning working points, as a function of p_T and η. Both working point efficiencies are similar to those calculated for EM jets.

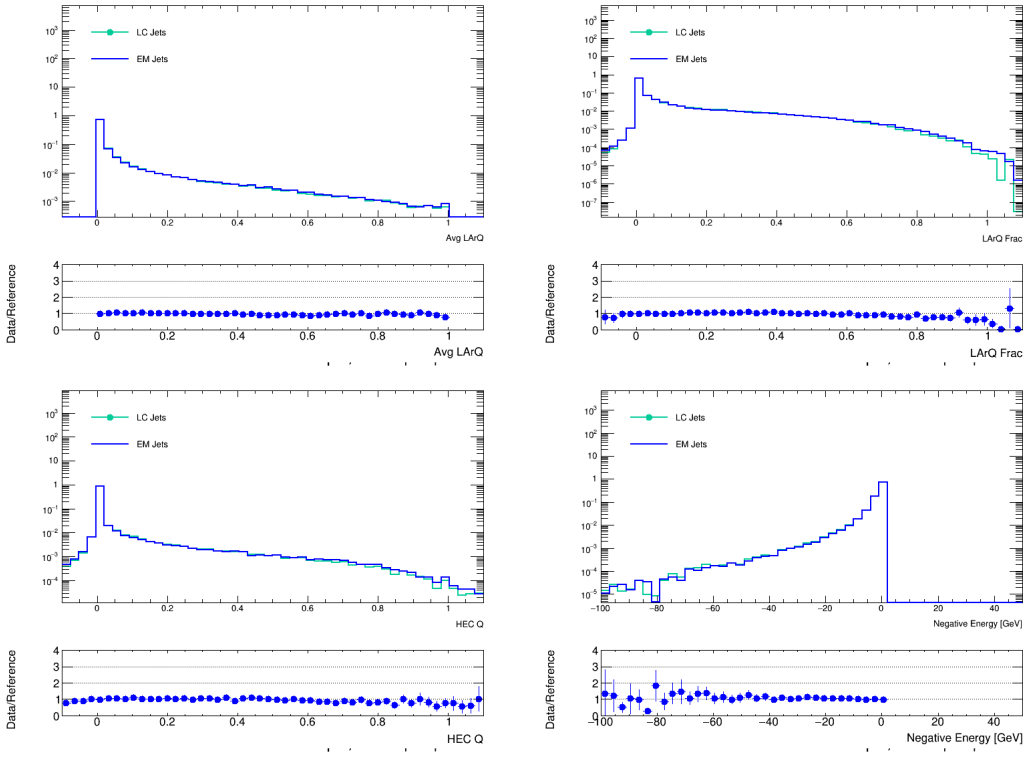


Figure A.5: Distributions of $\langle Q \rangle$, f^{Q}_{LAr}, f^{Q}_{HEC}, and E_{neg} are shown in 2016 data for both LC and EM jets.

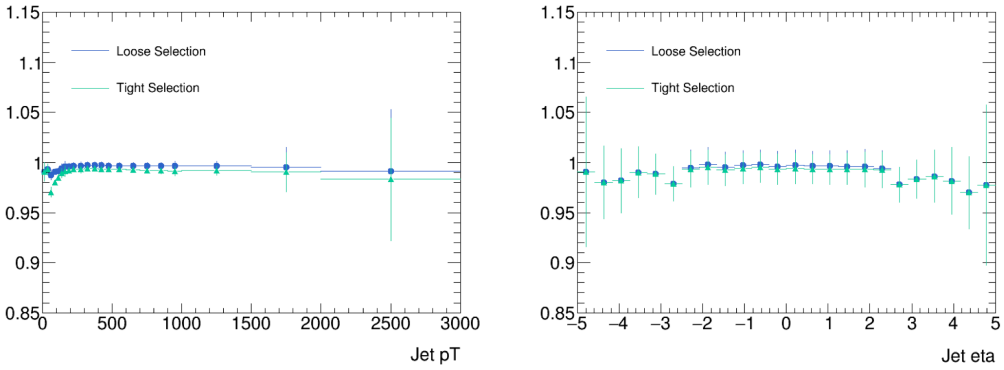


Figure A.6: EM jet quality selection efficiency for anti-k_T LCW jets measured with a tag-and-probe technique as a function of p_T and η (p_T > 100 GeV), for the Loose and Tight selection criteria. Only statistical uncertainties are shown.

B

For Electroweak SUSY: Additional Material

B.1 Low-E_T^{miss} Higgsino Regions

The low-E_T^{miss} phase space of the higgsino search is added to gain sensitivity to slightly higher mass splitting signals. These events have E_T^{miss} between 120 and 200 GeV. Since they are still selected using the inclusive E_T^{miss} triggers, scale factors are derived to correct for mis-modeling due to the trigger turn on. Two different low-E_T^{miss} regions were separately optimized for high and low mass

Variable	Selection Requirement					
E_T^{miss} [GeV]	[120, 200]					
E_T^{miss}/H_T^{lep} [GeV]	> 10					
M_T^S [GeV]	< 50					
	eMLLaa	eMLLab	eMLLb	eMLLc	eMLLd	eMLLe
$m(ee)$ [GeV]	-	-	[3.2,5]	[5,10]	[10, 20]	[20,30]
$m(\mu\mu)$ [GeV]	[1,2]	[2,3]	[3.2,5]	[5,10]	[10, 20]	[20,30]
	iMLLaa	iMLLab	iMLLb	iMLLc	iMLLd	iMLLe
m_{ll} [GeV]	< 2	< 3	< 5	< 10	< 20	< 30

Table B.1: Table of common event selection criteria for the low-E_T^{miss} low-Δm higgsino signal regions; ee and $\mu\mu$ channels are statistically independent and fit separately.

splitting samples, denoted as high-Δm and low-Δm respectively, which are orthogonal and simultaneously used in the fit. The optimization procedure was the same as for the high-E_T^{miss} regions, using N-1 plots of key analysis variables to determine optimal cut placement.

The preselection criteria for all low-E_T^{miss} regions is the same as that for the high-E_T^{miss} regions, found in Table 10.2. Signal region selection can be seen for the low-E_T^{miss} low-Δm in Table B.1; the binning in m_{ll} is consistent with the high-E_T^{miss} except for the removal of the two highest bins. Selection for the low-E_T^{miss} high-Δm signal regions can be found in Table B.2.

The same three control and two validation regions are built for all low-E_T^{miss} regions, defined in Table B.3.

Figure B.1 shows unblinded distributions of m_{ll}, M_T^S, and $p_T^{\ell 2}$ in the low-E_T^{miss} higgsino SR. Plots are shown N-1 style with the cut on the displayed variable not applied; single cuts are shown via arrows, while sliding cuts are not indicated.

Variable	Selection Requirement							
E_T^{miss} [GeV]	[120, 200]							
E_T^{miss}/H_T^{lep} [GeV]	< 10							
$m_T^{\ell 1}$ [GeV]	[10, 60]							
$p_T^{\ell_2}$ [GeV]	$> 5 + 0.25 \cdot m_{ll}$							
R_{ISR}	[0.8, 1.0]							
	eMLLaa	eMLLab	eMLLb	eMLLc	eMLLd	eMLLe	eMLLf	eMLLg
$m(ee)$ [GeV]	-	-	[3.2,5]	[5,10]	[10, 20]	[20,30]	[30,40]	[40,60]
$m(\mu\mu)$ [GeV]	[1,2]	[2,3]	[3.2,5]	[5,10]	[10, 20]	[20,30]	[30,40]	[40,60]
	iMLLaa	iMLLab	iMLLb	iMLLc	iMLLd	iMLLe	iMLLf	iMLLg
m_{ll} [GeV]	< 2	< 3	< 5	< 10	< 20	< 30	< 40	< 60

Table B.2: Table of common event selection criteria for the low-E_T^{miss} high-Δm higgsino signal regions; ee and $\mu\mu$ channels are statistically independent and fit separately.

Region	SR Orthogonality	Additional Requirements	Flavor
CR-top	Number of b-jets ≥ 1	No cut on E_T^{miss}/H_T^{lep} or $m_T^{\ell 1}$	$ee + \mu\mu + e\mu + \mu e$
CR-tau	$60 < m_{\tau\tau} < 120$ GeV	$0.6 < R_{ISR} < 1.0$, no cut on $m_T^{\ell 1}$	$ee + \mu\mu + e\mu + \mu e$
CR-VV	$0.6 < R_{ISR} < 0.8$	No cut on E_T^{miss}/H_T^{lep}, $m_T^{\ell 1} > 30$ GeV, $N_{jets} > 2$	$ee + \mu\mu + e\mu + \mu e$
VR-DF	$e\mu + \mu e$	-	$e\mu + \mu e$
VR-SS	Same-sign $\ell^{\pm}\ell^{\pm}$	No cut on E_T^{miss}/H_T^{lep}, $m_T^{\ell 1}$, or $p_T(\ell_2)$	$ee + \mu e, \mu\mu + e\mu$

Table B.3: Table of criteria for the low-E_T^{miss} higgsino control and validation regions, provided as differences from the signal region definitions. All regions also include the preselection requirements listed in Table 10.2.

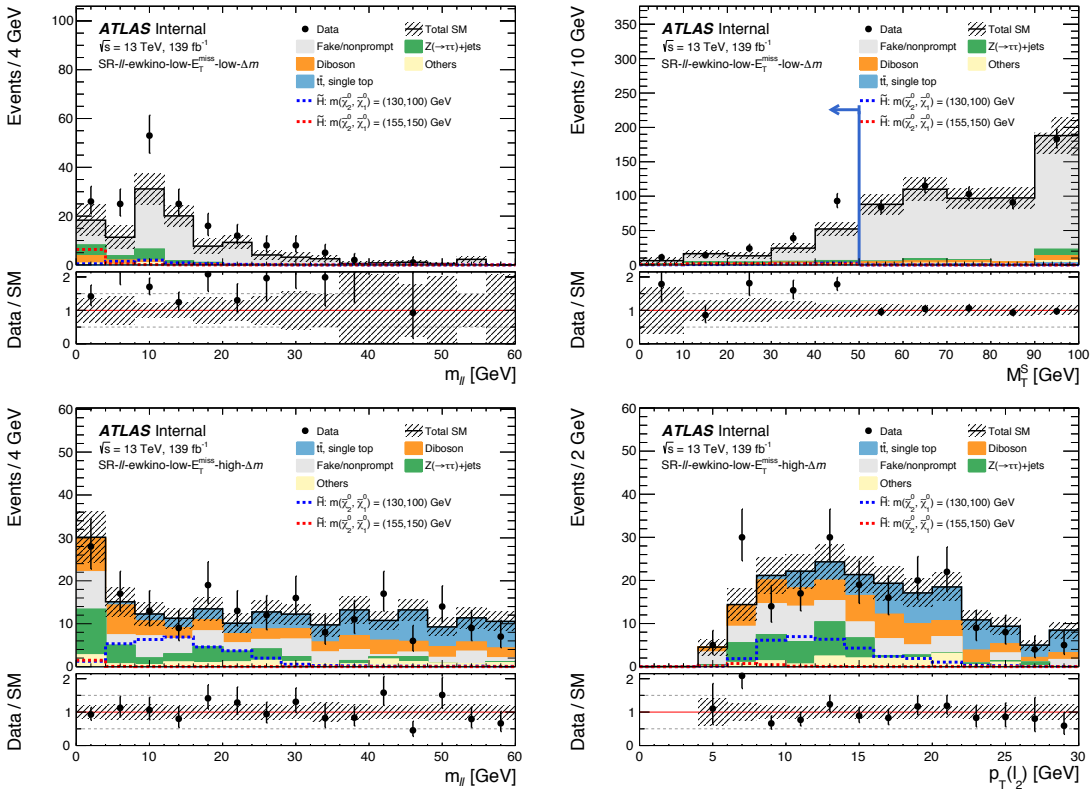


Figure B.1: Unblinded N-1 distributions in the low-E_T^{miss} higgsino SR, with arrows indicating the requirement. Uncertainty bands indicate all statistical and systematic uncertainties.

B.2 1L+Track Higgsino Regions

The one lepton plus track (1L+track) analysis is designed to add sensitivity to the lowest mass splitting region. Due to the correlation between $\widetilde{\chi}_2^0$-$\widetilde{\chi}_1^0$ mass splitting and lepton p_T, and the minimum lepton p_T requirements for reconstruction, the soft lepton higgsino signal regions fail to probe the region below mass splittings around 2 GeV. In the case of such a small mass splitting signal, the subleading final state lepton can be soft enough that is below reconstruction thresholds, but can instead be selected by the track left in the inner detector. This subsequently yields a final state with one soft

Variable	Selection Requirement					
E_T^{miss} [GeV]	> 200					
p_T^{track} [GeV]	< 5 GeV					
$E_T^{miss}/H_T^{lep+track}$ [GeV]	> 30					
$\lvert\Delta\phi(\ell t, p_T^{miss}\rvert$	< 1.0					
	eMLTa	eMLTb	eMLTc	eMLTd	eMLTe	eMLTf
m_{lt} [GeV]	[0.5,1]	[1,1.5]	[1.5,2]	[2,3]	[3,4]	[4,5]
	iMLTa	iMLTb	iMLTc	iMLTd	iMLTe	iMLTf
m_{lt} [GeV]	< 1	< 1.5	< 2	< 3	< 4	< 5

Table B.4: Table of common event selection criteria for the 1L+track higgsino signal regions.

lepton and a signal track with momentum as low as 500 MeV.

Construction of the 1L+track regions utilize identical lepton selection to the soft lepton analysis, and analysis variables that are analogous to their two lepton counterparts, albeit computed with one lepton and a track rather than two leptons. For example, the shape fit can be performed on m_{lt}, defined as the invariant mass of the lepton and track. Table B.4 gives the selection criteria defining the 1L+track higgsino signal region, and the shape fit binning in m_{lt}. The same preselection given in Table 10.2 and used for the two lepton regions also applies.

The background estimation differs from that of the two lepton regions due to the difference in dominant background process. The 1L+track analysis background primarily consists of associated track combinatorics, where a random track (from hadrons, non-prompt leptons, or spurious inner detector hits) is associated to the leading lepton instead of the track from the subleading lepton. Such a background is especially dominant at very low lepton/track momenta, a region where simulation does not provide very good estimates.

As a result, the strategy here is to use a completely data driven technique to estimate this back-

ground, which uses same-sign (SS) lepton + track events as a proxy for the opposite-sign (OS) signal region. Since the combinatoric background is agnostic to the sign of the objects, such an extrapolation is reasonable. Furthermore, the SS region is not found to have significant signal contamination, and no prompt lepton MC subtraction is necessary. In this way, the background estimate for the OS signal region is taken directly from SS data, with no control or validation regions required. Two uncertainties are assigned on this prediction, one for low-mass OS resonances, and one for SS/OS closure differences.

Figure B.2 shows unblinded distributions of m_{lt} and E_T^{miss} / H_T^{lt} in the 1L+track higgsino SR, in an N-1 style with the cut on the displayed variable not applied, but indicated by arrows.

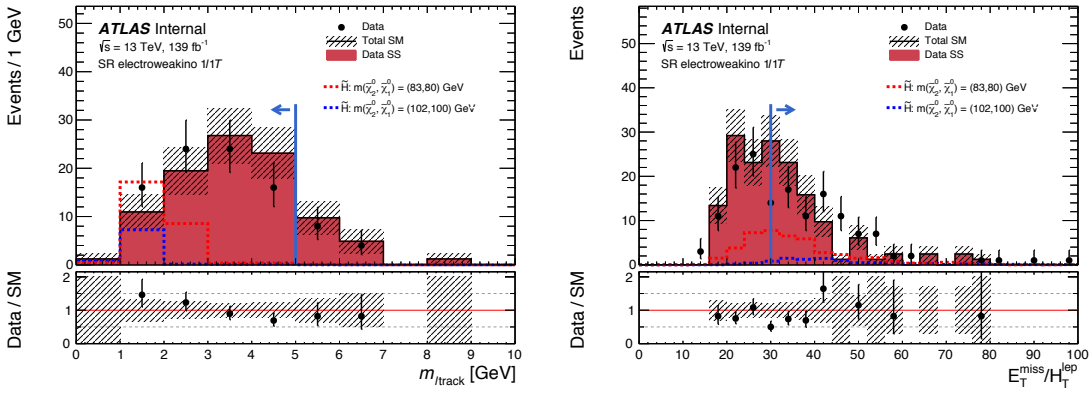


Figure B.2: Unblinded N-1 distributions in the 1L+track higgsino SR, with arrows indicating the requirement. Uncertainty bands indicate all statistical and systematic uncertainties.

References

[1] J. H. Christenson, J. W. Cronin, V. L. Fitch, and R. Turlay. Evidence for the 2π decay of the k_2^0 meson. *Phys. Rev. Lett.*, 13:138–140, Jul 1964.

[2] David J Griffiths. *Introduction to elementary particles; 2nd rev. version*. Physics textbook. Wiley, New York, NY, 2008.

[3] S. L. Glashow. Partial Symmetries of Weak Interactions. *Nucl. Phys.*, 22:579–588, 1961.

[4] Steven Weinberg. A Model of Leptons. *Phys. Rev. Lett.*, 19:1264–1266, 1967.

[5] Abdus Salam. Gauge unification of fundamental forces. *Rev. Mod. Phys.*, 52:525–538, Jul 1980.

[6] G. 't Hooft and M. Veltman. Regularization and renormalization of gauge fields. *Nuclear Physics B*, 44(1):189 – 213, 1972.

[7] J. J. Aubert, U. Becker, P. J. Biggs, J. Burger, M. Chen, G. Everhart, P. Goldhagen, J. Leong, T. McCorriston, T. G. Rhoades, M. Rohde, Samuel C. C. Ting, Sau Lan Wu, and Y. Y. Lee. Experimental observation of a heavy particle j. *Phys. Rev. Lett.*, 33:1404–1406, Dec 1974.

[8] J. E. Augustin, A. M. Boyarski, M. Breidenbach, F. Bulos, J. T. Dakin, G. J. Feldman, G. E. Fischer, D. Fryberger, G. Hanson, B. Jean-Marie, R. R. Larsen, V. Lüth, H. L. Lynch, D. Lyon, C. C. Morehouse, J. M. Paterson, M. L. Perl, B. Richter, P. Rapidis, R. F. Schwitters, W. M. Tanenbaum, F. Vannucci, G. S. Abrams, D. Briggs, W. Chinowsky, C. E. Friedberg, G. Goldhaber, R. J. Hollebeek, J. A. Kadyk, B. Lulu, F. Pierre, G. H. Trilling, J. S. Whitaker, J. Wiss, and J. E. Zipse. Discovery of a narrow resonance in e^+e^- annihilation. *Phys. Rev. Lett.*, 33:1406–1408, Dec 1974.

[9] M. L. Perl, G. S. Abrams, A. M. Boyarski, M. Breidenbach, D. D. Briggs, F. Bulos, W. Chinowsky, J. T. Dakin, G. J. Feldman, C. E. Friedberg, D. Fryberger, G. Goldhaber, G. Hanson, F. B. Heile, B. Jean-Marie, J. A. Kadyk, R. R. Larsen, A. M. Litke, D. Lüke, B. A. Lulu, V. Lüth, D. Lyon, C. C. Morehouse, J. M. Paterson, F. M. Pierre, T. P. Pun, P. A. Rapidis,

B. Richter, B. Sadoulet, R. F. Schwitters, W. Tanenbaum, G. H. Trilling, F. Vannucci, J. S. Whitaker, F. C. Winkelmann, and J. E. Wiss. Evidence for anomalous lepton production in $e^+ - e^-$ annihilation. *Phys. Rev. Lett.*, 35:1489–1492, Dec 1975.

[10] S. W. Herb, D. C. Hom, L. M. Lederman, J. C. Sens, H. D. Snyder, J. K. Yoh, J. A. Appel, B. C. Brown, C. N. Brown, W. R. Innes, K. Ueno, T. Yamanouchi, A. S. Ito, H. Jöstlein, D. M. Kaplan, and R. D. Kephart. Observation of a dimuon resonance at 9.5 gev in 400-gev proton-nucleus collisions. *Phys. Rev. Lett.*, 39:252–255, Aug 1977.

[11] Makoto Kobayashi and Toshihide Maskawa. CP-Violation in the Renormalizable Theory of Weak Interaction. *Progress of Theoretical Physics*, 49(2):652–657, 02 1973.

[12] UA1 Collaboration, CERN, Switzerland. Experimental observation of isolated large transverse energy electrons with associated missing energy at s=540 gev. *Physics Letters B*, 122(1):103 – 116, 1983.

[13] CDF Collaboration, Fermilab, USA. Observation of top quark production in $\bar{p}p$ collisions with the collider detector at fermilab. *Phys. Rev. Lett.*, 74:2626–2631, Apr 1995.

[14] Do Collaboration, Fermilab, USA. Observation of the top quark. *Phys. Rev. Lett.*, 74:2632–2637, Apr 1995.

[15] ATLAS Collaboration. Observation of a new particle in the search for the Standard Model Higgs boson with the ATLAS detector at the LHC. *Phys. Lett.*, B716:1–29, 2012.

[16] CMS Collaboration. Observation of a new boson at a mass of 125 GeV with the CMS experiment at the LHC. *Phys. Lett.*, B716:30–61, 2012.

[17] M. Tanabashi et al. Review of particle physics. *Phys. Rev. D*, 98:030001, Aug 2018.

[18] A. H. Broeils, K. G. Begeman, and R. H. Sanders. Extended rotation curves of spiral galaxies: dark haloes and modified dynamics. *Monthly Notices of the Royal Astronomical Society*, 249(3):523–537, 04 1991.

[19] Y. Fukuda, T. Hayakawa, E. Ichihara, K. Inoue, K. Ishihara, H. Ishino, Y. Itow, T. Kajita, J. Kameda, S. Kasuga, K. Kobayashi, Y. Kobayashi, Y. Koshio, M. Miura, M. Nakahata, S. Nakayama, A. Okada, K. Okumura, N. Sakurai, M. Shiozawa, Y. Suzuki, Y. Takeuchi, Y. Totsuka, S. Yamada, M. Earl, A. Habig, E. Kearns, M. D. Messier, K. Scholberg, J. L. Stone, L. R. Sulak, C. W. Walter, M. Goldhaber, T. Barszczxak, D. Casper, W. Gajewski, P. G.

Halverson, J. Hsu, W. R. Kropp, L. R. Price, F. Reines, M. Smy, H. W. Sobel, M. R. Vagins, K. S. Ganezer, W. E. Keig, R. W. Ellsworth, S. Tasaka, J. W. Flanagan, A. Kibayashi, J. G. Learned, S. Matsuno, V. J. Stenger, D. Takemori, T. Ishii, J. Kanzaki, T. Kobayashi, S. Mine, K. Nakamura, K. Nishikawa, Y. Oyama, A. Sakai, M. Sakuda, O. Sasaki, S. Echigo, M. Kohama, A. T. Suzuki, T. J. Haines, E. Blaufuss, B. K. Kim, R. Sanford, R. Svoboda, M. L. Chen, Z. Conner, J. A. Goodman, G. W. Sullivan, J. Hill, C. K. Jung, K. Martens, C. Mauger, C. McGrew, E. Sharkey, B. Viren, C. Yanagisawa, W. Doki, K. Miyano, H. Okazawa, C. Saji, M. Takahata, Y. Nagashima, M. Takita, T. Yamaguchi, M. Yoshida, S. B. Kim, M. Etoh, K. Fujita, A. Hasegawa, T. Hasegawa, S. Hatakeyama, T. Iwamoto, M. Koga, T. Maruyama, H. Ogawa, J. Shirai, A. Suzuki, F. Tsushima, M. Koshiba, M. Nemoto, K. Nishijima, T. Futagami, Y. Hayato, Y. Kanaya, K. Kaneyuki, Y. Watanabe, D. Kielczewska, R. A. Doyle, J. S. George, A. L. Stachyra, L. L. Wai, R. J. Wilkes, and K. K. Young. Evidence for oscillation of atmospheric neutrinos. *Phys. Rev. Lett.*, 81:1562–1567, Aug 1998.

[20] Michele Papucci, Joshua T. Ruderman, and Andreas Weiler. Natural SUSY Endures. *JHEP*, 09:035, 2012.

[21] Stephen P. Martin. A Supersymmetry primer. pages 1–98, 1997. [Adv. Ser. Direct. High Energy Phys.18,1(1998)].

[22] Mark A. Levinson, David E. Kaplan, Andrea Miller, and Carla Solomon. Particle Fever. 2015.

[23] Pierre Fayet. Supersymmetry and Weak, Electromagnetic and Strong Interactions. *Phys. Lett.*, 64B:159, 1976.

[24] Pierre Fayet. Spontaneously Broken Supersymmetric Theories of Weak, Electromagnetic and Strong Interactions. *Phys. Lett.*, 69B:489, 1977.

[25] Howard E. Haber. Introductory low-energy supersymmetry. In *Proceedings, Theoretical Advanced Study Institute (TASI 92): From Black Holes and Strings to Particles: Boulder, USA, June 1-26, 1992*, pages 589–686, 1993.

[26] Hans Peter Nilles. Phenomenological aspects of supersymmetry. In *Gauge theories, applied supersymmetry, quantum gravity. Proceedings, Workshop, Leuven, Belgium, July 10-14, 1995*, pages 81–105, 1995.

[27] John R. Ellis, J. S. Hagelin, Dimitri V. Nanopoulos, Keith A. Olive, and M. Srednicki. Supersymmetric Relics from the Big Bang. *Nucl. Phys.*, B238:453–476, 1984. [,223(1983)].

[28] Joakim Edsjo and Paolo Gondolo. Neutralino relic density including coannihilations. *Phys. Rev.*, D56:1879–1894, 1997.

[29] CMS Collaboration. SUSY theory cross sections plots. https://twiki.cern.ch/twiki/bin/view/CMSPublic/SUSYSMSSummaryPlots13TeV, 2017. [Online; accessed 1-March-2019].

[30] Riccardo Barbieri and G. F. Giudice. Upper Bounds on Supersymmetric Particle Masses. *Nucl. Phys.*, B306:63–76, 1988.

[31] Matthew R. Buckley, Angelo Monteux, and David Shih. Precision Corrections to Fine Tuning in SUSY. *JHEP*, 06:103, 2017.

[32] Scott D. Thomas and James D. Wells. Phenomenology of Massive Vectorlike Doublet Leptons. *Phys. Rev. Lett.*, 81:34–37, 1998.

[33] Zhenyu Han, Graham D. Kribs, Adam Martin, and Arjun Menon. Hunting quasi-degenerate higgsinos. *Physical Review D*, 89, 01 2014.

[34] Gianfranco Bertone, Dan Hooper, and Joseph Silk. Particle dark matter: evidence, candidates and constraints. *Physics Reports*, 405(5):279 – 390, 2005.

[35] Gerard Jungman, Marc Kamionkowski, and Kim Griest. Supersymmetric dark matter. *Physics Reports*, 267(5):195 – 373, 1996.

[36] N. Arkani-Hamed, A. Delgado, and G. F. Giudice. The Well-tempered neutralino. *Nucl. Phys.*, B741:108–130, 2006.

[37] Stefano Profumo, Tim Stefaniak, and Laurel Stephenson Haskins. The Not-So-Well Tempered Neutralino. *Phys. Rev.*, D96(5):055018, 2017.

[38] ATLAS Collaboration. Search for top-squark pair production in final states with one lepton, jets, and missing transverse momentum using 36 $\text{fb}^{?1}$ of $\sqrt{s} = 13$ TeV pp collision data with the ATLAS detector. *JHEP*, 06:108, 2018.

[39] ATLAS Collaboration. ATLAS Run 1 searches for direct pair production of third-generation squarks at the Large Hadron Collider. *Eur. Phys. J. C*, 75(CERN-PH-EP-2015-138):510. 54 p, Jun 2015. 53 pages plus author list + cover page (70 pages total), 24 figures, 10 tables, submitted to Eur. Phys. J., All figures including auxiliary figures are available at http://atlas.web.cern.ch/Atlas/GROUPS/PHYSICS/PAPERS/SUSY-2014-07/.

[40] ATLAS Collaboration. Search for direct production of charginos and neutralinos in events with three leptons and missing transverse momentum in 21 fb^{-1} of pp collisions at $\sqrt{s} =$ 8 TeV with the ATLAS detector. Technical Report ATLAS-CONF-2013-035, CERN, Geneva, Mar 2013.

[41] CMS Collaboration. A search for anomalous production of events with three or more leptons using 19.5/fb of sqrt(s)=8 TeV LHC data. Technical Report CMS-PAS-SUS-13-002, CERN, Geneva, 2013.

[42] ATLAS Collaboration. Search for direct production of charginos, neutralinos and sleptons in final states with two leptons and missing transverse momentum in pp collisions at $\sqrt{s} = 8$ TeV with the ATLAS detector. *JHEP*, 05:071, 2014.

[43] ATLAS Collaboration. Search for direct production of charginos and neutralinos in events with three leptons and missing transverse momentum in $\sqrt{s} = 8$TeV pp collisions with the ATLAS detector. *JHEP*, 04:169, 2014.

[44] ATLAS Collaboration. Search for the electroweak production of supersymmetric particles in $\sqrt{s}$=8 TeV pp collisions with the ATLAS detector. *Phys. Rev.*, D93(5):052002, 2016.

[45] ATLAS Collaboration. Dark matter interpretations of ATLAS searches for the electroweak production of supersymmetric particles in $\sqrt{s} = 8$ TeV proton-proton collisions. *JHEP*, 09:175, 2016.

[46] CMS Collaboration. Search for electroweak production of charginos and neutralinos in multilepton final states in proton-proton collisions at $\sqrt{s} = 13$ TeV. *JHEP*, 03:166, 2018.

[47] ALEPH, DELPHI, L3, and OPAL Experiments. Combined LEP Chargino Results, up to 208 GeV for low DM. http://lepsusy.web.cern.ch/lepsusy/www/inoslowdmsummer02/charginolowdm_pub.html, 2002. [Online; accessed 1-March-2019].

[48] ATLAS Collaboration. Search for electroweak production of supersymmetric states in scenarios with compressed mass spectra at $\sqrt{s} = 13$ TeV with the atlas detector. *Phys. Rev. D*, 97:052010, Mar 2018.

[49] CMS Collaboration. Search for new physics in events with two soft oppositely charged leptons and missing transverse momentum in proton-proton collisions at $\sqrt{s} = 13$ TeV. *Phys. Lett.*, B782:440–467, 2018.

[50] A. M. Sirunyan et al. Combined search for electroweak production of charginos and neutralinos in proton-proton collisions at $\sqrt{s} = 13$ TeV. *JHEP*, 03:160, 2018.

[51] ATLAS Experiment. ATLAS SUSY Combined Summary Plots. https://atlas.web.cern.ch/Atlas/GROUPS/PHYSICS/CombinedSummaryPlots/SUSY/, 2018. [Online; accessed 19-April-2019].

[52] ATLAS Collaboration. Search for direct pair production of higgsinos by the reinterpretation of the disappearing track analysis with 36.1 fb^{-1} of $\sqrt{s} = 13$ TeV data collected with the ATLAS experiment. Technical Report ATL-PHYS-PUB-2017-019, CERN, Geneva, Dec 2017.

[53] ATLAS Collaboration. Search for new phenomena in final states with an energetic jet and large missing transverse momentum in pp collisions at $\sqrt{s} = 8$ TeV with the ATLAS detector. *Eur. Phys. J.*, C75(7):299, 2015. [Erratum: Eur. Phys. J.C75,no.9,408(2015)].

[54] Stefania Gori, Sunghoon Jung, and Lian-Tao Wang. Cornering electroweakinos at the LHC. *JHEP*, 10:191, 2013.

[55] Lyndon R Evans and Philip Bryant. LHC Machine. *JINST*, 3:S08001. 164 p, 2008. This report is an abridged version of the LHC Design Report (CERN-2004-003).

[56] Esma Mobs. The CERN accelerator complex. Complexe des accélérateurs du CERN. Jul 2016. General Photo.

[57] ATLAS Collaboration. The ATLAS Experiment at the CERN Large Hadron Collider. *JINST*, 3:S08003, 2008.

[58] CMS Collaboration. The CMS Experiment at the CERN LHC. *JINST*, 3:S08004, 2008.

[59] LHCb Collaboration. The LHCb Detector at the LHC. *JINST*, 3:S08005, 2008.

[60] ALICE Collaboration. The ALICE experiment at the CERN LHC. *JINST*, 3:S08002, 2008.

[61] CERN. The High Luminosity LHC (HL-LHC). http://hilumilhc.web.cern.ch/about/hl-lhc-project, 2019. [Online; accessed 04-April-2019].

[62] Emma Tolley. Search for Evidence of Dark Matter Production in Monojet Events with the ATLAS Detector, December 2016.

[63] ATLAS Collaboration. Data Quality Information for Data. https://twiki.cern.ch/twiki/bin/view/AtlasPublic/RunStatsPublicResults2010, 2019. [Online; accessed 26-March-2019].

[64] ATLAS Collaboration. Luminosity Public Results Run2. https://twiki.cern.ch/twiki/bin/view/AtlasPublic/LuminosityPublicResultsRun2, 2019. [Online; accessed 26-March-2019].

[65] ATLAS Collaboration. Readiness of the ATLAS Liquid Argon Calorimeter for LHC Collisions. Readiness of the ATLAS Liquid Argon Calorimeter for LHC Collisions. *Eur. Phys. J. C*, 70(arXiv:0912.2642. CERN-PH-EP-2010-041):723–753. 31 p, May 2010. Comments: 31 pages, 34 figures, accepted in EPJC.

[66] ATLAS Collaboration. Monitoring and data quality assessment of the ATLAS liquid argon calorimeter. *JINST*, 9:P07024, 2014.

[67] T Kawamoto, S Vlachos, L Pontecorvo, J Dubbert, G Mikenberg, P Iengo, C Dallapiccola, C Amelung, L Levinson, R Richter, and D Lellouch. New Small Wheel Technical Design Report. Technical Report CERN-LHCC-2013-006. ATLAS-TDR-020, Jun 2013. ATLAS New Small Wheel Technical Design Report.

[68] ATLAS Collaboration. Performance of the ATLAS Trigger System in 2015. *Eur. Phys. J.*, C77(5):317, 2017.

[69] Joao Pequenao. Event Cross Section in a computer generated image of the ATLAS detector. Mar 2008.

[70] ATLAS Collaboration. Electron efficiency measurements with the ATLAS detector using the 2015 LHC proton-proton collision data. Technical Report ATLAS-CONF-2016-024, CERN, Geneva, Jun 2016.

[71] ATLAS Collaboration. Electron identification measurements in ATLAS using $\sqrt{s}$ = 13 TeV data with 50 ns bunch spacing. Technical Report ATL-PHYS-PUB-2015-041, CERN, Geneva, Sep 2015.

[72] ATLAS Collaboration. Muon reconstruction performance of the ATLAS detector in proton–proton collision data at $\sqrt{s}$ =13 TeV. *Eur. Phys. J.*, C76(5):292, 2016.

[73] ATLAS Collaboration. Jet energy measurement and its systematic uncertainty in proton-proton collisions at $\sqrt{s} = 7$ TeV with the ATLAS detector. *Eur. Phys. J.*, C75:17, 2015.

[74] Matteo Cacciari, Gavin P. Salam, and Gregory Soyez. The anti-k_t jet clustering algorithm. *JHEP*, 04:063, 2008.

[75] ATLAS Collaboration. Jet reconstruction and performance using particle flow with the ATLAS Detector. *Eur. Phys. J.*, C77(7):466, 2017.

[76] ATLAS Collaboration. Performance of pile-up mitigation techniques for jets in pp collisions at $\sqrt{s} = 8$ TeV using the ATLAS detector. *Eur. Phys. J.*, C76(11):581, 2016.

[77] ATLAS Collaboration. Expected performance of the ATLAS b-tagging algorithms in Run-2. Technical Report ATL-PHYS-PUB-2015-022, CERN, Geneva, Jul 2015.

[78] ATLAS Collaboration. Performance of missing transverse momentum reconstruction for the ATLAS detector in the first proton-proton collisions at at $\sqrt{s}$= 13 TeV. Technical Report ATL-PHYS-PUB-2015-027, CERN, Geneva, Jul 2015.

[79] Paul Jackson and Christopher Rogan. Recursive Jigsaw Reconstruction: HEP event analysis in the presence of kinematic and combinatoric ambiguities. *Phys. Rev.*, D96(11):112007, 2017.

[80] Kaoru Hagiwara and Toshifumi Yamada. Equal-velocity scenario for hiding dark matter at the LHC. *Phys. Rev.*, D91(9):094007, 2015.

[81] Haipeng An and Lian-Tao Wang. Opening up the compressed region of top squark searches at 13 TeV LHC. *Phys. Rev. Lett.*, 115:181602, 2015.

[82] Sebastian Macaluso, Michael Park, David Shih, and Brock Tweedie. Revealing Compressed Stops Using High-Momentum Recoils. *JHEP*, 03:151, 2016.

[83] Paul Jackson, Christopher Rogan, and Marco Santoni. Sparticles in motion: Analyzing compressed SUSY scenarios with a new method of event reconstruction. *Phys. Rev.*, D95(3):035031, 2017.

[84] T. Golling, H.S. Hayward, P.U.E. Onyisi, H.J. Stelzer, and P. Waller. The ATLAS Data Quality Defect Database System. *Eur. Phys. J. C*, 72(arXiv:1110.6119):1960. 6 p, Oct 2011. 6 pages, 3 figures, published in EPJ C. (v2: as published).

[85] ATLAS Collaboration. Characterisation and mitigation of beam-induced backgrounds observed in the ATLAS detector during the 2011 proton-proton run. *JINST*, 8(CERN-PH-EP-2012-313. CERN-PH-EP-2012-313):P07004. 58 p, Mar 2013.

[86] ATLAS Collaboration. Selection of jets produced in 13TeV proton-proton collisions with the ATLAS detector. 2015.

[87] ATLAS Collaboration. Search for long-lived, massive particles in events with displaced vertices and missing transverse momentum in $\sqrt{s}$ = 13 TeV pp collisions with the ATLAS detector. *Phys. Rev.*, D97(5):052012, 2018.

[88] Kyle Cranmer. Practical Statistics for the LHC. In *Proceedings, 2011 European School of High-Energy Physics (ESHEP 2011): Cheile Gradistei, Romania, September 7-20, 2011*, pages 267–308, 2015. [,247(2015)].

[89] Luca Lista. Practical Statistics for Particle Physicists. In *Proceedings, 2016 European School of High-Energy Physics (ESHEP2016): Skeikampen, Norway, June 15-28 2016*, pages 213–258, 2017.

[90] Javier Montejo Berlingen and Aurelio Juste Rozas. Search for new physics in $t\bar{t}$ final states with additional heavy-flavor jets with the ATLAS detector, Apr 2016. Presented 11 Jun 2015.

[91] Alexander L. Read. Presentation of search results: The CL(s) technique. *J. Phys.*, G28:2693–2704, 2002. [,11(2002)].

[92] M. Baak, G. J. Besjes, D. Côte, A. Koutsman, J. Lorenz, and D. Short. HistFitter software framework for statistical data analysis. *Eur. Phys. J.*, C75:153, 2015.

[93] Marcela Carena, R. L. Culbertson, S. Eno, Henry J. Frisch, and S. Mrenna. The Search for Supersymmetry at the Tevatron collider. *Rev. Mod. Phys.*, 71:937–981, 1999.

[94] S. Lammel. Supersymmetry at the Tevatron? In *Supersymmetry, supergravity and supercolliders. Proceedings, Theoretical Advanced Study Institute in elementary particle physics, TASI'97, Boulder, USA, June 2-27, 1997*, pages 393–432, 1998.

[95] Johan Alwall, Philip Schuster, and Natalia Toro. Simplified Models for a First Characterization of New Physics at the LHC. *Phys. Rev.*, D79:075020, 2009.

[96] Daniele Alves. Simplified Models for LHC New Physics Searches. *J. Phys.*, G39:105005, 2012.

[97] ATLAS Collaboration. The ATLAS Simulation Infrastructure. *Eur. Phys. J.*, C70:823–874, 2010.

[98] ATLAS Collaboration. Simulation of top quark production for the ATLAS experiment at sqrt(s) = 13 TeV. Technical Report ATL-PHYS-PUB-2016-004, CERN, Geneva, Jan 2016.

[99] Simone Alioli, Paolo Nason, Carlo Oleari, and Emanuele Re. A general framework for implementing NLO calculations in shower Monte Carlo programs: the POWHEG BOX. *JHEP*, 06:043, 2010.

[100] Torbjorn Sjostrand, Stephen Mrenna, and Peter Z. Skands. PYTHIA 6.4 Physics and Manual. *JHEP*, 05:026, 2006.

[101] ATLAS Collaboration. Monte Carlo Generators for the Production of a W or Z/γ^* Boson in Association with Jets at ATLAS in Run 2. Technical Report ATL-PHYS-PUB-2016-003, CERN, Geneva, Jan 2016.

[102] ATLAS Collaboration. Multi-Boson Simulation for 13 TeV ATLAS Analyses. Technical Report ATL-PHYS-PUB-2016-002, CERN, Geneva, Jan 2016.

[103] T. Gleisberg, Stefan. Hoeche, F. Krauss, M. Schonherr, S. Schumann, F. Siegert, and J. Winter. Event generation with SHERPA 1.1. *JHEP*, 02:007, 2009.

[104] ATLAS Collaboration. Modelling of the $t\bar{t}H$ and $t\bar{t}V$ $(V = W, Z)$ processes for $\sqrt{s} = 13$ TeV ATLAS analyses. Technical Report ATL-PHYS-PUB-2016-005, CERN, Geneva, Jan 2016.

[105] J. Alwall, R. Frederix, S. Frixione, V. Hirschi, F. Maltoni, O. Mattelaer, H. S. Shao, T. Stelzer, P. Torrielli, and M. Zaro. The automated computation of tree-level and next-to-leading order differential cross sections, and their matching to parton shower simulations. *JHEP*, 07:079, 2014.

[106] Torbjorn Sjostrand, Stephen Mrenna, and Peter Z. Skands. A Brief Introduction to PYTHIA 8.1. *Comput. Phys. Commun.*, 178:852–867, 2008.

[107] Matteo Cacciari, Gavin P. Salam, and Gregory Soyez. The Catchment Area of Jets. *JHEP*, 04:005, 2008.

[108] Kyle Cranmer. RooStats::NumberCountingUtils. https://root.cern.ch/root/html526/RooStats__NumberCountingUtils.html, 2008. [Online; accessed 7-March-2019].

[109] Simon Fink, Christian Boeser, and Steffen Roecker. Introduction to Boosted Decision Trees: A multivariate approach to classification problems. https://indico.scc.kit.edu/event/48/contributions/3410/, 2014. [Online; accessed 7-March-2019].

[110] Andreas Hocker et al. TMVA - Toolkit for Multivariate Data Analysis. 2007.

[111] ATLAS Collaboration. Observation and measurement of Higgs boson decays to WW* with the ATLAS detector. *Phys. Rev.*, D92(1):012006, 2015.

[112] M. Aaboud et al. Jet energy scale measurements and their systematic uncertainties in proton-proton collisions at $\sqrt{s} = 13$ TeV with the ATLAS detector. *Phys. Rev.*, D96(7):072002, 2017.

[113] ATLAS Collaboration. Jet Calibration and Systematic Uncertainties for Jets Reconstructed in the ATLAS Detector at $\sqrt{s} = 13$ TeV. Technical Report ATL-PHYS-PUB-2015-015, CERN, Geneva, Jul 2015.

[114] ATLAS Collaboration. Calibration of b-tagging using dileptonic top pair events in a combinatorial likelihood approach with the ATLAS experiment. Technical Report ATLAS-CONF-2014-004, CERN, Geneva, Feb 2014.

[115] ATLAS Collaboration. Calibration of the performance of b-tagging for c and light-flavour jets in the 2012 ATLAS data. Technical Report ATLAS-CONF-2014-046, CERN, Geneva, Jul 2014.

[116] Morad Aaboud et al. Search for a scalar partner of the top quark in the jets plus missing transverse momentum final state at $\sqrt{s}$=13 TeV with the ATLAS detector. *JHEP*, 12:085, 2017.

[117] Howard Baer, Vernon Barger, Peisi Huang, Dan Mickelson, Azar Mustafayev, Warintorn Sreethawong, and Xerxes Tata. Radiatively-driven natural supersymmetry at the LHC. *JHEP*, 12:013, 2013. [Erratum: JHEP06,053(2015)].

[118] Leif Lonnblad and Stefan Prestel. Matching Tree-Level Matrix Elements with Interleaved Showers. *JHEP*, 03:019, 2012.

[119] S. Agostinelli et al. Geant4: a simulation toolkit. *Nuclear Instruments and Methods in Physics Research Section A: Accelerators, Spectrometers, Detectors and Associated Equipment*, 506(3):250 – 303, 2003.

[120] ATLAS Experiment. ATLAS Monte Carlo Truth Classifier. https://twiki.cern.ch/twiki/bin/viewauth/AtlasProtected/MCTruthClassifier, 2019. [Online; accessed 17-April-2019].

[121] Zhi Zheng. Identification of very-low transverse momentum muons with the ATLAS experiment. Technical Report ATL-MUON-PROC-2018-018, CERN, Geneva, Nov 2018.

[122] ATLAS Collaboration. Luminosity determination in pp collisions at $\sqrt{s} = 8$ TeV using the ATLAS detector at the LHC. *Eur. Phys. J.*, C76(12):653, 2016.

[123] ATLAS Collaboration. ATLAS sensitivity to top squark pair production at the HL-LHC. Technical Report ATL-PHYS-PUB-2018-021, CERN, Geneva, Oct 2018.

[124] ATLAS Collaboration. ATLAS sensitivity to winos and higgsinos with a highly compressed mass spectrum at the HL-LHC. Technical Report ATL-PHYS-PUB-2018-031, CERN, Geneva, Nov 2018.

[125] J.L. Abelleira, D. Amorim, S.A. Antipov, A. Apyan, S. Arsenyev, J. Barranco, M. Benedikt, R. Bruce, F. Burkart, Y. Cai, M. Crouch, E. Cruz-Alaniz, S. Fartoukh, M. Giovannozzi, B. Goddard, G. Guillermo Cantón, M. Hofer, R. Kersevan, P. Martinez Mirave, V. Mertens, L. Mether, Y. Muttoni, Y. Nosochkov, K. Ohmi, K. Oide, J. Osborne, V. Parma, T. Pieloni, V. Raginel, S. Redaelli, T. Risselada, L. Rivkin, I. Ruehl, B. Salvant, D. Schoerling, A. Seryi, E. Shaposhnikova, C. Tambasco, L. Tavian, E. Todesco, R. Tomas, D. Tommasini, F. Valchkova-Georgieva, L. van Riesen-Haupt, V. Venturi, D. Wollmann, D. Zhou, and F. Zimmermann. High-energy LHC design. *Journal of Physics: Conference Series*, 1067:022009, sep 2018.

[126] Howard Baer, Tim Barklow, Keisuke Fujii, Yuanning Gao, Andre Hoang, Shinya Kanemura, Jenny List, Heather E. Logan, Andrei Nomerotski, Maxim Perelstein, et al. The International Linear Collider Technical Design Report - Volume 2: Physics. 2013.

[127] Mingyi Dong and Gang Li. CEPC Conceptual Design Report: Volume 2 - Physics & Detector. 2018.

[128] Morad Aaboud et al. Observation of $H \to b\bar{b}$ decays and VH production with the ATLAS detector. *Phys. Lett.*, B786:59–86, 2018.

[129] ATLAS Collaboration. Measurement of the w-boson mass in pp collisions at $\sqrt{s} = 7$ tev with the atlas detector. *The European Physical Journal C*, 78(2):110, Feb 2018.